



TECHNISCHE  
UNIVERSITÄT  
WIEN  
Vienna University of Technology

DISSERTATION

# Modeling tropospheric delays for space geodetic techniques

Ausgeführt zum Zwecke der Erlangung des akademischen Grades eines Doktors der  
technischen Wissenschaften unter der Leitung von

Univ.-Prof. Dipl.-Ing. Dr. Johannes Böhm  
E 120-4

Department of Geodesy and Geoinformation  
Research Group Advanced Geodesy

eingereicht an der Technischen Universität Wien  
Fakultät für Mathematik und Geoinformation

von

Dipl.-Ing. Daniel Landskron  
Matr.Nr. 0825868  
Treustraße 72/24  
1200 Wien

Wien, Mai 2017



BEGUTACHTER

Assoc. Prof. Dipl.-Ing. Dr. Thomas Hobiger  
Department of Earth and Space Science  
Chalmers University of Technology, Gothenburg, Sweden

Prof. Marcelo C. Santos, Ph.D, P.Eng.  
Geodesy and Geomatics Engineering  
University of New Brunswick, Fredericton, NB, Canada



# Acknowledgments

Writing a PhD thesis demands a huge amount of time and endeavor, which, as I can tell now from my own experience, is incomparable to that of a master thesis, not to mention a bachelor thesis. Although I have tried my best, this was - of course - only possible thanks to a number of persons who have helped me a lot in the course of writing my thesis and during my three years as a PhD student at TU Wien in general. I would sincerely like to thank...

...my supervisor Prof. Johannes Böhm for his eminently valuable and unimitable way of support and guidance of my research and eventually my thesis. As one of the world's experts for atmospheric effects in space geodesy he has made my life incomparably easier in such a way as he simply knew answers to every single one of my questions that arose within these three years. He purposefully guided me through my research and never left me in doubt whether I cannot finish what I started, but always encouraged me anew when suffering from throwbacks. Albeit it is not uncommon to eloquently exaggerate the gratitude for persons mentioned in the acknowledgments of a thesis, I can say with good conscience that I do not.

...my research colleagues Matthias Madzak and Armin Hofmeister who I shared my office with during my time at TU Wien and which both have already earned their doctoral degrees. They were always available for questions and created a very friendly and familiar atmosphere which I absolutely enjoyed working in.

...all remaining research colleagues at the Department of Geodesy and Geoinformation for their help and vivid conversations throughout the last three years.

...my fiancée Aleksandra Milojevic (recurring readers may notice that we got engaged since the publication of my master thesis) for her endless support in all respects and for always keeping me on the right track so as to be able to finish my PhD, something I could hardly have imagined a few years ago.

...my parents and grandparents for their patient education from an early age which eventually enabled me to drop out of the (involuntary) family tradition of not attending universities.

...the evaluators of my thesis, Prof. Marcelo Santos from University of New Brunswick in Canada and Prof. Thomas Hobiger from Chalmers University of Technology in Sweden for taking their precious time to review my thesis and providing me with important hints and feedback.

...the Austrian Science Fund (FWF) for the financial support within the project "Ray-traced delays in der Atmosphäre für geodätische VLBI", or "RADIATE VLBI" for short.

...and last but not least the online dictionaries [www.dict.cc](http://www.dict.cc) and [www.linguee.de](http://www.linguee.de) which I consulted an estimated 1.000.000 times throughout the time I wrote this thesis. I have already specified this very number in the acknowledgments of my master thesis, but this time it appears more realistic than ever before.

This doctoral thesis contains almost all my research topics of the last three years which I have worked as a project assistant at the Department of Geodesy and Geoinformation at TU Wien. I first encountered data processing, a sometimes protracted procedure which appears to be the main occupation of a researcher, 2013 during my semester abroad in Fairbanks, Alaska where I analyzed observational data from over 600 GPS<sup>1</sup> stations in order to derive a vertical crustal motion model for the whole of Alaska for my master thesis. After returning to Vienna, and when my diploma examination got closer and closer, I played with the idea of applying for a job as a researcher at my institute because I realized more and more how I enjoyed the data analysis in Alaska, albeit this might sound absurd to non-scientists. Sometimes you realize how much you enjoyed something only after it is over. My plan apparently fell on sympathetic ears of Prof. Johannes Böhm, who back then was also the supervisor of my master thesis. Certainly not for the first time in my life fate was kind to me in such a way as it turned out that Prof. Böhm had a pending project proposal in the field of tropospheric delay modeling which was accompanied by a new position at the institute. After some months of waiting he finally notified me that the project was accepted and that I got the job.

The field of atmospheric modeling for space geodesy is very interesting for me in two respects as (1) it represents the very field of geodesy which I am most interested in and (2) it is probably the only field of geodesy which overlaps with one of my major personal interests, environmental research and protection. Possibly item (2) positively influences item (1). After all, the atmosphere is that part of the earth where all 110 billion ( $1.1 \cdot 10^{11}$ ) people and possibly octillions ( $x \cdot 10^{48}$ ) of animals have spent their lives since the big bang and to which naturally great importance in research is attached. Through a concatenation of coincidences in the course of the universal evolution it contains the very mix of gases, the very range of temperatures and the very balance of pressure that enables us humans to live and us scientists to conduct research. But if one goes through life with eyes open it is undeniable that the current 7.5 billion ( $7.5 \cdot 10^9$ ) humans progressively endanger this habitat. Without going into any detail here as it probably has not a bit to do with the remaining 172 pages of this thesis, I can say that I indeed have the strong desire to bring myself into play in investigating the atmosphere. As a matter of course, increasing the accuracy of modeling propagation delays which electromagnetic signals experience due to their intolerance of gaseous matter by some few sub-millimeters certainly won't shift the

---

<sup>1</sup>Global Positioning System

imminent termination of mankind backwards, but still - there is a clear overlap. Therefore I confidently keep on researching in this field and can honestly say that I put all my scientific endeavor into it. Nevertheless, when being engrossed in the deepest depths of a research topic it happens quite often that one simply reels off calculations and determinations to finally get results while losing sight of the proper sense of one's doing. In other words, that one misses the forest for the trees. And it is probably one of the major challenges of researchers to always keep in mind the whys and wherefores of their actions. For this reason I am absolutely convinced that one cannot be successful in the long run without bearing a certain amount of passion for a job. This is what leads the way out of the forest and what makes the difference between an ordinary researcher and a successful researcher aside from intelligence and wisdom - passion.

Be that as it may, if you still kept reading up to this point your last name in all likelihood will be Böhm, Hobiger or Santos and your incentive may rather be official purposes than entirely voluntary nature, however I am highly grateful and - not least - proud that things worked out so well that I have been able to finish this thesis including results which I am very content with and that I am currently only a stone's throw away from receiving my PhD, what indeed means a lot to me. And it's up to you to decide at the end whether the final results of this thesis suggest that it evolved either from pure necessity or solely from true passion. Or maybe something in between? Be honest with yourself, so am I.





*Honesty is the best policy - when there is money in it.*

- Mark Twain (1835-1910)



# Kurzfassung

Elektromagnetische Wellen werden auf ihrem Signalweg durch die neutrale Atmosphäre oder Troposphäre verzögert und gekrümmt. Da es keine Möglichkeit gibt, diese troposphärische Laufzeitverzögerung mit ausreichender Genauigkeit direkt zu messen, muss sie stattdessen mittels Daten aus anderen Quellen modelliert werden. Fehlerhafte Modellierung dieser Laufzeitverzögerungen ist eine der Hauptfehlerquellen geodätischer Weltraumverfahren wie Very Long Baseline Interferometry (VLBI) und Global Navigation Satellite Systems (GNSS). Durch Verwendung sogenannter Mappingfunktionen können die Laufzeitverzögerungen von der Zenitrichtung auf die jeweilige Beobachtungselevation reduziert werden. Im Laufe der Zeit wurden immer genauere Mappingfunktionen entwickelt, wobei die Vienna Mapping Functions 1 (VMF1) das derzeit genaueste Modell darstellt. Nicht zuletzt da die Publikation der VMF1 bereits auf 2006 datiert, war es an der Zeit, an einem Nachfolger zu arbeiten. Auf diese Weise entstand die Vienna Mapping Functions 3 (VMF3), welcher der Großteil dieser Dissertation gewidmet ist. Die VMF3 ist gekennzeichnet durch räumlich und zeitlich variable  $b$  und  $c$  Koeffizienten und neue  $a$  Koeffizienten, welche auf Basis von Laufzeitverzögerungen aus Raytracing des Programmes *RADIATE* bestimmt worden sind. Eine Reihe von Vergleichen unterstreicht die Fähigkeit von VMF3, die Genauigkeit modellierter Laufzeitverzögerungen weiter zu steigern, besonders bei niedrigen Elevationen. Insbesondere Laufzeitverzögerungen bei niedrigen Elevationen, welche mit VMF3 modelliert werden, kommen deutlich näher an die Werte aus dem Raytracing als jene aus VMF1. Zusätzlich wurde eine neue Mappingfunktion mit dem Namen Global Pressure and Temperature 3 (GPT3) entwickelt, welche lediglich auf empirischen Werten beruht und das Ziel hat, die Leistungsfähigkeit der Mappingfunktion Global Pressure and Temperature 2 wet (GPT2w) weiter zu steigern. Trotz des komplexeren zugrundeliegenden Modells schafft es GPT3 jedoch nicht, die Leistung von GPT2w zu übertreffen sondern scheint dieser relativ gleichwertig zu sein. Dies zeigt sich in Vergleichen sowohl von Laufzeitverzögerungsunterschieden zu Raytracing als auch von Basislinienlängenwiederholbarkeiten (BLR) und deutet darauf hin, dass der derzeitige Stand der Technik bei empirischen Troposphärenmodellen bereits sehr hoch ist.

Neben Mappingfunktionen wurden auch neue Ansätze zur Modellierung azimuthaler Asymmetrie entworfen und getestet, im Besonderen für die Verwendung als a priori Werte in VLBI-Auswertungen. In diesem Gebiet gibt es nicht allzu viele vorhandene Modelle, wobei die Linear Horizontal Gradients (LHG) das womöglich wichtigste darstellen. Aus diesem Grund wurden neue a priori-Gradientenmodelle auf Basis von Laufzeitverzögerun-

gen aus Raytracing berechnet, die unter dem Namen GRAD zusammengefasst werden. Es zeigt sich anhand von Vergleichen von BLR aus VLBI-Auswertungen, dass diese in der Lage sind, die Genauigkeit modellierter Laufzeitverzögerungen deutlich zu steigern, und zwar um bis zu 5% im Vergleich zu LHG. Ein verfeinertes Gradientenmodell GRAD-2 schafft es hierbei, die Genauigkeit noch weiter zu steigern. Außerdem konnte herausgefunden werden, dass die Verwendung von a priori-Gradienten (und besonders jene von GRAD) in der VLBI-Auswertung eine höhere Bedeutung zukommt als bisher angenommen, da die übliche Gradientenschätzung nach der Methode der kleinsten Quadrate im Falle von Sessions mit einer geringen Anzahl an Beobachtungen schlechte Ergebnisse bringen kann. Die Verwendung von a priori-Gradienten schafft dem Abhilfe indem sie die Genauigkeit von über 90% aller VLBI Sessions zu steigern vermag. Zu guterletzt wurde ein globales empirisches Gradientengitter entworfen, welches derzeitige Gradientenmodelle an Leistung übertrifft und in GPT3 eingegliedert ist. Es ist auf einem  $5^\circ \times 5^\circ$ -Gitter mit jährlichen und halbjährlichen Komponenten realisiert und kann für jeden beliebigen Punkt auf der Erde angewandt werden. GPT3 schafft es, im Vergleich zur Vernachlässigung von a priori-Gradienten die BLR von 14% der Basislinien um mehr als 1 mm zu verbessern, während es nur 6% der Basislinien um mehr als 1 mm verschlechtert. Auch in Vergleichen von Laufzeitverzögerungsunterschieden zu Raytracing schneidet GPT3 besser ab als bestehende empirische Gradientenmodelle, jedoch sind empirische Gradientenmodelle ohnehin nur imstande einen kleinen Teil der eigentlichen azimuthalen Asymmetrie zu beschreiben da diese infolge von Wetterveränderungen ständig schwankt. Vor allem für die Bestimmung terrestrischer (TRF) und zälestischer Referenzrahmen (CRF) sind empirische Gradienten aber dennoch von großer Bedeutung.

# Abstract

Electromagnetic waves are delayed and bent during their passage through the neutral atmosphere or troposphere. As there is no chance to directly measure tropospheric delays with sufficient accuracy, they need to be modeled using data from other sources. Incorrect modeling of these delays is one major error source for space geodetic techniques such as Very Long Baseline Interferometry (VLBI) and Global Navigation Satellite Systems (GNSS). By the use of mapping functions the delays can be scaled from zenith direction to the respective elevation of observation. With the passing of time more and more accurate mapping functions have been developed, yet peaking at the performance of the Vienna Mapping Functions 1 (VMF1). Not least because VMF1 dates back to 2006 it was advisable to work on a successor. By this means the Vienna Mapping Functions 3 (VMF3) arose, to which the bulk of this thesis is devoted. It is characterized by spatially and temporally varying  $b$  and  $c$  coefficients and new  $a$  coefficients calculated on the basis of ray-traced delays from the ray-tracer *RADIATE*. Several comparisons prove the ability of VMF3 to further enhance the accuracy of modeled tropospheric delays, especially at low elevation angles. Slant delays modeled with the VMF3 approach approximate the ray-traced delays significantly better than with the VMF1 approach. Apart from that, a new mapping function which is based solely on empirical values is developed as well, referred to as Global Pressure and Temperature 3 (GPT3). It is designed in order to improve the existing Global Pressure and Temperature 2 Wet (GPT2w) model, which is currently regarded as a very accurate empiric troposphere model. In spite of the more sophisticated underlying model, GPT3 is not able to surpass the performance of GPT2w but appears to be equivalent. This is proven both on the basis of comparisons of delay differences to ray-tracing as well as baseline length repeatabilities (BLR). It prompts the conclusion that the state of the art of (empirical) troposphere modeling under current conditions is already very advanced.

Apart from the new mapping functions, new approaches to model azimuthal asymmetry were designed and tested as well, especially for a priori use in VLBI analysis. There are not too many existing models in the field of horizontal a priori gradients, with the most important probably being the Linear Horizontal Gradients (LHG). For this reason, new a priori gradient models were determined based on ray-traced delays from *RADIATE* which are referred to as GRAD. These turns out to significantly improve the accuracy of tropospheric delays. This is proven by BLR comparisons in VLBI analysis, where its application lowers the BLR up to 5% compared to LHG. An extended gradient model

(GRAD-2) brings a further slight improvement compared to GRAD. Moreover it was found that, in general, the application of a priori gradients (especially that of GRAD) in VLBI analysis is more important than previously assumed, because the usual estimation through least-squares adjustments might not yield reliable results for sessions which do not possess a high number of observations. Application of a priori gradients produces relief in this respect, increasing the accuracy of a whole 90% of the sessions in VLBI history. Last but not least, a global grid containing empirical values for horizontal gradients is developed and included in GPT3, which is able to outperform existing models for empirical gradients. It is applicable to any point on Earth through provision on a  $5^\circ \times 5^\circ$  grid and is refined with a temporal variation. In terms of BLR, GPT3 is able to improve 14% of the baselines by more than 1 mm and degrade only 6% by more than 1 mm with respect to no a priori gradients. GPT3 performs better than existing empirical gradient models also in delay comparisons, however empirical gradients are able to describe only a very limited part of the actual azimuthal asymmetry as it is fluctuating rapidly due to random weather variations. Nevertheless, particularly for the determination of terrestrial reference frames (TRF) and celestial reference frames (CRF) the use of a priori gradients is essential.

# Contents

<b>Acknowledgments</b>	<b>i</b>
<b>Inhaltsangabe</b>	<b>vii</b>
<b>Abstract</b>	<b>ix</b>
<b>1 Introduction</b>	<b>1</b>
<b>2 Fundamentals</b>	<b>5</b>
2.1 Fundamentals of mapping functions and zenith delays . . . . .	5
2.1.1 Fundamentals of VMF1 . . . . .	9
2.1.2 Fundamentals of GPT2w . . . . .	11
2.2 Fundamentals of azimuthal asymmetry . . . . .	12
<b>3 Site-Augmentation of Troposphere Models</b>	<b>17</b>
3.1 Recalculation of MTT coefficients . . . . .	17
3.1.1 Comparison of temperature input from various sources . . . . .	19
3.2 Site-augmentation of GPT2w (SA-GPT2w) . . . . .	20
3.2.1 Correlation between the quantities . . . . .	21
3.2.2 Determination of universal weighting coefficients . . . . .	24
3.2.3 Determination of non-universal weighting coefficients . . . . .	26
3.2.4 Application of SA-GPT2w . . . . .	28
3.2.5 Results . . . . .	29
3.2.5.1 Comparison with delays of VMF1 . . . . .	29
3.2.5.2 Comparison with delays from VLBI analysis using VieVS . . . . .	32
3.2.5.3 Comparison with delays from GNSS analysis . . . . .	34
3.2.5.4 Comparison of BLR . . . . .	43
3.2.6 Conclusions . . . . .	44
3.3 Site-augmentation of VMF1 . . . . .	46
3.3.1 Application of the site-augmented VMF1 . . . . .	47
3.3.2 Conclusions . . . . .	49
<b>4 Determination of new mapping function concepts</b>	<b>51</b>
4.1 Determination of reprocessed VMF1 mapping function coefficients . . . . .	53
4.1.1 Empirical values for b and c, analytically calculating a . . . . .	53

4.1.2	Empirical values for b and c, least-squares adjustment for a . . . . .	55
4.2	Least-squares adjustment for a, b and c . . . . .	56
4.3	Determination of a new discrete mapping function (VMF3) . . . . .	58
4.4	Determination of a new empirical mapping function (GPT3) . . . . .	66
4.5	Comparisons and results . . . . .	69
4.5.1	Comparison of BLR . . . . .	70
4.5.2	Comparison of modeled delays with ray-traced delays . . . . .	74
4.6	Conclusions . . . . .	88
<b>5</b>	<b>Azimuthal asymmetry</b>	<b>91</b>
5.1	Determination of discrete horizontal gradients . . . . .	91
5.1.1	Determination of horizontal gradients for the time period of CONT11	92
5.1.1.1	Determining gradients using the standard gradient formula	92
5.1.1.2	Determining gradients using extended gradient formulae . .	96
5.1.1.3	Estimating gradients in VLBI analysis . . . . .	100
5.1.2	Determination of horizontal gradients for nine years of VLBI data .	103
5.1.2.1	Comparison with other gradients . . . . .	104
5.1.2.2	Comparison of BLR . . . . .	105
5.1.3	Comparison of modeled delays with ray-traced delays . . . . .	111
5.1.4	Results . . . . .	115
5.2	Determination of an empirical gradient grid . . . . .	115
5.2.1	Deflections of the vertical (DOV) represented as horizontal gradients	121
<b>6</b>	<b>Conclusions and Outlook</b>	<b>125</b>
	<b>Appendices</b>	<b>129</b>
<b>A</b>	<b>List of variables, acronyms and explanations of important terms</b>	<b>130</b>
<b>B</b>	<b>Quality of the meteorological data</b>	<b>140</b>
B.1	Problems of the meteorological measurements in the NGS-files . . . . .	140
B.2	Comparing several meteorological data . . . . .	141
<b>C</b>	<b>Additional figures</b>	<b>144</b>
	<b>Epilogue</b>	<b>147</b>
	<b>Bibliography</b>	<b>149</b>
	<b>List of Figures</b>	<b>157</b>
	<b>List of Tables</b>	<b>165</b>
	<b>Curriculum Vitae</b>	<b>171</b>



# 1. Introduction

Positioning on Earth using space geodetic methods has become a crucial field in the current technological standard and is assumed to become even more important in the near future. Satellite-based positioning and navigation on smart phones grew to become integral parts for society and are nowadays indispensable for upholding the economic system of our world. Although only a very low percentage of users may be aware of the theory behind deriving positions through Global Navigation Satellite Systems (GNSS) in the blink of an eye, even fewer may know about the space geodetic framework which makes the launch and operation of a GNSS possible in the first place. This includes determination of terrestrial coordinate frames, satellite orbits, celestial motions and terrestrial motions as well as external effects acting on satellites. All these frameworks could not have been derived without interaction with the three other major space geodetic techniques aside from GNSS: Very Long Baseline Interferometry (VLBI), Satellite Laser Ranging (SLR)<sup>1</sup> and Doppler Orbitography and Radiopositioning Integrated by Satellite (DORIS).

On the other hand, none of the aforementioned frameworks could have been determined without detailed knowledge about the propagation of electromagnetic waves. Findings of physicists over hundreds of years built the basis for measuring the travel time of electromagnetic signals with such high precision. Today we know that the propagation velocity of electromagnetic waves through non-vacuum media such as the Earth's atmosphere deviates from speed of light for different reasons. In fact, signals thus experience a time delay. However, as the chemical composition of matter in the atmosphere fluctuates heavily both on the temporal and the spatial scale, the actual propagation time and propagation path of signals cannot be determined exactly. Instead they need to be modeled what constitutes a major error potential in all four space geodetic techniques and has long since been an important topic of research. For geodetic purposes the atmosphere is separated into two parts. The ionosphere is *"considered to be that region of an atmosphere where significant numbers of free thermal (<1 eV) electrons and ions are present"* [Schunk and Nagy, 2009] and extends from about 60 km to up to 3000 km height, with the maximum electron concentration occurring at around 300 km. On the other hand, the neutral atmosphere *"is an atmosphere consisting of neutral gas, in contrast with the ionosphere"* [Selsis, 2011]<sup>2</sup>. As the title of this thesis suggests, the ionosphere's influence is dropped here on behalf of the neutral atmosphere. Within the neutral atmosphere there is another separation

---

<sup>1</sup>which includes also Lunar Laser Ranging (LLR)

<sup>2</sup>it became established in geodesy to sloppily use the term *troposphere* synonymously for *neutral atmosphere*, although these two terms physically do not exactly mean the same

made, that is into a hydrostatic and a wet part. The hydrostatic part decelerates electromagnetic signals by around two meters in zenith direction and is rather easy to be determined when having information about the pressure at the site. On the other hand, the wet delay accounts for only a tenth of the hydrostatic delay but is very difficult to be precisely determined.

The most accurate way of obtaining tropospheric delays and mapping functions nowadays is by ray-tracing through numerical weather models (NWM). Unlike terrestrial methods, ray-tracing is capable of considering the effect of the whole atmosphere including information that could not be captured otherwise. Nevertheless, even NWM can describe the actual state of the atmosphere only to a certain degree, as the information is reduced and compressed on the one hand to a limited number of height levels (up to e.g.  $\sim 25$ ) and on the other hand to a certain horizontal resolution, e.g.  $1^\circ \times 1^\circ$ , what equals to a grid size of  $\sim 110$  km at the Earth's surface. Ray-traced delays, however, have to be produced separately for each observation at a certain azimuth and elevation angle what limits its use especially for GNSS where it is absolutely impossible to compute delays for all observations. For this reason, the information from ray-tracing is packed to mapping functions, which can then "simulate" the delay for any elevation angle. These mapping functions can appropriately be applied to all observations without need for initial calculation on the part of the user.

Despite intensive research and significant advances in the past and present, errors in troposphere modeling still represent a major error source for space geodetic techniques what obviously leaves much room for improvement. Enhanced knowledge about signal delays in the troposphere would enable more precise products of space geodetic techniques and in consequence more accurate positioning. Apart from that, the Global Geodetic Observing System (GGOS) has set goals for VLBI accuracy of 1 mm in position and 0.1 mm/yr in velocity. There would be no chance to achieve these goals without gaining considerable improvements in modeling the troposphere. For this reason there still remains vital necessity for research in tropospheric effects on space geodetic signals through improving currently used models, such as this thesis addresses.

The structure of this thesis is as follows: first, the fundamentals shall give a general understanding of the basics which are assumed in the further course (Chapter 2). Thereafter, Chapter 3 discusses possibilities of augmenting the performance of existing troposphere models through in situ measured meteorological data, the most important output being the Site-Augmented GPT2w (SA-GPT2w, Section 3.2), where the empirical troposphere model Global Pressure and Temperature 2 wet (GPT2w) is augmented by temperature and humidity measurements at the station. Chapter 4 represents the most important part of this thesis that contains determination of a new discrete mapping function (Vienna Mapping Functions 3 (VMF3), Section 4.3) as well as a new empirical mapping function

(Global Pressure and Temperature 3 (GPT3), Section 4.4)<sup>3</sup>. The final Chapter 5 comprises of important findings in modeling azimuthal asymmetry of tropospheric delays in particular involving new discrete gradients to be applied a priori in VLBI analysis (GRAD, Section 5.1) as well as an empirical gradient grid suited for any space geodetic technique. Finally, Chapter 6 sums up the results of all chapters and discusses their impact and importance for troposphere modeling.

---

<sup>3</sup>the name VMF3 is chosen to be consistent in the VMF series, because *Böhm et al.* [2005] drafted the Vienna Mapping Function 2 (VMF2) which also includes an azimuthal dependency component but has never become operational as it was not able to sufficiently improve the results [*Johannes Böhm*, personal communication, 2017/02]. Apart from that, thus consistency with GPT3, which is based on the same underlying data, is granted



## 2. Fundamentals

Electromagnetic signals such as those naturally emitted from quasars and recorded by VLBI antennas or artificially generated by GNSS satellites and recorded by GNSS antennas do not constantly propagate in a straight line from source to receiver, but are delayed and bent during their passage through non-vacuum media such as the Earth's atmosphere. The propagation delay of radio waves arising during its passage through the troposphere can usually not be directly measured<sup>1</sup> nor can it be eliminated by measurements in two different frequencies as is possible for the ionospheric delay<sup>2</sup>. Instead, the delay has to be approximated through modeling. For very detailed descriptions of the emergence of tropospheric delays it is referenced to *Hofmeister* [2016], *Böhm et al.* [2013a] and *Nilsson et al.* [2013].

The modeling of tropospheric delays can appropriately be split into two parts: the first part considers only variations in the delay owing to different elevations, with the delays temporarily assumed to be equivalent for all azimuths around the site. The second part considers also these very variations owing to different azimuths. Likewise the fundamentals are split into these two parts, and in general the whole thesis is set up on the basis of this distinction.

### 2.1. Fundamentals of mapping functions and zenith delays

The tropospheric delay at a given observation elevation  $\varepsilon$  is generally modeled by means of multiplying the delay in zenith direction  $\Delta L^z$  with a mapping function  $mf(\varepsilon)$  which maps the delay from the vertical down to the observed elevation<sup>3</sup> (Eq. (2.1)).

$$\Delta L(\varepsilon) = \Delta L_h^z \cdot mf_h(\varepsilon) + \Delta L_w^z \cdot mf_w(\varepsilon) \quad (2.1)$$

---

<sup>1</sup>using so-called water vapor radiometers would allow determining the wet part of the path delay in a certain direction quite accurately under optimal conditions; such devices, however, are very costly and inhere some observation limitations, which is why they are not considered in this thesis

<sup>2</sup>this can be done because the ionosphere is a dispersive medium; as a result, the phase velocity of an electromagnetic wave depends on its frequency. The troposphere, however, is non-dispersive for electromagnetic waves up to 15 GHz [*Hofmann-Wellenhof et al.*, 1992], which includes VLBI (2.3 GHz and 8.4 GHz, respectively) as well as GNSS (approximately 1.1 GHz to 1.6 GHz)

<sup>3</sup>what is meant here is the elevation angle in vacuum, that is, the elevation angle at which the atmosphere is entered and not the elevation at which the antenna observes; due to geometric bending effect, these two do not exactly coincide

In Eq. (2.1) it becomes obvious that the modeling is generally split into a hydrostatic and a wet part<sup>4</sup>. This separation is particularly pronounced at small elevation angles, while the idea behind is to decrease the influence of variations in the wet part, which happen more rapidly than can be modeled with six-hourly time intervals [Böhm *et al.*, 2006a]. By using in situ measurements of pressure  $p$ , the zenith hydrostatic delay  $\Delta L_h^z$  can be determined very accurately through the following equation, devised by Saastamoinen [1972] and revised by Davis *et al.* [1985]:

$$\Delta L_h^z = \frac{0.0022768 \cdot p}{1 - 0.00266 \cdot \cos(2\varphi) - 0.28 \cdot 10^{-6} \cdot h_{ell}} \quad (2.2)$$

This calculation of the zenith hydrostatic delay  $\Delta L_h^z$  is common usage in both GNSS and VLBI analysis. Therefore it is imperative to know about the local pressure at the time of the measurement. In case no direct measurement is possible, the pressure value can also be extracted from numerical weather models or, accepting further losses in accuracy, from empirical troposphere models.

Determination of the zenith wet delay  $\Delta L_w^z$  is infinitely more difficult as there is no chance to acquire precise values from surface measurements only. Whereas  $\Delta L_h^z$  can be calculated from in situ pressure only,  $\Delta L_w^z$  is dependent on the whole distribution of water vapor above the site. However, with in situ information about the water vapor pressure  $e$  one can at least approximate  $\Delta L_w^z$  using the formula by Askne and Nordius [1987] (Eq. (2.3)), which is a rigorous way of approximating zenith wet delays from surface data down to the present day:

$$\Delta L_w^z = 10^{-6} \cdot \left( 16.5203 + \frac{377600}{T_m} \right) \cdot \frac{R_d \cdot e}{g_m \cdot (\lambda + 1)} \quad (2.3)$$

where  $R_d$  is the specific gas constant for dry constituents which equals  $287.0464 \frac{J}{K \cdot kg}$  and  $g_m$  is the mean gravity which equals  $9.80665 \frac{m}{s^2}$ <sup>5</sup>. Here, water vapor pressure  $e$  is the dominant factor which must first be converted from relative humidity  $f$  and temperature  $T$  using the so-called "Magnus formula" (see Kraus [2004]):

$$e = \frac{f}{100} \cdot 6.1078 \cdot \exp^{\frac{17.1 \cdot T}{235 + T}} \quad (2.4)$$

The simplest possible form of a mapping function is the equation  $mf(\varepsilon) = \frac{1}{\sin(\varepsilon)}$ , which assumes the atmosphere to be flat and planar. For the range of all possible elevations from zenith to horizon, the resulting mapping factors are outlined in Fig. 2.1 together with the respective mapping function from VMF1, which is regarded as the "true" value here. It is obvious that mapping functions are most important for smaller elevation angles. According to Nilsson *et al.* [2013], the mapping approach  $mf(\varepsilon) = \frac{1}{\sin(\varepsilon)}$  would even be sufficient for elevations above 20° what is also proven by Fig. 2.1. In order to gain higher accuracy, Marini [1972] developed a new model in which mapping functions are set up

<sup>4</sup>the effect of atmospheric bending as a result of refraction is accounted for by the hydrostatic part

<sup>5</sup>in the original paper, the normal gravity dependent on latitude and height is used; however, as it does not impair the accuracy in any way, it is replaced by the mean gravity here

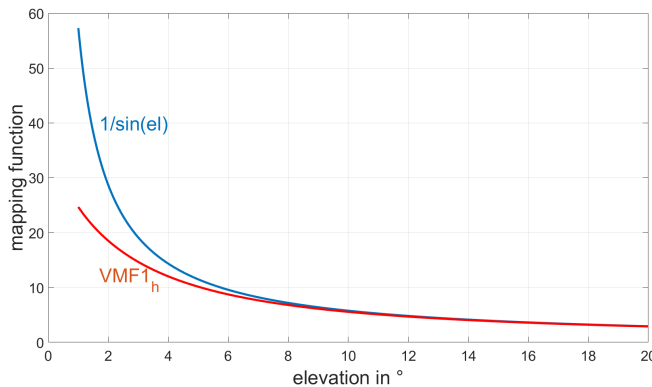


Figure 2.1.: Comparison of the simple mapping function approach  $mf(\varepsilon) = \frac{1}{\sin(\varepsilon)}$  with the hydrostatic VMF1, in this case exemplarily for VLBI station WETTZELL on September 15, 2011, 00:00. It can be seen that the mapping functions diverge particularly at low elevations.

as a continued fraction of  $mf(\varepsilon) = \frac{1}{\sin(\varepsilon)}$  valid for any horizontally stratified atmosphere. Nowadays, its truncated form by *Herring* [1992] is generally used in space geodesy (Eq. (2.5)).

$$mf(\varepsilon) = \frac{1 + \frac{a}{1 + \frac{b}{1 + c}}}{\sin(\varepsilon) + \frac{a}{\sin(\varepsilon) + \frac{b}{\sin(\varepsilon) + c}}} \quad (2.5)$$

Unlike  $mf(\varepsilon) = \frac{1}{\sin(\varepsilon)}$ , the arrangement of the mapping function coefficients  $a$ ,  $b$  and  $c$  is designed to consider the effect of the atmosphere's curvature, which results from the Earth's curvature. *Herring* [1992] defines  $a$ ,  $b$  and  $c$  as coefficients that depend on integrals of refractivity through the atmosphere. How these coefficients can be derived will be explained in Section 2.1.1. Due to the fact that the coefficients  $b$  and  $c$  are at subordinated positions in Eq. (2.5), errors in them influence the result (i.e. the value of the mapping function) less strongly than errors in the  $a$  coefficient. Obviously, the  $c$  value has the least influence. On the other hand, even small errors in the  $a$  coefficient may have a vast impact on the result. With decreasing thickness of the atmosphere compared to the Earth radius, the atmosphere appears more planar and the mapping function approaches  $\frac{1}{\sin(\varepsilon)}$  [*Niell*, 2000].

Mapping functions can be of empirical or discrete nature; empirical mapping functions are based on averaged experience values of past years, while discrete mapping functions use real observation data at discrete times. As a matter of course, the latter are thought to be more precise as they are able to consider the real state of the atmosphere at the time of the observation. In the following a short overview of the history of developing mapping functions is given. Improvements in atmosphere mapping functions have generally always resulted in significant advances in the accuracy of geodetic products [*Davis et al.*, 1985; *Niell*, 1996].

The continued fraction form by *Marini* [1972] from Eq. (2.5) is the basis for almost all

mapping functions developed until today. It was first used in a slightly different shape with two coefficients  $a$  and  $b$  in *Marini and Murray* [1973] for the hydrostatic delay.

*Lanyi* [1984] invented the same-named Lanyi Mapping Functions, which require surface temperature as input and adopt a series of complex physical equations for the calculation of the slant total delay. Probably due to its intricate formulae and the non-provision of a ready-to-use script, the Lanyi Mapping Functions did not gain wide acceptance in troposphere modeling.

*Herring* [1992] invented the MIT Temperature (MTT) mapping functions which strongly depend on surface measurements of temperature as well, but based on a straightforward and easy-to-use equation system. Here, the truncated continued fraction form as written in Eq. (2.5) was first used. The coefficients for MTT were developed by ray-tracing through atmospheres with temperature and water vapor profiles by rawinsondes which were launched from 10 locations close to VLBI stations in the US. 16 elevation angles between  $3^\circ$  and  $90^\circ$  were chosen. The resulting equations for the hydrostatic and wet mapping function coefficients  $a$ ,  $b$  and  $c$ , each dependent on geographic latitude  $\varphi$ , station height  $h$  (in km) and temperature  $T$  (in  $^\circ\text{C}$ ), read:

$$\begin{aligned}
 a_h &= [1.2320 + 0.0139 \cdot \cos(\varphi) - 0.0209 \cdot h + 0.00215 \cdot (T - 10)] \cdot 10^{-3} \\
 b_h &= [3.1612 - 0.1600 \cdot \cos(\varphi) - 0.0331 \cdot h + 0.00206 \cdot (T - 10)] \cdot 10^{-3} \\
 c_h &= [71.244 - 4.2930 \cdot \cos(\varphi) - 0.1490 \cdot h - 0.00210 \cdot (T - 10)] \cdot 10^{-3} \\
 a_w &= [0.5830 - 0.0110 \cdot \cos(\varphi) - 0.0520 \cdot h + 0.00140 \cdot (T - 10)] \cdot 10^{-3} \\
 b_w &= [1.4020 - 0.1020 \cdot \cos(\varphi) - 0.1010 \cdot h + 0.00200 \cdot (T - 10)] \cdot 10^{-3} \\
 c_w &= [45.850 - 1.9100 \cdot \cos(\varphi) - 1.2900 \cdot h + 0.01500 \cdot (T - 10)] \cdot 10^{-3}
 \end{aligned} \tag{2.6}$$

A separate section of this thesis is dedicated to the MTT, in which it is tested to which extent re-calculated MTT coefficients influence the resulting delays (Section 3.1).

The most important developments of mapping functions around the millennium were the New Mapping Functions (NMF) [*Niell*, 1996] and the Isobaric Mapping Functions (IMF) [*Niell*, 2000]. The former represent an empirical model which does not require any measurement data but only geographical information and the day of year (doy) of the observation. It was of particular importance for GNSS stations which are seldom equipped with meteorological sensors. The IMF, on the other hand, is the first mapping function in which data from numerical weather models (NWM) containing information about the current state of the atmosphere is incorporated, what proves to be the optimal data input to this day. Similar to the VMF, which was introduced four years later (cf. Section 2.1.1), the coefficients  $b$  and  $c$  are of empirical nature while all information of the NWM is condensed in the  $a$  coefficients.

In 2004, the Vienna Mapping Functions (VMF) [*Böhm*, 2004] were developed which, unlike IMF, exploit the complete information from NWM and originally aimed at improving particularly the wet part of IMF. The empirical coefficients  $b$  and  $c$  were taken from



IMF for the hydrostatic part and from NMF for the wet part, respectively.

The follow-on Vienna Mapping Functions 1 (VMF1) [Böhm *et al.*, 2006a] are characterized by new empirical values for  $b_h$  and  $c_h$  and thus re-calculated  $a$  coefficients. More on this in the upcoming Section 2.1.1.

Böhm *et al.* [2006b] also developed a new empirical mapping function in the same year, the Global Mapping Functions (GMF), acting on some deficiencies of NMF. The GMF has equivalent coefficients  $b$  and  $c$  as VMF1, but the  $a$  coefficients were not determined discretely from real NWM data, but got empirical values from spherical harmonics expansions. In contrast to NMF, there is also a longitudinal variation and biases at high latitudes are diminished.

Although not directly for the purpose of deriving mapping functions, Hobiger *et al.* [2008a] successfully performed ray-tracing through NWM of the Japanese Meteorological Agency (JMA) for deriving tropospheric slant delays for precise point positioning (PPP).

Lagler *et al.* [2013] designed Global Pressure and Temperature 2 (GPT2), which is some kind of improved version of GMF and the empirical troposphere model Global Pressure and Temperature (GPT) [Böhm *et al.*, 2007], which provides climatological values for pressure and temperature.

In order to describe the wet part of the delay more closely, the successor Global Pressure and Temperature 2 wet (GPT2w) [Böhm *et al.*, 2015] bases on most values from GPT2 but got new humidity parameters. For a close description of GPT2w, see Section 2.1.2.

### 2.1.1. Fundamentals of VMF1

As already mentioned before, the VMF1 are based on the same model as VMF, but with new empirical coefficients  $b_h$  and  $c_h$ . As a consequence, the resulting  $a$  coefficients get different values than those from VMF. The specifications for the determination of VMF1 are defined in Table 2.1. The mapping function coefficients  $b$  and  $c$  have empirical values, while the  $a$  coefficients are directly calculated for the elevation angle  $3.3^\circ$ . This is also referred to as the "fast approach" in Böhm *et al.* [2006a]. The coefficients  $b_h$ ,  $b_w$  as well as  $c_w$  are constants, while  $c_h$  is dependent on day and latitude. The values read:

$$\begin{aligned}
 b_h &= 0.0029 \\
 b_w &= 0.00146 \\
 c_w &= 0.04391 \\
 c_h &= 0.062 + \left( \left( \cos \left( \frac{\text{doy} - 28}{365.25} 2\pi + \Psi \right) + 1 \right) \cdot \frac{c_{11}}{2} + c_{10} \right) \cdot (1 - \cos(\varphi))
 \end{aligned} \tag{2.7}$$

where  $\varphi$  is the latitude of the site in radians,  $\Psi = 0$  for sites on the northern hemisphere and  $\Psi = \pi$  for sites on the southern hemisphere,  $c_{10} = 0.001$  for sites on the northern

Table 2.1.: *Properties of the ray-traced delays which are used to determine VMF1 [Böhm, 2004; Böhm et al., 2006a].*

PARAMETER	SPECIFICATION
Ray-tracing software	Simple 1D ray-tracer
NWM	ECMWF ERA-40 Re-Analysis (1979-2001), ECMWF Operational (2002-today)
Horizontal resolution of the NWM	$2.0^\circ \times 2.5^\circ$
Horizontal coverage	all IVS, IGS and IDS stations, and on a global grid ( $2.0^\circ \times 2.5^\circ$ spatial resolution)
Vertical coverage	15 pressure levels (1979-2003/08/26), 21 pressure levels (2003/08/27-today)
Temporal resolution	6-hourly at 00:00, 06:00, 12:00 and 18:00 each day from 1979-today (IVS), 2002-today (IGS+IDS), 1979-today (grid), additionally forecast data up to 2 days in future [Böhm et al., 2009]
Tuned for elevation	$3.3^\circ$ (initial elevation at site)

hemisphere and  $c_{10} = 0.002$  for sites on the southern hemisphere, and  $c_{11} = 0.005$  for sites on the northern hemisphere and  $c_{11} = 0.007$  for sites on the southern hemisphere. By inserting  $mf(\varepsilon) = \frac{\Delta L}{\Delta L^z}$ , which can be derived from ray-tracing, and solving Eq. (2.5) for  $a$ , the hydrostatic and wet  $a$  coefficients can be calculated:

$$a = - \frac{mf(\varepsilon) \cdot \sin(\varepsilon) - 1}{mf(\varepsilon)} - \frac{1}{\sin(\varepsilon) + \frac{b}{\sin(\varepsilon) + c}} - \frac{1}{1 + \frac{b}{1 + c}} \quad (2.8)$$

Thus, the information of the NWM is included in the  $a$  coefficients. As they are the determining elements of the mapping function, shortcomings in the empirical  $b$  and  $c$  coefficients can usually be compensated by them. This is also due to the high correlation between the three coefficients [Böhm, 2004].

Exact values for mapping functions are highly important, as according to a rule of thumb by Böhm et al. [2006a], the resulting error in station height is approximately 1/5 of the mapping function error at  $5^\circ$  elevation.

As already outlined in Table 2.1, the VMF1 data is published on the one hand station-wise and on the other hand on a grid, six-hourly each. If analyses are made for IGS, IVS or IDS stations, VMF1 coefficients can be extracted directly for these sites and just need to be interpolated temporally to the very times of the observations. If, however, the site is arbitrarily located in the field, one needs to rely on the grid-wise VMF1. The user needs to bilinearly interpolate the VMF1 values from four surrounding grid points

to his position. Given the grid size of  $2.0^\circ \times 2.5^\circ$ , these grid points can be up to 180 km away each. It stands to reason that this simplification leads to a loss in accuracy. When looking closely at the station-wise VMF1, the situation is not necessarily different though as all information from the NWM is interpolated to the discrete location of the stations beforehand, what results in a comparable loss of accuracy. For recent data, however, NWM with a higher horizontal resolution of  $0.25^\circ \times 0.25^\circ$  are used for the interpolation. *Kouba* [2008] found in a test study that the gridded VMF1 data, interpolated at 11 IGS stations, compared quite well with the station-wise ones. Highest precision can of course be assured for the very locations of the grid points themselves.

Not long after the advent of VMF1, *Böhm et al.* [2009] developed the VMF1-FC in which VMF1 coefficients are also available up to two days in advance, what opens the possibility of using VMF1 for real-time tasks as well. They found a very good agreement between parameters derived from analysis and forecasting data of the ECMWF, albeit the hydrostatic troposphere parameters can be forecasted more accurately than wet parameters [*Böhm and Schuh*, 2007b].

### 2.1.2. Fundamentals of GPT2w

Global Pressure and Temperature 2 wet (GPT2w) is an empirical model<sup>6</sup> for tropospheric delays by *Böhm et al.* [2015]. Following on its predecessors GPT and GPT2, it is considered the most accurate empirical tropospheric delay model to date. It provides mean values plus annual and semi-annual amplitudes of the following quantities, optionally based on a  $5^\circ \times 5^\circ$  and a  $1^\circ \times 1^\circ$  grid<sup>7</sup>:

- $p$ ..... pressure (hPa)
- $T$ ..... temperature ( $^\circ\text{C}$ )
- $dT$ ..... temperature lapse rate ( $\frac{^\circ\text{C}}{\text{km}}$ )
- $T_m$ ..... mean temperature weighted with water vapor pressure (K)
- $e$ ..... water vapor pressure (hPa)
- $a_h$ ..... hydrostatic mapping function coefficient (valid at sea level)
- $a_w$ ..... wet mapping function coefficient
- $\lambda$ ..... water vapor decrease factor
- $N$ ..... geoid undulation (m)

All these quantities were derived from monthly mean pressure level data of ERA-Interim fields provided by the ECMWF. As input for GPT2w, only geographic longitude  $\lambda$ , geographic latitude  $\varphi$ , ellipsoidal height  $h_{ell}$  and the modified Julian date (MJD) are needed.

<sup>6</sup>also referred to as a blind model

<sup>7</sup>for all comparisons drawn in this thesis, the  $5^\circ \times 5^\circ$  version is used

The parameters  $T_m$  and  $\lambda$  are new with respect to GPT2 in order to be consistent with the required input arguments of the zenith wet delay approximation formula by *Askne and Nordius* [1987] (Eq. (2.3)).

Empirical tropospheric delay models such as GPT2w are particularly needed for applications where there is no chance to use (more accurate) real-time data such as from VMF1. This can either be due to lacking internet connection, or simply because real-time data is available only for specific sites on Earth. Thus, empirical troposphere models are of particular importance for many GNSS applications. On the other hand, applications which do not require highest-possible accuracy also often use empirical models.

## 2.2. Fundamentals of azimuthal asymmetry

On the account of modeling tropospheric delays using mapping functions a necessary simplification is made: the slant delay  $\Delta L_0(\varepsilon)$  as calculated through zenith delay multiplied by the mapping function (Eq. (2.1) on page 5) is assumed to be equivalent for all azimuths  $\alpha$  around a site. In real-life conditions, however, this presumed symmetry is not correct because the delay actually depends on the cardinal direction where the signal comes from. There are mainly three reasons for azimuthal asymmetry<sup>8</sup>:

1. Because of the rotation of the earth, the resulting centrifugal force causes the Earth's x-axis and y-axis (both of which point to the equator) to be longer than the z-axis (which points to the North Pole). The same force acts on the atmosphere as well, which is why the height of the tropopause is larger at the equator than at the poles<sup>9</sup>. For signals traveling through the atmosphere, this causes a systematic effect; given the site Vienna (48° 12') for example, signals coming from quasars or satellites located to the south travel longer through the atmosphere than signals coming from the north and therefore experience a higher delay. When standing at the north pole, the delay is virtually equal in all directions.
2. The height of the tropopause is generally lower in cold conditions and higher in warm conditions. The reason for this is that higher temperatures lead to higher convection which eventually lifts the tropopause up [*Geerts and Limacre, 1997*]. For this reason, the tropopause over the poles is up to 2 km lower in winter than in summer. As a result of increasing atmospheric greenhouse gases accompanied by a rise in tropospheric temperature, the tropopause is further lifting [*Santer et al., 2003*].
3. The refractivity of air mainly depends on temperature, pressure, humidity,  $CO_2$  composition and density [*Jones, 1981*]. Since these quantities are highly variable both on the temporal and the spatial scale, the resulting delay depends on the

<sup>8</sup>also referred to as "azimuthal anisotropy"

<sup>9</sup>also referred to as the "atmospheric bulge"

composition of the air along the signal path which is different for every azimuthal direction. If there is an active front west of the observation site, a signal travelling through this front experiences a different delay than a signal coming from the east. This is considered as a random effect.

Considering azimuthal asymmetry due to the non-spherical shape of the tropopause<sup>10</sup> and due to variations of the refractivity owing to various weather phenomena came not long after the invention of first mapping functions for the symmetric part. In the following section, there is a listing of the beginnings of utilizing horizontal tropospheric gradients as a tool to model azimuthal asymmetry in space geodetic observations.

*Gardner* [1977] found that horizontal refractivity gradients cause errors in laser ranging measurements and furthermore introduced correction formulae to compensate for those effects. For this purpose he used meteorological data from eight weather stations, comprising of temperature and pressure gradients from radiosonde measurements.

*Herring* [1992] estimated horizontal gradients from almost three years of VLBI data from five VLBI stations in the US and Europe that participated in the IRIS<sup>11</sup> project. Especially at sites which frequently observe at small elevation angles significant gradient effects were detected. Mean values for horizontal north gradients  $G_n$  and east gradients  $G_e$  amount to up to -0.29 mm and -0.15 mm, respectively.

*Davis et al.* [1993] estimated horizontal gradients from data from a ground-based water vapor radiometer on a test site in Sweden. They set a focus on azimuthal changes and consequently invented a cosine model based on "delay gradients" in north and east direction which is still used today in its basic structure and constituted the basis for subsequent research.

*Chen and Herring* [1997] closely analyzed the effects of azimuthal asymmetry on the propagation delay of space geodetic data. They invented an analytical way of modeling azimuthal dependency based on sine and cosine signals which is common usage still nowadays - of which more later in Section 2.2.

*MacMillan and Ma* [1997] estimated gradients in VLBI analysis and studied their effect on TRF and CRF, whereby they found that errors can largely be reduced by estimating gradients in VLBI analysis. They also determined gradients calculated from a three-dimensional meteorological model and found good agreement with those estimated in the analysis. The agreement between these two types of gradients, that is estimated gradients and a priori gradients, will be a major topic throughout this chapter.

*Bar-Sever and Kroger* [1998] estimated tropospheric gradients from GPS measurements and inferred that they resemble real atmospheric moisture gradients observed with a water vapor radiometer. They suggested to model azimuthal asymmetry for low-elevation observations (below 15°) rather than neglecting all low-elevation observations, as was common

---

<sup>10</sup>which is the upper boundary of the troposphere

<sup>11</sup>International Radio Interferometric Surveying

usage at that time.

In order to be able to model variations in the slant delay depending on azimuth as well as possible, a further term must be added to the total delay formula (Eq. (2.1) on page 5), which so far only accounts for the symmetric part of the delay. Thus, the total delay  $\Delta L(\alpha, \varepsilon)$  caused by the (electrically) neutral atmosphere considering anisotropy for varying azimuths  $\alpha$  can be calculated by the following formula by *MacMillan* [1995] based on the cosine model by *Davis et al.* [1993]:

$$\Delta L(\alpha, \varepsilon) = \underbrace{\Delta L_0(\varepsilon)}_{\text{isotropic part}} + \underbrace{mf_g(\varepsilon) \cdot [G_n \cdot \cos(\alpha) + G_e \cdot \sin(\alpha)]}_{\text{anisotropic part}} \quad (2.9)$$

where  $\Delta L_0(\varepsilon)$  is the delay without horizontal gradients (azimuthal isotropy), depending on elevation only (= Eq. (2.1)),  $mf_g(\varepsilon)$  is the gradient mapping function,  $G_n$  is the horizontal north gradient in m and  $G_e$  is the horizontal east gradient in m<sup>12</sup>.

As can be seen, the effect of azimuthal asymmetry is determined entirely by the gradient mapping function  $mf_g(\varepsilon)$  and two gradient variables  $G_n$  and  $G_e$ . The former maps the azimuthally asymmetric part of the delay for the elevation, while the gradient variables  $G_n$  and  $G_e$  determine the alteration of the delays with altered azimuth, which is based on the idea of a "tilting" of the atmosphere [*Herring*, 1992]. Values for them typically range from sub-millimeter to several millimeters, depending on the location and current weather situation. Following Eq. (2.9) and assuming both  $G_n$  and  $G_e$  to be 1 mm and a low elevation of 5°, the additional delay for an electromagnetic signal due to azimuthal asymmetry lies between 90 and 130 mm. If  $G_n$  and  $G_e$  were half as large, namely 0.5 mm each, then the delay excess would be only half as large as well.

The gradient mapping function  $mf_g(\varepsilon)$  is thought to model the increasing refractivity due to the longer signal path for decreasing elevations. On its basis the influence of azimuthal asymmetry increases with decreasing elevation angles of the observations. As a rule of thumb it can be said that for all observations below 15° elevation azimuthal asymmetry has to be considered while above it can be neglected [*Johannes Böhm*, personal communication, 2014/08]. There are two main types for the gradient mapping function  $mf_g(\varepsilon)$ : one is suggested by *MacMillan* [1995] (Eq. (2.10)) and the other one by *Chen and Herring* [1997] (Eq. (2.11)).

$$mf_g(\varepsilon) = mf_h(\varepsilon) \cdot \cot(\varepsilon) \quad (2.10)$$

$$mf_g(\varepsilon) = \frac{1}{\sin(\varepsilon) \cdot \tan(\varepsilon) + C} \quad (2.11)$$

As the formula of *Chen and Herring* [1997] prevailed in science, it is used from now on in this section. The one by *MacMillan* [1995] is neglected, not least because of its singularity at the horizon. First-mentioned requires assumption of an exponential decay

<sup>12</sup>because their values usually range between -2 mm and 2 mm, horizontal gradients are commonly specified in millimeter. However, they must be plugged in this formula in the SI unit (m)

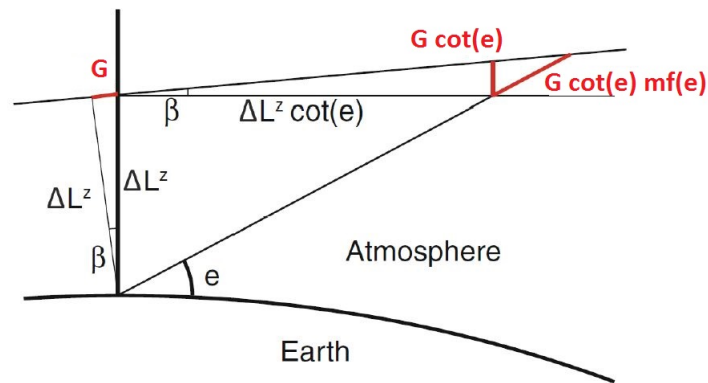


Figure 2.2.: From Nilsson et al. [2013]: the context between a horizontal gradient  $G$  and the resulting angle  $\beta$  from zenith direction. In this way the signal experiences an additional delay that equals  $mf_g(\varepsilon) = mf_h(\varepsilon) \cdot \cot(\varepsilon)$ , what corresponds to the assumption of MacMillan [1995] (Eq. (2.10)).

of the horizontal gradient with increasing height [Chen and Herring, 1997]. The gradient mapping function coefficient  $C$  can be written by:

$$C = \frac{3H}{R_e} \quad (2.12)$$

The scale height  $H$  is the height of the neutral atmosphere when assuming constant density with height and conservation of the total mass [Nilsson et al., 2013]. Assuming scale heights  $H_h$  of 6.5 km for the hydrostatic part and  $H_w$  of 1.5 km for the wet part, Chen and Herring [1997] get values of  $C_h = 0.0031$  and  $C_w = 0.0007$  for the gradient mapping function coefficient,  $R_e$  being the Earth radius. For modeling total gradients the factor  $C = 0.0032$  can be used [Herring, 1992].

In theory, a horizontal gradient  $G$  can be described by a tilting of the mapping function by an angle  $\beta$  which thus extends the signal path, and can be approximated by:

$$\beta \approx \frac{G}{\Delta L^z} \quad (2.13)$$

where  $\Delta L^z$  is the zenith delay. Figure 2.2 outlines the theory behind.

Usually, horizontal gradients are estimated from large numbers of observations within data analysis such as done by the International GNSS Service (IGS) or in the Vienna VLBI Software VieVS [Böhm et al., 2012]. Apart from that, gradients can also be determined a priori, that is, without need for any actual VLBI or GNSS observations.





### 3. Site-Augmentation of Troposphere Models

A large part of this thesis is dedicated to site-augmentation of existing models which is supposed to improve performance. Three different models are contemplated for this purpose, each of which experiencing a different kind of site-augmentation. First, the coefficients of the MTT mapping function [Herring, 1992] are recalculated (Section 3.1). In Section 3.2 the performance of GPT2w is augmented through in situ meteorological data, what represents the centerpiece of this chapter (SA-GPT2w). At the end it is also tried to site-augment VMF1 by means of in situ meteorological data in order to increase the temporal resolution (Section 3.3). The functional principle of the latter two can best be outlined by means of the flow chart in Fig. 3.1.

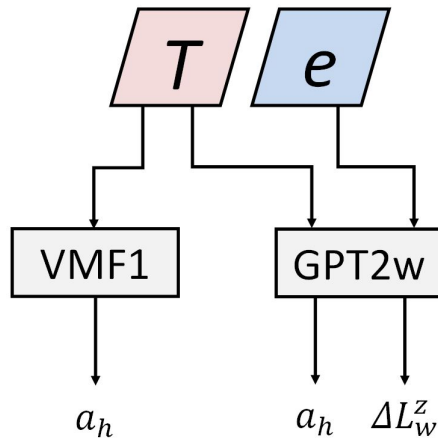


Figure 3.1.: Flow chart of the general principle of the site-augmentations of GPT2w and VMF1.

#### 3.1. Recalculation of MTT coefficients

Because computer performance and thus the performance of ray-tracing has enormously improved throughout the last 20 years, the idea arose to recalculate the MTT coefficients from a longer time period and wider station network. To accomplish this, VMF1 data of the whole year 2014 was used. The VMF1-files contain (amongst others) the coefficients  $a_h$  and  $a_w$  calculated from ray-traced delays and temperature values from NWM for every VLBI station on Earth at four epochs per day (cf. Fig. 3.3 on page 21), while  $b$  and  $c$  are used in their empirical shape. This allows determination of the constant coefficients from Eq. (2.6) in least-squares adjustments. Figure 3.2 shows all 19 stations used for that purpose. Stations PENTICTN and DV-VLBA are only seldom active nowadays, but

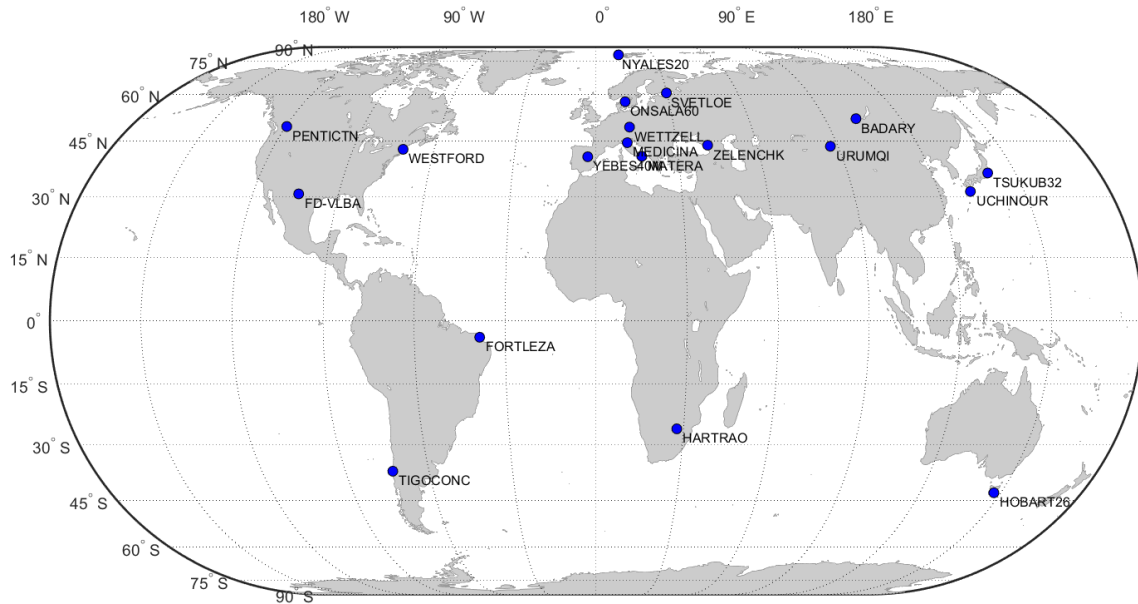


Figure 3.2.: Map of 19 VLBI stations which are used for calculating new coefficients for the MTT mapping function by means of a least-squares adjustment.

still the VMF1 values are calculated for these two stations on a regular basis and thus facilitating their use in the adjustment which is important for reaching uniform global coverage. The main selection criterion for these stations is to achieve an as uniform as possible distribution on Earth.

Eventually, the MTT coefficients are recalculated for all stations depicted in Fig. 3.2 for the whole year 2014, resulting in the following equations:

$$\begin{aligned}
 a_h &= [1.2188 + 0.0273 \cdot \cos(\varphi) - 0.0150 \cdot h + 0.00212 \cdot (T - 10)] \cdot 10^{-3} \\
 b_h &= [2.9000 - 0.0000 \cdot \cos(\varphi) - 0.0000 \cdot h + 0.00000 \cdot (T - 10)] \cdot 10^{-3} \\
 c_h &= [64.3727 - 1.5161 \cdot \cos(\varphi) - 0.2224 \cdot h - 0.05260 \cdot (T - 10)] \cdot 10^{-3} \\
 a_w &= [0.5515 - 0.0042 \cdot \cos(\varphi) - 0.0298 \cdot h + 0.00098 \cdot (T - 10)] \cdot 10^{-3} \\
 b_w &= [1.4600 - 0.0000 \cdot \cos(\varphi) - 0.0000 \cdot h + 0.00000 \cdot (T - 10)] \cdot 10^{-3} \\
 c_w &= [43.9100 - 0.0000 \cdot \cos(\varphi) - 0.0000 \cdot h + 0.00000 \cdot (T - 10)] \cdot 10^{-3}
 \end{aligned} \tag{3.1}$$

Analyzing CONT11 using on the one hand the old MTT coefficients and on the other hand the new ones shows virtually no difference in the resulting baseline length repeatabilities (BLR)<sup>1</sup>. It is merely noticeable that the repeatabilities of all baselines containing stations KOKEE and WESTFORD become consistently poorer with the new coefficients, although only by a tenth of a millimeter.

Furthermore, slant delays at 5° elevation are calculated for all 19 stations used in the

<sup>1</sup>for short time periods like CONT11 or CONT14, the BLR is simply defined as the standard deviation of this set of baseline lengths. For longer process lists (such as that analyzed in Section 4.5.1), absolute plate motions and other site discontinuities for each station have to be considered as well

Table 3.1.: *Mean BLR (cm) from VLBI analysis when applying the MTT mapping function for CONT11, using temperature from the NGS-files (1), from numerical weather models (2) and from the empirical models GPT (3) and GPT2w (4).*

TEMPERATURE SOURCE	BLR (cm)
(1) $T$ from NGS	1.13
(2) $T$ from NWM	1.12
(3) $T$ from GPT	1.11
(4) $T$ from GPT2w	1.11

adjustment from 2009 through 2014 and compared to slant delays from VMF1. Temperatures from the NWM are used as input here. The resulting bias between the original MTT and the recalculated one is only in the sub-mm range.

### 3.1.1. Comparison of temperature input from various sources

The dominating input parameter in MTT is temperature. However, temperatures from different sources are not always consistent (see Appendix B.2). Moreover, the input of surface measurements of temperature is not sufficient to describe the whole temperature distribution above the site. Thus there always remains an inaccuracy component in the calculated coefficients compared to mapping functions which utilize real-time information from NWM. In addition, the MTT mapping function is known to have a bad performance in case of temperature inversions above the site<sup>2</sup> [Johannes Böhm, personal communication, 2014/11].

The current section contains a comparison of the performance of MTT for temperature input from several origins which is based upon determination of mean baseline length repeatabilities for the time period of CONT11. VLBI analyses are carried out using MTT for temperatures from four different sources<sup>3</sup>. The mean baseline length repeatability in case of using VMF1 serves as a benchmark and is 1.09 cm (= best possible BLR). When regarding Table 3.1, the BLR is surprisingly lowest (best) when using temperatures from the empirical models and worst when using the temperature measurements directly from the site. Closer investigation shows that this scenario is most distinct for all baselines containing station HOBART12. When excluding it the mean BLR becomes 1.03 cm for (1)-(3) and 1.02 cm for (4). Unfortunately a solid reason for this strange behaviour could not be found yet.

<sup>2</sup>a temperature inversion means that at some layer temperature begins to increase with altitude, unlike the normal case of dropping temperature with increasing altitude

<sup>3</sup>from its activation in mid-2011 through end of November 2014, VLBI station FORTLEZA did not make any measurements of meteorological quantities, therefore the values from the NWM were used for this station instead

Taking all aspects into consideration it can be concluded that the original MTT coefficients were determined accurately enough and that a revision of the coefficients using more data than it was possible back in 1992 does not yield a considerable improvement. The vulnerability of the MTT mapping function to temperature inversions above the site is obviously only because of a lack of information of the distribution above the site and not because of poorly determined coefficients.

### 3.2. Site-augmentation of GPT2w (SA-GPT2w)

The acquisition of precise values for zenith wet delays  $\Delta L_w^z$  has long been topic of research, in particular in the field of GNSS. For selected sites such as stations operated by the IGS, values for zenith total delays  $\Delta L^z$  are regularly published as determined from sophisticated processing strategies requiring high numbers of observations. The user can then deduce the zenith wet delay from it (see Section 3.2.5.3 for more details). However, for arbitrary sites on Earth the situation is different; when lacking access to information from NWM, users have to draw on empirical models associated with significantly lower accuracy. GPT2w is such an empirical model, providing output arguments such as water vapor pressure  $e$ , mean temperature  $T_m$  and water vapor pressure lapse rate  $\lambda$ , each valid at the height of the topography. These quantities can then be inserted into the formula of *Askne and Nordius* [1987] (Eq. (2.3)) to derive approximate values for the zenith wet delay. However, apart from the loss of accuracy as the input arguments are only of empirical nature while the real values are highly variable both temporally and spatially, there is additionally the fact that the zenith wet delay depends not only on the water vapor at the site but rather on its whole distribution above the site. The values resulting from GPT2w + Eq. (2.3) are therefore only of moderate precision. *Dousa and Elias* [2014] expended the effort towards augmenting the performance of empirical models and found a solution which requires meteorological in situ measurements and also vertical humidity characteristics from NWM. Although thus the resulting zenith wet delays get more accurate by a factor of 2 to 3, the question remains of how to achieve improved zenith wet delays when having no information from NWM at all.

In this section a new, different method is presented which augments the empirical zenith wet delay by using *only* in situ measurements aside from empirical information. In fact, it was found that the performance of GPT2w can be enhanced by using in situ measurements of meteorological quantities such as temperature  $T$  and water vapor pressure  $e$ . Nowadays it is a simple task to install meteorological sensors at a GNSS site in order to measure the aforementioned quantities<sup>4</sup>. A thermometer can directly measure  $T$  in °C and a hygrometer can measure the relative humidity  $f$  in percent<sup>5</sup>. The augmentation is only

<sup>4</sup>at VLBI stations meteorological sensors are standardly mounted, predominantly for a priori calculation of  $\Delta L_h^z$

<sup>5</sup>in terms of simplification, in the following there is always talk of the "measured water vapor pressure  $e$ ", although in the proper meaning of the word it is not directly measured

```

# 2006 July 5
# Vienna Mapping Function 1 VMF1
#
# J. Boehm, B. Werl, H. Schuh,
# Troposphere mapping functions for GPS and very long baseline interferometry
# from European Centre for Medium-Range Weather Forecasts operational analysis data,
# Journal of Geophysical Research, Vol. 111, B02406, doi:10.1029/2005JB003629, 2006.
#
# columns:
# -----
# station name (8 characters)
# modified Julian date
# hydrostatic coefficient a
# wet coefficient a
# hydrostatic zenith delay
# wet zenith delay
# mean temperature of the atmosphere above the site in Kelvin
# pressure at the site in hPa
# temperature at the site in Celsius
# water vapour pressure at the site in hPa
# orthometric height of the station (using geoid EGM96)
#
AIRA      55556.00  0.00125042  0.00048440  2.2442  0.0510  283.3  984.49  17.61  11.63  290.8
AIRA      55556.25  0.00125025  0.00056263  2.2434  0.0575  279.6  984.74  17.54  11.78  290.8
AIRA      55556.50  0.00125106  0.00060990  2.2421  0.0670  277.8  983.68  18.08  11.24  290.8
AIRA      55556.75  0.00125138  0.00059788  2.2443  0.0650  278.4  984.25  18.12  11.59  290.8
ALGOPARK  55556.00  0.00119793  0.00054855  2.2556  0.0332  257.8  990.43  -9.07  2.49  260.7
ALGOPARK  55556.25  0.00119745  0.00055358  2.2562  0.0280  256.9  990.44  -10.42  2.30  260.7
ALGOPARK  55556.50  0.00119671  0.00054909  2.2554  0.0220  256.2  990.61  -11.90  2.02  260.7
ALGOPARK  55556.75  0.00119819  0.00053801  2.2514  0.0177  256.6  989.20  -10.62  1.72  260.7
ARECIBO   55556.00  0.00126023  0.00045180  2.1758  0.0551  284.6  952.81  17.51  14.66  515.1
ARECIBO   55556.25  0.00125942  0.00043900  2.1826  0.0880  284.9  955.07  18.81  14.39  515.1
ARECIBO   55556.50  0.00126020  0.00045017  2.1745  0.0975  285.6  952.08  19.63  15.11  515.1
ARECIBO   55556.75  0.00125931  0.00046898  2.1797  0.1170  284.6  954.48  18.64  16.30  515.1

```

Figure 3.3.: *An extract of a VLBI VMF1-file of the year 2011. There is one such file per year since 1979, each containing VMF1 data for more than 100 VLBI stations in a temporal resolution of four epochs per day.*

possible due to clear correlations between the quantities, as the upcoming Section 3.2.1 addresses.

### 3.2.1. Correlation between the quantities

The station-wise VMF1-files contain, amongst others, on the one hand temperature  $T$ , pressure  $p$  and water vapor pressure  $e$  at the Earth's surface and on the other hand the  $a_h$  coefficient and the zenith wet delay  $\Delta L_w^z$  for all VLBI sites and a set of GNSS sites on Earth. Both  $a_h$  as well as  $\Delta L_w^z$  are determined by ray-tracing through numerical weather models. Figure 3.3 shows an extract of a station-wise VMF1-file with the appropriate columns description. Investigating these quantities with each other reveals clear correlations, the degree of which can be estimated by means of the correlation coefficient  $r$ . This very coefficient can be calculated in order to test the mutual dependency between two datasets  $x$  and  $y$ . The maximal correlation coefficient is 1, which means that dataset  $x$  is totally dependent on dataset  $y$  and vice versa, whereas the minimum value is 0 for which

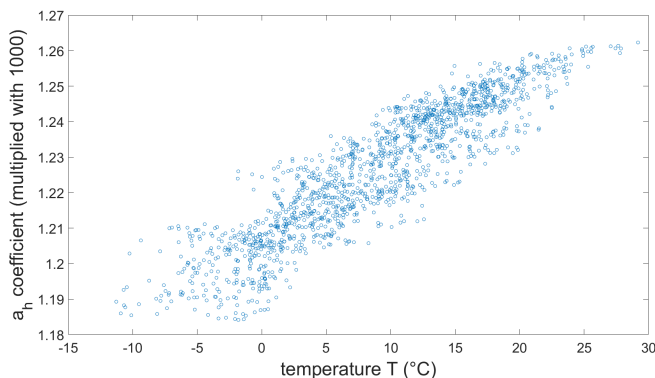


Figure 3.4.: *Correlation between surface temperature  $T$  and the mapping function coefficient  $a_h$ . Here, the blue points mark all 1460 NWM epochs of the year 2011 for VLBI station WETTZELE, each with their respective temperatures on the x-axis and  $a_h$  coefficients on the y-axis. Their close-to-line alignment reveals a clear correlation between the two datasets. In fact, the correlation coefficient for these points is 0.91.*

Table 3.2.: *Correlation coefficients between the quantities averaged over all 14 CONT11 stations from 2011 through 2014 [Landskron et al., 2016d].*

CORRELATION COEFFICIENTS	
between $T$ and $a_h$	0.86
between $e$ and $\Delta L_w^z$	0.83
between $T$ and $\Delta L_w^z$	0.61

the two datasets are uncorrelated. Its calculation reads [Sachs, 1974]:

$$r = \frac{\sum(x - \bar{x}) \cdot (y - \bar{y})}{\sqrt{\sum(x - \bar{x})^2 \cdot \sum(y - \bar{y})^2}} \quad (3.2)$$

where  $\bar{x}, \bar{y}$  are the averages of  $x$  and  $y$ , respectively.

The datasets to be tested here are  $T$ ,  $e$ ,  $a_h$  and  $\Delta L_w^z$ . Plotting them to each other reveals Figs. 3.4 to 3.6, which serve as a kind of graphical correlation coefficient; the more the data points approximate a straight line, the higher their correlation is.

Averaging data of the 14 VLBI stations which participated in CONT11 for all VLBI sessions in the time of 2011 through 2014 yields the correlation coefficients listed in Table 3.2. The correlation coefficients are highest for continental stations located in predominantly dry climate zones (e.g. BADARY) and worst for stations in tropical regions<sup>6</sup> where the humidity is temporally highly variable (e.g. FORTLEZA). Also the correlation coefficient between  $e$  and  $a_h$  (0.71) was calculated, but this turned out not to be able to improve the results. For comparison, the correlation coefficient between pressure  $p$  at the site and the zenith hydrostatic delay  $\Delta L_h^z$  is 0.995, what means that  $\Delta L_h^z$  is completely dependent on  $p$ .

<sup>6</sup>the tropics range between 23.5 N and 23.5 S

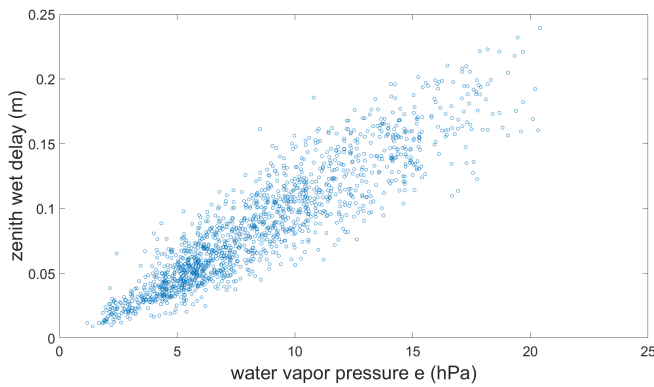


Figure 3.5.: Correlation between surface water vapor pressure  $e$  and zenith wet delay  $\Delta L_w^z$ . Here, again, the blue points mark all 1460 NWM epochs of the year 2011 for VLBI station WETTZELE, each with their respective water vapor pressures on the x-axis and zenith wet delays on the y-axis. Their close-to-line alignment reveals a clear correlation between the two datasets. In fact, the correlation coefficient for these points is also 0.91 [Landskron et al., 2016d].

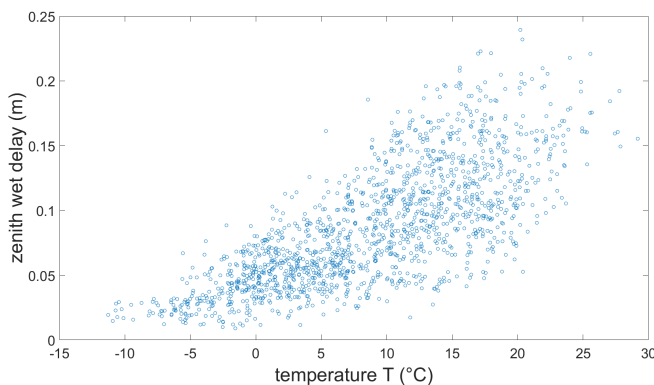


Figure 3.6.: Correlation between surface temperature  $T$  and the zenith wet delays  $\Delta L_w^z$ . This correlation is not as distinct as with water vapor pressure, the correlation coefficient for these points of same data as in Figs. 3.4 and 3.5 is only 0.74 [Landskron et al., 2016d].

### 3.2.2. Determination of universal weighting coefficients

In order to infer  $a_h$  and  $\Delta L_w^z$  from the measured meteorological quantities and to augment the empirical quantities from GPT2w, certain weighting factors need to be determined. More precisely, a weighting factor  $M_{a_h}$ , which connects temperature with the  $a_h$  coefficient and two weighting factors  $M_{zwd_1}$  and  $M_{zwd_2}$  which connect temperature and water vapor pressure with the zenith wet delay have to be found. The idea behind this is that these factors shall each weight the differences between the respective NWM and GPT2w values. This leads to the following three formulae (3.3) to (3.5), which are the framework of the site-augmented GPT2w (in the following referred to as SA-GPT2w).

Eq. (3.3) enables augmentation of the  $a_h$  coefficient by means of information about temperature at the site using a universal weighting coefficient  $M_{a_h}$ .

$$a_{h_{VMF1}} - a_{h_{GPT2w}} = M_{a_h} \cdot (T_{VMF1} - T_{GPT2w}) \quad (3.3)$$

It was also tested to append a quadratic term  $.. + M_{a_{h2}} \cdot (T_{VMF1} - T_{GPT2w})^2$ , however, this did not lead to better results. Equation (3.4) allows augmentation of the zenith wet delay by means of information about the temperature at the site using a universal weighting coefficient  $M_{zwd}$ .

$$\Delta L_{w_{VMF1}}^z - \Delta L_{w_{GPT2w}}^z = M_{zwd} \cdot (T_{VMF1} - T_{GPT2w}) \quad (3.4)$$

In this way,  $\Delta L_{w_{GPT2w}}^z$  can be augmented without additional knowledge of humidity at the station. The term  $\Delta L_{w_{GPT2w}}$  is determined with the formula of *Askne and Nordius* [1987] (Eq. (2.3)), utilizing the input values  $e$ ,  $T_m$  and  $\lambda$  each from GPT2w. Equation (3.5) enables augmentation of the zenith wet delay  $\Delta L_w^z$  by means of information about temperature and water vapor pressure at the site using two universal weighting coefficients  $M_{zwd_1}$  and  $M_{zwd_2}$ .

$$\Delta L_{w_{VMF1}}^z - \Delta L_{w_{GPT2w}}^z = M_{zwd_1} \cdot (T_{VMF1} - T_{GPT2w}) + M_{zwd_2} \cdot (e_{VMF1} - e_{GPT2w}) \quad (3.5)$$

This is much more accurate than using only the temperature information as done in Eq. (3.4). Here, it was also tested to append a combined term  $.. + M_{zwd_3} \cdot (T_{VMF1} - T_{GPT2w}) \cdot (e_{VMF1} - e_{GPT2w})$ , however, it did not change the results either.

Data for these equations comes on the one hand from the station-wise VMF1-files for the six years from 2009 through 2014 and on the other hand from GPT2w, each for 19 select VLBI stations. All  $M$  coefficients are determined by means of least-squares adjustments<sup>7</sup>. The 19 VLBI stations, which represent an as uniform as possible global distribution, are chosen for the adjustment (Fig. 3.7).

In the following, only the least-squares adjustment for determination of  $M_{zwd_1}$  and  $M_{zwd_2}$  is introduced, as the determinations of  $M_{a_h}$  and  $M_{zwd}$  follow the same scheme.

<sup>7</sup> $M_{a_h}$  and  $M_{zwd}$  could have also been determined analytically as they are the only unknown parameter in Eqs. (3.3) and (3.4) using the mean or median instead of the least-squares approach, but this had decreased the ability to exclude extreme values and outliers



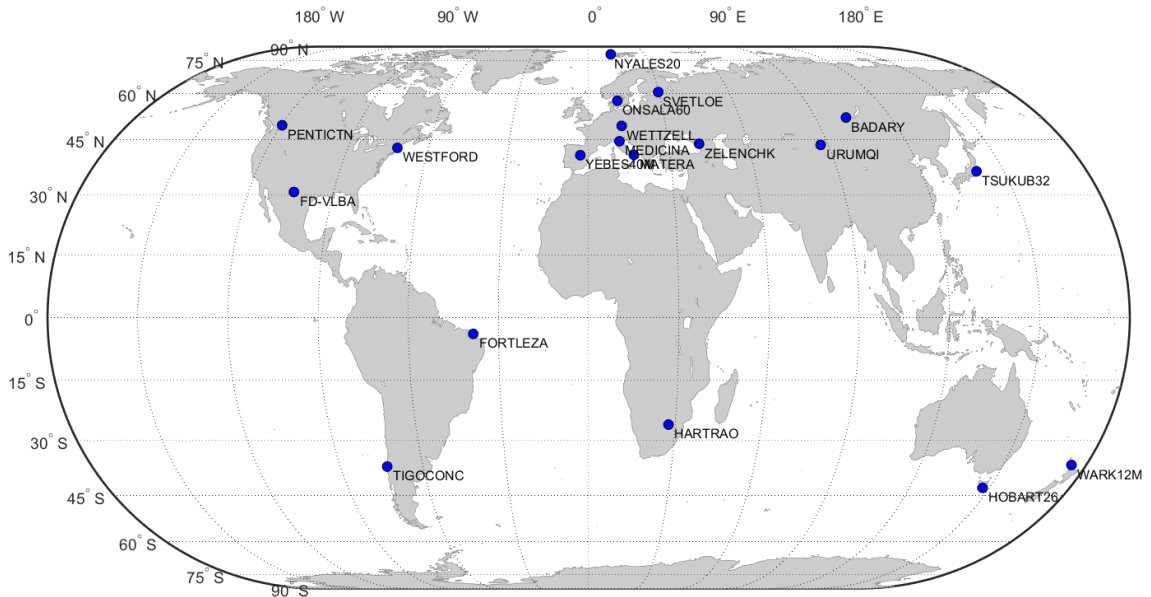


Figure 3.7.: Map of 19 VLBI stations which are used for the determination of the  $M$  coefficients for SA-GPT2w in least-squares adjustments. VLBI station PENTICTN has not carried out any observation, and stations FD-VLBA and URUMQI have only contributed with a few observations in the specified time window, but as the VMF1-files are available for these stations in the same way as for all the others, they are included.

The design matrix  $A$  is devised by partial derivation of Eq. (3.5) with respect to  $M_{zwd_1}$  and  $M_{zwd_2}$ . This yields  $T_{NWM} - T_{GPT2w}$  and  $e_{NWM} - e_{GPT2w}$ , respectively. The observation vector  $l$  equals  $\Delta L_{wVMF1}^z - \Delta L_{wGPT2w}^z$ . The  $M$  coefficients can then be calculated by:

$$\begin{bmatrix} M_{zwd_1} \\ M_{zwd_2} \end{bmatrix} = (A^T P A)^{-1} A^T P l \quad (3.6)$$

where  $P$  is the weight matrix, being a unit matrix here<sup>8</sup>. Carrying out analogous least-squares adjustment for all three Eqs. (3.3) to (3.5) yields the coefficients listed in Table 3.3.

One last note for the sake of completeness: The meteorological input data for the calculation of  $M$  coefficients here comes from NWM, more precisely from the VMF1-files. Additionally, there were also  $M$  coefficients calculated from NGS data, what was associated with more work. Although the new  $M_{NGS}$  coefficients got slightly different values than the original ones, their application on all measurements did not cause any major differences. Hence, the original coefficients determined as described in this section are kept as they are.

<sup>8</sup>and being a unit matrix in all remaining least-squares tasks of this thesis as well, therefore  $P$  is not mentioned anymore in further consequence

Table 3.3.: Values for the  $M$  coefficients as determined from NWM data of 19 VLBI stations from 2009-2014 [Landskron et al., 2016d].

$M$ COEFFICIENTS	
$M_{a_h}$	$1.3 \cdot 10^{-6}$
$M_{zwd}$	$1.8 \cdot 10^{-3}$
$M_{zwd_1}$	$4.9 \cdot 10^{-4}$
$M_{zwd_2}$	$9.2 \cdot 10^{-3}$

### 3.2.3. Determination of non-universal weighting coefficients

The only possibility to model changes in any quantity in an empirical way is when they follow a systematic trend; there is no chance to model random changes empirically. Therefore, this section covers several methods that attempt to detect systematic trends in the  $M$  coefficients<sup>9</sup>, which then could be modeled empirically. Since the  $M$  coefficients vary both temporally and spatially, it was tested whether any systematics can be found in order to possibly get a more realistic connection between  $T$  and  $a_h$ ,  $T$  and  $\Delta L_w^z$  and also between  $e$  and  $\Delta L_w^z$ .

#### Temporal dependence

First of all, a possible temporal dependence was investigated. In case there is any annual systematics in the signal, there may be a possibility to properly model it. To achieve this, a different data input is needed. In the foregoing section, the station-wise version of the VMF1-files was used; from now on, the grid-wise VMF1-files will be utilized. They contain same data pattern as the station-wise VMF1-files, but for all 13104 grid points on a  $2.0^\circ \times 2.5^\circ$  ( $\varphi \times \lambda$ ) grid at four epochs per day (00:00, 06:00, 12:00, 18:00 UT)<sup>10</sup>. By means of a least-squares adjustment using Eq. (3.6) again, one global  $M$  coefficient is determined for each epoch, averaged over all grid points.

Fig. 3.8 shows the development of  $M_{a_h}$  averaged over all grid points for each year from 2012 through 2014. It can be seen that the different lines do not systematically overlap; distinctively low or high values in one year do not recur in the other years. Therefore it can be stated that there is generally no seasonal behaviour in  $M_{a_h}$ , and so is it the case for  $M_{zwd}$ ,  $M_{zwd_1}$  and  $M_{zwd_2}$  as well. It was also checked whether there is any annual systematics for each of the two hemispheres alone, but the result was the same. Eventually, the presence of a "time-of-day" dependence was investigated, but here again no systematics could be found. To be concluded, there is no systematic temporal dependence of the  $M$

<sup>9</sup>as explained before, there are several  $M$  coefficients:  $M_{a_h}$ ,  $M_{zwd}$ ,  $M_{zwd_1}$  and  $M_{zwd_2}$ ; when there is talk of one (generalized)  $M$  coefficient in the following, then this means one of them each

<sup>10</sup>this corresponds to the very four daily epochs for which the NWM are published

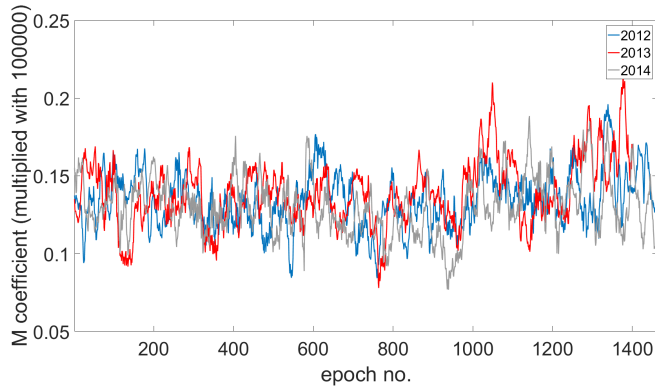


Figure 3.8.: Plot for the seasonal behaviour of the  $M_{a_h}$  coefficient. The different colours each represent one year.

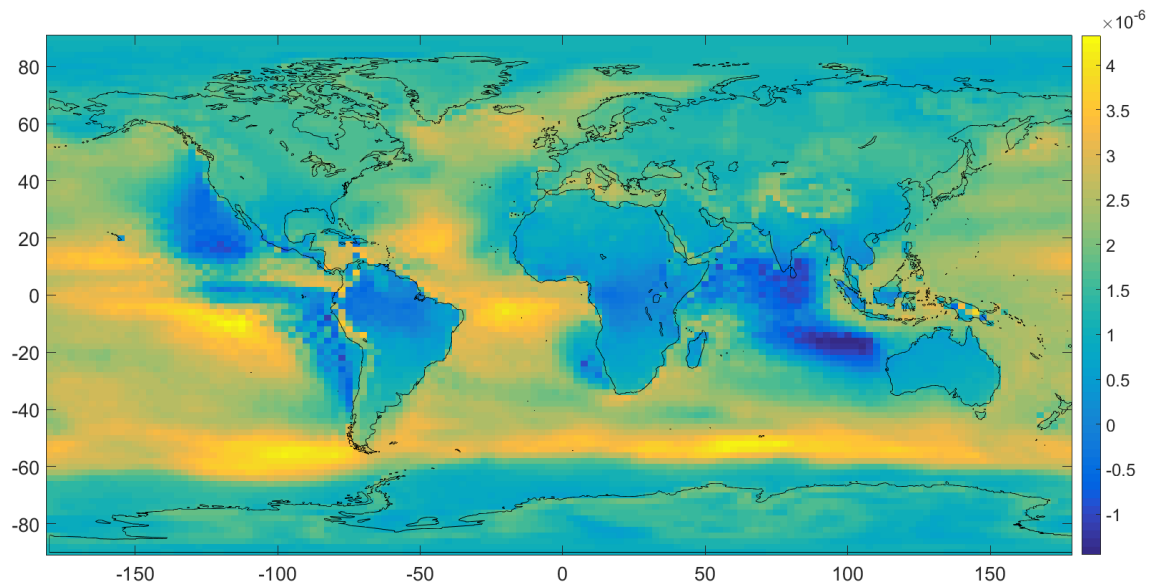


Figure 3.9.: Map showing temporally averaged values for the  $M_{a_h}$  coefficient of Eq. (3.3). The values vary especially over the seas, where it is apparently connected to ocean currents. On land, the values only slightly deviate around the equator.

coefficient.

### Spatial dependence

Next it was tested whether the  $M$  coefficients may exhibit a systematic spatial dependency. This was accomplished by determining  $M$  coefficients for each of the 13104 grid points separately in a least-squares adjustment. Figure 3.9 shows the resulting coefficients for  $M_{a_h}$ , corresponding plots for  $M_{zwd}$ ,  $M_{zwd_1}$  and  $M_{zwd_2}$  can be found in the appendix (Figs. C.1 to C.3). From these figures it can be concluded that the variations in the  $M$  coefficients on land are generally not very distinct, however spatial dependencies are obvious. Their effect on the results of SA-GPT2w is determined in the upcoming Section 3.2.5.

There were also universal  $M$  coefficients calculated from all grid points (Table 3.4). These coefficients were also calculated for the period of 2012 to 2014 and for onshore

Table 3.4.: Values for the  $M$  coefficients as determined from NWM data of all 13104 grid points from 2012-2014.

$M$ COEFFICIENTS	
$M_{a_h}$	$0.7 \cdot 10^{-6}$
$M_{zwd}$	$1.5 \cdot 10^{-3}$
$M_{zwd_1}$	$-1.4 \cdot 10^{-4}$
$M_{zwd_2}$	$1.6 \cdot 10^{-3}$

grid points only, because offshore grid points are subject to high variations which are not relevant for GNSS or VLBI stations anyway, as they are usually mounted on land. Using these coefficients instead of those from Table 3.3 improves the resulting  $a_h$  coefficient minimally, but deteriorates the zenith wet delay considerably. Therefore, the universal grid points from Table 3.4 are not considered in the following.

### 3.2.4. Application of SA-GPT2w

There are generally two types of site-augmentation with SA-GPT2w depending on which meteorological quantities are actually measured in situ [Landskron *et al.*, 2016d] plus a third approach where the zenith wet delay is directly calculated from in situ meteorological data. The formulae are actually equal to those in Section 3.2.2, but slightly shifted and rearranged for the input quantities.

1. SA-GPT2w 1: When measuring only temperature  $T$  directly at the site, the  $a_h$  coefficient and, to some extent, the empirical zenith wet delay  $\Delta L_{wGPT2w}^z$  can be augmented. To do so, the following formulae must be applied:

$$a_h = a_{hGPT2w} + M_{a_h} \cdot (T - T_{GPT2w}) \quad (3.7)$$

$$\Delta L_w^z = \Delta L_{wGPT2w}^z + M_{zwd} \cdot (T - T_{GPT2w}) \quad (3.8)$$

where  $T$  is the temperature measured at the site,  $a_h$  is the augmented  $a_h$  coefficient and  $\Delta L_w^z$  is the augmented zenith wet delay.

2. SA-GPT2w 2: When measuring both temperature  $T$  and water vapor pressure  $e$  at the site, the maximum augmentation of SA-GPT2w can be achieved<sup>11</sup>. The augmentation of  $a_h$  remains the same, while that of the zenith wet delay  $\Delta L_w^z$  is extended to Eq. (3.10).

$$a_h = a_{hGPT2w} + M_{a_h} \cdot (T - T_{GPT2w}) \quad (3.9)$$

$$\Delta L_w^z = \Delta L_{wGPT2w}^z + M_{zwd_1} \cdot (T - T_{GPT2w}) + M_{zwd_2} \cdot (e - e_{GPT2w}) \quad (3.10)$$

<sup>11</sup>as a matter of course, as  $T$  is needed for the conversion of relative humidity  $f$  to  $e$ , it is not possible to measure only  $e$  (see Eq. (2.4) on page 6)

where  $e$  is the water vapor pressure measured at the site.

3. SA-GPT2w 3: instead of applying Eq. (3.10), the in situ  $e$  can also be directly inserted into the formula by *Askne and Nordius* [1987] (Eq. (2.3) on page 6).

The augmentation of  $a_h$  only affects low elevations, as it alters the hydrostatic mapping function  $mf_h$  which increases with decreasing elevation angles. On the other hand, the augmentation of the zenith wet delay is independent of the observation elevation, as the name "zenith" suggests.

Finally some specific bounds for the in situ data are set. Temperature sensors should usually be set up in the shade so as not to be subject to direct sunlight which may affect the measured temperature. However, in terms of measurements with cheap equipment carried out by laymen it may happen that the sensor does not measure the actual temperature in the shade. Likewise, plain pressure and water vapor pressure measurements might be defective as well. The only way of detecting gross errors in the in situ data is by comparing it to the empirical data from GPT2w. By this means the observable is regarded as faulty and GPT2w is used instead of SA-GPT2w, if the difference between the observable and the respective empirical value is larger than a certain threshold. Therefore, if the following conditions are not met, SA-GPT2w shall not be applied:

$$\begin{aligned} |T_{meas} - T_{GPT2w}| &\leq 20 \text{ }^\circ\text{C} \\ |p_{meas} - p_{GPT2w}| &\leq 50 \text{ hPa} \\ |e_{meas} - e_{GPT2w}| &\leq 15 \text{ hPa} \end{aligned} \tag{3.11}$$

Obviously, this is not a perfect solution. Assuming a temperature measurement may actually be absolutely correct but sufficiently different from the empirical value, it will mistakenly be discarded. But still, the compromise is to rather eliminate gross errors and accept slight loss of data instead of the reverse. Moreover, it is rarely the case that the bounds are exceeded by real causes anyway.

### 3.2.5. Results

In the following, four ways of estimating the quality of the site-augmented GPT2w are investigated. In the first three, delays are computed with SA-GPT2w and then compared to delays from different sources. The fourth way includes whole VLBI analyses and computes baseline length repeatabilities which are then compared to each other. Hereafter, the results of all options are presented.

#### 3.2.5.1. Comparison with delays of VMF1

In this first comparison it is assumed that the delays and mapping factors of VMF1 are the "true" delays, which, however, is not necessarily correct. Indeed, using real-time data

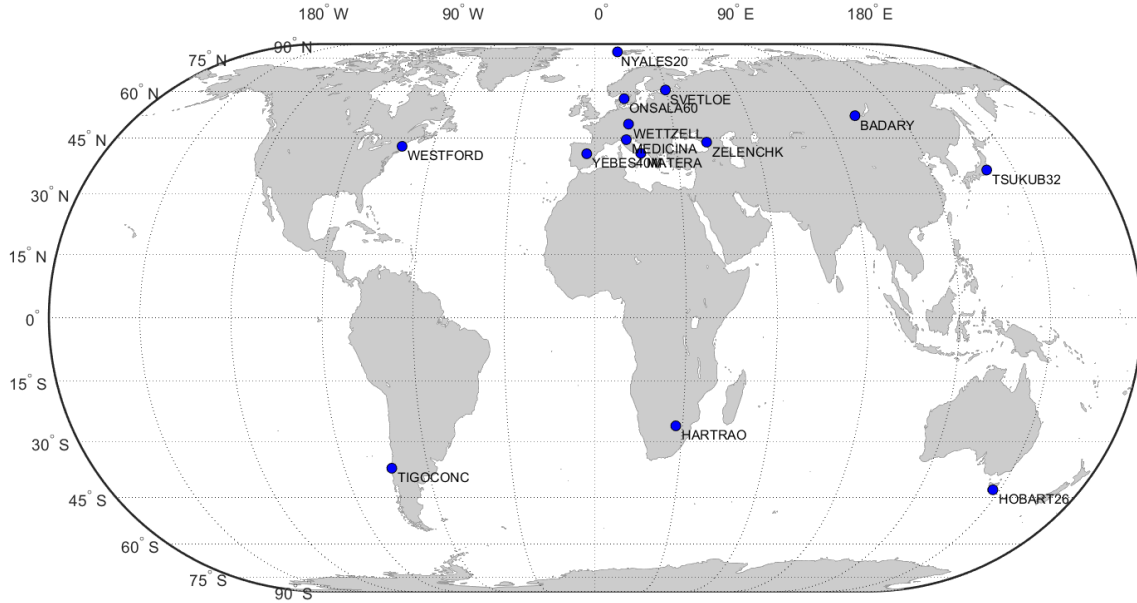


Figure 3.10.: *Map of 14 VLBI stations that were selected for assessing the performance of SA-GPT2w.*

from NWM yields results close to reality, but still only *close* to reality, as there is no chance to get to know the *true* values<sup>12</sup>. Nevertheless, there are even more realistic values for the zenith wet delay  $\Delta L_w^z$  than those from ray-tracing, as will be pointed out at a later stage.

To compare the performance of the augmented  $a_h$  coefficients, slant hydrostatic delays  $\Delta L_h$  at  $5^\circ$  elevation are produced, while the augmented zenith wet delays  $\Delta L_w^z$  are directly compared to those from VMF1. As input,  $T$  and  $e$  from the NGS-files are used, that is, the meteorological measurements which are made together with the VLBI observations. The comparison is done for the 14 VLBI stations shown in Fig. 3.10 during the period of 2011 through 2014. These VLBI stations are different from those from Fig. 3.7 on page 25 for the following reasons:

- FORTLEZA had not collected any meteorological measurements from mid-2011 through November 2014.
- FD-VLBA, PENTICTN and URUMQI carried out no or only few measurements in the specified time interval, therefore there are no usable NGS-files containing these stations (see caption of Fig. 3.7).

Thus, the global coverage is not as uniform as in Fig. 3.7, but still as uniform as possible, as the global coverage of VLBI stations on Earth is concentrated particularly to the northern hemisphere and especially to Europe anyway.

<sup>12</sup>in the course of this thesis, there is often talk of "true" values even though this is, strictly speaking, not true. However, in the absence of physically true and absolute values, the values to which the highest possible accuracy is attributed are commonly referred to as the "true" values

Table 3.5.: Mean absolute differences in slant hydrostatic delay  $\Delta L_h$  at  $5^\circ$  elevation (first column) and zenith wet delay  $\Delta L_w^z$  (second column) between high quality values from VMF1 and several SA-GPT2w approaches averaged over 14 VLBI stations and all epochs from 2011-2014. The input parameters for SA-GPT2w,  $T$  and  $e$ , come from the NGS-files.

TROPOSPHERE MODEL	MEAN ABS. DIFF.	MEAN ABS. DIFF.
	$\Delta L_h(5^\circ)$ (cm)	$\Delta L_w^z$ (cm)
GPT2w	1.5	2.7
universal $M$ :		
SA-GPT2w 1	1.2	2.5
SA-GPT2w 2	1.2	2.0
SA-GPT2w 3	1.2	2.1
geographically dependent $M$ :		
SA-GPT2w 1	1.3	2.5
SA-GPT2w 2	1.3	2.1
MTT	1.8	2.7
MTT (new coefficients)	1.7	2.7

The results of this comparison are shown in Table 3.5 together with further mapping functions in order to get an extensive overview. The slant hydrostatic delays and zenith wet delays are calculated each as mean absolute differences of all observations of the 14 VLBI stations for the period of 2011 through 2014. The zenith hydrostatic delay  $\Delta L_h^z$ , which is needed for the calculation of  $\Delta L_h$ , is taken from NWM. It can be seen that measuring temperature  $T$  improves the slant hydrostatic delay  $\Delta L_h$  by 20% and slightly improves also the zenith wet delay  $\Delta L_w^z$ , while additional measurement of water vapor pressure  $e$  improves  $\Delta L_w^z$  by one quarter. Consequently, it definitively makes sense to measure  $T$  and  $e$  in situ as it significantly improves the performance of GPT2w. The application of geographically dependent  $M$  coefficients, however, does not affect the results in any way. Figure 3.11 illustrates the improvement in  $\Delta L_w^z$  for VLBI station WETTZELL.

Drawbacks of this comparison:

- The problems with the meteorological data in the NGS-files (as described in Appendix B.1) come into effect also here. Hence, the reliability of the meteorological measurements is not totally ensured. In particular, undetected gross errors in the NGS meteorological data such as those at KOKEE or WETTZELL result in completely wrong values for the augmented  $a_h$  and  $\Delta L_w^z$ , what in further consequence distorts the final results.
- The VMF1 delays, which serve as the reference values here, may be one of the most accurate ones available, however, they are still only approximations of the "true" delay.

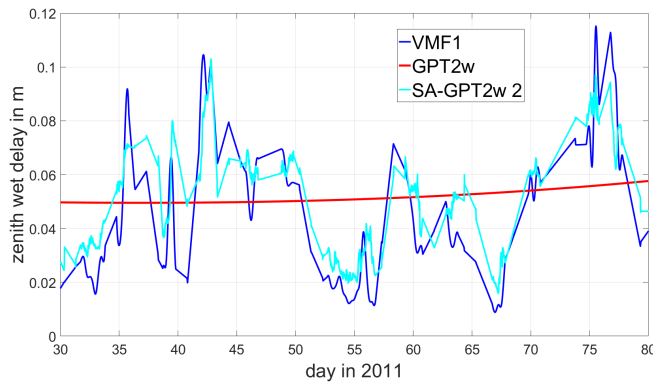


Figure 3.11.: Comparison of zenith wet delays  $\Delta L_w^z$  for station WETTZELL during the first quarter of 2011. It can be seen that when using the in situ meteorological measurements, the curve of SA-GPT2w approximates that of the VMF1-files much better than the empirical GPT2w does, which appears as a kind of averaged curve.

For this investigation, as already mentioned in the beginning of this section, the observational meteorological data from the NGS-files was used. However, also values  $T$  and  $e$  from the VMF1-files, that is from the NWM, were tested as input. This is a realistic scenario too because some users may have access to NWM and thus to real-time values of  $T$  and  $e$ , but do not have ray-tracing programmes which would be able determine real-time zenith wet delays. Fortunately, this yielded very similar results as those in Table 3.5. In other words, for the performance of SA-GPT2w it does not matter whether the meteorological input comes from NGS or from NWM.

### 3.2.5.2. Comparison with delays from VLBI analysis using VieVS

Within the least-squares adjustment of the Vienna VLBI Software *VieVS* [Böhm *et al.*, 2012] it is possible to determine values for the zenith wet delay which are even more exact than those from VMF1. In addition, the temporal resolution can thus be increased from six hours from the VMF1-files to 20 minutes. This investigation is carried out for the time and stations of CONT11. For this purpose the standard VLBI analysis approach is used (see Table A.3 in the appendix on page 138) with only one slight change: the zenith wet delays are estimated every 20 minutes. Consequently, the zenith wet delays from the other sources need to be interpolated to the 20 minutes interval as well in order to be able to be compared to each other. This yields the numbers in Table 3.6. They are quite identical with those from the comparison in Table 3.5 on page 31; when measuring temperature only, a slight improvement can be achieved, while additional measurement of water vapor pressure improves the results significantly, albeit to a lesser extent than before. Here too the geographically dependent  $M$  coefficients do not yield a further improvement (Fig. 3.12).

Drawbacks of this comparison:

- Since the comparison can be carried out only for short-term campaigns like CONT11 or CONT14, the results are not as meaningful as in the comparison with VMF1 from the previous section, where the differences were calculated for all VLBI observations



Table 3.6.: Mean absolute differences in zenith wet delay  $\Delta L_w^z$ , between high quality zenith wet delays estimated in VieVS and several SA-GPT2w approaches averaged over 13 VLBI stations during CONT11. The input parameters for SA-GPT2w,  $T$  and  $e$ , come from the NGS-files.

TROPOSPHERE MODEL	MEAN ABS. DIFF.
	$\Delta L_w^z$ (cm)
VMF1	1.2
GPT2w	3.6
universal $M$ :	
SA-GPT2w 1	3.5
SA-GPT2w 2	3.0
SA-GPT2w 3	3.0
geographically dependent $M$ :	
SA-GPT2w 1	3.5
SA-GPT2w 2	3.1

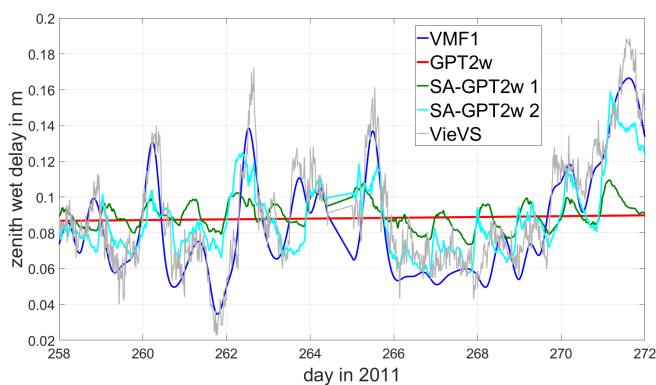


Figure 3.12.: Comparison of several zenith wet delays  $\Delta L_w^z$  for station HOBART12 during the VLBI campaign CONT11. Here as well, in situ meteorological measurements get the curve of SA-GPT2w to approximate the VMF1-files much better than GPT2w alone does.

in the long time period from 2011 through 2014.

- Although more realistic than those from VMF1, these zenith wet delays are not perfect either.
- The problems concerning the quality of the meteorological data of the NGS-files arise also here.

### 3.2.5.3. Comparison with delays from GNSS analysis

Up to this point we have dealt with the potential of the site-augmented GPT2w with respect to quantities from VLBI. Utilizing data of a large net of stations which continuously measure signals coming from multiple GNSS satellites simultaneously, however, there is the possibility to determine zenith wet delays  $\Delta L_w^z$  even more accurately than with the ray-tracing approach [Teke *et al.*, 2011]. These zenith wet delays can be derived only indirectly though; on the basis of the precise point positioning (PPP) approach<sup>13</sup>, special processing techniques are capable of combining the measurements of all tracked GNSS satellites at different elevations to compute tropospheric zenith total delays  $\Delta L^z$  for a certain GNSS station [Hackman *et al.*, 2015]. This is performed at 16 of the 18 IGS analysis centers [Jean and Dach, 2016]. The IGS provides these zenith total delays in two different versions, depending on the latency: "ultra-rapid tropospheric  $\Delta L^z$ " with a latency of only 2-3 hours and an accuracy of 6 mm, or "final tropospheric  $\Delta L^z$ " with a latency of maximum 4 weeks and an accuracy of 4 mm [igs.org/products, date of access: 2016/03]. For this work the latter are used as the higher accuracy is preferred to the shorter latency. They were downloaded from the website of the CDDIS<sup>14</sup> at GSFC<sup>15</sup> [ftp://cddis.gsfc.nasa.gov/gnss/products, date of access: 2016/08], which is one of the four IGS global data centers.

Availability of the related in situ measured pressure enables determination of the respective zenith hydrostatic delay  $\Delta L_h^z$  using the equation by Saastamoinen [1972] (Eq. (2.2) on page 6), what in further consequence leads to the zenith wet delay by simply subtracting the hydrostatic part from the total delay. In this section, the performance of SA-GPT2w regarding these high-precision zenith wet delays from GNSS is investigated.

In order to gain zenith wet delays with adequate accuracy so as to serve as reference values, high-precision information about pressure at the site is necessary in addition to the aforementioned zenith total delays from the IGS. Empirical models are not sufficient for this purpose; hence, meteorological information from three different sources is considered,

<sup>13</sup>the precise point positioning (PPP) method allows determination of absolute single positions at the centimeter-level through knowledge of very accurate clock and orbit products; instead of employing the clock and ephemeris data broadcast by the satellites, data from a global network of reference stations is provided by one of various PPP services [Kaplan and Hegarty, 2006]. The drawback of PPP is, however, an inevitable convergence time of around 30 minutes in order to achieve the abovementioned accuracy

<sup>14</sup>Crustal Dynamics Data Information System

<sup>15</sup>Goddard Space Flight Center

each of them described in a separate subsection:

1.  $p$ ,  $T$  and  $e$  come from official weather stations located close to the respective IGS stations
2.  $p$ ,  $T$  and  $e$  come from a subset of IGS stations that are equipped with in situ meteorological sensors
3.  $p$ ,  $T$  and  $e$  come from NWM data of the ECMWF

### Meteorological data from weather stations

The general reference for the following is [Landskron *et al.*, 2015a].

A number of IGS stations around the world has weather stations in their immediate vicinity continuously measuring the meteorological parameters  $p$ ,  $T$  and  $e$ . The data of these weather stations was provided by ZAMG<sup>16</sup>. As this data is basically recorded in order to feed weather prediction, its quality can be considered very high. So as to ensure high correlation in the meteorological conditions between the sites of the weather station and the GNSS device, maximum horizontal and vertical distances between them have to be defined; on the one hand, only GNSS stations are used which are less than 10 km away from a respective weather station. Pressure is fairly constant on the horizontal spatial scale but in terms of temperature and water vapor pressure distances exceeding this boundary value would be a considerable uncertainty factor. On the other hand, there are also differences in altitude between the GNSS stations and the respective weather stations, what may cause similar problems as with horizontal distances. Here, the limit value is set to 100 meters height difference. Unlike  $T$  and  $e$ , pressure is vertically extrapolated from the ellipsoidal height of the weather station to the ellipsoidal height of the GNSS antenna by simply assuming a pressure lapse rate of 1 hPa per 8 meters in order to warrant highest possible accuracy of the resulting zenith hydrostatic delays  $\Delta L_h^z$ . Considering a temporal resolution of four epochs per day during 2013, data of 29 relevant IGS/weather station pairs can be used. The map in Fig. 3.13 shows their locations.

Inserting  $T$  and  $e$  from the weather stations into Eqs. (3.8) and (3.10) and comparing the resulting zenith wet delays to the reference values yields results that are very close to those of the preceding investigations, as Fig. 3.14 and Table 3.7 point out. The two bar plots in Fig. 3.15 show to which extent the augmentation is capable of improving the results for individual stations. In terms of SA-GPT2w 1 (that is, using only  $T$ ) the overall improvement in  $\Delta L_w^z$  is 5% with the majority of stations brought closer to the ray-traced delays. In contrast, SA-GPT2w 2 (that is, using  $T$  and  $e$ ) improves  $\Delta L_w^z$  much more significantly for all stations.

Overall, meteorological measurements of  $T$  and  $e$  turn out to distinctively improve the

<sup>16</sup>Zentralanstalt für Meteorologie und Geodynamik; the Austrian central institute for meteorology and geodynamics

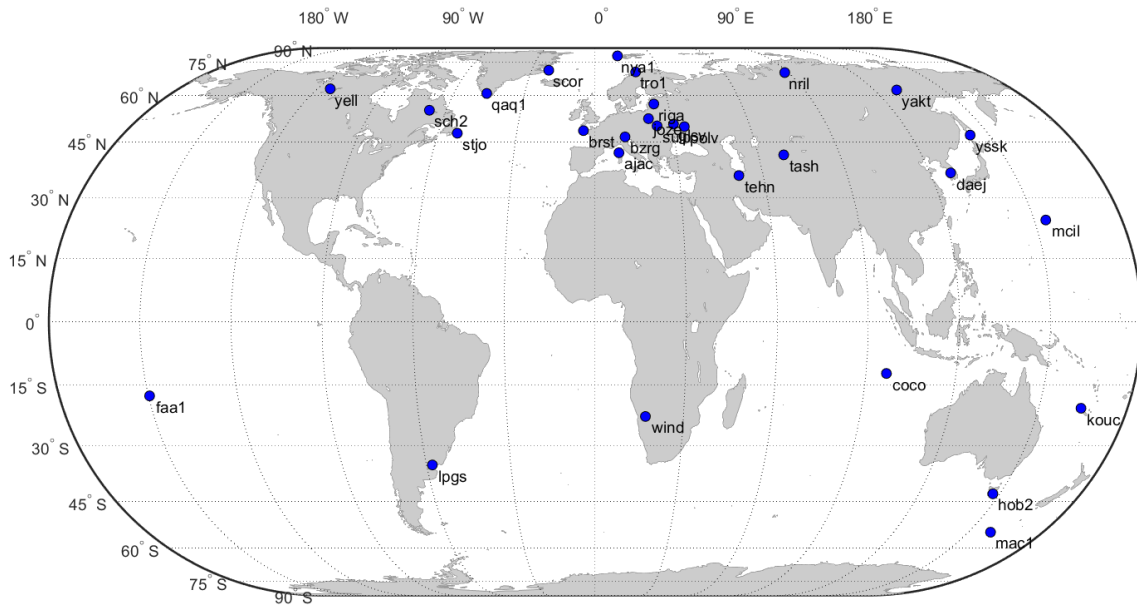


Figure 3.13.: Map of 29 IGS stations that each have a close-by weather station in order to estimate the performance of SA-GPT2w for GNSS applications.

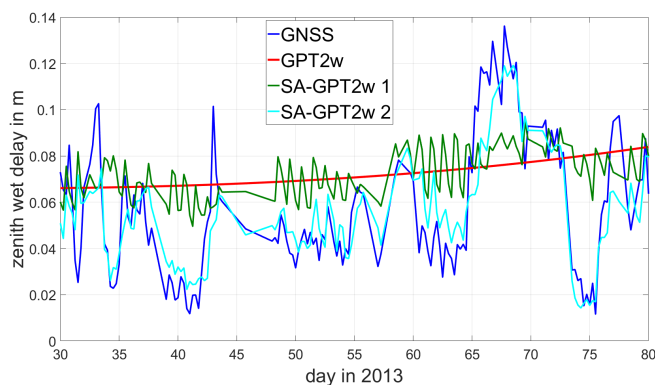


Figure 3.14.: Comparison of  $\Delta L_w^z$  from various sources for IGS station BZRG in Bolzano, Italy during the first quarter of 2013: the true  $\Delta L_w^z$  (dark blue), the empirical  $\Delta L_w^z$  from GPT2w (red), the  $\Delta L_w^z$  augmented by using in situ measured  $T$  (green) and the  $\Delta L_w^z$  augmented by using in situ measured  $T$  and  $e$  (light blue) [Landskron et al., 2016d].

Table 3.7.: Mean absolute differences in zenith wet delay  $\Delta L_w^z$  between high quality zenith wet delays from the IGS and several SA-GPT2w approaches averaged over 29 IGS stations and all epochs in 2013. The input parameters for SA-GPT2w,  $T$  and  $e$ , come from close-by weather stations.

TROPOSPHERE MODEL	MEAN ABS. DIFF. $\Delta L_w^z$ (cm)
GPT2w	2.8
universal $M$ :	
SA-GPT2w 1	2.7
SA-GPT2w 2	2.0
SA-GPT2w 3	2.0
geographically dependent $M$ :	
SA-GPT2w 1	2.7
SA-GPT2w 2	2.0

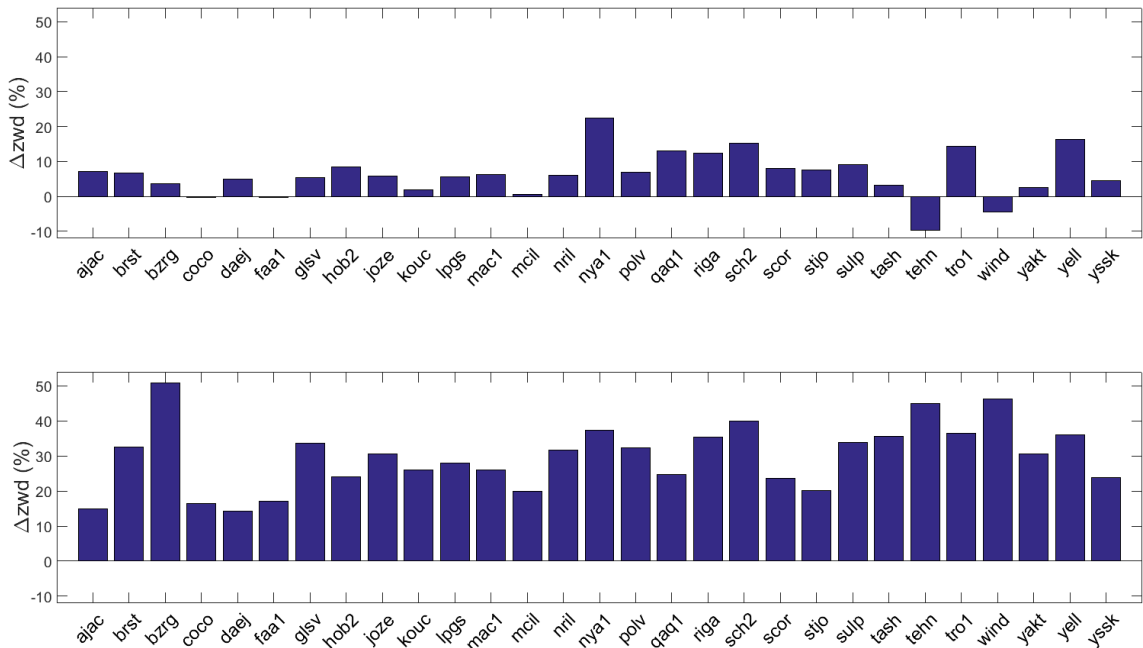


Figure 3.15.: Top: Station-wise improvement in  $\Delta L_w^z$  (%) of SA-GPT2w 1 compared to GPT2w only, using the universal  $M$  coefficient. Bottom: Station-wise improvement in  $\Delta L_w^z$  (%) of SA-GPT2w 2 compared to GPT2w only, also using the universal  $M$  coefficients.

resulting zenith wet delays. The application of the spatially dependent  $M$  coefficients is once again not necessary.

### Meteorological data from IGS in situ sensors

The general reference for the following is *Landskron et al.* [2016a].

A limited number of IGS stations is equipped with temperature, pressure and humidity sensors capable of measuring meteorological quantities together with the GNSS observations, particularly intended for the extraction of precipitable water vapor from the zenith total delay  $\Delta L^z$  [*Hackman and Byram, 2014*]. Thus an optimal correlation between meteorological data and tropospheric delays can be ensured because the distance between meteorological sensor and GNSS antenna is virtually zero, which was not the case in the preceding comparison for weather stations. Unfortunately, on the other hand the quality of data is fairly poor. Considering the period of 2013, many stations had to be excluded from the analysis beforehand because their meteorological data was simply useless, as the following itemization reveals:

- entirely wrong  $T$ ,  $p$  or  $e$  measurements (11 stations)
- occasionally wrong  $T$ ,  $p$  or  $e$  measurements (2 stations)
- only to a limited extent standardized data format
- wrong timestamps of the measurements at some stations

Apart from that, the exact coordinates of the meteorological sensors are provided only of half of the stations. Of those provided, the distances between meteorological sensors and GNSS devices is in the range of some meters. Although it is very likely that the remaining stations have their meteorological sensors mounted in the immediate vicinity of the GNSS device as well, it remains an element of uncertainty. After exclusion of all affected stations, 26 IGS stations remained (Fig. 3.16).

As evident from Fig. 3.17 and Table 3.8, in situ measurements of  $T$  and  $e$  again induce significant improvement in augmenting the empirical delays compared to the high precision ones.

Overall, SA-GPT2w leads to a significant improvement in the resulting zenith wet delays  $\Delta L_w^z$  also in this investigation.

### Meteorological data from NWM

Unlike with the two foregoing comparisons, here no data from GNSS analysis is used. Instead, it was tested to which extent SA-GPT2w can improve the results when the meteorological data comes from NWM of the ECMWF while the ray-traced  $\Delta L_w^z$  through them are regarded as the reference values.  $T_{NWM}$  and  $e_{NWM}$ , respectively, are utilized

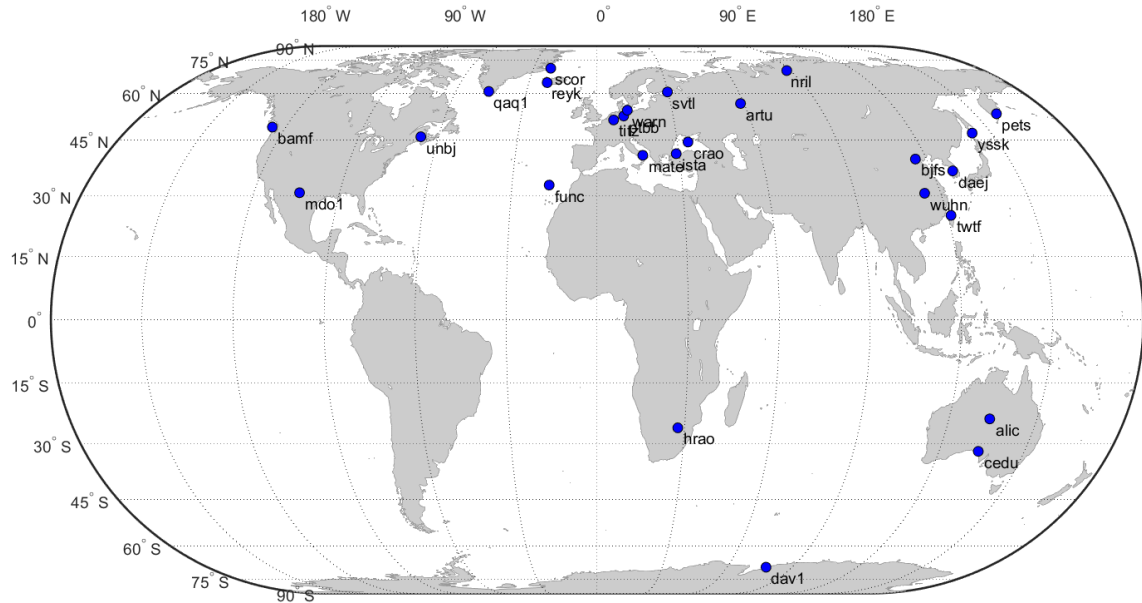


Figure 3.16.: Map of 26 selected IGS stations that are equipped with temperature, pressure and humidity sensors in order to estimate the performance of SA-GPT2w for GNSS applications.

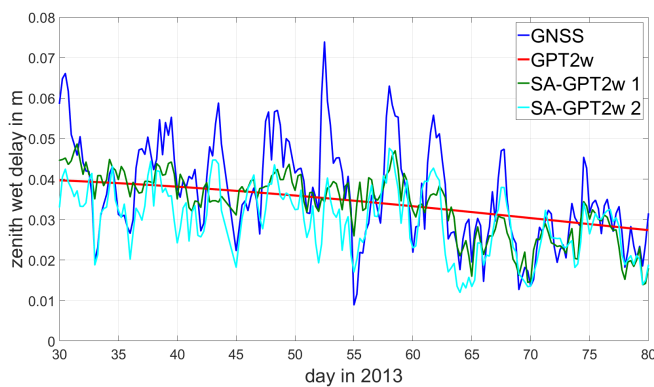


Figure 3.17.: Comparison of  $\Delta L_w^z$  from various sources for IGS station DAV1 at Davis Station in Antarctica during the first quarter of 2013: the true  $\Delta L_w^z$  (dark blue), the empirical  $\Delta L_w^z$  from GPT2w (red), the  $\Delta L_w^z$  augmented by using in situ measured  $T$  (green) and the  $\Delta L_w^z$  augmented by using in situ measured  $T$  and  $e$  (light blue). As this station is located at a very high latitude ( $-68^\circ 34' 48''$ ) what involves a generally lower water vapor content of the air, measuring  $T$  alone yet augments the empirical delay very well, although in some places the correlation is very low.

Table 3.8.: Mean absolute differences in zenith wet delay  $\Delta L_w^z$  between high quality zenith wet delays from the IGS and several SA-GPT2w approaches averaged over 26 IGS stations and all epochs in 2013. The input parameters for SA-GPT2w,  $T$  and  $e$  come from meteorological sensors mounted directly at the GNSS site.

TROPOSPHERE MODEL	MEAN ABS. DIFF. $\Delta L_w^z$ (cm)
GPT2w	2.8
universal $M$ :	
SA-GPT2w 1	2.6
SA-GPT2w 2	2.1
SA-GPT2w 3	2.1
geographically dependent $M$ :	
SA-GPT2w 1	2.7
SA-GPT2w 2	2.1

to augment the empirical  $\Delta L_w^z$ . The time period considered is 2011 through 2014 (5868 epochs for each station) and the 45 selected stations are shown on the map in Fig. 3.18. The resulting differences in  $\Delta L_w^z$  are outlined in Table 3.9.

The availability of NWM data for the entire network of IGS stations facilitates another investigation; it was already introduced earlier that the performance of the site-augmented GPT2w may not yield satisfying results in tropical areas or generally in areas with a high amount of water vapor in the air. However, due to lacking meteorological data for such stations, no general conclusion could be drawn so far. As opposed to this, NWM data is available for virtually every IGS station situated in close proximity of the equator, what enables a comparison with ray-traced delays. Data of 13 stations (Fig. 3.19) close to the equator in the time period of 2011 through 2014 is analyzed what leads to the results in Table 3.10. As expected, the augmentation does not work as well as for stations located in temperate and dry areas, but there is still an improvement visible. The version SA-GPT2w 1, however, slightly degrades  $\Delta L_w^z$  and should therefore not be used for sites in the tropics.

All in all, as with the foregoing comparisons, the improvement of the empirical  $\Delta L_w^z$  using meteorological information from NWM distinctively improves the results. Thus, it can be concluded that meteorological quantities from NWM are perfectly suited as input values for SA-GPT2w as well. This is of particular importance for users who have access to NWM but no chance of performing ray-tracing to obtain more exact delays; instead, they can easily create the empirical delays with GPT2w and augment them with the NWM quantities.



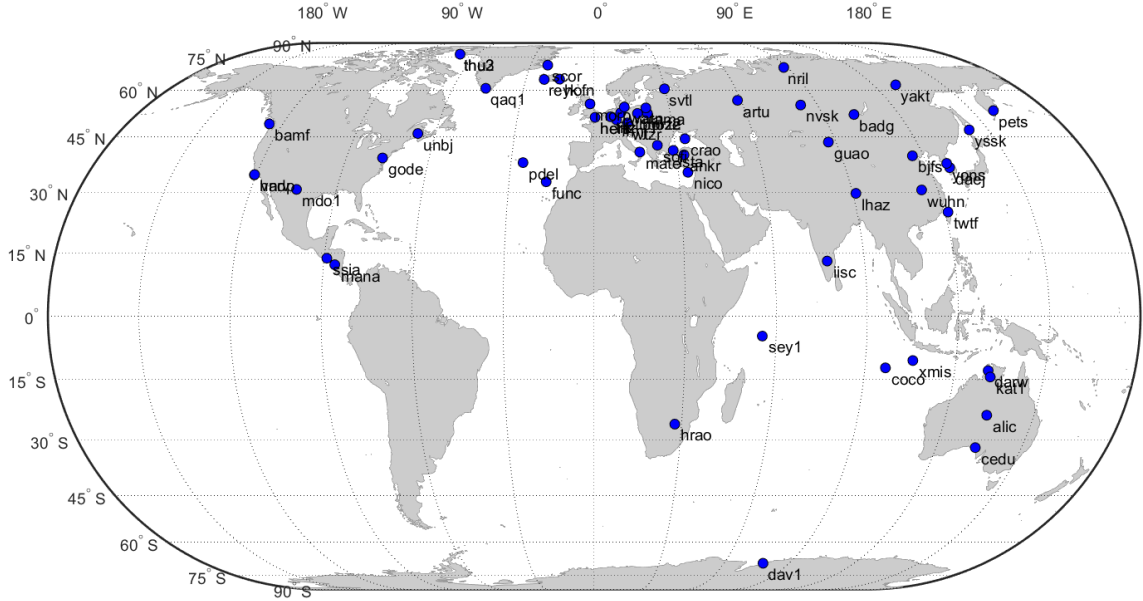


Figure 3.18.: Map of 45 IGS stations that were selected for analyzing the potential of meteorological quantities from NWM as input for SA-GPT2w in order to augment empirical  $\Delta L_w^z$ . These stations are simply those of the two previous GNSS comparisons combined.

Table 3.9.: Mean absolute differences in zenith wet delay  $\Delta L_w^z$  between ray-tracing and several SA-GPT2w approaches averaged over 45 IGS stations and all epochs from 2011-2014. The input parameters for SA-GPT2w,  $T$  and  $e$  come from NWM interpolated to the very location of the IGS site.

TROPOSPHERE MODEL	MEAN ABS. DIFF. $\Delta L_w^z$ (cm)
GPT2w	3.0
universal $M$ :	
SA-GPT2w 1	2.9
SA-GPT2w 2	2.2
SA-GPT2w 3	2.1
geographically dependent $M$ :	
SA-GPT2w 1	2.8
SA-GPT2w 2	2.1

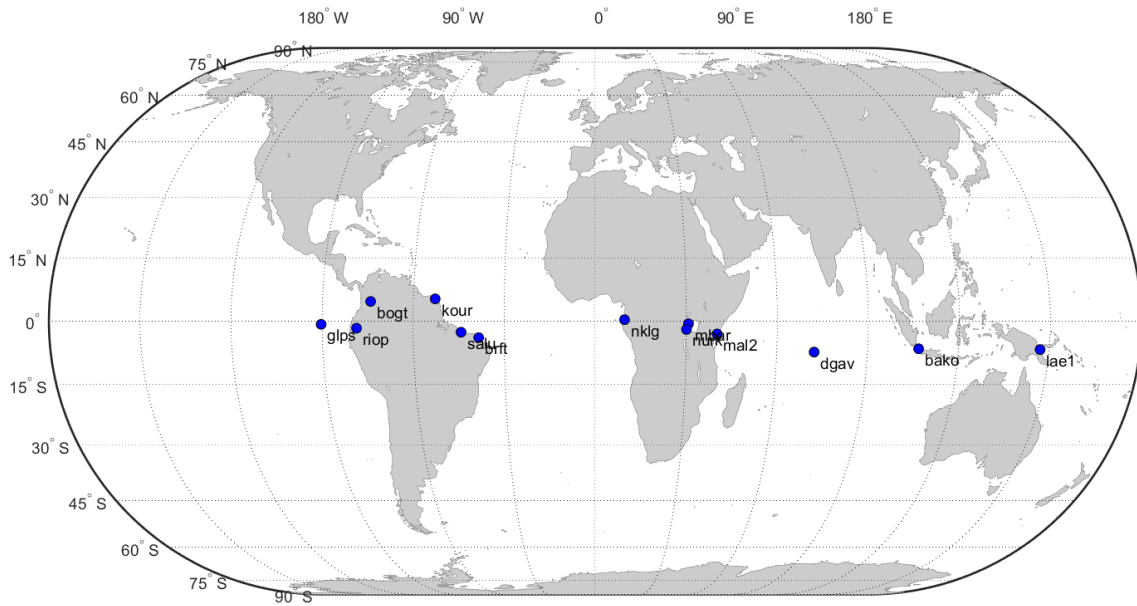


Figure 3.19.: Map of 13 IGS stations that were selected for analyzing the potential of site-augmented GPT2w for GNSS stations located close to the equator. The meteorological quantities as input for SA-GPT2w in order to augment empirical  $\Delta L_w^z$  come from NWM.

Table 3.10.: Mean absolute differences in zenith wet delay  $\Delta L_w^z$  between ray-tracing and several SA-GPT2w approaches averaged over 13 IGS stations close to the equator and all epochs from 2011-2014. The input parameters for SA-GPT2w,  $T$  and  $e$  come from NWM interpolated to the very location of the respective IGS site.

TROPOSPHERE MODEL	MEAN ABS. DIFF. $\Delta L_w^z$ (cm)
GPT2w	2.8
universal $M$ :	
SA-GPT2w 1	2.9
SA-GPT2w 2	2.5
SA-GPT2w 3	2.6
geographically dependent $M$ :	
SA-GPT2w 1	2.6
SA-GPT2w 2	2.6

Table 3.11.: Mean BLR (cm) from VLBI analyses for different time periods considering several kinds of models. The input parameters for SA-GPT2w,  $T$  and  $e$ , come from the NGS-files. The last column shows the averaged values from CONT11 and CONT14, which are regarded as the final results.

TROPOSPHERE MODEL	BLR (cm)	BLR (cm)	BLR (cm)
	CONT11	CONT14	MEAN
VMF1	3.10	2.58	<b>2.84</b>
GPT2w	13.17	11.36	<b>12.27</b>
universal $M$ :			
SA-GPT2w 1	12.65	10.79	<b>11.72</b>
SA-GPT2w 2	10.56	7.39	<b>8.98</b>
SA-GPT2w 3	10.55	7.46	<b>9.00</b>
geographically dependent $M$ :			
SA-GPT2w 1	12.31	10.49	<b>11.40</b>
SA-GPT2w 2	9.92	7.37	<b>8.65</b>

#### 3.2.5.4. Comparison of BLR

Comparing baseline length repeatabilities (BLR) with each other holds a key advantage as against the comparison of delays: there is a true value that is targeted, namely zero. As reaching a BLR of zero is not achievable in reality however, the purpose is to get as close as possible to this value. The lower a certain BLR, the higher the quality of the tested model what allows absolute statements about how well a certain model fits.

The baseline lengths are calculated in *VieVS* for the period and stations of CONT11 and CONT14, as well as for a longer process list containing 1339 sessions from 2006 through 2014, each using the VieVS standard approach without estimating zenith wet delays. Usually, this estimation of zenith wet delays is common practice in VLBI analysis, however, it is not applied in this investigation as it would disguise the performance of the a priori modeling using SA-GPT2w. The results are displayed in Tables 3.11 and 3.12.

Table 3.11 allows to draw some conclusions:

- The best results are achieved with SA-GPT2w 2, using spatially dependent  $M$  coefficients, yielding a BLR 29.5% better than with using GPT2w.
- The improvement when measuring only temperature is more distinct than in the preceding comparisons, in fact 4.5% with respect to GPT2w.
- Interestingly, when using GPT2w plus improving only  $a_h$ , the BLR becomes slightly worse (13.20 cm > 13.17 cm for CONT11). This would mean that the augmentation of  $a_h$  is pointless.

Table 3.12.: *Mean BLR (cm) from VLBI analyses for 1339 VLBI sessions from 2006-2014 considering several kinds of models. Stations TIGOCONC and DSS13 were excluded from the solution, as repeatabilities of baselines containing these stations are extraordinarily high.*

TROPOSPHERE MODEL	BLR (cm)
VMF1	4.19
GPT2w	11.61
universal $M$ :	
SA-GPT2w 1	11.28
SA-GPT2w 2	9.28
SA-GPT2w 3	9.36

- Unlike the previous comparisons, here the version with the geographically dependent  $M$  coefficients yields a noticeable improvement in the BLR, ranging between 2.7% and 3.7% improvement with respect to the universal coefficients.
- In VLBI, zenith wet delays are usually estimated in the analysis, therefore the here shown augmentation of empirical zenith wet delays would be redundant. However, this comparison was just done in order to show that generally the augmentation of zenith wet delays would have the potential to significantly improve also BLR, what can be utilized for many fields of application other than VLBI.
- The only drawbacks of this comparison are the short time period and again the quality of the meteorological data. Apart from that, the results are fairly meaningful.

Concerning Table 3.12, the BLR improve significantly by 20% when using SA-GPT2w 2 instead of the standard GPT2w, more precisely, for 82% of the baselines (373 of 453). This is very similar to the results of Table 3.11, but more meaningful because of the longer time span.

### 3.2.6. Conclusions

Taking all of the above sections into consideration, the importance and the performance of the site-augmented GPT2w (SA-GPT2w) can be concluded as follows:

In many GNSS applications there is no access to real-time information from NWM. Therefore, empirical troposphere models are needed. By incorporating in situ meteorological data the performance of these empirical models, more precisely the accuracy of the zenith wet delays  $\Delta L_w^z$ , can be brought to a new level. Measuring temperature  $T$  improves the resulting delays by about 5% while additional measurement of  $e$  substantially improves them by approximately one quarter to one third. This is of particular impor-

tance for GNSS applications whereas in VLBI the zenith wet delay is usually estimated in the data analysis, why an augmentation of the a priori zenith wet delay does not make sense. Instead, the hydrostatic  $a$  coefficient can be augmented through information about temperature at the site, even though this plays a minor role for the final accuracy. But yet the resulting slant hydrostatic delays  $\Delta L_h$  at  $5^\circ$  elevation can thus be improved by more than  $1/5$ , however in BLR comparisons there is no improvement visible.

The advantages of SA-GPT2w can be summarized as follows:

- Best performance is achieved in all non-tropical regions, that is, stations where the amount of water vapor in the air is not extraordinarily high. However, even there an improvement of the resulting zenith wet delays can be attained.
- Best performance of the augmentation when measuring only  $T$  (= SA-GPT2w 1) is achieved at very high latitudes where there is generally a low water vapor content.
- SA-GPT2w 2 is only marginally better than SA-GPT2w 3. This may be due to the fact that water vapor pressure  $e$  is sufficient for the augmentation and additional  $T$  (as is needed in SA-GPT2w 2) brings only a marginal further improvement.
- In terms of the analysis, SA-GPT2w is not associated with more work for the user as the algorithm can be applied just as GPT2w.
- Besides, the standard GPT2w yields slightly better results than MTT even though it is entirely empirical, while MTT utilizes in situ measurements of temperature.

On the other hand, there are also disadvantages:

- The algorithm is prone to faulty measurements of the meteorological quantities. Like the flaws in the NGS-files, as mentioned above, it might as well happen to any GNSS user that temperature measurements are not correct due to e.g. incidence of direct sunlight. There are (loose) bounds designed to detect and eliminate gross errors, however, many faulty values may slip through.
- The augmentation of zenith wet delays using SA-GPT2w 1 does not work in very moist or tropical regions as information about temperature is not sufficiently indicative of the zenith wet delay when the air is too humid.

In general, the performance of SA-GPT2w is limited by the following 3 factors:

- Measurements of temperature or water vapor pressure at the Earth's surface are only partly representative for their distribution above the site. There may be temperature inversions at certain heights which influence the resulting  $a_h$  coefficient much more than the temperature at the site does. The same is true for weather fronts, which induce rapid changes of the air's water vapor content. As opposed to this, in situ measurement of pressure is almost entirely representative for the distribution above the site, since (assuming hydrostatic equilibrium) the weights of all air layers add up to the total weight measured at the Earth's surface. Only because winds prohibit

a perfect hydrostatic equilibrium the resulting error is about 0.2 mm path delay [Nilsson *et al.*, 2013], while under severe weather conditions it can reach up to 20 mm [Davis *et al.*, 1985].

- As is shown in Table 3.2 on page 22, the correlations between the respective quantities are quite distinctive, but SA-GPT2w would work perfectly only if all of them were 1. This is related to the problem described in the preceding item.
- In reality, the  $M$  coefficients are geographically and temporally dependent. However, these variations are impossible to be modeled in an empirical way as the coefficients are fluctuating randomly and quickly, subject to the current weather situation. Therefore, the suggested usage of universally valid  $M$  coefficients cannot describe the actual state flawlessly and even a refining to geographically dependent  $M$  coefficients cannot solve this problem.

### 3.3. Site-augmentation of VMF1

Similar to the site-augmentation of the blind troposphere model GPT2w it is tested whether an improvement of the performance of VMF1 can be achieved by incorporating information of in situ measurements.

The standard way of applying VMF1 in VLBI analysis is such that values for the hydrostatic mapping function coefficient  $a_h$  and the zenith wet delay  $\Delta L_w^z$ , amongst others, are provided at each NWM epoch, namely at 00:00, 06:00, 12:00 and 18:00 UT each day. However, VLBI antennas usually do not perform measurements at these very epochs but at irregular times in between. The values of  $a_h$  and  $\Delta L_w^z$  are therefore commonly interpolated from the surrounding NWM epochs to the exact time of measurement, for instance by applying a Lagrange interpolation. In case of *VieVS*, the Lagrange interpolation uses five epochs before and after as sampling points in order to interpolate the respective value at the desired time (Fig. 3.20)<sup>17</sup>. The shortcoming of this approach is that in reality both  $a_h$  and  $\Delta L_w^z$  do not progress as regularly as the interpolation predicts them to, but rather fluctuate irregularly between the NWM epochs. Since temperature  $T$  is correlated with  $a_h$ , it might be possible for a station that  $a_h$  exhibits a significant peak between epochs 12:00 and 18:00 due to a temporary rise in temperature, what of course cannot be captured by the Lagrange interpolation. Likewise, it might as well happen that the real zenith wet delays have peaks between the NWM epochs that cannot be captured by the Lagrange interpolation either, as Fig. 3.20 depicts. For this reason it is attempted to increase the number of  $a_h$  coefficients and zenith wet delays by additionally utilizing in situ measurements of meteorological quantities which are done together with every VLBI measurement. That is, for every observation epoch of each VLBI station, temperature,

<sup>17</sup>after this investigation, in 2015, the interpolation method used in *VieVS* was changed to spline interpolation

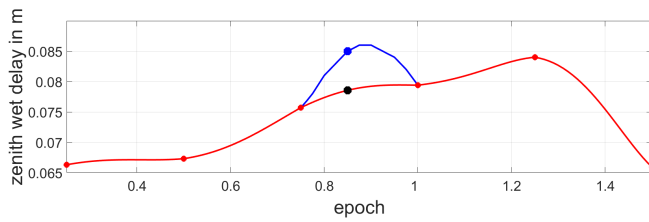


Figure 3.20.: The red line shows  $\Delta L_w^z$  as determined by the Lagrange interpolation (red dots represent NWM epochs), while the blue line shows a possible progression of the real  $\Delta L_w^z$ . The difference between the black dot and the blue dot then marks the error in the modeled  $\Delta L_w^z$ .

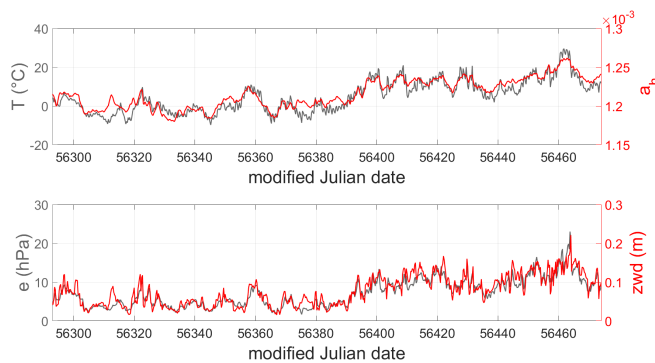


Figure 3.21.: Context between  $T$  and  $a_h$  (top) and between  $e$  and  $\Delta L_w^z$  (bottom) for VLBI station WETTZELL during first half of 2013.

pressure and water vapor pressure are measured directly at the site and saved in the NGS-file. More precisely,  $T$  can be used to augment  $a_h$  and  $e$  for  $\Delta L_w^z$ , respectively, analogously to SA-GPT2w. Thus, the temporal resolution of VMF1 is thought to be increased.

### 3.3.1. Application of the site-augmented VMF1

The basic idea of the temporally augmented VMF1 approach is the assumption that when temperature  $T$  between two NWM epochs rises, the respective  $a_h$  must rise as well. The same is assumed for  $e$  and  $\Delta L_w^z$ . This assumption is supported by the distinct correlation between the quantities, as illustrated in Fig. 3.21 (also cf. Table 3.2 on page 22). Here it can be seen that a long-term context between the quantities is undoubtedly existing, but in the short term, an increase in one value is not always accompanied by an increase in the related value. In order to model the augmentation, several approaches, most of which quite similar to each other, were devised and tested with only the final one described in more detail later. Unfortunately, it needs to be noted already at this point that ultimately neither of the approaches was able to improve accuracy though.

At the NWM epochs, there are both  $T$  and  $e$  as well as  $a_h$  and  $\Delta L_w^z$  available from the NWM, while at the observational epochs only  $T$  and  $e$  are available from in situ data. The augmentation approach is now such that data from the two NWM epochs surrounding the observation epoch is used to determine  $a_h$  and  $\Delta L_w^z$  at the observational epoch. As meteorological data from NWM is not always consistent with that from observational data

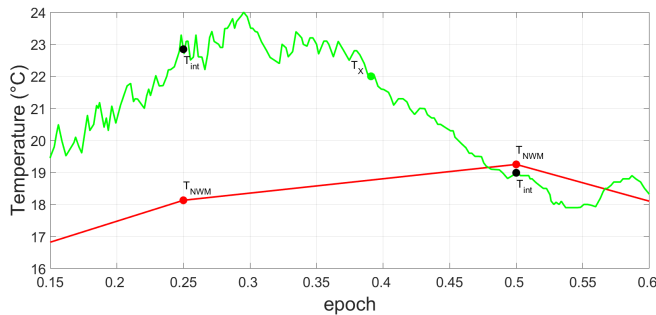


Figure 3.22.: Exemplary  $T$  from in situ measurement (green) and from NWM (red) at station WETTZELL in early 2011. The  $T_{int}$  are linearly interpolated from the observational data to the NWM epochs, and it can be seen that they are considerably different from the respective NWM values. The green dot  $T_X$  marks an exemplary point for which the augmented VMF1 shall be applied.

(see Appendix B), special arrangements need to be made. This in further consequence implies that the meteorological data from NWM cannot be used because it is not related to the in situ measured meteorological data. Instead, the in situ temperature is linearly interpolated from the surrounding observational epochs to the NWM epochs ( $T_{int}$ ). This is possible without significant loss in accuracy since there are generally numerous observational epochs per day, and the maximum possible distance for the interpolation is six hours. Figure 3.22 shows this graphically.

So the general assumption of the site-augmented VMF1 is that the variation in  $T$  is equivalent to that of  $a_h$  and the variation of  $e$  equivalent to  $\Delta L_w^z$ , respectively. However, as  $\Delta L_w^z$  is usually estimated very accurately in VLBI analysis anyway, the site-augmentation is carried out only for  $a_h$ . The  $M_{a_h}$  coefficient from SA-GPT2w (see Table 3.3 on page 26) is applied in order to infer from the variation of  $T$  to that of  $a_h$ . For this purpose,  $T_{int} - T_{NWM}$  is created for both surrounding NWM epochs and the two resulting  $a_h$  are then linearly interpolated with respect to the modified Julian date. Through this linear interpolation, the difference between the scales of  $T_{int}$  and  $T_{NWM}$  is corrected. In other words, the (larger) difference between the two  $T_{int}$  is mapped down to the difference between the two  $T_{NWM}$ , which is necessary since the desired  $a_h$  shall refer to the NWM scale.

A set of bounds is applied in order to prevent errors or unrealistic values in the results. For all values that do not pass these bounds, the standard VMF1 shall be used.

- The linear interpolation of  $T_{int}$  works only if there is at least one observation data point on either side of  $T_{NWM}$ .
- There may be flaws in the in situ measurements which in further consequence affect  $T_{int}$ , what can be detected and prevented by setting a maximum difference between  $T_{int}$  and  $T_{NWM}$ .
- Another indicator for flawed NGS meteorological data may be when the development



of  $T_{int}$  is highly disproportionate to that of  $T_{NWM}$ . In Fig. 3.22, for instance,  $T_{int}$  processes distinctively differently than  $T_{NWM}$ . However, in this case the difference is still small enough to pass the bound.

### 3.3.2. Conclusions

As already mentioned, the site-augmented VMF1 unfortunately does not yield an improvement in accuracy compared to the standard VMF1. This is found by comparing baseline length repeatabilities for CONT11 with each other. In addition, when augmenting only  $a_h$ , the resulting difference in BLR is too small to be detected at all. Averaged over all stations and epochs of CONT11, the augmented  $a_h$  differ only by 0.13% from the standard ones. Therefore, the performance of augmenting  $\Delta L_w^z$  also has to be considered in order to draw conclusions about the performance of the general augmentation algorithm. There may be a number of reasons why the augmentation algorithm does not improve  $a_h$ , but the following explanations seem quite obvious though:

- The short-term correlations between  $T$  and  $a_h$  as well as between  $e$  and  $\Delta L_w^z$  are not high enough to be applied in this high-precision field. It works well for the site-augmentation of GPT2w (cf. Section 3.2) where the purpose is to augment empirical values of moderate quality. However, the correlations do not seem to have the potential to improve high-quality data such as VMF1 values. Close examination of Fig. 3.21 reveals that a change in  $T$  from one epoch to the next only seldom comes with an equivalent change in  $a_h$ . The long-term correlation between  $T$  and  $a_h$  is proved by the considerably high correlation coefficient of 0.86 (cf. Table 3.2 on page 22), however, the short-term correlation between two consecutive epochs is apparently insufficient.
- The observational meteorological data is surprisingly different from that of NWM. The reason for this is not totally clear (cf. Appendix B.1), but it is beyond question that thus the performance of the site-augmented VMF1 is strongly limited.
- There may be a minor loss in accuracy due to the linear interpolation of  $T_{int}$  and  $e_{int}$ , but as far as could be found out, this error is negligible.



## 4. Determination of new mapping function concepts

The determination of new, advanced mapping functions constitutes the major part of this thesis. Compared to the other sections, whether it be consideration of azimuthal asymmetry, determination of a new empirical troposphere model or the site-augmentation of already existing empirical troposphere models, the influence of mapping functions on the resulting positions is considerably higher. To put it another way, flaws in mapping functions cause higher positioning errors than flaws in any of the other aforementioned approaches in tropospheric delay modeling. This holds especially for low elevation observations, as these experience the longest signal path through the troposphere. The lower the accuracy of a mapping function, the more deficient the resulting modeled delay and, in turn, the higher the positioning error. *Böhm et al.* [2006a] stated a rule of thumb that the error in station height is one fifth of the error in the mapping function at an elevation of  $5^\circ$ . For this reason, the longest section of this thesis is dedicated to the description of new approaches in determining mapping functions.

The showpiece of this chapter is undoubtedly the Vienna Mapping Functions 3 (VMF3). But before explaining its concept and application in the minutest details, an introduction to the motives of designing a new mapping function is given. This contains the determination of reprocessed VMF1 coefficients (Section 4.1) and the "rigorous" determination of all three coefficients in one least-squares adjustment (Section 4.2), which later serves as the framework for VMF3. The VMF3 themselves are presented in Section 4.3. Additionally, a new empirical troposphere model GPT3 is designed based on the same data (Section 4.4). Eventually the performance of all new models is assessed (Section 4.5) before breaking everything down into the final conclusions of this chapter (Section 4.6). The several new models will be given certain names each, which might create confusion as they more or less resemble each other. For this reason, Tab. 4.1 shall serve as a guide for upcoming names and labels which sooner or later come up during this chapter.

As already mentioned at an earlier stage, the Vienna Mapping Functions 1 (VMF1) are thought to be the most accurate mapping functions to date and are commonly used at institutions all over the world. However, as their publication dates back to 2006, many new approaches were evolved in recent years such as the Adaptive Mapping Functions (AMF) by *Gegout et al.* [2011], the UNB-VMF1<sup>1</sup> [*Santos et al.*, 2012], which are based

---

<sup>1</sup>University of New Brunswick VMF1

Table 4.1.: *A list of all mapping function approaches mentioned in this chapter.*

IDENTIFIER	NAME	REMARK
VMF1	Vienna Mapping Functions 1	
VMF1 <sub>repro</sub>	reprocessed VMF1; empirical $b$ and $c$ , $a$ for 3° elevation	referred to as 'fast approach' in <i>Böhm</i> [2004]
VMF1 <sub>reproLSM</sub>	reprocessed VMF1; empirical $b$ and $c$ , $a$ from LSM	
VMF <sub>LSM</sub>	$a$ , $b$ and $c$ from LSM	referred to as 'rigorous approach' in <i>Böhm</i> [2004]
VMF3	Vienna Mapping Functions 3; empirical $b$ and $c$ , $a$ for 3° elevation	
VMF3 <sub>LSM</sub>	Vienna Mapping Functions 3; empirical $b$ and $c$ , $a$ from LSM	
GPT2w	Global Pressure and Temperature 2 wet	
GPT3	Global Pressure and Temperature 3	

on the same model as VMF1 but use different ray-tracing software and different NWM (NCEP<sup>2</sup>), the gridded UNB-VMF1 [*Urquhart et al.*, 2014b] which, equivalent in design to UNB-VMF1, were determined for the same grid size as the gridded VMF1, or the Potsdam Mapping Factors PMF [*Zus et al.*, 2014], to name but a few. However, none of them were able to outperform VMF1 yet. Also at our institute the call for a revised VMF1 got louder and is one of the objectives of the project "Radiate VLBI" which this thesis is based on. In addition to the reasons of age, *Zus et al.* [2015] found shortcomings in VMF1 due to its tuning for the specific elevation of 3.3°, station heights and orbital altitudes. Apart from the potential for improving VMF1, there has always been a general endeavor in the geodetic community to find possibilities to precisely model observations at ever lower elevations in order to improve the observation geometry, increase the amount of data and to derive valuable meteorological data [*Rocken et al.*, 2001]. With the advent of VMF1 it became possible to model delays down to 3° elevation which it is tuned for [*Böhm et al.*, 2006a]. Observations even below this elevation are yet believed to further improve the observation geometry, but solving this problem would require a general revision of the continued fraction form (Eq. (2.5) on page 7). Extending it by a fourth coefficient  $d$  does not yield significant improvement [*Urquhart*, 2014a], why a different, probably more sophisticated equation would need to be devised.

In the following sections, new concepts are introduced which are all based on the same

<sup>2</sup>United States National Centers for Environmental Prediction

idea as VMF1, that is, extracting information from the NWM by means of ray-tracing and approximating these ray-traced delays on the basis of a model with the equation of *Marini* [1972] (Eq. (2.5)). The Vienna Mapping Functions 3 (VMF3) turn out to be the major achievement in this respect. First, the general concept of all approaches is elucidated (Sections 4.1 to 4.3) in order to get a clear understanding of the theories behind. In Section 4.5, the approaches are then compared with each other for a variety of tasks so that general statements about the performance and quality of each approach can be made. All findings and conclusions are then summarized in Section 4.6.

## 4.1. Determination of reprocessed VMF1 mapping function coefficients

As mentioned in Tab. 2.1 on page 10, ray-traced delays determined for VMF1 are calculated with a simple 1D-ray-tracer. The main reason for this was the high computational requirements of ray-tracing back in 2006. In the eleven years since then, however, the computational performance of ordinary computers has increased dramatically what in turn opens new possibilities for the application of more sophisticated ray-tracing approaches. More precisely, nowadays thousands of 2D ray-traced delays can easily be calculated in virtually no time at all. Two-dimensional ray-tracing means the ray path well considers varying refractivities at different pressure levels, what results in a curve-like, piecewise linear succession of straight lines. At first sight this may appear three-dimensional, as the ray path propagates through all three planes of the Euclidean geometry. Three-dimensional (3D) ray-tracing, however, also takes variations in azimuth at the different height levels into account, while for 2D ray-tracing the ray path is limited to a vertical plane [*Hofmeister*, 2016]. Thus, the ray path of 3D ray-tracing turns out to be close to a space curve. Figure 4.1 shows the basic principle of ray-tracing. For more information on ray-tracing please refer to the dissertation of *Hofmeister* [2016], where the fundamentals are explained in the minutest details. *Hobiger et al.* [2008b] also provide an extensive overview of ray-tracing algorithms for modeling tropospheric delays.

In the following, the determination of reprocessed VMF1 coefficients is discussed. For this purpose, two approaches will be explained below. Their performance is then assessed through a set of comparisons, as is shown in Section 4.6.

### 4.1.1. Empirical values for $b$ and $c$ , analytically calculating $a$

This approach is equal to the standard VMF1 concept regarding its basic idea, the only two functional differences are that (1) ray-traced delays from the 2D ray-tracing software *RADIATE* are used and (2) that the underlying NWM has a denser horizontal resolution, namely  $1^\circ \times 1^\circ$ . That is, the same empirical coefficients  $b$  and  $c$  as in VMF1 are used, but the  $a$  coefficients, which are calculated strictly for the elevation of  $3^\circ$ , get new values.

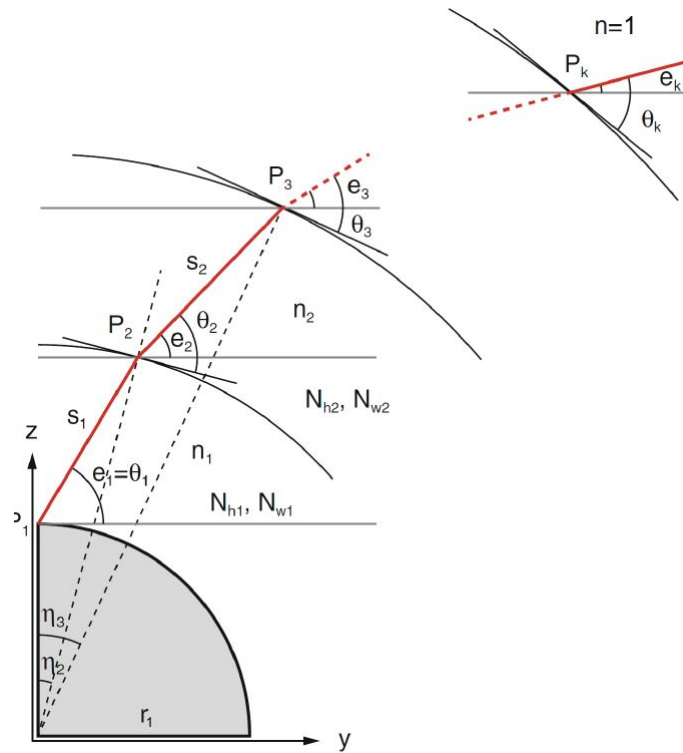


Figure 4.1.: From Nilsson et al. [2013]: The geometric principle of the piecewise linear ray-tracing approach which is used as the basis for the determination of mapping functions. Note that the refractivity changes only with every height level (pressure level). For reasons of simplicity, here only the 1D case is shown.

Thus, it can be tested to which extent the new ray-tracer, and to a lesser extent the denser NWM, are able to improve the results. This approach is henceforth referred to as VMF1<sub>repro</sub>.

#### 4.1.2. Empirical values for $b$ and $c$ , least-squares adjustment for $a$

In this approach the empirical values from VMF1 are used for  $b$  and  $c$  as well, but the coefficients  $a$  are not determined strictly for the elevation of  $3^\circ$  but are fitted to ray-traced mapping functions in an iterative least-squares adjustment for a set of elevations. In the following, this approach will be referred to as VMF1<sub>reproLSM</sub>. The idea behind it is to test whether the faster (in terms of computational time) VMF1<sub>repro</sub> is able to keep up with VMF1<sub>reproLSM</sub>, which underlies a more advanced model and therefore demands more computational time.

Ray-tracing is performed for a set of elevations and azimuths which vary for the different tasks. The exact specifications differ from case to case, as will be shown in Section 4.5. However, common to all cases is that all ray-traced delays at the same elevation but with different azimuths are averaged to one single delay each. This shall simulate delays that are independent of azimuth. Moreover, the selected elevations ought to exhibit a broad and sensible spatial distribution between  $3^\circ$  and  $90^\circ$ <sup>3</sup>, because on the one hand the performance of ray-tracing decreases with decreasing elevation angles but on the other hand the importance of accurate mapping functions increases with decreasing elevation angles. Apart from that, the number of elevations shall be kept as small as possible as to minimize computational effort.

For the least-squares adjustment the design matrix  $A$  is devised by partial derivation of the continued fraction form Eq. (2.5) with respect to the unknown coefficient  $a$ , which in the following Eq. (4.1) is simply abbreviated with  $mf$ . Please note that the design matrix must be set up separately each for the hydrostatic and the wet part.

$$A = \begin{bmatrix} \frac{\partial mf(\varepsilon_1)}{\partial a} \\ \frac{\partial mf(\varepsilon_2)}{\partial a} \\ \vdots \\ \frac{\partial mf(\varepsilon_n)}{\partial a} \end{bmatrix} \quad (4.1)$$

This may look straightforward. However, when conducting the derivation in Eq. (4.1) for

---

<sup>3</sup>since the equation by Marini (Eq. (2.5)) is only valid for elevations above  $3^\circ$

a given elevation, the equation transforms to:

$$\frac{\partial \text{mf}(\varepsilon)}{\partial a} = \frac{1}{\left(\frac{b}{c+1} + 1\right) \left(\sin(\varepsilon) + \frac{a}{\sin(\varepsilon) + \frac{b}{c+\sin(\varepsilon)}}\right) \frac{\frac{a}{c+1} + 1}{\left(\sin(\varepsilon) + \frac{a}{\sin(\varepsilon) + \frac{b}{c+\sin(\varepsilon)}}\right)^2 \left(\sin(\varepsilon) + \frac{b}{c+\sin(\varepsilon)}\right)}} \quad (4.2)$$

It quickly becomes clear that we are dealing with a nonlinear problem here as the derivative  $a$  appears on the left as well as on the right side of the equation, which prohibits a simple least-squares adjustment like it is done e.g. for the derivation of horizontal gradients (see Chapter 5.1.1.1 on page 92). In order to solve nonlinear equation systems, an iterative least-squares adjustment must be performed instead which is associated with significantly more work and computational time. For this purpose certain starting values for  $a$  are needed in the first run, which are set to the more or less realistic values of  $a_{h_0} = 0.0012$  and  $a_{w_0} = 0.00055$ . The observation vector  $l$  is obtained by subtracting the computed mapping functions  $L_0$  (using Eq. (2.5)) from the observed values  $L$  acquired by ray-tracing.

$$\begin{aligned} l &= L - L_0 \\ &= \text{mf}_{\text{observed}} - \text{mf}_{\text{computed}} \end{aligned} \quad (4.3)$$

The unknowns  $x$ , in an iterative approach meaning the additions to the starting values of  $a$ , are determined through:

$$x = (A^T A)^{-1} A^T l \quad (4.4)$$

The new, iterated values for  $a$  are simply determined by

$$a_1 = a_0 + x \quad (4.5)$$

and then inserted into the least-squares adjustment for a further iteration, what means that the design matrix  $A$  and the computed observation vector  $L_0$  are rearranged. This is done until the additions  $x$  are smaller than  $10^{-12}$ , so that convergence is guaranteed and the resulting value for  $a$  is of sufficient accuracy<sup>4</sup>. Only five iterations are required to achieve this on average, at minimum four and at maximum nine. It should be noted that the hydrostatic coefficients converge faster than their wet counterparts, because the variation of underlying ray-traced mapping functions is less pronounced.

## 4.2. Least-squares adjustment for $a$ , $b$ and $c$

In this approach all three mapping function coefficients are determined together in a least-squares adjustment. It is referred to as the "rigorous approach" in *Böhm et al.* [2006a], but

<sup>4</sup>at 3° elevation, this corresponds to an accuracy of approximately  $6 \cdot 10^{-9} m$  of the resulting delay



will here be called  $\text{VMF}_{\text{LSM}}$  for the sake of consistency. This procedure is thought to be most realistic since it utilizes the full information of the NWM [Böhm, 2004], whereas the other concepts possess an element of uncertainty through the simplified use of empirical coefficients.

The basic model regarding elevations and azimuths is similar to that of the preceding section where only the  $a$  coefficient is estimated, but here not two but six coefficients must be fitted to the ray-traced delays. The design matrix  $A$  for the hydrostatic as well as for the wet part thus extends to:

$$A = \begin{bmatrix} \frac{\partial \text{mf}(\varepsilon_1)}{\partial a} & \frac{\partial \text{mf}(\varepsilon_1)}{\partial b} & \frac{\partial \text{mf}(\varepsilon_1)}{\partial c} \\ \frac{\partial \text{mf}(\varepsilon_2)}{\partial a} & \frac{\partial \text{mf}(\varepsilon_2)}{\partial b} & \frac{\partial \text{mf}(\varepsilon_2)}{\partial c} \\ \vdots & \vdots & \vdots \\ \frac{\partial \text{mf}(\varepsilon_n)}{\partial a} & \frac{\partial \text{mf}(\varepsilon_n)}{\partial b} & \frac{\partial \text{mf}(\varepsilon_n)}{\partial c} \end{bmatrix} \quad (4.6)$$

Obviously, all three coefficients must be calculated in the same  $A$  matrix, what in consequence means that they will be highly correlated with each other. On the other hand, this high correlation is the reason why all three coefficients have to be estimated in one adjustment and not separately. The partial derivative with respect to  $a$  remains unchanged (see Eq. (4.2)), whereas the derivatives with respect to  $b$  and  $c$  read:

$$\frac{\partial \text{mf}(\varepsilon)}{\partial b} = \frac{a \left( \frac{a}{\frac{b}{c+1} + 1} + 1 \right)}{\left( \sin(\varepsilon) + \frac{a}{\sin(\varepsilon) + \frac{b}{c + \sin(\varepsilon)}} \right)^2 (c + \sin(\varepsilon)) \left( \sin(\varepsilon) + \frac{b}{c + \sin(\varepsilon)} \right)^2} \quad (4.7)$$

$$\frac{a}{\left( \frac{b}{c+1} + 1 \right)^2 \left( \sin(\varepsilon) + \frac{a}{\sin(\varepsilon) + \frac{b}{c + \sin(\varepsilon)}} \right) (c + 1)}$$

and:

$$\frac{\partial \text{mf}(\varepsilon)}{\partial c} = \frac{a b}{\left( \frac{b}{c+1} + 1 \right)^2 \left( \sin(\varepsilon) + \frac{a}{\sin(\varepsilon) + \frac{b}{c + \sin(\varepsilon)}} \right) (c + 1)^2} \quad (4.8)$$

$$\frac{a b \left( \frac{a}{\frac{b}{c+1} + 1} + 1 \right)}{\left( \sin(\varepsilon) + \frac{a}{\sin(\varepsilon) + \frac{b}{c + \sin(\varepsilon)}} \right)^2 (c + \sin(\varepsilon))^2 \left( \sin(\varepsilon) + \frac{b}{c + \sin(\varepsilon)} \right)^2}$$

Again, appropriate initial values are needed.  $a_{h_0}$  and  $a_{w_0}$  are unaltered, while the remaining coefficients are set to:

$$\begin{aligned} b_{h_0} &= 0.0029 \\ b_{w_0} &= 0.00146 \\ c_{h_0} &= 0.065 \\ c_{w_0} &= 0.04391 \end{aligned} \quad (4.9)$$

By iteration and steady rearrangement of Eq. (4.4), the values for the coefficients are fitted to the ray-traced mapping functions. The question of how many iterations are needed in order to reach convergence<sup>5</sup> is not as easy to answer as in the preceding section. Even worse, for some tasks no convergence can be achieved at all. These limitations will be specified case-by-case in the upcoming Sections 4.3 and 4.5.

### 4.3. Determination of a new discrete mapping function (VMF3)

For a number of reasons, the simultaneous estimation of the mapping function coefficients  $a$ ,  $b$  and  $c$  may most likely be not as promising as initially assumed:

- Convergence of the coefficients cannot be guaranteed, as mentioned before and to be discussed in detail in Section 4.5.
- *Böhm* [2004] found that for solutions on a global grid, the interpolation to an arbitrary point, which has to be performed separately for each of the three coefficients  $a$ ,  $b$  and  $c$ , involves the danger of losing the inherent high correlation between them.
- In theory, creating a new concept for indeed empirical but close-to-reality values for the subordinated coefficients  $b$  and  $c$  and hence determining discrete  $a$  coefficients on a sub-daily basis appears to be an approach that approximates the "real" coefficients from a simultaneous estimation very precisely anyway, why provision of VMF<sub>LSM</sub> may be redundant.

For this reason it was decided that the new mapping function shall follow the same scheme as VMF1, that is, subordinated coefficients  $b$  and  $c$  of empirical nature and discrete  $a$  coefficients comprising of the full information of the NWM. For  $b$  and  $c$ , however, a new strategy shall be conceived, not least because of the detected shortcomings. On the following pages, the general concept of VMF3 is introduced.

First, ray-tracing data was produced on a global grid for 120 consecutive epochs from 2001 to 2010, following the properties listed in Tab. 4.2. That is, 32 ray-traced delays had to be calculated per grid point and epoch what amounted in overall 9.953.280 ray-traced delays. Assuming a calculation time of 0.8 milliseconds per ray-traced delay [*Hofmeister*, 2016], a total time of only 2.2 hours can be assumed for the calculation of all necessary delays. However, what is additionally very time-consuming in ray-tracing is the loading time of the NWM, which are provided in so-called .grib-files that are up to several GB large. After averaging the delays for all azimuths to mean values, the approach in Section 4.2 was applied in order to rigorously determine all three coefficients  $a$ ,  $b$  and  $c$  in an iterative least-squares adjustment. This worked out without any problems at an average rate of convergence of six iterations (minimum five, maximum ten). To put it another way, thus VMF<sub>LSM</sub> coefficients  $a$ ,  $b$  and  $c$  were determined discretely for all 2592 grid points at

---

<sup>5</sup>referred to as the "rate of convergence"

Table 4.2.: *Properties of the ray-traced delays that were generated for the derivation of VMF3, in addition to the ray-tracing standard approach (see Tab. A.4 in the appendix on page 139).*

PARAMETER	SPECIFICATION
Ray-tracing software	<i>RADIATE</i> [Hofmeister, 2016]; 2D ray-tracer
NWM	ECMWF ERA Interim Pressure Level Data
Horizontal resolution of the NWM	$1^\circ \times 1^\circ$
Horizontal coverage	global grid with a resolution of $5^\circ \times 5^\circ$ (lat: $[87.5^\circ, -87.5^\circ]$ , lon: $[2.5^\circ, 357.5^\circ]$ ), resulting in 2592 grid points
Temporal resolution	mean values for every month from 2001 through 2010 (= 120 epochs)
Elevations per point	4 ( $3.3^\circ, 5^\circ, 15^\circ$ and $30^\circ$ )
Azimuths per point	8 ( $0^\circ:45^\circ:315^\circ$ )

each of the 120 epochs.

The task now is to deduce empirical information from the discrete coefficients  $b_h$ ,  $b_w$ ,  $c_h$  and  $c_w$ . So as to attain higher precision than VMF1, merely averaging the coefficients to constants would be insufficient. Instead, they get a temporal as well as a spatial dependence. The first is accomplished by means of estimating seasonal fits containing annual and semi-annual terms, whereas the latter is managed through a spherical harmonics expansion up to degree and order 12.

### Temporal Dependence

In Lagler *et al.* [2013] a seasonal fit formula was introduced that appears to be appropriate for modeling for temporal variations of the mapping function coefficients  $b$  and  $c$  such as different amplitudes and phases. Exemplarily for the coefficient  $b_h$ , it reads as follows:

$$\begin{aligned}
 b_h = & A_0 + A_1 \cdot \cos\left(\frac{doy}{365.25} 2\pi\right) + B_1 \cdot \sin\left(\frac{doy}{365.25} 2\pi\right) + \\
 & A_2 \cdot \cos\left(\frac{doy}{365.25} 4\pi\right) + B_2 \cdot \sin\left(\frac{doy}{365.25} 4\pi\right)
 \end{aligned}
 \tag{4.10}$$

$A_0$  represents the mean value of the respective coefficient,  $A_1$  and  $B_1$  are the annual amplitudes of the seasonal fit,  $A_2$  and  $B_2$  the semi-annual amplitudes and *doy* is the day of year. To fit these parameters (except for *doy*) to the  $VMF_{LSM}$  data, once more a least-squares adjustment is carried out, or rather 10000 least-squares adjustments, since it needs to be done each for four coefficients  $b_h$ ,  $b_w$ ,  $c_h$  and  $c_w$  and the 2592 grid points individually. The observation vector  $l$  simply consists of the respective  $VMF_{LSM}$  coefficients at all 120

epochs for each grid point, outlined in the below Eq. (4.11) again for  $b_h$ :

$$l = \begin{bmatrix} b_{h_1} \\ b_{h_2} \\ \vdots \\ b_{h_{120}} \end{bmatrix} \quad (4.11)$$

The design matrix  $A$  contains the partial derivatives of Eq. (4.10):

$$A = \begin{bmatrix} \frac{\partial b_h(t_1)}{\partial A_0} & \frac{\partial b_h(t_1)}{\partial A_1} & \frac{\partial b_h(t_1)}{\partial B_1} & \frac{\partial b_h(t_1)}{\partial A_2} & \frac{\partial b_h(t_1)}{\partial B_2} \\ \frac{\partial b_h(t_2)}{\partial A_0} & \frac{\partial b_h(t_2)}{\partial A_1} & \frac{\partial b_h(t_2)}{\partial B_1} & \frac{\partial b_h(t_2)}{\partial A_2} & \frac{\partial b_h(t_2)}{\partial B_2} \\ \vdots & \vdots & \vdots & \vdots & \vdots \\ \frac{\partial b_h(t_n)}{\partial A_0} & \frac{\partial b_h(t_n)}{\partial A_1} & \frac{\partial b_h(t_n)}{\partial B_1} & \frac{\partial b_h(t_n)}{\partial A_2} & \frac{\partial b_h(t_n)}{\partial B_2} \end{bmatrix} \quad (4.12)$$

Unlike the determination of  $\text{VMF}_{\text{LSM}}$ , Eq. (4.12) is a system of linear equations, as pointed out in the subsequent Eqs. (4.13) to (4.17):

$$\frac{\partial b_h(t_1)}{\partial A_0} = 1 \quad (4.13)$$

$$\frac{\partial b_h(t_1)}{\partial A_1} = \cos\left(\frac{\text{doy}}{365.25}2\pi\right) \quad (4.14)$$

$$\frac{\partial b_h(t_1)}{\partial B_1} = \sin\left(\frac{\text{doy}}{365.25}2\pi\right) \quad (4.15)$$

$$\frac{\partial b_h(t_1)}{\partial A_2} = \cos\left(\frac{\text{doy}}{365.25}4\pi\right) \quad (4.16)$$

$$\frac{\partial b_h(t_1)}{\partial B_2} = \sin\left(\frac{\text{doy}}{365.25}4\pi\right) \quad (4.17)$$

The unknown parameters, that is, empirical coefficients  $b_h$ ,  $b_w$ ,  $c_h$  and  $c_w$  for each of the 2592 grid points, are then determined by:

$$\begin{bmatrix} A_0 \\ A_1 \\ B_1 \\ A_2 \\ B_2 \end{bmatrix} = (A^T A)^{-1} A^T l \quad (4.18)$$

In Fig. 4.2, resulting parameters are shown for the empirical coefficient  $b_h$  on the whole grid, whereas Fig. 4.3 outlines an extract of how well fitting Eq. (4.10) to the discrete values of  $b_h$  works out. Fig. 4.4 contains the respective standard deviations of the grid parameters, which, when regarding the scale of the color bar, are distinctively lower than the parameter values themselves.

It was also tried to apply a 2D median filter in *MATLAB* to the data, which is supposed to smooth the overall grid. The idea behind a 2D median filter is that each output

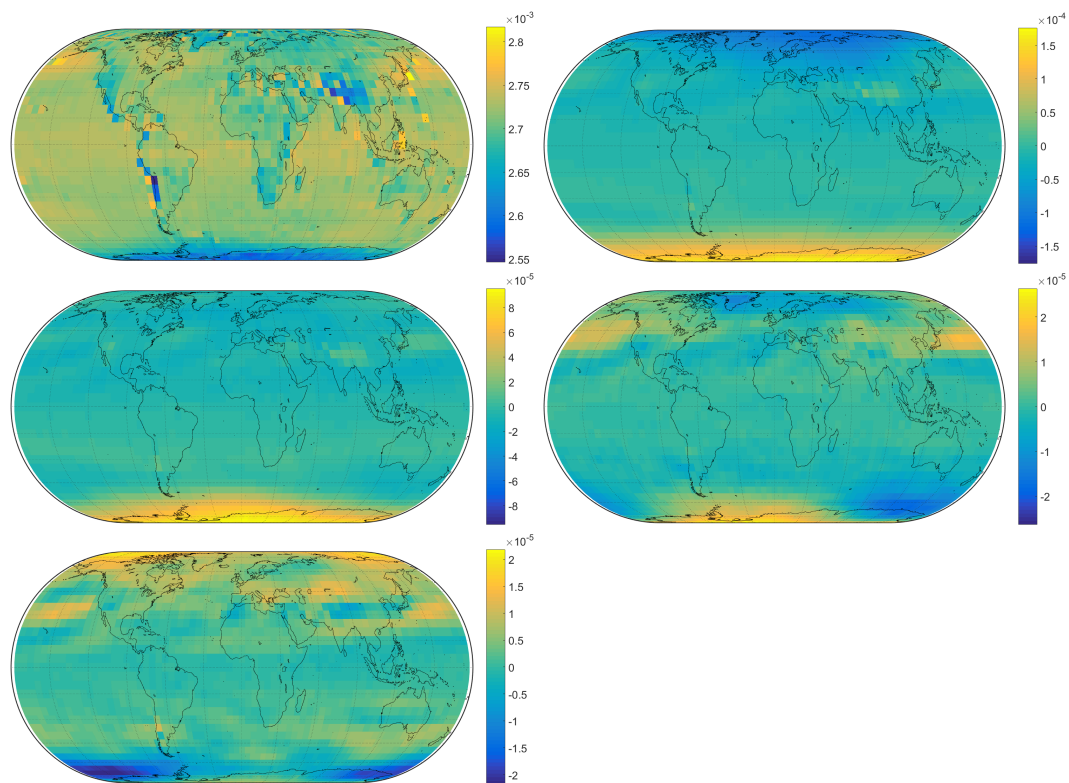


Figure 4.2.: *Parameters of the seasonal fit for the mapping function coefficient  $b_h$ . Top left: mean values  $A_0$ , top right: annual amplitude  $A_1$ , center left: annual amplitude  $B_1$ , center right: semi-annual amplitude  $A_2$ , bottom left: semi-annual amplitude  $B_2$ .*

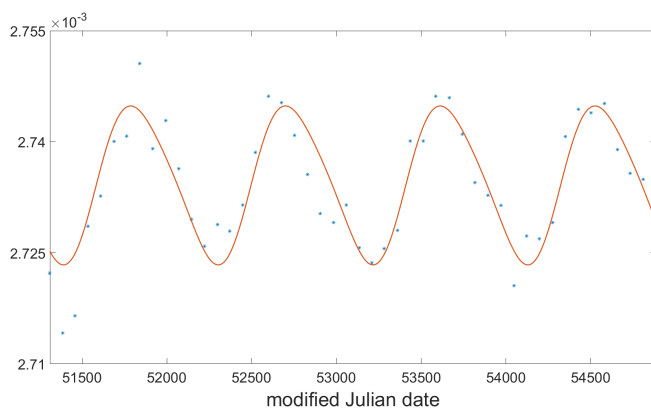


Figure 4.3.: *Data fitting of  $b_h$  exemplarily for the grid point  $\varphi = 7.5^\circ$  and  $\lambda = 237.5^\circ$  from 2001 to 2004.*

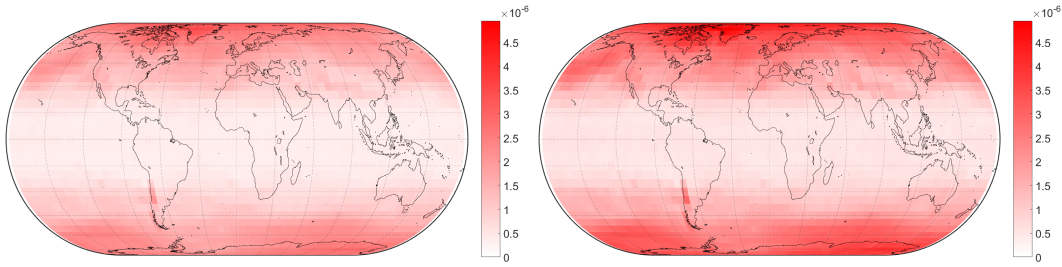


Figure 4.4.: Standard deviations of the parameters of the seasonal fit for the mapping function coefficient  $b_h$ . Left: standard deviation of mean values  $A_0$ , right: standard deviation of the amplitudes  $A_1$ ,  $B_1$ ,  $A_2$  and  $B_2$ , all of which are equivalent. It is obvious that the amplitudes generally have a higher standard deviation than the mean values. At a rough estimate, given the uncertainty of  $2 \cdot 10^{-6}$  in  $A_0$  and of  $5 \cdot 10^{-6}$  in all amplitudes of  $b_h$  (as is the case at the poles), the resulting slant hydrostatic delay at  $5^\circ$  elevation would change at worst by 3 mm.

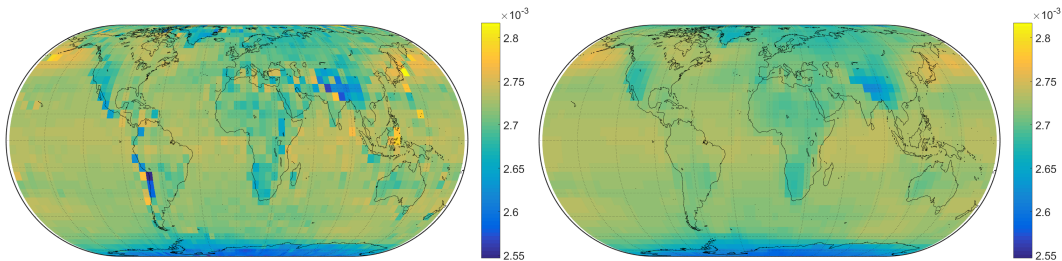


Figure 4.5.: The effect of filtering using the example of the parameter  $A_0$  of  $b_h$ ; left: the original grid (corresponds to the top left plot in Fig. 4.2), right: the grid after applying a 2D median filter.

value contains the median value in a 3-by-3 neighborhood around the corresponding value [[de.mathworks.com/help/images/ref/medfilt2.html](http://de.mathworks.com/help/images/ref/medfilt2.html), date of access: 2016/10]. Thus, in particular the effect of outliers or extreme values can be significantly reduced by splitting its amplitude to the neighboring values. Figure 4.5 illustrates the effect of this median filter on the grid using the example of the mean value  $A_0$  of the mapping function coefficient  $b_h$ . The 2D median filter was analogously tested for the annual and semi-annual amplitudes  $A_1$ ,  $B_1$ ,  $A_2$  and  $B_2$  as well. However, in the actual comparison it turned out that the filtering has a slightly adverse effect on the results, for which reason it was finally not applied to the data.

## Spatial Dependence

The empirical coefficients  $b_h$ ,  $b_w$ ,  $c_h$  and  $c_w$  now have a temporal dependence through the seasonal fit, as described above, for each of the 2592 grid points. The five defining parameters of each coefficient could be provided in a text file, analogous to the parameters in GPT2 and GPT2w. Thus, a user would be able to read empirical coefficients which fit

to the location and time of the observation as well as possible. However, the provision on a grid would not be entirely satisfying as its loading requires a considerable amount of time. For a long series of observations this might lead to substantial issues in computational time. On this account, an alternative way for facilitating a spatial dependence had to be found.

Spherical harmonics are used for representations of the geoid, the gravitational field or the magnetic field of the earth, where discrete values are conveniently represented by functions on the surface of a sphere. They are also applied for mapping the ionosphere or describing phase center variations in GPS [Böhm and Schuh, 2001]. The exactness of the representation in each case depends on the degree of expansion. For degree  $n$  and order  $m$ , the spherical harmonics at a given polar distance  $\vartheta$  and longitude  $\lambda$ <sup>6</sup> are written as [Heiskanen and Moritz, 1967]:

$$Y_{nm} = \sum_{n=0}^{\infty} \sum_{m=0}^n \underbrace{P_{nm}(\cos(\vartheta)) \cdot \cos(m\lambda)}_{=C_{nm}} \cdot a_{nm} + \underbrace{P_{nm}(\cos(\vartheta)) \cdot \sin(m\lambda)}_{=S_{nm}} \cdot b_{nm} \quad (4.19)$$

where  $P_{nm}$  are referred to as associated Legendre functions of degree  $n$  and order  $m$  while  $a_{nm}$  and  $b_{nm}$  are the coefficients of the spherical harmonics expansion, that is, the target variables that are to be determined. The formulation of the associated Legendre functions is preceded by the Legendre polynomials, which hold for  $m = 0$  and hence are referred to as zonal harmonics, as the longitude-dependent terms in Eq. (4.19) thus vanish. They can be determined by means of the so-called Rodrigues' formula:

$$P_n(\cos(\vartheta)) = \frac{1}{2^n \cdot n!} \frac{\partial^n}{\partial \cos(\vartheta)^n} (\cos(\vartheta)^2 - 1)^n \quad (4.20)$$

Appending the order  $m$ , Eq. (4.20) can be extended to:

$$P_{nm}(\cos(\vartheta)) = (1 - \cos(\vartheta)^2)^{m/2} \frac{\partial^m}{\partial \cos(\vartheta)^m} P_n(\cos(\vartheta)) \quad (4.21)$$

Setting the degree of expansion to  $n = m = 12$ , all 91 Legendre functions  $P_{nm}$  must be determined using Eq. (4.21) and then be multiplied with the terms  $\cos(m\lambda)$  and  $\sin(m\lambda)$  in order to obtain the functions  $C_{nm}$  and  $S_{nm}$ . Differentiating Eq. (4.19) for every grid point (36 polar distances and 72 longitudes) with respect to the unknown spherical harmonics

---

<sup>6</sup>the third spherical coordinate besides polar distance and longitude, Earth radius  $R_e$ , is 1

coefficients  $a_{nm}$  and  $b_{nm}$  yields the extensive design matrix:

$$A = \begin{bmatrix} \frac{\partial Y_{0,0}(\vartheta_1, \lambda_1)}{\partial a_{0,0}} & \frac{\partial Y_{1,0}(\vartheta_1, \lambda_1)}{\partial a_{1,0}} & \frac{\partial Y_{1,1}(\vartheta_1, \lambda_1)}{\partial a_{1,1}} & \frac{\partial Y_{2,1}(\vartheta_1, \lambda_1)}{\partial a_{2,1}} & \dots & \frac{\partial Y_{12,12}(\vartheta_1, \lambda_1)}{\partial a_{12,12}} \\ \frac{\partial Y_{0,0}(\vartheta_1, \lambda_2)}{\partial a_{0,0}} & \frac{\partial Y_{1,0}(\vartheta_1, \lambda_2)}{\partial a_{1,0}} & \frac{\partial Y_{1,1}(\vartheta_1, \lambda_2)}{\partial a_{1,1}} & \frac{\partial Y_{2,1}(\vartheta_1, \lambda_2)}{\partial a_{2,1}} & \dots & \frac{\partial Y_{12,12}(\vartheta_1, \lambda_2)}{\partial a_{12,12}} \\ \vdots & \vdots & \vdots & \vdots & \ddots & \vdots \\ \frac{\partial Y_{0,0}(\vartheta_2, \lambda_1)}{\partial a_{0,0}} & \frac{\partial Y_{1,0}(\vartheta_2, \lambda_1)}{\partial a_{1,0}} & \frac{\partial Y_{1,1}(\vartheta_2, \lambda_1)}{\partial a_{1,1}} & \frac{\partial Y_{2,1}(\vartheta_2, \lambda_1)}{\partial a_{2,1}} & \dots & \frac{\partial Y_{12,12}(\vartheta_2, \lambda_1)}{\partial a_{12,12}} \\ \frac{\partial Y_{0,0}(\vartheta_2, \lambda_2)}{\partial a_{0,0}} & \frac{\partial Y_{1,0}(\vartheta_2, \lambda_2)}{\partial a_{1,0}} & \frac{\partial Y_{1,1}(\vartheta_2, \lambda_2)}{\partial a_{1,1}} & \frac{\partial Y_{2,1}(\vartheta_2, \lambda_2)}{\partial a_{2,1}} & \dots & \frac{\partial Y_{12,12}(\vartheta_2, \lambda_2)}{\partial a_{12,12}} \\ \vdots & \vdots & \vdots & \vdots & \ddots & \vdots \\ \frac{\partial Y_{0,0}(\vartheta_{36}, \lambda_{72})}{\partial a_{0,0}} & \frac{\partial Y_{1,0}(\vartheta_{36}, \lambda_{72})}{\partial a_{1,0}} & \frac{\partial Y_{1,1}(\vartheta_{36}, \lambda_{72})}{\partial a_{1,1}} & \frac{\partial Y_{2,1}(\vartheta_{36}, \lambda_{72})}{\partial a_{2,1}} & \dots & \frac{\partial Y_{12,12}(\vartheta_{36}, \lambda_{72})}{\partial a_{12,12}} \end{bmatrix}$$

$$\begin{bmatrix} \frac{\partial Y_{0,0}(\vartheta_1, \lambda_1)}{\partial b_{0,0}} & \frac{\partial Y_{1,0}(\vartheta_1, \lambda_1)}{\partial b_{1,0}} & \frac{\partial Y_{1,1}(\vartheta_1, \lambda_1)}{\partial b_{1,1}} & \frac{\partial Y_{2,1}(\vartheta_1, \lambda_1)}{\partial b_{2,1}} & \dots & \frac{\partial Y_{12,12}(\vartheta_1, \lambda_1)}{\partial b_{12,12}} \\ \frac{\partial Y_{0,0}(\vartheta_1, \lambda_2)}{\partial b_{0,0}} & \frac{\partial Y_{1,0}(\vartheta_1, \lambda_2)}{\partial b_{1,0}} & \frac{\partial Y_{1,1}(\vartheta_1, \lambda_2)}{\partial b_{1,1}} & \frac{\partial Y_{2,1}(\vartheta_1, \lambda_2)}{\partial b_{2,1}} & \dots & \frac{\partial Y_{12,12}(\vartheta_1, \lambda_2)}{\partial b_{12,12}} \\ \vdots & \vdots & \vdots & \vdots & \ddots & \vdots \\ \frac{\partial Y_{0,0}(\vartheta_2, \lambda_1)}{\partial b_{0,0}} & \frac{\partial Y_{1,0}(\vartheta_2, \lambda_1)}{\partial b_{1,0}} & \frac{\partial Y_{1,1}(\vartheta_2, \lambda_1)}{\partial b_{1,1}} & \frac{\partial Y_{2,1}(\vartheta_2, \lambda_1)}{\partial b_{2,1}} & \dots & \frac{\partial Y_{12,12}(\vartheta_2, \lambda_1)}{\partial b_{12,12}} \\ \frac{\partial Y_{0,0}(\vartheta_2, \lambda_2)}{\partial b_{0,0}} & \frac{\partial Y_{1,0}(\vartheta_2, \lambda_2)}{\partial b_{1,0}} & \frac{\partial Y_{1,1}(\vartheta_2, \lambda_2)}{\partial b_{1,1}} & \frac{\partial Y_{2,1}(\vartheta_2, \lambda_2)}{\partial b_{2,1}} & \dots & \frac{\partial Y_{12,12}(\vartheta_2, \lambda_2)}{\partial b_{12,12}} \\ \vdots & \vdots & \vdots & \vdots & \ddots & \vdots \\ \frac{\partial Y_{0,0}(\vartheta_{36}, \lambda_{72})}{\partial b_{0,0}} & \frac{\partial Y_{1,0}(\vartheta_{36}, \lambda_{72})}{\partial b_{1,0}} & \frac{\partial Y_{1,1}(\vartheta_{36}, \lambda_{72})}{\partial b_{1,1}} & \frac{\partial Y_{2,1}(\vartheta_{36}, \lambda_{72})}{\partial b_{2,1}} & \dots & \frac{\partial Y_{12,12}(\vartheta_{36}, \lambda_{72})}{\partial b_{12,12}} \end{bmatrix} \quad (4.22)$$

Performing the differentiation exemplarily for the first term of Eq. (4.22) proves that the equation system is linear:

$$\frac{\partial Y_{0,0}(\vartheta_1, \lambda_1)}{\partial a_{0,0}} = C_{0,0}(\vartheta_1, \lambda_1) = P_{0,0}(\cos(\vartheta_1)) = 1 \quad (4.23)$$

The observation vectors  $l$  consist of mean values  $A_0$  and amplitudes  $A_1$ ,  $B_1$ ,  $A_2$  and  $B_2$  of each of the empirical mapping function coefficients  $b_h$ ,  $b_w$ ,  $c_h$  and  $c_w$ , e.g.:

$$l_{b_{h_{A_0}}} = \begin{bmatrix} b_{h_{A_0}}(\vartheta_1, \lambda_1) \\ b_{h_{A_0}}(\vartheta_1, \lambda_2) \\ \vdots \\ b_{h_{A_0}}(\vartheta_2, \lambda_1) \\ b_{h_{A_0}}(\vartheta_2, \lambda_2) \\ \vdots \\ b_{h_{A_0}}(\vartheta_{36}, \lambda_{72}) \end{bmatrix} \quad (4.24)$$

The solutions of the least-squares adjustments are spherical harmonics coefficients  $a_{nm}$  and  $b_{nm}$  which allow analytical representations of each of the parameters of the mapping function coefficients from the global grid. As already mentioned before, the spherical



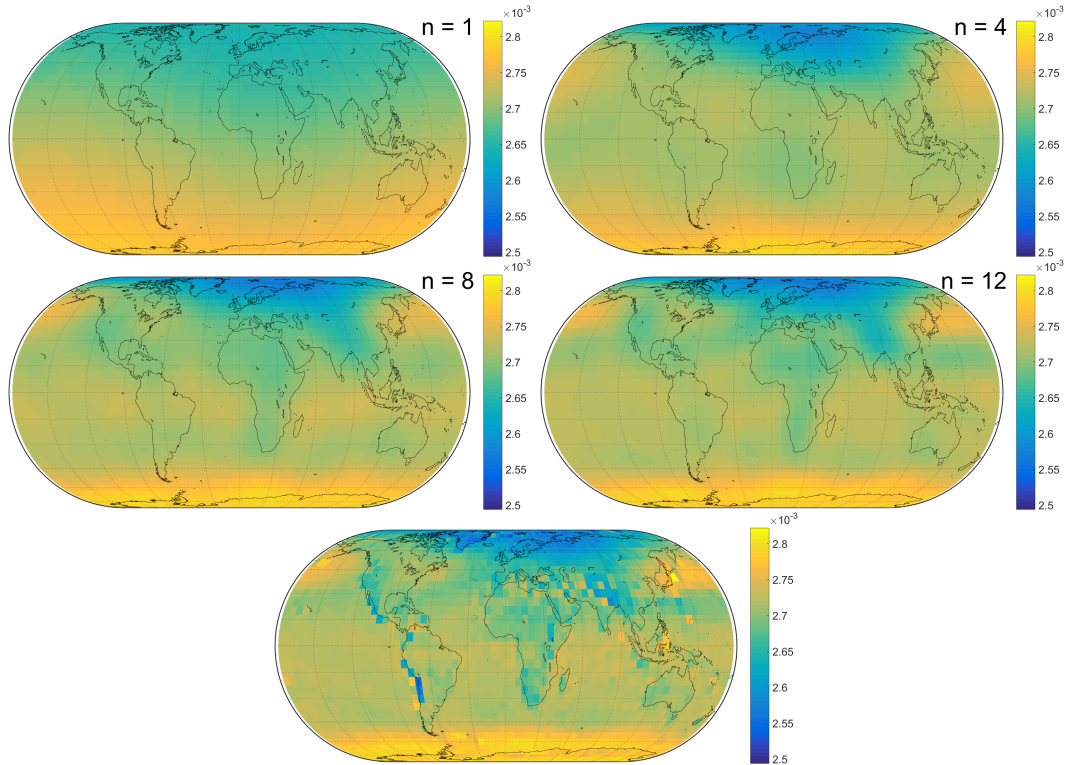


Figure 4.6.: *Spherical harmonics of the coefficient  $b_h$  for increasing degrees  $n$  of expansion at the arbitrary epoch January 15, 2001 (MJD: 51924). Top left: degree  $n = 1$ , top right: degree  $n = 4$ , center left: degree  $n = 8$ , center right: final degree  $n_{max} = 12$ . Bottom: the original grid which is to be represented by the spherical harmonics.*

harmonics are expanded to degree and order 12. Higher degrees unfortunately led to underestimations instead of further improvements. Figure 4.6 depicts how well the increasing degree  $n$  is able to represent the grid. This nicely points out the principle of spherical harmonics: the higher the degree of expansion, the finer the grid can be resolved as more and more tesseral functions<sup>7</sup> are considered. The single values in the bottom map that jump out of their regional trends, however, can obviously not be resolved. Nevertheless, despite the comparatively low degree of expansion the representation of the global grid through spherical harmonics hardly involves any loss in accuracy, as will be shown in the upcoming Section 4.5.

On the basis of these empirical coefficients  $b_h$ ,  $b_w$ ,  $c_h$  and  $c_w$  possessing a temporal as well as a spatial dependence, the discrete coefficients  $a_h$  and  $a_w$  can be calculated from the information of the ray-traced delays. To this end, the two formula systems in Sections 4.1.1 and 4.1.2 are applied, yielding coefficients which are henceforth referred to as VMF3 and VMF3<sub>LSM</sub>, respectively. This implies that ray-tracing is performed for a set of azimuths and elevations which vary for the different tasks. Again, the question is whether

<sup>7</sup>in mathematics, tesseral functions have a chessboard-like shape on a spherical surface [de.wikipedia.org/wiki/Tesseral, date of access: 2016/11]

VMF3, which overall requires less computational time, can keep up with VMF3<sub>LSM</sub>. The performance of VMF3 and VMF3<sub>LSM</sub> will be explained in Section 4.5.

#### 4.4. Determination of a new empirical mapping function (GPT3)

In the previous section, new empirical values were determined for the mapping function coefficients  $b$  and  $c$  involving a seasonal fit for the long-term temporal variation on the one hand and a spherical harmonics expansion for the spatial variation on the other hand. On the basis of these empirical coefficients and actual tropospheric delays from ray-tracing through NWM, discrete values for the remaining  $a$  coefficients were calculated. These  $a$  coefficients thus carry the bulk of information about the state of the troposphere.

But if one requires a fully empirical mapping function for reasons such as lacking internet connection or simply because real-time data is not available for the desired site, empirical values for the  $a$  coefficients have to be obtainable as well. Its expression through empirical methods can easily be done by ascertaining temporal and spatial dependencies as done for  $b_h$ ,  $b_w$ ,  $c_h$  and  $c_w$  (cf. Section 4.3) also for  $a_h$  and  $a_w$ . In the following, the exact procedure of their calculation is described. It is only one of several tested strategies, which turned out to be the most sensible one.

The  $b$  and  $c$  coefficients are adopted from VMF3, that is, represented in spherical harmonics up to degree and order 12. On their basis new values for  $a$  are determined on a regular  $5^\circ \times 5^\circ$  grid, yielding coefficients at 2592 grid points and 120 epochs. What is important here is that the empirical  $a_h$  have to be valid at sea level, while the underlying ray-traced delays were determined for the respective height of the grid point above sea level<sup>8</sup>; that is, a height correction has to be applied first. For the wet part this is no big deal as the height dependency of wet mapping functions is believed to be too small for having a noticeable impact on the resulting delays, but for the hydrostatic part the situation is different. There is no way yet to directly reduce  $a_h$  between two heights but only the whole mapping function  $mf_h$ . Niell [1996] devised an equation based on the continued fraction form by Marini [1972] (Eq. (2.5) on page 7) which accounts for the decrease of  $mf_h$  with decreasing height:

$$mf_{h_0} = mf_{h_1} - \frac{h_{ell}}{1000} \cdot \left( \frac{1}{\sin(\varepsilon)} - \frac{1 + \frac{a_{ht}}{1 + \frac{b_{ht}}{1 + c_{ht}}}}{\sin(\varepsilon) + \frac{a_{ht}}{\sin(\varepsilon) + \frac{b_{ht}}{\sin(\varepsilon) + c_{ht}}}} \right) \quad (4.25)$$

where  $mf_{h_0}$  is the hydrostatic mapping function at reduced height 0 (usually sea level),  $mf_{h_1}$  is the hydrostatic mapping function at height 1 (usually at the topography),  $h_{ell}$  is the ellipsoidal height in meters,  $a_{ht} = 2.53 \cdot 10^{-5}$ ,  $b_{ht} = 5.49 \cdot 10^{-3}$  and  $c_{ht} = 1.14 \cdot 10^{-3}$ . The reduced  $a_h$  are thus determined in a least-squares adjustment with  $mf_h$  (reduced to sea level) and  $b_h$  and  $c_h$  from VMF3 (valid at the Earth's surface) as input. They are then

<sup>8</sup>here is always talk of the ellipsoidal height  $h_{ell}$

valid at a fictional height slightly below sea level because they compensate the effect of  $b_h$  and  $c_h$  being valid at the Earth's surface and not at sea level. Blind, empirical values for  $a_h$  are eventually gathered by passing the just determined  $a_h$  through the seasonal fit adjustment as described in the paragraph "Temporal Dependence" of the preceding Section 4.3 for  $b$  and  $c$ .

In Chapter 5.2 a global grid containing empirical horizontal gradients will be issued. The grid is based on the same ray-tracing data in the same grid size as the empirical mapping function coefficients  $a_h$  and  $a_w$  so to be able to combine them with each other. The result is a new  $5^\circ \times 5^\circ$  empirical troposphere grid with the consecutive name GPT3 (Global Pressure and Temperature 3). Overall, GPT3 holds the following parameters:

- $p$ ..... pressure (hPa)
- $T$ ..... temperature ( $^\circ\text{C}$ )
- $dT$ ..... temperature lapse rate ( $\frac{^\circ\text{C}}{\text{km}}$ )
- $T_m$ ..... mean temperature weighted with water vapor pressure (K)
- $e$ ..... water vapor pressure (hPa)
- $a_h$ ..... hydrostatic mapping function coefficient (valid at sea level)
- $a_w$ ..... wet mapping function coefficient
- $\lambda$ ..... water vapor decrease factor
- $N$ ..... geoid undulation (m)
- $G_{n_h}$ ..... hydrostatic north gradient (m)
- $G_{e_h}$ ..... hydrostatic east gradient (m)
- $G_{n_w}$ ..... wet north gradient (m)
- $G_{e_w}$ ..... wet east gradient (m)

$a_h$ ,  $a_w$ ,  $G_{n_h}$ ,  $G_{n_w}$ ,  $G_{e_h}$  and  $G_{e_w}$  are new, the remaining meteorological parameters are adopted from GPT2w as they stand. For the determination of the empirical gradient variables  $G_{n_h}$ ,  $G_{n_w}$ ,  $G_{e_h}$  and  $G_{e_w}$  it is referenced to Chapter 5.2. The meteorological parameters are left unchanged for a good reason as their quality is already close to the top of technical means. The  $a$  coefficients are supposed to be of slightly higher accuracy than those of GPT2w owing to its more sophisticated underlying ray-tracing algorithms. The empirical gradient grid further extends the range of parameters of existing GPT troposphere models, replacing the existing empirical gradient models APG and DAO which are both standalone functions. More to the empirical gradients, as mentioned before, is covered in Chapter 5.2. Figures 4.7 and 4.8 display world maps of the resulting  $a_h$  and  $a_w$  plus their amplitudes and standard deviations.

Highest values of  $a_h$  are found in low latitudes, whereas lowest values occur at the poles.

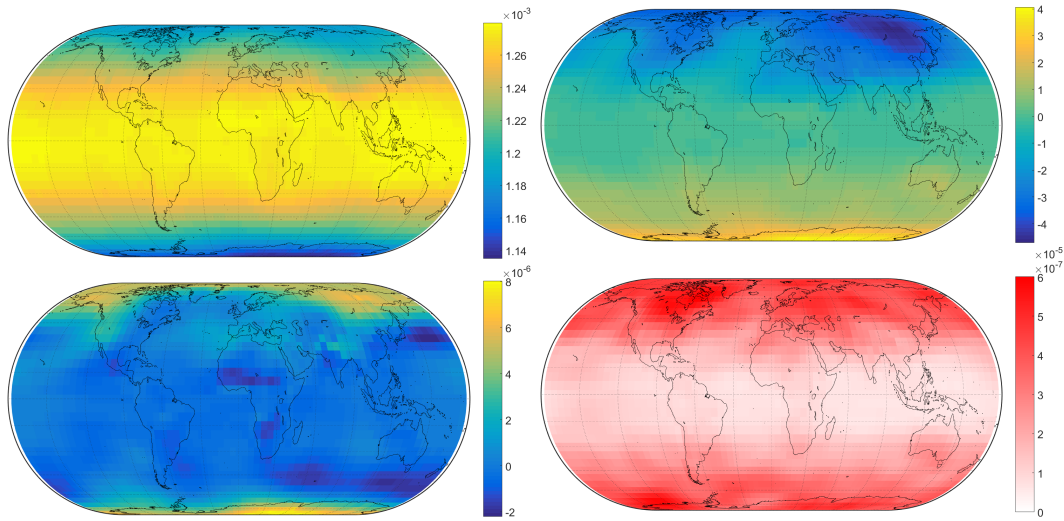


Figure 4.7.: Mean values  $A_0$  (top left), seasonal amplitudes  $A_1$  (top right), half-seasonal amplitudes  $A_2$  (bottom left) and standard deviation of the residuals of  $A_0$  (bottom right) of the hydrostatic mapping function coefficient  $a_h$  from GPT3. At a rough estimate, given the uncertainty of  $6 \cdot 10^{-7}$  in  $A_0$  and of  $8 \cdot 10^{-7}$  in all amplitudes of  $a_h$  (as is the case at the poles), the resulting slant hydrostatic delay at  $5^\circ$  elevation would change at worst by 4 mm.

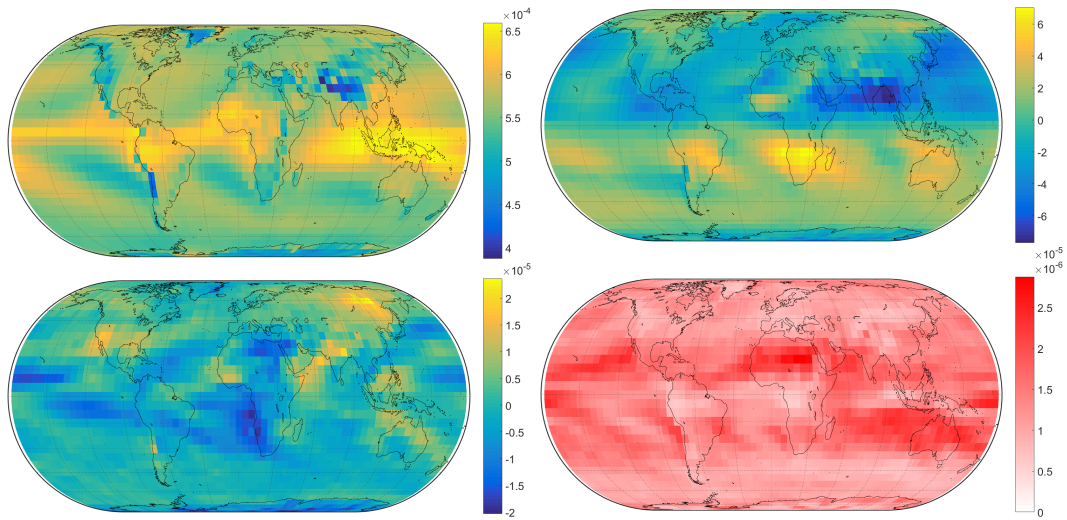


Figure 4.8.: Mean values  $A_0$  (top left), seasonal amplitudes  $A_1$  (top right), half-seasonal amplitudes  $A_2$  (bottom left) and standard deviation of the residuals of  $A_0$  (bottom right) of the wet mapping function coefficient  $a_w$  from GPT3. At a rough estimate, given the uncertainty of  $3 \cdot 10^{-6}$  in  $A_0$  and of  $4 \cdot 10^{-6}$  in all amplitudes of  $a_h$  (as is the case over North Africa), the resulting slant wet delay at  $5^\circ$  elevation would change at worst by 0.3 mm.

This behaviour is very symmetric in the northern as well as the southern hemisphere. Interestingly, the highest standard deviations more or less correlate with the lowest values of  $a_h$ . The seasonal amplitudes  $A_1$  do not follow this symmetry due to the opposite warm and cold season of year. In case of the wet mapping function coefficient  $a_w$  the situation is not that systematic, although the seasonal amplitude  $A_1$  reveals the summer/winter behaviour again. Values of  $a_w$  peak around the equator but generally behave very randomly. What is striking in the plots of the mean values of  $a$  is that the hydrostatic part is absolutely smooth over the globe, while the wet part exhibits erratic variations over prominent mountain ranges such as the Himalayas, the Andes or the Rockies. Recalling the fact that  $a_w$  is valid for the respective height of the topography but is assumed to not requiring a height correction, the question arises whether the latter assumption is really true. It seems as if the wet part is very well dependent on height, in fact the values become lower with increasing altitude. There is possibly the necessity of a new height correction including also the wet part. This new height correction then should not hold for the mapping functions  $mf_h$  and  $mf_w$ , but only for the coefficients  $a_h$  and  $a_w$  so as to be easier to apply. It is planned within our research group to determine such a new height correction, however not early enough to be included in this thesis. For this reason, the model GPT3 as is presented in this thesis is only a temporary realization; its final version will be published in a separate publication anytime soon.

Besides, GPT3 consists also of an exact conversion of MJD to doy, while in GPT2w the MJD is referenced to January 1, 2000 (MJD: 51544) and the average number of days per year is set to be 365.25. Although thus the results do not perceptibly change, this approach appears to be more consistent. The introduction of diurnal and semi-diurnal amplitudes, as planned in *Böhm et al.* [2015] for a future successor of GPT2w, however, is not realized in GPT3. Apart from that, since GPT3 uses the same seasonal fit (Eq. (4.10)) as GPT2 and GPT2w there is no chance to consider long-term trends (climatological effects, e.g. increase of temperature over the years) because there is no slope term in this equation.

Eventually, the potential ability of GPT3 to exceed the performance of existing empirical models is to be assessed in the course of the subsequent Section 4.5.

## 4.5. Comparisons and results

In this section several comparisons are made in order to estimate the performance of the various VMF and GPT approaches, in particular that of VMF3. The overall question is whether or not the current benchmark in troposphere modeling, Vienna Mapping Functions 1 (VMF1), can be outperformed by any of the new approaches. In terms of empirical troposphere modeling it is attempted to top GPT2w. Results of all comparisons are summarized and discussed in the subsequent Section 4.6.

Table 4.3.: *Properties of the ray-traced delays that were generated using the ray-tracer RADIATE for the time period of CONT11, in addition to the ray-tracing standard approach (see Tab. A.4 on page 139).*

PARAMETER	SPECIFICATION
Ray-tracing software	<i>RADIATE</i> [Hofmeister, 2016]; 2D ray-tracer
NWM	ECMWF operational data
Horizontal resolution of the NWM	(1) $0.125^\circ \times 0.125^\circ$ , (2) $1^\circ \times 1^\circ$
Horizontal coverage	14 CONT11 stations (cf. appendix A on page 134)
Temporal resolution	6-hourly at 00:00, 06:00, 12:00 and 18:00 UTC each day of the two weeks of CONT11 (= 64 epochs)
Elevations per point	7 ( $3^\circ$ , $5^\circ$ , $7^\circ$ , $10^\circ$ , $15^\circ$ , $30^\circ$ and $70^\circ$ ) <sup>9</sup>
Azimuths per point	16 ( $0^\circ$ : $22.5^\circ$ : $337.5^\circ$ )

#### 4.5.1. Comparison of BLR

##### Comparisons for the time period of CONT11

In *Landskron et al.* [2015c], new  $a$  coefficients are determined by means of least-squares adjustments for ray-traced delays at different elevation angles, an approach which in this thesis is referred to as  $\text{VMF1}_{\text{reproLSM}}$  (cf. Section 4.1.2). For this purpose, ray-tracing was performed using the ray-tracer *RADIATE* [Hofmeister, 2016] for the standard ray-tracing approach (see Tab. A.4 in the appendix on page 139) and the properties in Tab. 4.3.

$\text{VMF1}_{\text{reproLSM}}$  is determined twice, once for the (best possible) NWM resolution of  $0.125^\circ \times 0.125^\circ$  and once for the NWM resolution of  $1^\circ \times 1^\circ$ , in order that the NWM resolution's influence can be clearly assessed as well. This adds up to 112 ray-traced delays per approach (2), per station (14) and per epoch (64) and results in 200.704 delays overall. Determination of baseline length repeatabilities (BLR) in *VieVS* using the standard approach (see Tab. A.3 in the appendix on page 138) for VMF1 and the two  $\text{VMF1}_{\text{reproLSM}}$  approaches generally show no difference (Tab. 4.4). It can be concluded that there is no difference in the mapping functions when using the  $1^\circ \times 1^\circ$  instead of the  $0.125^\circ \times 0.125^\circ$  NWM resolution. When comparing each baseline separately, the differences between them are only in the range of 0.2 mm at maximum. In *Hofmeister* [2016], a similar comparison was made with ray-traced delays through NWM with  $0.125^\circ \times 0.125^\circ$  on the one hand and  $1^\circ \times 1^\circ$  on the other hand as input to the VLBI analysis. When estimating zenith wet delays as well as horizontal gradients in VLBI analysis, the differences in BLR are also very low, but with 2 mm on average significantly higher as in this comparison. Besides, there seems to be no reason for using reprocessed coefficients instead of VMF1 at all.

<sup>9</sup>elevations lower than  $3^\circ$  are thought not to be modeled correctly by mapping functions using the continued fraction form by *Marini* [1972] and *Herring* [1992] [*Niell*, 1996], therefore they are omitted

Table 4.4.: Mean BLR (cm) from VLBI analyses for different NWM resolutions for CONT11.

TROPOSPHERE MODEL	BLR (cm)
VMF1	1.01
VMF1 <sub>reproLSM</sub> (0.125°×0.125°)	1.01
VMF1 <sub>reproLSM</sub> (1°×1°)	1.01

Table 4.5.: Mean BLR (cm) from VLBI analyses considering several kinds of mapping functions for the time period of CONT11. In column (1), zenith wet delays  $\Delta L_w^z$  are NOT estimated in VLBI analysis, while in column (2)  $\Delta L_w^z$  are estimated in VLBI analysis.

TROPOSPHERE MODEL	(1) (cm)	(2) (cm)
(a) VMF1	2.76	1.01
(b) VMF1 <sub>repro</sub> ( $\Delta L_w^z$ from RADIATE)	1.97	1.01
(c) VMF3 <sub>LSM</sub>	2.76	1.01
(d) VMF3 <sub>LSM</sub> ( $\Delta L_w^z$ from RADIATE)	1.97	1.01
(f) GPT2w	2.77	1.02
(g) GPT3	2.78	1.02

Apart from the BLR comparison, there were also differences between ray-traced delays and VMF1 and VMF1<sub>reproLSM</sub> (0.125°×0.125°) calculated, in order to test whether the new  $a$  coefficients are able to better approximate the ray-traced delays, which are regarded as the "true" delays<sup>10</sup>. This comparison showed that, averaged over all stations and epochs of CONT11, VMF1<sub>reproLSM</sub> brings the modeled delays closer to the ray-traced delays by 8% (52.2 mm < 56.4 mm) at 5° elevation. Unlike the BLR comparison in Tab. 4.4 this is a clear indicator that VMF1<sub>reproLSM</sub> performs better than VMF1, although the improvements are very small.

In Tab. 4.5 mean BLR for different kinds of discrete as well as empirical mapping functions are outlined for two cases: (1) NO estimation of zenith wet delays  $\Delta L_w^z$  in VLBI analysis (2) estimation of  $\Delta L_w^z$  in VLBI analysis. Except for lines (b) and (d), a priori zenith wet delays are taken from the VMF1-files.

From these tables it can be concluded that when estimating zenith wet delays  $\Delta L_w^z$  in VLBI analysis it does not matter at all which mapping function is used. Even empirical

<sup>10</sup>in this section there is again frequently talk of certain values of quantities which are regarded as "true" values, even though this is not fully correct. The reason for this is the lack of "real true values", especially in case of tropospheric delays, as there is no chance to determine such. If there is a method to determine a very precise approximation of the value (e.g. ray-tracing), then this value is referred to as the "true" value during the comparison

ones yield virtually the same results as discrete ones. This is also a consequence of the high average elevation angles of VLBI observations which equals  $37.2^\circ$ , as determined from the elevations of all 6.1 million VLBI observations between 1999 and 2014. When not estimating zenith wet delays in VLBI analysis, there is also no difference in the BLR for the different mapping factors. Lowest BLR may then be reached by using zenith wet delays from *RADIATE* instead of those from the VMF1-files. However, additional estimation of  $\Delta L_w^z$  in VLBI analysis makes this improvement useless.

### Comparisons for nine years of VLBI data

The VLBI campaign CONT11 is ideally suited for troposphere research such as comparing the performance of mapping functions as shown in the preceding section. However, because its time frame encompasses only two weeks, the results might not be sufficiently meaningful depending on the task. Investigations concerning azimuthal asymmetry as explained in Chapter 5.1.2.2 will introduce another scenario where the two-week CONT11 campaign is obviously not sufficient for the determination of particular phenomena. Comparisons over longer time periods have to be considered as well in order to guarantee the trustworthiness of the presented new models.

Geodetic VLBI observational data is available from 1979 on, but the quality of the early sessions is basically fairly low. In Chapter 5 there are comparisons undertaken for horizontal gradients, accounting for the azimuthally asymmetric part of the tropospheric delay which are available only starting 2006, while others required an end date of 2014. These nine years from 2006 to 2014 alone carry nearly 5000 VLBI sessions (compare: CONT11 consists of only 15 sessions). Excluding all intensive sessions and further sessions which have been found inappropriate for such comparisons, after all 1338 sessions remained that were eventually used for the analysis (Fig. 4.9). In view of this high number of observations spread over almost a decade, this session list is also used for the comparisons made throughout this section.

As for CONT11, mean BLR for different kinds of discrete as well as empirical mapping functions are determined for all sessions from 2006 through 2014. Again, two cases are considered: (1) NO estimation of zenith wet delays  $\Delta L_w^z$  in VLBI analysis (2) estimation of  $\Delta L_w^z$  in VLBI analysis. Except for lines (b) and (d), a priori zenith wet delays are taken from the VMF1-files (Tab. 4.6). Resulting magnitudes are generally higher than those of the CONT11 comparison (Table 4.5) because there are also loads of sessions with a comparably small number of observations, what impairs the BLR as the quality of the parameter estimation in *VieVS* analysis decreases. The performance of the various mapping functions is, again, almost equal. The only significant difference comes from using a priori zenith wet delays  $\Delta L_w^z$  from *RADIATE* (1.b and 1.d), but its estimation in VLBI renders the use of a priori values useless. When estimating  $\Delta L_w^z$  (column 2), there are only marginal differences for the various mapping functions.





### 4.5.2. Comparison of modeled delays with ray-traced delays

Determining and comparing BLR is just one way of assessing the performance of a certain troposphere model; modeling slant delays and referring them to a reference value proves to be a convenient approach as well [Böhm *et al.*, 2006b; Gegout *et al.*, 2011; Dousa and Elias, 2014; Böhm *et al.*, 2015, just to name a few]. The reference values shall represent, in the best case, the true delay or something very close to it. For the upcoming comparisons the delays from ray-tracing are regarded as the true values. Also Urquhart *et al.* [2013] found ray-tracing as a rigorous benchmark for the evaluation of mapping functions. The closer the modeled delays of a certain approach get to the ray-traced delays, the better they are. The delay differences are mostly specified at  $5^\circ$  elevation in order to satisfy the rule of thumb by Böhm *et al.* [2006a], stating that the resulting station height error equals to approximately one fifth of it. This comparison is on the one hand done for 2592 points on a regular  $5^\circ \times 5^\circ$  grid and on the other hand for a set of discrete VLBI station locations with both eventually yielding very similar results.

#### Comparison for a global grid

The first delay comparison is done for the global  $5^\circ \times 5^\circ$  grid which was already used for the determination of the  $b$  and  $c$  coefficients of VMF3 (cf. Section 4.3) and the empirical troposphere model GPT3 (cf. Section 4.4). In Table 4.2 on page 59 the settings of the ray-tracing are listed. Forming the differences between the ray-traced delays averaged over all eight azimuths and the new troposphere mapping functions VMF1<sub>repro</sub>, VMF1<sub>reproLSM</sub>, VMF3 and VMF3<sub>LSM</sub> as well as GPT3 enables an assessment of their performance<sup>11</sup>. VMF<sub>LSM</sub>, the version where all three mapping function coefficients are estimated at once which is assumed to be the most accurate mapping approach, is also included here. For all methods the same zenith delays from *RADIATE* are used so that the difference in the delays can solely be attributed to the difference in mapping factors. The empirical mapping functions GMF and GPT2w are compared to GPT3 in this investigation what has to be treated with caution, because GPT3 was determined precisely for the ray-traced delays which are regarded as the reference values, what is not the case for GMF and GPT2w.

Before looking at the general comparison between the methods, it is shown that the spherical harmonics expansion for  $b$  and  $c$  is indeed able to represent the grid very precisely. What was already indicated graphically in Fig. 4.6 on page 65 is now proven by Table 4.7, namely that the representation in spherical harmonics entails only a very small, inevitable loss of precision. Consequently, VMF3<sub>LSM</sub> (gridded) is not considered in later comparisons anymore.

<sup>11</sup>the new VMF models tested here are all based on ray-tracing through NWM with a spatial resolution of  $1^\circ \times 1^\circ$ . The versions from the  $0.125^\circ \times 0.125^\circ$  NWM as occurring in Section 4.5.1 are only available for the period of CONT11 and therefore inappropriate for the following

Table 4.7.: *Mean absolute differences in slant total delay  $\Delta L$  at  $5^\circ$  elevation between ray-tracing and VMF3, once for  $b$  and  $c$  from the  $5^\circ \times 5^\circ$  grid (= VMF3<sub>LSM</sub> (gridded)) and once for  $b$  and  $c$  from spherical harmonics (= VMF3<sub>LSM</sub> (spherical harmonics)), averaged over all 2592 grid points and 120 epochs. VMF<sub>LSM</sub> is also presented here as a comparative value.*

TROPOSPHERE MODEL	$\Delta L$ (mm)
VMF <sub>LSM</sub>	0.35
VMF3 <sub>LSM</sub> (gridded)	0.58
VMF3 <sub>LSM</sub> (spherical harmonics)	0.82

What is of prime importance is the performance of VMF3 vs. VMF1<sub>repro</sub>. Figures 4.10 and 4.11 show biases and standard deviations, respectively, for their differences to ray-tracing. The increase in accuracy is fairly obvious, both in terms of bias and standard deviation. It is also evident that the bulk of delay comes from the hydrostatic part  $\Delta L_h$  whereas there is no considerable alteration in  $\Delta L_w$  between VMF3 and VMF1<sub>repro</sub>. Regarding the biases in Fig. 4.10, VMF1<sub>repro</sub> has evident shortcomings in mountainous areas such as the Himalayas or the Rocky Mountains for instance. In those regions VMF3 comes significantly closer to the ray-traced delays with improvements up to 8 mm, what corresponds to more accurate station heights by more than 1 mm. Residuals remain especially in the Himalayas what is a result of the spherical harmonics expansion of  $b$  and  $c$ , which overly smooths the underlying grid owing to the fairly low expansion to degree and order 12. VMF3 is also able to reduce the residuals of VMF1<sub>repro</sub> over the ocean although their cause is not clear. In Fig. 4.11 it shows up that VMF3 significantly reduces the standard deviations in polar regions, however it is again not clear where they come from. As outlined in Fig. 4.12, VMF3<sub>LSM</sub> is able to further decrease the delay differences to ray-tracing, while it does not change the systematic behaviour. In Fig. 4.13 the differences between GPT2w and GPT3 to the ray-traced delays averaged over all 120 epochs are outlined. At most places on Earth, GPT3 lowers the bias of the residuals with respect to GPT2w. The standard deviation, which is more meaningful in this respect, however, is lowered only slightly and it cannot be stated with the naked eye which grid points improve or degrade.

Tabs. 4.8 to 4.10 summarize the differences between ray-traced delays and the different mapping function methods for  $5^\circ$  elevation and  $3.3^\circ$  elevation, respectively.

These figures and tables say a great deal about the performance of the new determined mapping functions, as they are assumed to be very meaningful because of the vast amount of data utilized:

- The best approximation of the ray-traced delays is achieved with VMF<sub>LSM</sub>, that approach where all three coefficients  $a$ ,  $b$  and  $c$  are estimated together in one least-

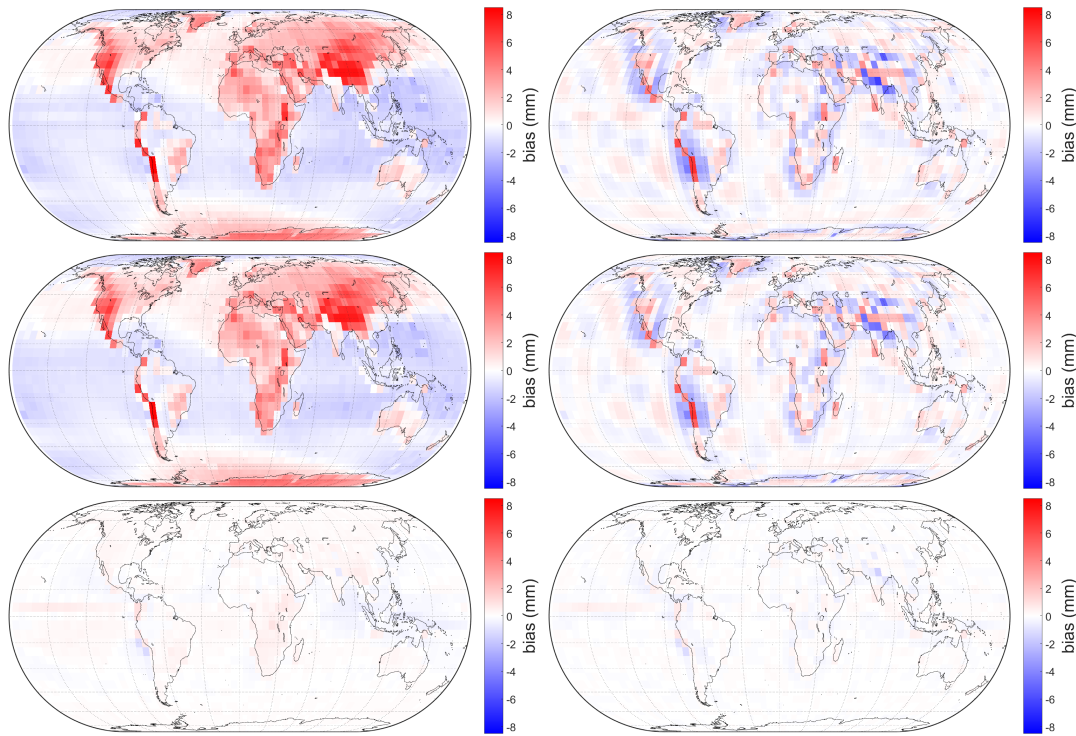


Figure 4.10.: Differences in slant delays at  $5^\circ$  elevation between  $VMF1_{repro}$  (left) and  $VMF3$  (right) to the ray-traced delays, averaged over all 120 epochs (= bias). Top: differences in slant total delay  $\Delta L$ , center: differences in slant hydrostatic delay  $\Delta L_h$ , and bottom: differences in slant wet delay  $\Delta L_w$  [Landskron et al., 2016c].

Table 4.8.: Mean absolute differences (first column), bias (second column) and standard deviation (third column) in slant total delay  $\Delta L$  at  $5^\circ$  elevation between ray-tracing and several mapping function approaches, averaged over all 2592 grid points and 120 epochs.

TROPOSPHERE MODEL	MEAN ABS. DIFF. $\Delta L$ (mm)	BIAS $\Delta L$ (mm)	$\sigma \Delta L$ (mm)
$VMF_{LSM}$	0.35	0.00	0.43
$VMF1_{repro}$	1.73	0.58	1.23
$VMF1_{reproLSM}$	1.49	0.50	1.08
$VMF3$	0.93	-0.04	0.84
$VMF3_{LSM}$	0.82	-0.03	0.73
GMF	10.21	-2.08	10.47
GPT2w	6.85	0.32	8.26
GPT3	6.44	-1.03	7.98

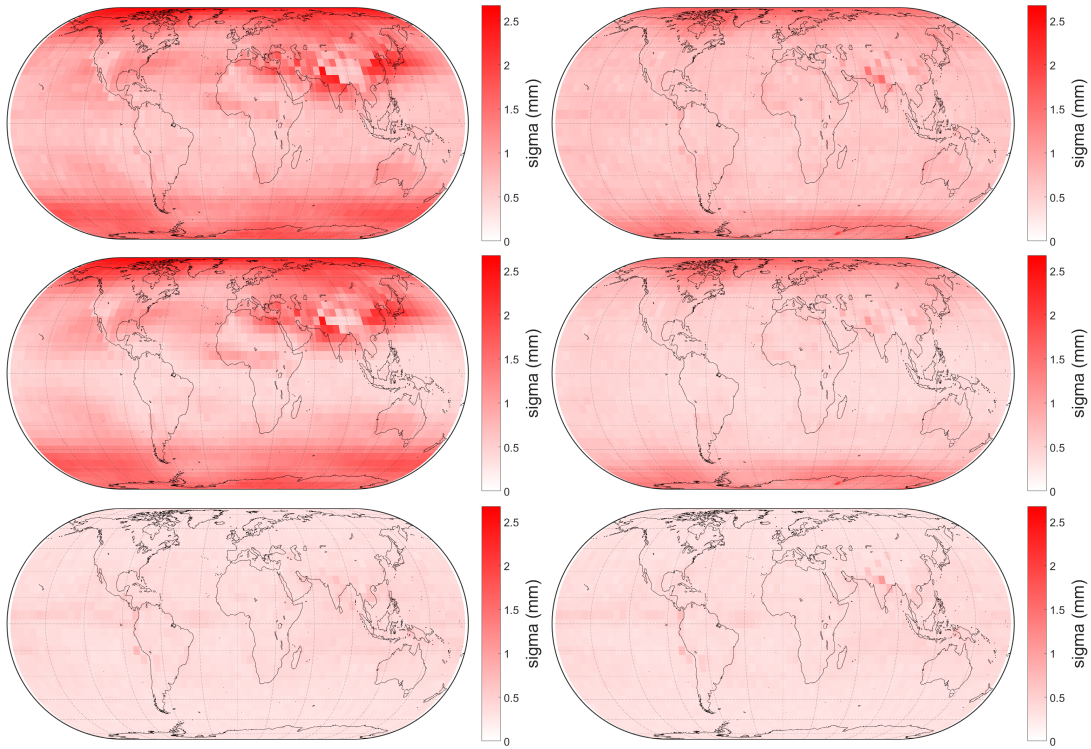


Figure 4.11.: Standard deviation  $\sigma$  of the differences in slant delays at  $5^\circ$  elevation between  $VMF1_{repro}$  (left) and  $VMF3$  (right) to the ray-traced delays, averaged over all 120 epochs. Top:  $\sigma$  for slant total delay  $\Delta L$ , center:  $\sigma$  for slant hydrostatic delay  $\Delta L_h$ , and bottom:  $\sigma$  for slant wet delay  $\Delta L_w$  [Landskron et al., 2016c].

Table 4.9.: Mean absolute differences (first column), bias (second column) and standard deviation (third column) in slant total delay  $\Delta L$  at  $3.3^\circ$  elevation between ray-tracing and several mapping function approaches, averaged over all 2592 grid points and 120 epochs.

TROPOSPHERE MODEL	Mean Abs. Diff. $\Delta L$ (mm)	BIAS $\Delta L$ (mm)	$\sigma\Delta L$ (mm)
$VMF_{LSM}$	0.49	0.00	0.59
$VMF1_{repro}$	0.49	0.00	0.59
$VMF1_{reproLSM}$	0.78	0.21	0.73
$VMF3$	0.49	0.00	0.59
$VMF3_{LSM}$	0.58	0.01	0.66
GMF	24.01	-4.27	24.66
GPT2w	15.85	1.72	19.41
GPT3	14.83	0.01	18.91

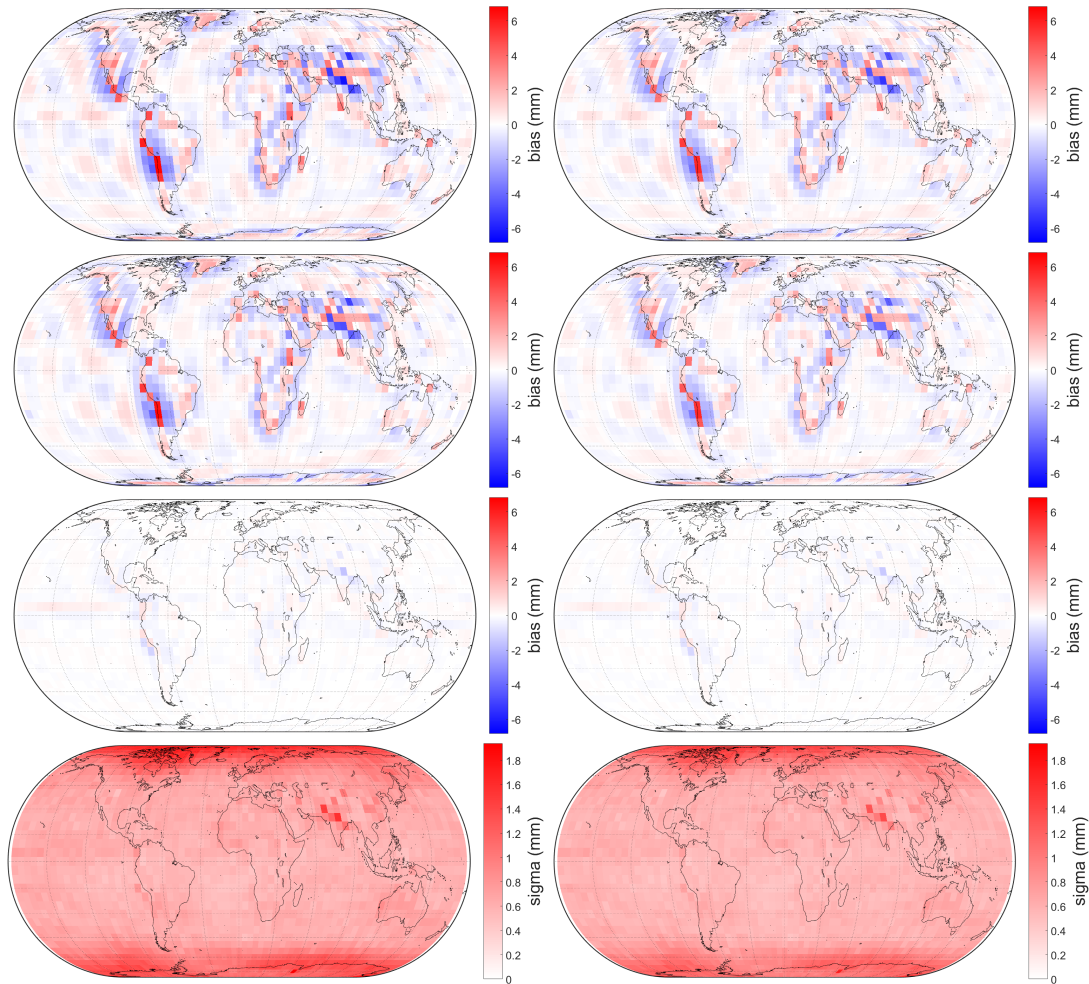


Figure 4.12.: Differences in slant delays at  $5^\circ$  elevation between VMF3 (left) and VMF3<sub>LSM</sub> (right) to the ray-traced delays, averaged over all 120 epochs. Top: bias in slant total delay  $\Delta L$ , center top: bias in slant hydrostatic delay  $\Delta L_h$ , center bottom: bias in slant wet delay  $\Delta L_w$  and bottom: standard deviation in slant total delay  $\Delta L$ . The general shape is the same, but the amplitudes of VMF3<sub>LSM</sub> are slightly lower in bias as well as in standard deviation.

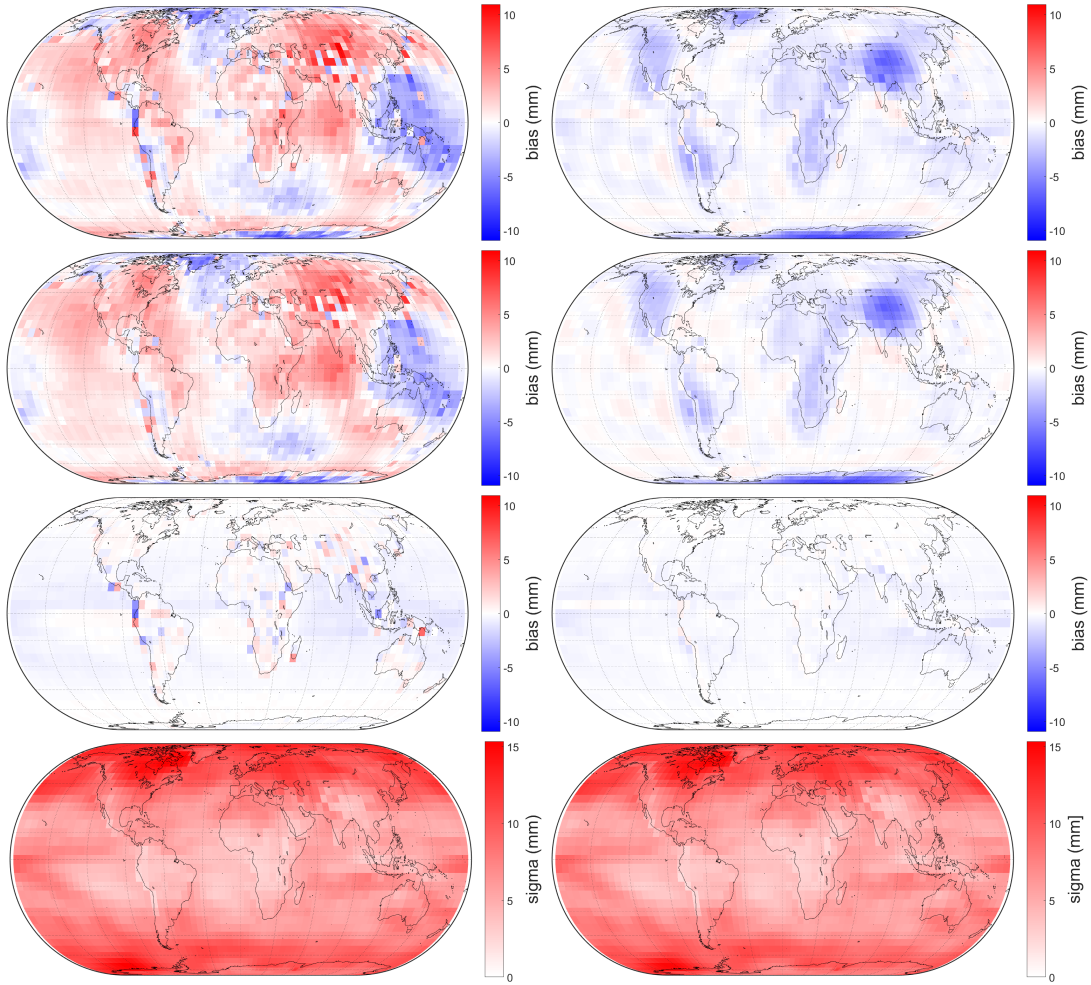


Figure 4.13.: Differences in slant delays at  $5^\circ$  elevation between GPT2w (left) and GPT3 (right) to the ray-traced delays, averaged over all 120 epochs (= bias). Top: bias in slant total delay  $\Delta L$ , center top: bias in slant hydrostatic delay  $\Delta L_h$ , center bottom: bias in slant wet delay  $\Delta L_w$  and bottom: standard deviation in slant total delay  $\Delta L$ . The bias is significantly reduced with GPT3 but the standard deviation is only slightly lower.

Table 4.10.: Mean absolute differences in slant total delay  $\Delta L$ , slant hydrostatic delay  $\Delta L_h$  and slant wet delay  $\Delta L_w$  at  $5^\circ$  elevation between ray-tracing and VMF1<sub>repro</sub>/VMF3, averaged over all 2592 grid points and 120 epochs. The values for  $\Delta L$  in the left column are just overtaken from Table 4.8.

TROPOSPHERE MODEL	$\Delta L$ (mm)	$\Delta L_h$ (mm)	$\Delta L_w$ (mm)
VMF <sub>LSM</sub>	0.35	0.25	0.27
VMF1 <sub>repro</sub>	1.73	1.67	0.31
VMF1 <sub>reproLSM</sub>	1.49	1.43	0.30
VMF3	0.93	0.84	0.30
VMF3 <sub>LSM</sub>	0.82	0.73	0.30

squares adjustment. However, this estimation succeeds only on the regular  $5^\circ \times 5^\circ$  grid, but not for discrete stations, as pointed out in the upcoming section.

- VMF3 gets significantly closer to the ray-traced delays than VMF1<sub>repro</sub> for both the LSM version as well as the non-LSM ones where the  $a$  coefficients were calculated for the elevation  $3.3^\circ$  only. As the zenith delays come from the same source, this can be solely attributed to the more proper mapping concept which VMF3 is based on. It is a meaningful indicator that VMF3 can further increase the current accuracy in tropospheric delay modeling.
- The non-LSM versions of VMF1 and VMF3 fit better at the elevation  $3.3^\circ$  which is hardly surprising since the mapping factors were calculated for precisely this elevation. At  $5^\circ$ , the LSM versions fit distinctively better than the non-LSM and also for the remaining two elevations  $15^\circ$  and  $30^\circ$  (figures not contained in the tables).
- The bulk of improvement when using VMF3 comes from the hydrostatic part of the delay while the wet delay hardly changes.
- VMF3 performs better in mountainous areas than VMF1<sub>repro</sub> due to the latter's apparent deficiencies in the empirical coefficients  $b$  and  $c$ .
- Of the empirical mapping functions, GPT3 gets closest to the ray-traced delays but it is assumed that the fact that GPT3 was determined for the same ray-traced delays which it is compared to here may influence the results to some extent. However, the comparison in the upcoming part, which is done for 33 VLBI stations, is untainted by this. Highest biases of GPT3 occur in the Himalayas and in Antarctica, however it is not known why. It is also not clear why there is a generally negative bias of GPT3 in Fig. 4.13.
- What can be stated very well from the comparison is that GPT3 as well as GPT2w approximate the ray-traced delays more accurately than GMF.

### Comparison for 33 VLBI stations

The second delay comparison is made for a high number of sites around the world. These sites in fact represent VLBI stations, although the comparison itself does not require any actual VLBI observations; they were chosen just for reasons of convenience as the delays thus can be used for different topics and comparisons, too. Figure 4.14 displays the locations of the stations on a world map. The years from 1999 and 2014 are chosen because ray-traced delays from *RADIATE* are available for this very time frame<sup>12</sup>. Table 4.11 comprises the specifications for the generation of ray-traced delays. 112 ray-traced delays were calculated per site and epoch. In case of the ray-traced delays for the grid there were only 32 ray-traced delays per station and epoch, which decreased the calculation time per site approximately fourfold. A plain visualization of the ray-traced delays that had to

<sup>12</sup>in the meantime, ray-traced delays became available for the whole VLBI history, that is, from 1979 on



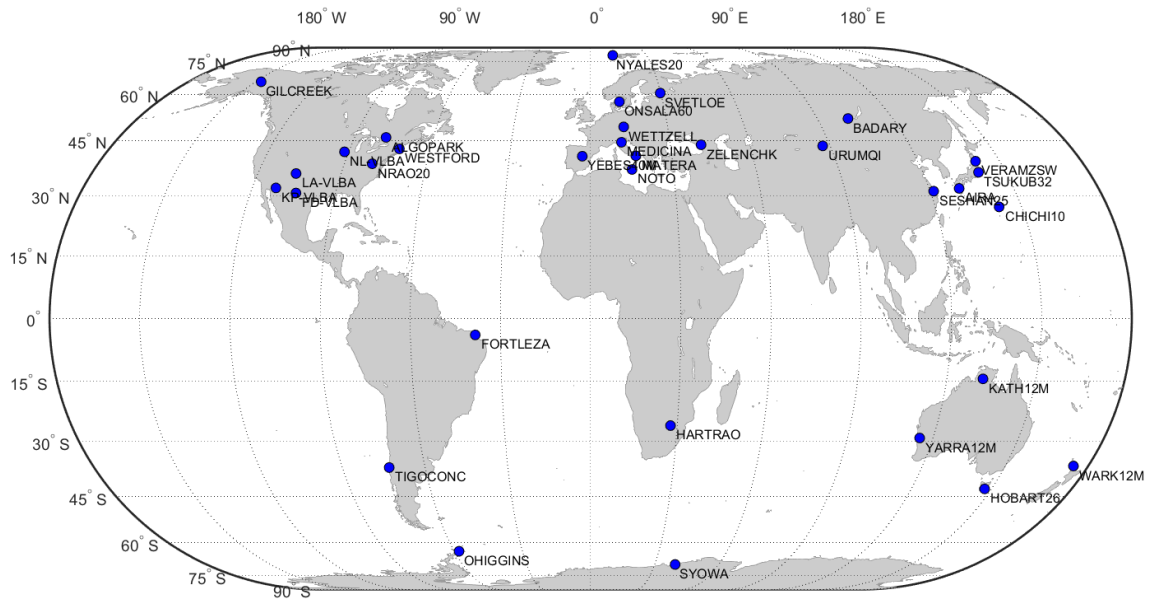


Figure 4.14.: Map of all 33 VLBI stations that were selected for the comparison of slant delays w.r.t. ray-traced delays from 1999-2014.

Table 4.11.: Properties of the ray-traced delays that were generated using the ray-tracer *RADIATE* from 1999-2014, in addition to the ray-tracing standard approach (see Table A.4 on page 139).

PARAMETER	SPECIFICATION
Ray-tracing software	<i>RADIATE</i> [Hofmeister, 2016]; 2D ray-tracer
NWM	ECMWF ERA Interim Pressure Level Data + ECMWF operational data
Horizontal resolution of the NWM	$1^\circ \times 1^\circ$
Horizontal coverage	33 VLBI stations
Temporal resolution	6-hourly at 00:00, 06:00, 12:00 and 18:00 UTC each day from 1999 through 2014 (= 23376 epochs)
Elevations per point	7 ( $3^\circ$ , $5^\circ$ , $7^\circ$ , $10^\circ$ , $15^\circ$ , $30^\circ$ and $70^\circ$ )
Azimuths per point	16 ( $0^\circ$ : $22.5^\circ$ : $337.5^\circ$ )

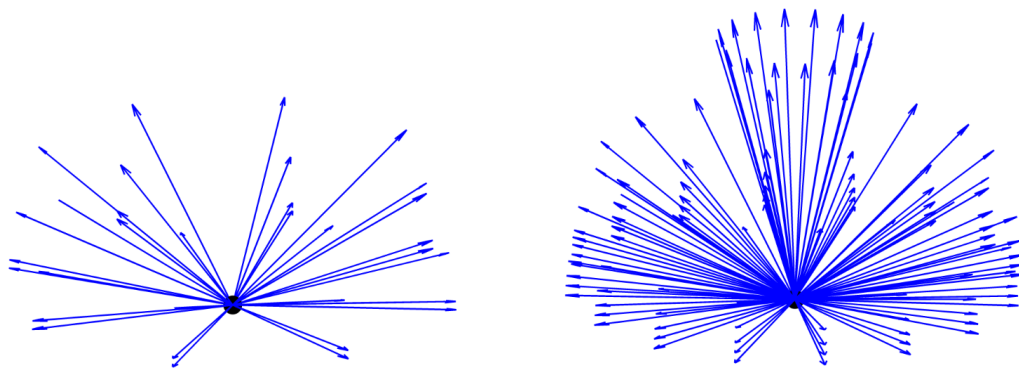


Figure 4.15.: *Left: the 32 ray vectors that were generated for each considered grid point of the global  $5^\circ \times 5^\circ$  grid. Right: the 112 ray vectors that were generated for each active VLBI station from 1999-2014. As usual for this purpose, lower elevations are covered more densely than higher elevations since they are greatly influenced by azimuthal asymmetry.*

be generated for every grid point is featured in Fig. 4.15, which shows very distinctively the difference to those of Table 4.2.

Even though ray-traced delays were only produced for epochs that are stringently required for the interpolation, they add up to a huge number: all in all, 25.426.800 delays had to be created<sup>13</sup>. For the piecewise-linear method of the *Fortran* version of *RADIATE* considering a horizontal NWM resolution of  $1^\circ \times 1^\circ$ , a mean calculation time of 0.8 milliseconds per ray-traced delay is to be expected [Hofmeister, 2016]<sup>14</sup>. Despite the vast number of ray-traced delays, a rough estimate of no more than 3.4 hours was needed for their calculation, however a significant amount of time must be added which is consumed for the loading of the several GB large NWM data files. The FORTRAN version of *RADIATE* is about 207 times faster with respect to the *MATLAB* version which it was originally programmed in [Hofmeister, 2016], what would be equivalent to one month of calculation time. Just a marginal note: increasing the NWM resolution from  $1^\circ \times 1^\circ$  to  $0.125^\circ \times 0.125^\circ$ , as was done in investigations for CONT11, had increased the calculation time roughly 64-fold, resulting in 9 days calculation time for the *Fortran* version and tremendous 6 years for the *MATLAB* version, exclusive of the loading time of the NWM data files each. For this reason, the higher-resolved NWM were dropped with good conscience.

The criteria for the choice of stations was to achieve an as even as possible global distribution on the one hand and a high amount of data on the other hand, which depends on the activity of the respective VLBI station. Participation in a CONT campaign is generally a good indicator for a regularly observing station, which is why most of the

<sup>13</sup>1999: 1.285.386, 2000: 1.115.184, 2001: 1.243.648, 2002: 1.487.808, 2003: 1.572.480, 2004: 1.625.232, 2005: 1.701.504, 2006: 1.662.976, 2007: 1.567.776, 2008: 1.648.752, 2009: 1.594.656, 2010: 1.487.360, 2011: 1.703.296, 2012: 1.805.664, 2013: 1.950.592, 2014: 1.974.336 ray-traced delays

<sup>14</sup>this test was carried out for a 64-bit Microsoft Windows 7 machine with an Intel Core i3-2120 CPU at 3.3 GHz and with 8 GB RAM

Table 4.12.: Mean absolute differences (first column), bias (second column) and standard deviation (third column) in slant total delay  $\Delta L$  at  $5^\circ$  elevation between ray-tracing and several mapping function approaches, averaged over all 33 stations and epochs from 1999-2014.

TROPOSPHERE MODEL	MEAN ABS. DIFF. $\Delta L$ (mm)	BIAS $\Delta L$ (mm)	$\sigma\Delta L$ (mm)
VMF1 <sub>repro</sub>	3.98	2.66	4.24
VMF1 <sub>reproLSM</sub>	3.47	2.32	3.71
VMF3	2.97	1.72	3.57
VMF3 <sub>LSM</sub>	2.64	1.58	3.15
GMF	19.69	-1.66	25.79
GPT2w	18.95	-0.53	24.74
GPT3	18.98	-2.43	24.69

selected stations in Fig. 4.14 have also participated in CONT11 and/or CONT14. Overall it must be noted that the data amount varies significantly for these stations; WETTZELL (Wetzell, Germany) disposes of data of almost all 23000 epochs<sup>15</sup> while SYOWA (Showa Station, Antarctica), for instance, possesses barely 1000 epochs, but nevertheless SYOWA is important for guaranteeing the global distribution in this comparison.

On this basis the performance of the various new mapping functions can be assessed through subtraction from the ray-traced delays, which are again averaged over all azimuths in order to get horizontally anisotropic reference values. In Tabs. 4.12 and 4.13 the delays are modeled using zenith delays from one and the same source, in order to compare merely the influence of the mapping factors alone and subtracted from the ray-traced delays. This is equal to what is done in the comparison for the  $5^\circ \times 5^\circ$  grid in the preceding section. As a matter of course the numbers in the tables are derived through weighted means for the stations; this means that the influence of WETTZELL is roughly 23 times higher than that of SYOWA owing to the higher number of observations. The standard VMF1 is not included in these comparisons although it is determined similarly, but adjusted to ray-traced delays from a different programme and different NWM input (cf. Section 2.1.1). By this means it cannot be assumed that VMF1 approximates the ray-traced delays from *RADIATE* very well since it is simply not designed to do so. Consequently, results of VLBI analysis such as BLR remain the only way of comparing the performance of VMF1 to other mapping functions. The version VMF<sub>LSM</sub> where all three mapping function coefficients were determined at once does not succeed for individual stations. Apparently the problem is that the ray-traced wet mapping factors  $mf_w$  fluctuate so severely that there is no chance to define universal starting values for  $a_w$ ,  $b_w$  and  $c_w$  in such a way that they ensure rapid convergence of the LSM for all points and epochs. For the hydrostatic

<sup>15</sup>this implies that WETTZELL observed nearly every day between 1999 and 2014

Table 4.13.: *Mean absolute differences (first column), bias (second column) and standard deviation (third column) in slant total delay  $\Delta L$  at  $3^\circ$  elevation between ray-tracing and several mapping function approaches, averaged over all 33 stations and epochs from 1999-2014.*

TROPOSPHERE MODEL	MEAN ABS. DIFF. $\Delta L$ (mm)	BIAS $\Delta L$ (mm)	$\sigma\Delta L$ (mm)
VMF1 <sub>repro</sub>	0.52	0.00	0.64
VMF1 <sub>reproLSM</sub>	1.62	-1.02	1.75
VMF3	0.52	0.00	0.64
VMF3 <sub>LSM</sub>	1.17	-0.45	1.50
GMF	56.28	-8.38	72.74
GPT2w	54.35	-5.34	70.09
GPT3	54.49	-8.22	70.21

$m f_h$  convergence is achieved already after few iterations like in all other LSM approaches, but the  $m f_w$  immediately and regularly diverge. The reason for this is most likely that for the regular  $5^\circ \times 5^\circ$  grid monthly mean NWM are used (cf. Table 4.2) in which all values, including  $m f_w$ , are strongly smoothed. For this reason, the approach VMF<sub>LSM</sub> has to be dropped here.

What is most important is to assess the potential of VMF3 to improve VMF1 and of GPT3 to improve GPT2w, respectively, as depicted in Figs. 4.16 to 4.19.

The differences between the various methods in Tabs. 4.12 and 4.13 are fairly large because the comparisons are done at the very small elevation angles of  $3.3^\circ$  and  $5^\circ$ , respectively. In VLBI the mean observation angle is fairly high at approximately  $37^\circ$ . Table 4.14 now shows the averaged differences between the ray-traced delays (once more regarded as the true delays) at the real elevation angles and the modeled delays from several approaches. Another difference of this comparison, beside the elevation, is that here the non-consideration of azimuthal asymmetry negatively influences the results, while in the tests from Tabs. 4.12 and 4.13 this was not necessary as the delays from all azimuths were averaged beforehand. This, however, does not impair the comparability of the methods since they are all affected in the same magnitude. The comparison is done again for the same 33 VLBI stations which are responsible for almost 80% of all observations carried out in the time period of 1999 to 2014 (4.8 million of 6.1 million). Although the distinctions are only marginal, it becomes apparent that VMF3 is slightly better than VMF1, while in case of the empirical mapping functions no difference can be detected.

Analogously to the comparison for the global grid, the conclusions of Tabs. 4.12 and 4.13 as well as Figs. 4.16 to 4.19 are summarized in the following itemization:

- When basically comparing the VMF3 approaches to those of VMF1<sub>repro</sub> it soon

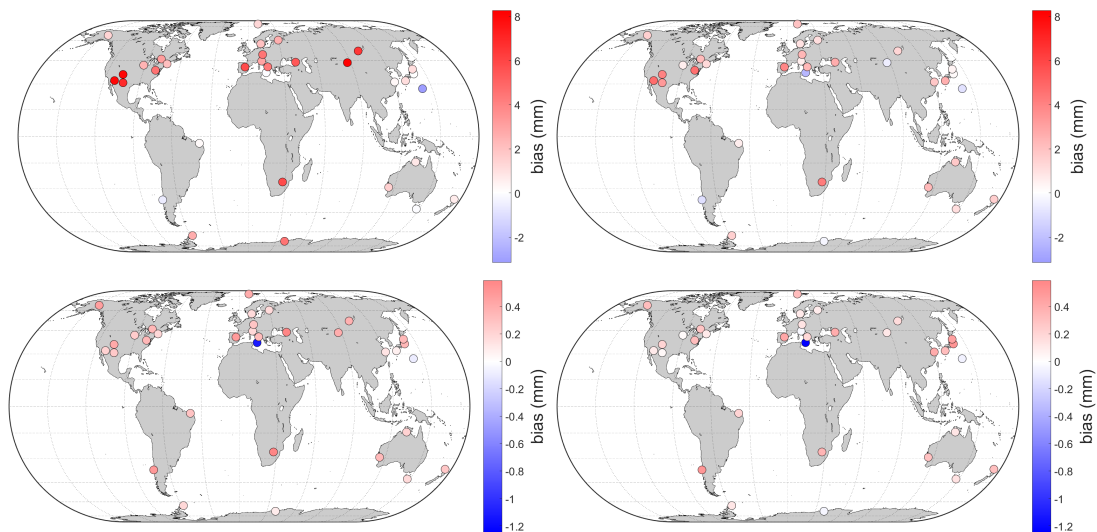


Figure 4.16.: Mean differences in slant hydrostatic delays (top) and slant wet delays (bottom) at  $5^\circ$  elevation between  $VMF1_{repro}$  (left) and  $VMF3$  (right) to the ray-traced delays.  $VMF3$  outperforms  $VMF1_{repro}$  at 25 of the 33 stations in hydrostatic as well as wet delay.

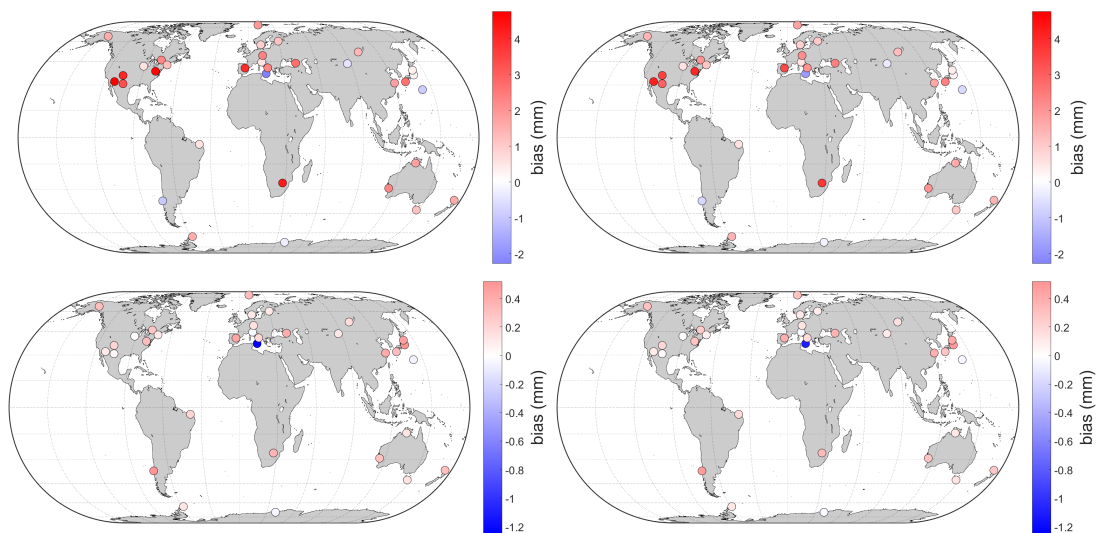


Figure 4.17.: Mean differences in slant hydrostatic delays (top) and slant wet delays (bottom) at  $5^\circ$  elevation between  $VMF3$  (left) and  $VMF3_{LSM}$  (right) to the ray-traced delays. Interestingly, this leads to a general improvement at every single station.

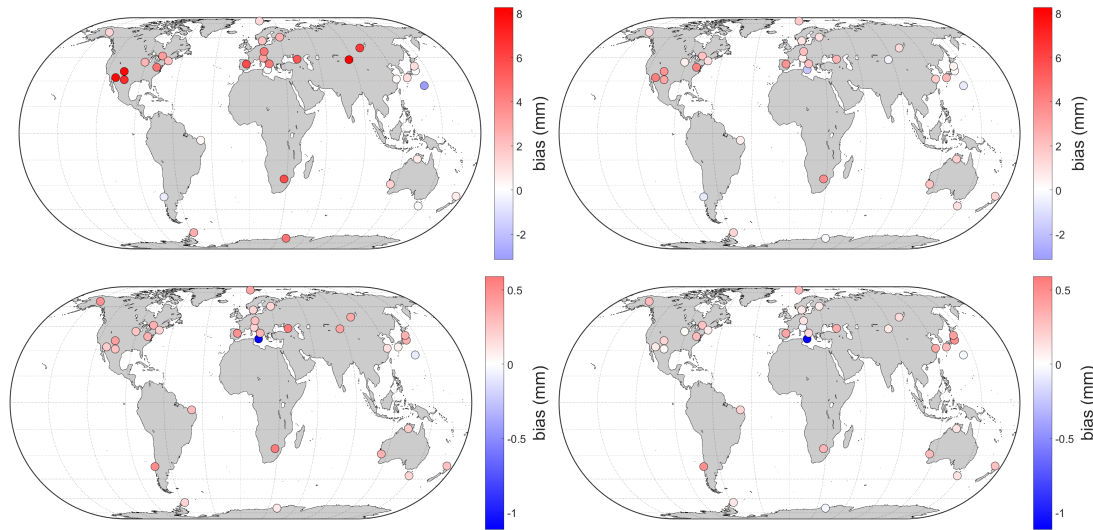


Figure 4.18.: Mean differences in slant hydrostatic delays (top) and slant wet delays (bottom) at  $5^\circ$  elevation between  $VMF1_{repro}$  (left) and  $VMF3_{LSM}$  (right) to the ray-traced delays.  $VMF3_{LSM}$  outperforms  $VMF1_{repro}$  at 27 of the 33 stations in hydrostatic delay and at all stations in wet delay.

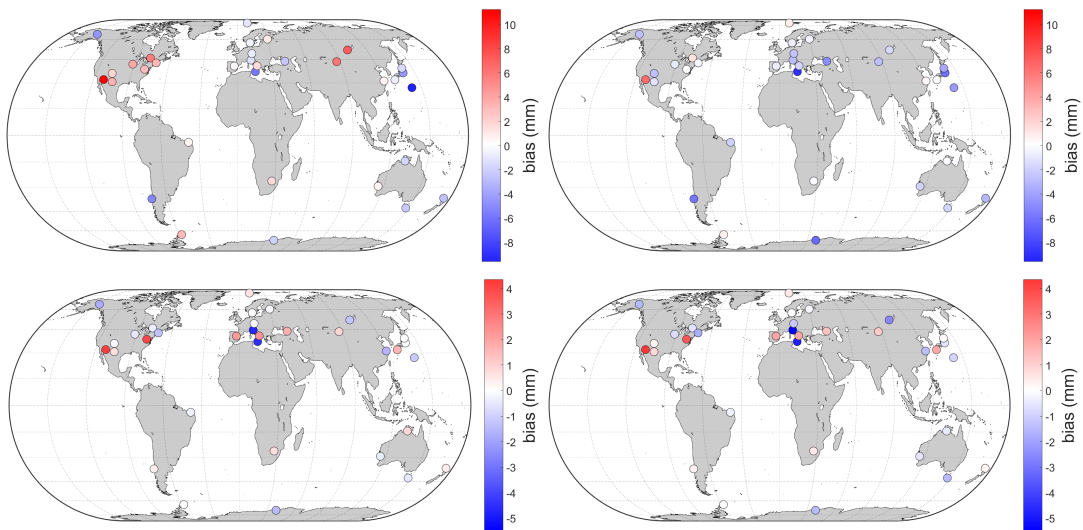


Figure 4.19.: Mean differences in slant hydrostatic delays (top) and slant wet delays (bottom) at  $5^\circ$  elevation between  $GPT2w$  (left) and  $GPT3$  (right) to the ray-traced delays.  $GPT3$  improves slant hydrostatic delays at 17 of the 33 stations and slant wet delays at 15 of the 33 stations compared to  $GPT2w$ .

Table 4.14.: *Mean absolute differences at the observed elevation angles in slant total delay  $\Delta L$  (first column), slant hydrostatic delay  $\Delta L_h$  (second column) and slant wet delay  $\Delta L_w$  (third column) between ray-tracing and several mapping function approaches, averaged over all 33 stations and epochs from 1999-2014.*

TROPOSPHERE MODEL	$\Delta L$ (mm)	$\Delta L_h$ (mm)	$\Delta L_w$ (mm)
VMF1 <sub>repro</sub>	4.43	1.86	3.79
VMF3	4.36	1.84	3.72
VMF3 <sub>LSM</sub>	4.36	1.84	3.72
GMF	4.58	2.01	3.83
GPT2w	4.57	1.99	3.83
GPT3	4.58	2.01	3.83

becomes clear that the VMF3 ones fit better than that of VMF1. The delays of VMF3 reproduce the ray-traced delays appreciably better for both the version where the  $a$  coefficients were calculated for an elevation of  $3^\circ$  as well as the LSM version. The best fitting model turns out to be VMF3<sub>LSM</sub> which gets up to 1/3 closer to the ray-traced delays than VMF1<sub>repro</sub>.

- For an elevation of  $3^\circ$  the LSM versions perform worse than the non-LSM versions, while for elevation  $5^\circ$  (and also all higher elevation angles whose figures are not listed here) they are superior. This is due to the fact that the non-LSM mapping factors were calculated for precisely the elevation  $3^\circ$ , which is also why they have a bias of zero at this elevation.
- At  $3^\circ$  elevation the modeled delays generally approximate the ray-traced delays better than at  $5^\circ$ . This is no surprise for the non-LSM mapping functions determined exactly for the elevation of  $3^\circ$  (see item above), but very astonishing for those from LSM. So far no reason for this phenomenon could be found.
- Comparing Fig. 4.16 with Fig. 4.10 on page 76 shows clear agreement; all regions of the grid where VMF3 is better than VMF1<sub>repro</sub> are accompanied by a station-wise improvement, too. In central Asia, for example, VMF3 significantly reduces the residuals what can also be seen in the station-wise improvement of VLBI stations BADARY and ZELENCHK. On the other hand, over Australia the residuals of VMF3 are fairly equal to those of VMF1<sub>repro</sub> what corresponds to the VLBI stations KATH12M, WARK12M or YARRA12M. However, the large improvement over Japan is not reflected in the stations plot.
- Although the GPT3 mapping function coefficients  $a_h$  and  $a_w$  are determined from new, highly accurate ray-traced delays they perform only approximately at the same level as GPT2w. This is very surprising because the same ray-traced delays as in VMF3 were used which, however, achieves an appreciable improvement over VMF1.

Nevertheless, after the planned determination of a new height correction GPT3 is expected to get a little closer to the ray-traced delays.

- As in the previous comparison on the global grid, GMF is outperformed by both GPT2w and GPT3.

## 4.6. Conclusions

In this section, new mapping function concepts were developed generally based on well-known mapping approaches. The main achievement in this respect is the Vienna Mapping Function 3, which was determined in two different versions. The quality of these new mapping functions was then assessed through different comparisons in order to get final conclusions, which are listed in the following itemization:

- VMF3 obviously surpasses VMF1<sub>repro</sub> in the delay comparisons, which means that it is able to simulate the ray-traced delays more accurately. This is due to the more sophisticated representation of the empirical  $b_h$ ,  $b_w$ ,  $c_h$  and  $c_w$  coefficients which all inhere a temporal as well as a spatial variation. For comparison, in VMF1<sub>repro</sub> only the coefficient  $c_h$  is variable for time and latitude. The standard VMF1 can not be included in the delay comparisons as it was generated for different ray-traced delays.
- The mapping factors of VMF3<sub>LSM</sub>, where ray-traced delays from a set of elevations are taken into consideration, perform even better than (standard) VMF3 which is determined strictly for the single elevation of 3°. Its calculation lasts approximately twice as long<sup>16</sup> which, however, does not affect the users.
- The approach VMF<sub>LSM</sub>, where all three coefficients  $a$ ,  $b$  and  $c$  are estimated at once yields best results for the delay comparison on a grid, but cannot be determined for discrete station locations as the LSM fails for the highly variable wet mapping factors. Otherwise, VMF<sub>LSM</sub> would be the most accurate model for that purpose. But according to *Böhm* [2004], the individual interpolation of each of the three coefficients would be dangerous even on the grid because of their high correlation with each other.
- Regarding the comparably small improvement of VMF3 over VMF1, the question arises whether users shall convert to VMF3 at all; it must be decided individually whether it is worth the change in favor of highest precision.
- In BLR comparisons, however, it does not matter which mapping function is used, as each achieves more or less same accuracy. Using NWM with a resolution of  $0.125^\circ \times 0.125^\circ$  instead of  $1^\circ \times 1^\circ$  as basis for the determination of mapping functions does not seem to change BLR either.
- The new ray-traced zenith wet delays from *RADIATE* are more accurate than those

<sup>16</sup>while the calculation time for the underlying ray-traced delays increases seven-fold



from the VMF1-files. This substantially affects BLR when zenith wet delays  $\Delta L_w^z$  are not additionally estimated in VLBI analysis.

- In general, it appears as if the modeling of tropospheric delays using the VMF approaches is already very close to the highest level of technical means. This is made clearest by the fact that in the delay difference comparison the modeled delays get very close to the ray-traced delays. As long as (1) the ray-traced NWM stagnate at the comparably low temporal resolution of six hours and a vertical resolution of merely 25 height levels [*Hofmeister, 2016*] and (2) the equation by Marini (Eq. (2.5) on page 7), which prohibits observations at elevations below  $3^\circ$ , is maintained as the fundamental mapping concept, it is not expected that any further significant improvements in mapping accuracy can be achieved. On the contrary one has to keep in mind that determination of NWM even in these allegedly "low" resolutions can be handled only by the fastest and strongest supercomputers currently available in the world.
- The mapping functions of the new empirical troposphere model GPT3 perform marginally better those of GPT2w for delay differences to ray-tracing. This holds both for the hydrostatic as well as the wet part of the delay. In BLR comparisons there is no difference though. A new height correction for mapping functions as well as additional estimation of sub-daily parameters could have some room for improvement, however it is assumed, too, that current empirical troposphere models are already close to top level.



## 5. Azimuthal asymmetry

The previous chapters covered the mapping of delays from zenith direction down to arbitrary elevation angles using different strategies, all of which assume symmetry for all azimuths around the station. However, as already described in the fundamentals, this is only a simplification. For that reason a further term must be added to the troposphere modeling formula to take azimuthal asymmetry into account, yielding Eq. (2.9) on page 14. Horizontal tropospheric north  $G_n$  and east gradients  $G_e$  are the very variables into which all information about the delay variation with azimuth is incorporated. The current chapter comes up with the determination of new, discrete values for these gradients determined from ray-traced delays from *RADIATE* (Section 5.1.1.1). Additionally, higher order gradient formulae are designed to model azimuthal symmetry more accurately (Section 5.1.1.2). The determined gradients are referred to as GRAD [*Landskron et al., 2015c*] and can be used as a priori values to VLBI analysis. The quality of GRAD is assessed through a number of comparisons, covered in Sections 5.1.2.2, 5.1.2.1 and 5.1.3. Apart from these discrete gradients, the ray-traced delays are also used to design an empirical gradient grid which can be utilized for determination of azimuthal asymmetry at any point on Earth (Section 5.2). This grid is then included in the empirical troposphere model GPT3 after being subjected to a range of comparisons proving its quality.

### 5.1. Determination of discrete horizontal gradients

In this section, horizontal tropospheric north  $G_n$  and east gradients  $G_e$  are calculated discretely from ray-traced delays by applying different approaches, both established ones and new ones. The idea here is that these gradients can then be used as a priori gradients in VLBI analysis, what is thought to improve the accuracy of the modeling of tropospheric delays. The basic assumption of this whole chapter is that the delays obtained from ray-tracing are again regarded as the "true" delays. These ray-traced delays are then to be approximated as accurately as possible by means of modeling using Eq. (2.9). The general concept of the gradient application is to first calculate them each for the NWM epochs, that is, at four epochs per day, namely 00:00, 06:00, 12:00 and 18:00 UTC, so that they can later be interpolated from the surrounding NWM epochs to the very times of the VLBI measurements by means of e.g. a spline interpolation. A direct calculation of a priori gradient pairs for the very epochs of the VLBI measurements may sound more sensible in the first place, but is not done for the following two reasons: the NWM, upon the basis

Table 5.1.: *Properties of the ray-traced delays that were generated using the ray-tracer RADIATE for the time period of CONT11, in addition to the ray-tracing standard approach (see Table A.4 on page 139).*

PARAMETER	SPECIFICATION
Ray-tracing software	<i>RADIATE</i> [Hofmeister, 2016]; 2D ray-tracer
NWM	ECMWF operational data
Horizontal resolution of the NWM	(1) $0.125^\circ \times 0.125^\circ$ , (2) $1^\circ \times 1^\circ$
Horizontal coverage	14 CONT11 stations (cf. appendix A on page 134)
Temporal resolution	6-hourly at 00:00, 06:00, 12:00 and 18:00 UTC each day of the two weeks of CONT11 (= 64 epochs)
Elevations per point	7 ( $3^\circ$ , $5^\circ$ , $7^\circ$ , $10^\circ$ , $15^\circ$ , $30^\circ$ and $70^\circ$ )
Azimuths per point	16 ( $0^\circ:22.5^\circ:337.5^\circ$ )

of which the gradients are calculated, are available only six-hourly which means that they would need to be interpolated anyway for this purpose what would be accompanied by a comparable loss in accuracy. Apart from that, even if neglecting the previous fact, this would require too much calculation time<sup>1</sup>.

Initially, a priori gradients are calculated and tested for the VLBI campaign CONT11, what allows first estimations of the performance (Section 5.1.1). At a later stage this is done for the whole range of VLBI measurements from 2006 through 2014, from which final conclusions can be drawn (Section 5.1.2).

### 5.1.1. Determination of horizontal gradients for the time period of CONT11

For the time period of CONT11, ray-traced delays were computed with the ray-tracing program *RADIATE* using the ray-tracing standard approach (see Table A.4 in the appendix on page 139) for the specifications listed in Table 5.1 that serve as the basis for the subsequent calculation of the horizontal gradients. The difference to the gradients which later will be determined for the nine years of 2006 and 2014 is the substantially higher NWM resolution.

#### 5.1.1.1. Determining gradients using the standard gradient formula

In a first step, the ray-traced slant delays  $\Delta L$  of all 16 azimuths are averaged for each elevation and station, in order to simulate an azimuthally isotropic signal. Likewise, there would be the possibility to calculate the median instead of the mean, what would in theory mitigate the influence of potential extreme values. However, as extreme values are

<sup>1</sup>for the same two reasons, mapping function coefficients are determined at the NWM epochs as well

rather attributable to certain weather phenomena than to flaws in their calculation it is crucial for them to be considered in the determination of horizontal gradients, therefore the median is not utilized. By subtraction of the averaged values from the actual delays at each azimuth, only the asymmetric parts of the delays  $\Delta L_{res}(\alpha, \varepsilon)$  remain. This changes Eq. (2.9) to:

$$\Delta L_{res}(\alpha, \varepsilon) = m f_g(\varepsilon) \cdot [G_n \cdot \cos(\alpha) + G_e \cdot \sin(\alpha)] \quad (5.1)$$

As the left side of the equation is known from ray-tracing, the unknowns  $G_n$  and  $G_e$  can be determined through a least-squares adjustment using partial derivatives. Following *Niemeier*, [2008], the gradients are calculated through:

$$\begin{bmatrix} G_n \\ G_e \end{bmatrix} = \hat{x} = (A^T A)^{-1} A^T l \quad (5.2)$$

where  $A$  is the design matrix, composed of the partial derivatives with respect to  $G_n$  and  $G_e$  and  $l$  is a vector containing all observations. The design matrix is constructed for each station as follows:

$$A = \begin{bmatrix} \frac{\partial \Delta L_{res}(\alpha_1, \varepsilon_1)}{\partial G_n} & \frac{\partial \Delta L_{res}(\alpha_1, \varepsilon_1)}{\partial G_e} \\ \frac{\partial \Delta L_{res}(\alpha_2, \varepsilon_1)}{\partial G_n} & \frac{\partial \Delta L_{res}(\alpha_2, \varepsilon_1)}{\partial G_e} \\ \frac{\partial \Delta L_{res}(\alpha_3, \varepsilon_1)}{\partial G_n} & \frac{\partial \Delta L_{res}(\alpha_3, \varepsilon_1)}{\partial G_e} \\ \vdots & \vdots \\ \frac{\partial \Delta L_{res}(\alpha_1, \varepsilon_2)}{\partial G_n} & \frac{\partial \Delta L_{res}(\alpha_1, \varepsilon_2)}{\partial G_e} \\ \frac{\partial \Delta L_{res}(\alpha_2, \varepsilon_2)}{\partial G_n} & \frac{\partial \Delta L_{res}(\alpha_2, \varepsilon_2)}{\partial G_e} \\ \vdots & \vdots \\ \frac{\partial \Delta L_{res}(\alpha_{16}, \varepsilon_7)}{\partial G_n} & \frac{\partial \Delta L_{res}(\alpha_{16}, \varepsilon_7)}{\partial G_e} \end{bmatrix} \quad (5.3)$$

what results in 112x2 entries, while the appropriate observation vector  $l$  contains the delay residuals (the anisotropic parts of the delays) for each azimuth and elevation per station and epoch in the same order as in  $A$ :

$$l = \begin{bmatrix} \Delta L_{res}(\alpha_1, \varepsilon_1) \\ \Delta L_{res}(\alpha_2, \varepsilon_1) \\ \Delta L_{res}(\alpha_3, \varepsilon_1) \\ \vdots \\ \Delta L_{res}(\alpha_1, \varepsilon_2) \\ \Delta L_{res}(\alpha_2, \varepsilon_2) \\ \vdots \\ \Delta L_{res}(\alpha_{16}, \varepsilon_7) \end{bmatrix} \quad (5.4)$$

By means of Eq. (5.2), the horizontal north and east gradients for all 14 CONT11 stations at each of the 64 epochs can be determined. That is, one set of gradients  $G_{n_h}$ ,  $G_{n_w}$ ,  $G_{e_h}$

and  $G_{e_w}$  for each station and each epoch. As already explained in Section 2.2, the higher the latitude of the station, the lower the north gradient  $G_n$  of this station is expected to be, and vice versa.

In order to be able to assess the quality of the calculated gradients, standard deviations for the gradients need to be determined. For this purpose the system residuals  $v$  of the adjustment are calculated by:

$$v = A \cdot x - l \quad (5.5)$$

and the cofactor matrix  $Q_{xx}$ , which is the inverse of the normal equation matrix  $N$ , through:

$$Q_{xx} = N^{-1} = (A^T A)^{-1} \quad (5.6)$$

what eventually allows the determination of the standard deviations  $\sigma_{G_n}$  and  $\sigma_{G_e}$ :

$$\begin{aligned} \sigma_{G_n} &= \sqrt{Q_{xx(1,1)}} \cdot \sqrt{\frac{v^T \cdot v}{n_f}} \\ \sigma_{G_e} &= \sqrt{Q_{xx(2,2)}} \cdot \sqrt{\frac{v^T \cdot v}{n_f}} \end{aligned} \quad (5.7)$$

where  $Q_{xx(i,j)}$  is the respective entry in the primary diagonal of the cofactor matrix and  $n_f$  is the degree of freedom  $n_f = n - u$ , with  $n$  being the number of observations and  $u$  being the number of unknowns (here:  $n = 112$ ,  $u = 2$ ).

Figs. 5.1 and 5.2 show comparisons of the north and east gradients for VLBI station WETTZELL. There is a distinction made between total and separated gradients; total gradients  $G_n$  and  $G_e$  are used directly for total delays while for separated gradients it is discriminated between hydrostatic gradients  $G_{n_h}$  and  $G_{e_h}$  and wet gradients  $G_{n_w}$  and  $G_{e_w}$ , which are then usually added together. As already mentioned in Section 2.2, this becomes visible in the gradient mapping function coefficient  $C$  in Eq. (2.11). For total gradients, the total coefficient  $C = 0.0032$  is applied and for separated gradients the hydrostatic and wet coefficients  $C_h = 0.0031$  and  $C_w = 0.0007$ . Averaged over all 14 CONT11 stations, mean absolute north and east gradients are systematically smaller when separated into a hydrostatic and wet part, being 0.38 mm on average for  $G_n$  (over 0.52 mm for the total approach) and 0.26 mm on average for  $G_e$  (over 0.39 mm for the total approach), respectively, as visible in Fig. 5.1 for station WETTZELL. The mean standard deviation is also slightly smaller for the separated approach (0.19 mm < 0.24 mm).

As already mentioned before, elevations below  $3^\circ$  are usually not considered in troposphere modeling as they cause several problems in the models. As a result, there are only few VLBI measurements made at or below these small elevation angles. In the following, it is tested to which extent the standard deviations of the resulting horizontal gradients are affected if ray-traced delays at  $1^\circ$  and  $2^\circ$  are considered additionally. As shown in Fig. 5.2 exemplarily for station WETTZELL, mean absolute total north and east gradients get systematically larger when adding the elevations  $1^\circ$  and  $2^\circ$ : 0.69 mm > 0.52 mm for

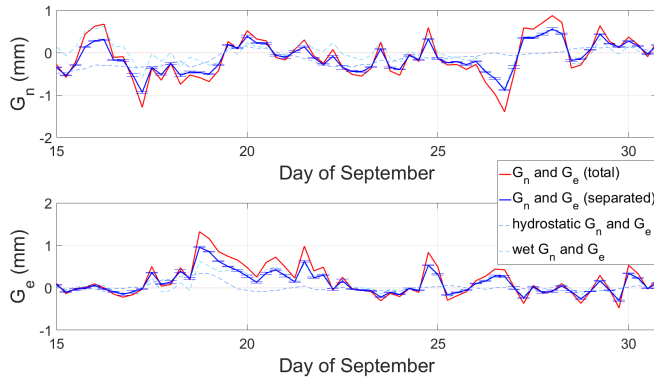


Figure 5.1.: Comparison of horizontal north (top) and east (bottom) gradients for VLBI station WETTZELL derived by using total slant delays (red line) and separated slant delays (blue line) during CONT11. The dashed lines represent the hydrostatic and wet parts of the gradients from the separated approach. Additionally, there are errorbars for the standard deviations (for better visibility only plotted for the separated approach).

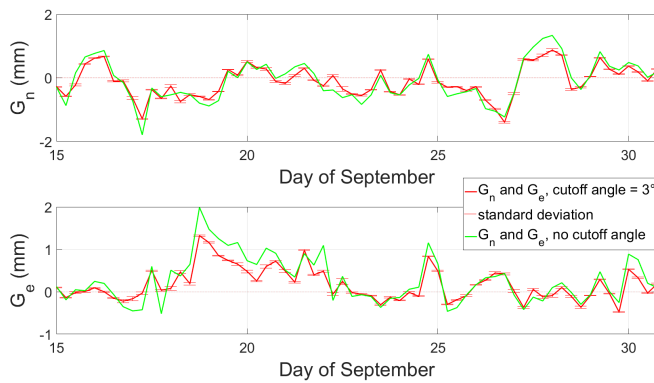


Figure 5.2.: Comparison of horizontal north (top) and east (bottom) gradients derived by using slant total delays for the standard elevation angles [ $3^\circ$ ,  $5^\circ$ ,  $7^\circ$ ,  $10^\circ$ ,  $15^\circ$ ,  $30^\circ$ ,  $70^\circ$ ] (red line) and for additionally adding the elevation angles [ $1^\circ$ ,  $2^\circ$ ] (green line) for VLBI station WETTZELL (Wetzell, Bavaria, Germany) during CONT11.

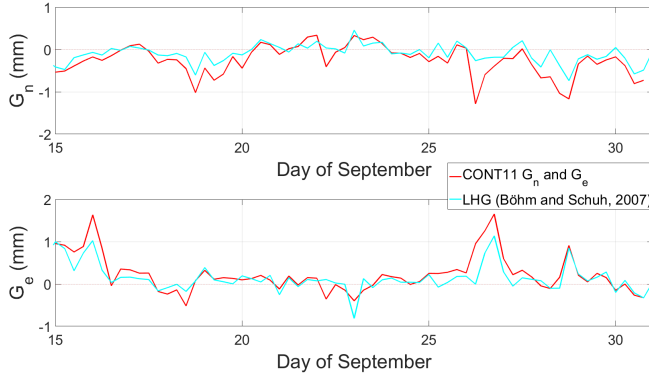


Figure 5.3.: Comparison of horizontal total north (top) and east (bottom) gradients from ray-tracing (red line) to the LHG by Böhm and Schuh [2007a] (cyan line) for VLBI station NYALES20 (Ny Alesund, Svalbard, Norway) during CONT11.

$G_n$  and  $0.54 \text{ mm} > 0.39 \text{ mm}$  for  $G_e$ , respectively, averaged over all 14 CONT11 stations. Moreover, it is notable that the mean standard deviation gets almost twice as large in this way ( $0.43 \text{ mm}$  over  $0.24 \text{ mm}$ ). A possible reason may be that the performance of ray-tracing is very limited at such low elevations as the assumption of a certain number of pressure levels might be too simple. As a consequence, the lower boundary for considered elevations remains at  $3^\circ$ .

Up to this point this chapter proved that the separated approach and a cut-off angle of  $3^\circ$  are sensible approaches in order ensure highest possible accuracy, consequently they are assumed for all further research. In order to assess the general performance of the new horizontal gradients, they are first compared to the Linear Horizontal Gradients (LHG) from Böhm and Schuh [2007a], who calculated both hydrostatic and wet  $G_n$  and  $G_e$  for all geodetic VLBI stations on Earth at four epochs per day since 2006 (Fig. 5.3). Unlike the approach explained in this chapter so far, they did not use ray-tracing to manage this but calculated the gradients directly from NWM data of the ECMWF. The long-time pattern in Fig. 5.3 is obviously very similar although the LHG are generally smaller in size, as proven by absolute values averaged over all 14 CONT11 stations:  $0.33 \text{ mm} < 0.52 \text{ mm}$  for  $G_n$  and  $0.28 \text{ mm} < 0.39 \text{ mm}$  for  $G_e$ . Additionally, this plot reveals that due to the high latitude of the VLBI station in Ny Alesund on Svalbard ( $78^\circ 55' 48'' \text{ N}$ ) the north gradients are predominantly negative because of the larger atmospheric height towards south.

### 5.1.1.2. Determining gradients using extended gradient formulae

In the standard gradient formula Eq. (2.9) by Chen and Herring [1997], the part  $G_n \cdot \cos(\alpha)$  determines the azimuthal asymmetry in north-south direction whereas  $G_e \cdot \sin(\alpha)$  determines the azimuthal asymmetry in east-west direction. Thus two extrema in the asymmetric delay residuals can be modeled, one positive and one negative. Due to the simple sinusoidal structure of the model, a shortcoming is that a maximum in any azimuthal direction is always accompanied by a minimum of opposite sign in an angular distance of  $180^\circ$  ( $\pi$ ). This may represent systematic effects like the atmospheric bulge quite well, but random effects such as weather fronts or variable atmosphere heights due to local



temperature differences set limits in such a way that the consequent extremum does not have a counterpart in the opposite direction. As an attempt to overcome this problem the standard gradient formula Eq. (2.9) was extended by higher order terms based on spherical harmonics. In geometrical respect, extended gradient variables are intended to model more delay extrema than the two from the standard gradient formula. In fact, two new gradient formulae<sup>2</sup> were studied (Eqs. (5.8) and (5.9)) [Landskron *et al.*, 2015b]:

$$\begin{aligned} \Delta L(\alpha, \varepsilon) = \Delta L_0(\varepsilon) + m f_g(\varepsilon) \cdot [G_n \cdot \cos(\alpha) + G_e \cdot \sin(\alpha) \\ + G_{n_2} \cdot \cos(2a) + G_{e_2} \cdot \sin(2a)] \end{aligned} \quad (5.8)$$

and

$$\begin{aligned} \Delta L(\alpha, \varepsilon) = \Delta L_0(\varepsilon) + m f_g(\varepsilon) \cdot [G_n \cdot \cos(\alpha) + G_e \cdot \sin(\alpha) \\ + G_{n_2} \cdot \cos(2a) + G_{e_2} \cdot \sin(2a) + G_{n_3} \cdot \cos(3a) + G_{e_3} \cdot \sin(3a)] \end{aligned} \quad (5.9)$$

By means of the extended gradient variables  $G_{n_2}$ ,  $G_{e_2}$ ,  $G_{n_3}$  and  $G_{e_3}$  the azimuthal asymmetry is thought to be described more precisely. They can be calculated analogously to  $G_n$  and  $G_e$  by means of simply extending the design matrix  $A$  from Eq. (5.3), what is shown in Eq. (5.10) for the second gradient formula Eq. (5.8). The residuals  $\Delta L_{res}(\alpha, \varepsilon)$  are again determined by subtracting the term  $\Delta L_0(\varepsilon)$  from Eqs. (5.8) and (5.9).

$$A = \begin{bmatrix} \frac{\partial \Delta L_{res}(\alpha_1, \varepsilon_1)}{\partial G_n} & \frac{\partial \Delta L_{res}(\alpha_1, \varepsilon_1)}{\partial G_e} & \frac{\partial \Delta L_{res}(\alpha_1, \varepsilon_1)}{\partial G_{n_2}} & \frac{\partial \Delta L_{res}(\alpha_1, \varepsilon_1)}{\partial G_{e_2}} \\ \frac{\partial \Delta L_{res}(\alpha_2, \varepsilon_1)}{\partial G_n} & \frac{\partial \Delta L_{res}(\alpha_2, \varepsilon_1)}{\partial G_e} & \frac{\partial \Delta L_{res}(\alpha_2, \varepsilon_1)}{\partial G_{n_2}} & \frac{\partial \Delta L_{res}(\alpha_2, \varepsilon_1)}{\partial G_{e_2}} \\ \frac{\partial \Delta L_{res}(\alpha_3, \varepsilon_1)}{\partial G_n} & \frac{\partial \Delta L_{res}(\alpha_3, \varepsilon_1)}{\partial G_e} & \frac{\partial \Delta L_{res}(\alpha_3, \varepsilon_1)}{\partial G_{n_2}} & \frac{\partial \Delta L_{res}(\alpha_3, \varepsilon_1)}{\partial G_{e_2}} \\ \vdots & \vdots & \vdots & \vdots \\ \frac{\partial \Delta L_{res}(\alpha_1, \varepsilon_2)}{\partial G_n} & \frac{\partial \Delta L_{res}(\alpha_1, \varepsilon_2)}{\partial G_e} & \frac{\partial \Delta L_{res}(\alpha_1, \varepsilon_2)}{\partial G_{n_2}} & \frac{\partial \Delta L_{res}(\alpha_1, \varepsilon_2)}{\partial G_{e_2}} \\ \frac{\partial \Delta L_{res}(\alpha_2, \varepsilon_2)}{\partial G_n} & \frac{\partial \Delta L_{res}(\alpha_2, \varepsilon_2)}{\partial G_e} & \frac{\partial \Delta L_{res}(\alpha_2, \varepsilon_2)}{\partial G_{n_2}} & \frac{\partial \Delta L_{res}(\alpha_2, \varepsilon_2)}{\partial G_{e_2}} \\ \vdots & \vdots & \vdots & \vdots \\ \frac{\partial \Delta L_{res}(\alpha_{16}, \varepsilon_7)}{\partial G_n} & \frac{\partial \Delta L_{res}(\alpha_{16}, \varepsilon_7)}{\partial G_e} & \frac{\partial \Delta L_{res}(\alpha_{16}, \varepsilon_7)}{\partial G_{n_2}} & \frac{\partial \Delta L_{res}(\alpha_{16}, \varepsilon_7)}{\partial G_{e_2}} \end{bmatrix} \quad (5.10)$$

The observation vector from Eq. (5.4) remains unchanged. From this follows that the solution vector can be set up as:

$$\begin{bmatrix} G_n \\ G_e \\ G_{n_2} \\ G_{e_2} \end{bmatrix} = \hat{x} = (A^T A)^{-1} A^T l \quad (5.11)$$

Obviously, the extended gradient variables are determined for the same specifications from Table 4.3 on page 70 as the standard gradient variables  $G_n$  and  $G_e$  in the previous Section 5.1.1.1. Owing to the sufficient over-determination resulting from the high number of

<sup>2</sup>henceforth also referred to as "second gradient formula" and "third gradient formula"

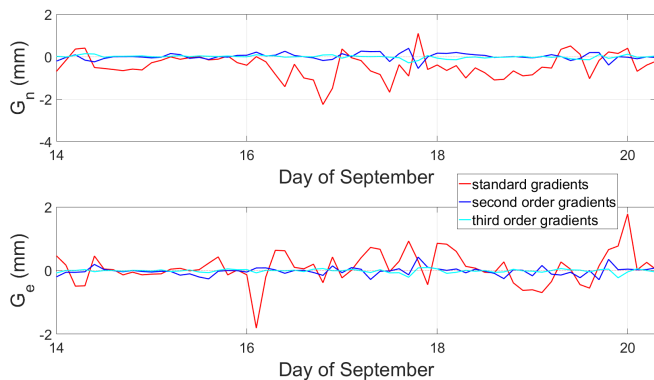


Figure 5.4.: *Comparison of the various gradients for station WESTFORD (Westford, Massachusetts, USA) for the time period of CONT11.*

ray-traced delays per station, the resulting values for  $G_n$  and  $G_e$  are equivalent no matter if they are estimated from the standard gradient formula, the second gradient formula or from the third gradient formula. Thus, the extended gradient variables can be regarded just as additional refinements to the standard gradients  $G_n$  and  $G_e$ .

The new horizontal gradients are henceforth referred to as GRAD; GRAD-1 means those from the standard gradient formula, GRAD-2 those from the second gradient formula, while GRAD-3 analogously refers to those from the third gradient formula. In general,  $G_n$  and  $G_e$  are considerably larger in size than  $G_{n_2}$ ,  $G_{e_2}$ , which in turn are larger than  $G_{n_3}$  and  $G_{e_3}$  (Fig. 5.4). The capability of a certain gradient approach to describe the azimuthal asymmetry can be assessed by determination of the residuals between the ray-traced delays and the modeled delays. Figure 5.5 shows this exemplarily for VLBI station WESTFORD at a single epoch.

Calculating and averaging these residuals in the slant total delays for all 14 CONT11 stations and for the whole 15 days of CONT11 shows that they decrease by 69% when using the standard gradient formula Eq. (2.9) (GRAD-1), by 78% when using the second gradient formula Eq. (5.8) (GRAD-2) and by 81% when using the third gradient formula Eq. (5.9) (GRAD-3). In other words, two-thirds of the azimuthal asymmetry can be described by using the standard gradient formula and even more when using extended gradient formulae. This is a first clear indicator that the extended gradient formulae are indeed capable of describing azimuthal asymmetry more precisely. The two plots in Fig. 5.6 illustrate this. On the one hand azimuthal asymmetry is most pronounced in north and south direction, what is a result of the systematic effect of the atmospheric bulge. Nevertheless, the three gradient formulae model these residuals very well, while the performance in east and west direction is somewhat poorer. On the other hand, even more importantly, it is evident that the extended gradient formulae are able to model the residuals more closely than the standard gradient formula by *Chen and Herring* [1997] does. In particular, there is a significant increase in accuracy when using GRAD-2 instead of GRAD-1.

To summarize, the preceding figures and numbers prove the vital necessity of considering azimuthal asymmetry in general, and, on the other hand, it points out the clear benefit

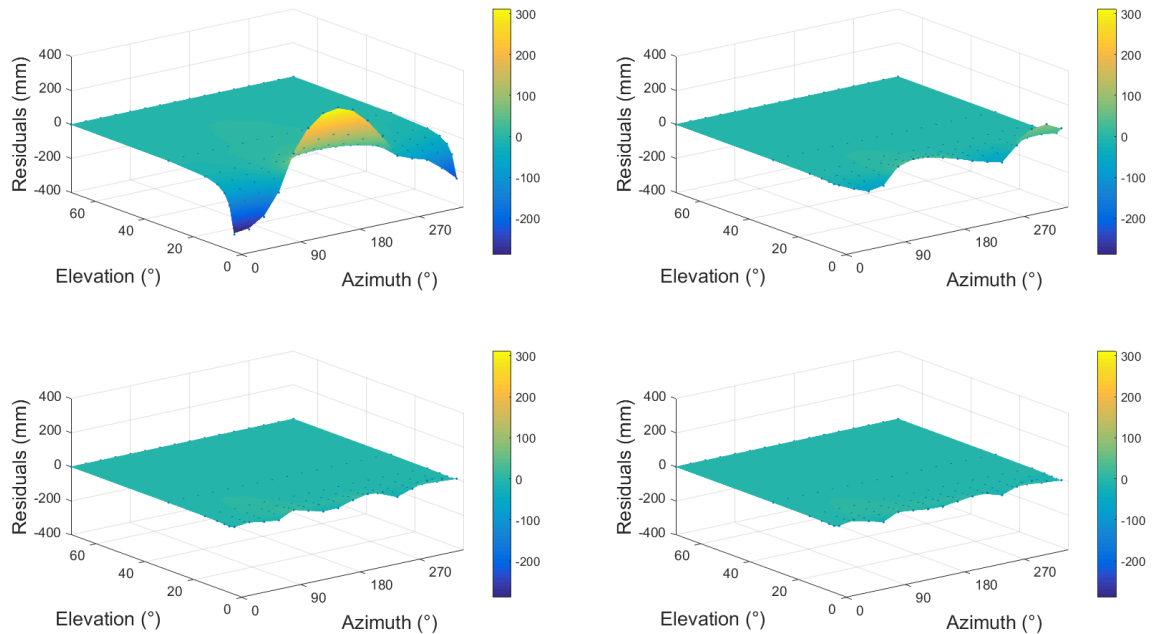


Figure 5.5.: Comparison of the residuals in slant total delays for station WESTFORD (Westford, Massachusetts, USA) for the epoch September 26, 2011, 18:00 GMT [Land-skron et al., 2015b]. Top left: residuals after subtraction of a mean over the 16 constantly distributed azimuths without applying any gradient formula; simply put, the yellow and blue amplitudes show the presence of azimuthal asymmetry, and it is obvious that its influence is highest for low-elevation observations. The high residuals in north ( $0^\circ$  azimuth) and south ( $180^\circ$  azimuth) direction are mainly a result of the high latitude location of the site and the consequent effect of the atmospheric bulge. Top right: residuals after applying gradients by using the standard gradient formula (GRAD-1); this lowers the residuals significantly, what means that thus the bulk of azimuthal asymmetry is explained. However, small amplitudes between the cardinal points remain. Bottom left: residuals after applying gradients by using the second gradient formula (GRAD-2); again, the residuals are lowered considerably, also the amplitudes between the cardinal directions almost vanish. Bottom right: residuals after applying gradients by using the third gradient formula (GRAD-3); the residuals hardly change compared to the second gradient formula.

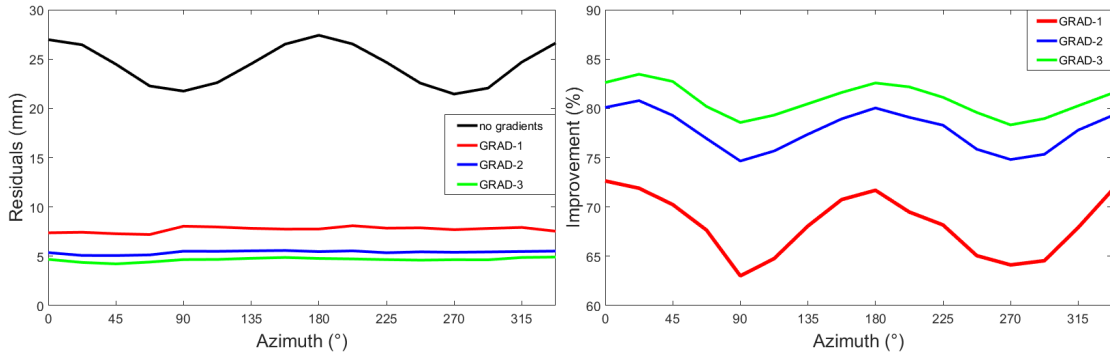


Figure 5.6.: Comparison of mean absolute residuals that arise from azimuthal asymmetry averaged over all stations and epochs of CONT11. Left: comparison of the residuals for the different gradient models. Right: the percental improvement of the gradient models w.r.t. no consideration of azimuthal asymmetry.

of the extended gradient formulae which prove to be a notable tool to model azimuthal asymmetry more precisely. These comparisons however represent only theoretical benefits; through VLBI analyses which make use of these new gradients and assessment of their performance by means of comparisons of BLR, conclusions about absolute benefits of the new gradients can be drawn, as the subsequent Section 5.1.1.3 addresses.

### 5.1.1.3. Estimating gradients in VLBI analysis

In the preceding section, horizontal gradients  $G_n$  and  $G_e$  and extended gradient variables  $G_{n_2}$ ,  $G_{e_2}$ ,  $G_{n_3}$  and  $G_{e_3}$  were calculated from ray-traced delays for the time period of CONT11. These can then be used as a priori values in a VLBI analysis. Within a VLBI analysis using the VLBI software *VieVS* there is the possibility to estimate a number of quantities in a least-squares adjustment such as zenith wet delay ( $\Delta L_w^z$ ), polar motion ( $x_{pol}$ ,  $y_{pol}$ ),  $dUT1^3$ , source coordinates (right ascension  $\alpha$ , declination  $\delta$ ), antenna coordinates ( $X$ ,  $Y$ ,  $Z$ ), clock parameters and also the very horizontal gradients  $G_n$  and  $G_e$ , as is the case with *VieVS* [Böhm *et al.*, 2012]. This is done since the estimated parameter values are thought to have highest possible precision as a consequence of the sufficient over-determination owing to the high number of observations. Important in case of the actual chapter is the estimation of  $G_n$  and  $G_e$  what is common practice in VLBI analysis and can be done regardless of whether a priori gradients are used or not. According to MacMillan [1995], estimation of gradients can improve baseline length repeatabilities by up to 8 mm. *VieVS* adopts the standard gradient formula of Chen and Herring [1997]

<sup>3</sup> $dUT1 = UT1 - UTC$ ; that is the Earth's rotation minus the atomic time, what corresponds to the irregularities of the Earth's rotation

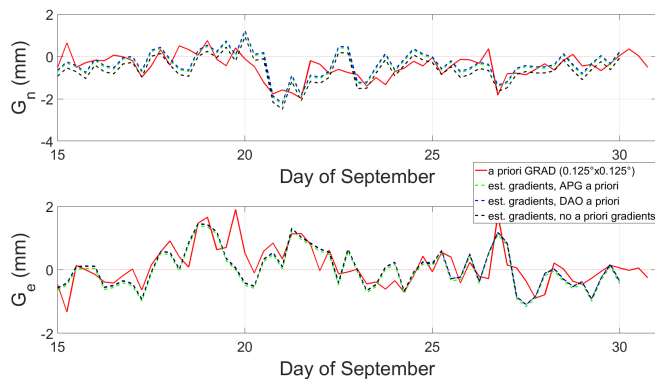


Figure 5.7.: Comparison of the horizontal north (top) and east (bottom) gradients from ray-traced delays (red line) and from estimation in VLBI analysis using *VieVS* for all three a priori gradient approaches (dotted green, cyan and blue line) for VLBI station *ONSALA60* (Onsala, Sweden) during *CONT11*.

(Eq. (2.9))<sup>4</sup> for the estimation. *Teke et al.* [2008] made detailed investigations concerning gradients estimated in *VieVS* together with gradients from many other sources for the time period of *CONT08* (August 12, 2008 to August 26, 2008). In the following, the question is approached whether it makes sense for VLBI analysis to apply a priori gradients in addition to the anyway performed gradient estimation.

In *VieVS*, there is only the possibility to choose either between the usage of two types of empirical a priori gradients, or no a priori gradients (for fundamentals of empirical gradients see Section 5.2):

1. using the empirical a priori gradient model APG [*Böhm et al.*, 2013b], which has been determined by ray-tracing through monthly mean pressure level re-analysis data of the ECMWF
2. using the empirical a priori gradient model from the Data Assimilation Office (DAO) [*MacMillan and Ma*, 1997] which has been determined by vertical integration over horizontal refractivity gradients
3. using no a priori gradients

The gradients for all three approaches were estimated and plotted together with the solution derived from ray-traced delays as described in the preceding Section (Fig. 5.7). Here it can be seen that the general pattern of the lines is very similar which approves the good quality of the new gradients. However, mean absolute values of the gradients estimated in the VLBI analysis are somewhat larger in size than the calculated ones: 0.63 mm vs. 0.52 mm for  $G_n$  and 0.53 vs. 0.39 mm for  $G_e$ . The lines for the three VLBI analysis approaches almost coincide for the east gradient but differ slightly but visibly for the north gradient

<sup>4</sup>there was extensive research done for whether the azimuthally asymmetric part can be described in more detail by directly using the extended gradient formulae (Eqs. 5.8 and 5.9) for gradient estimation in the VLBI analysis instead. This means that values for the gradient variables  $G_{n_2}$  and  $G_{e_2}$  and also  $G_{n_3}$  and  $G_{e_3}$ , respectively, are determined within the least-squares adjustment in addition to the standardly estimated parameters. Contrary to the expectations, this slightly impaired the results, though. The reason is most likely that the number of parameters to be determined in the least-squares adjustment is already at the maximum considering the limited number of observations so that additional parameters negatively affect the overall accuracy

Table 5.2.: From Landskron et al. [2015b]: Mean BLR (cm) from VLBI analyses considering several kinds of a priori gradients for the time period of CONT11. In column (1), only a priori gradients are used, while in column (2) the gradients are additionally estimated in the VLBI analysis using the standard gradient formula.

GRADIENT MODEL	(1) (cm)	(2) (cm)
(a) no a priori gradients	1.20	1.07
(b) LHG	1.14	1.06
(c) GRAD-1	1.10	1.06
(d) GRAD-2	1.09	1.03
(e) GRAD-3	1.09	1.04
(f) APG	1.20	1.07
(g) DAO	1.20	1.07

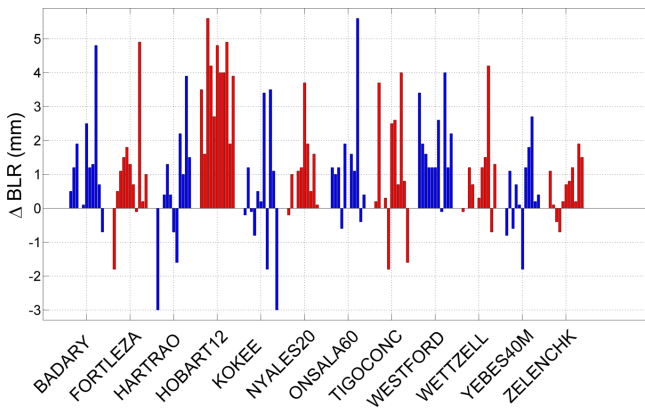


Figure 5.8.: Station-wise improvement in BLR from VLBI analyses when using GRAD-2 instead of using no a priori gradients for the time period of CONT11. Referring to Table 5.2 this corresponds to the use of approach 1.d instead of 1.a. All bars above zero imply improved repeatability of the respective baselines for GRAD-2.

in case of this VLBI station. These differences stem from the fact that due the fairly high latitude of ONSALA60 ( $57^{\circ} 24' N$ ) the azimuthal isotropy owing to the atmospheric bulge is very distinctive; this systematic effect is captured in APG and DAO, what in further consequence slightly improves the estimated gradients.

In order to assess the general quality of the new gradients GRAD, VLBI analyses were performed for a variety of other a priori gradients and the resulting BLR were compared to each other. For each of the scenarios enumerated in Table 5.2, there were two VLBI analyses (using the *VieVS* standard approach, see Table A.3 in the appendix on page 138) done for the time period of CONT11: (1) only introducing the a priori gradients, (2) additionally estimating gradients in the analysis using the standard gradient formula of *Chen and Herring* [1997]. In addition to GRAD and the empirical a priori gradients, also the Linear Horizontal Gradients (LHG) by *Böhm and Schuh* [2007a] were added to the comparison. Close inspection of the baselines which cause the large increase in accuracy from approach 1.d over 1.a yields Fig. 5.8.

Table 5.2 and Fig. 5.8 allow to draw several conclusions:

- In general, an estimation of gradients in the VLBI analysis is imperative for best possible quality. This was already shown in the paper by *Böhm and Schuh* [2007a].
- Consideration of a priori gradients has the potential to significantly improve the results.
- The new gradients GRAD-1 yield a significant improvement in BLR over LHG, in addition, a further improvement can be reached through the second gradient formula (GRAD-2), for both cases (1) and (2).
- Considering the lacking ability to further improve the results, the third gradient formula (Eq. (5.9)) will be neglected.
- The usage of empirical a priori gradients does not seem to have any influence.

Table 5.2 and its conclusions reveal that a priori gradients are an important factor for attaining highest possible accuracy in VLBI and that there is vital necessity to make further research in a priori gradients. Comparing these results with those of Fig. 5.5 and Fig. 5.6 generally shows accordance. As already mentioned at an earlier stage, consideration of azimuthal asymmetry only marginally influences observations above  $15^\circ$  elevation, which, however, make up the majority of VLBI observations. For this reason, the achieved improvement is not larger still. For the upcoming Section 5.1.2, where a priori gradients are determined and tested for the nine years of VLBI data, the approach GRAD-3 is neglected as it is not capable of improving the results in any way.

### 5.1.2. Determination of horizontal gradients for nine years of VLBI data

As the findings of the previous Section 5.1.1 are very promising, the next step was to determine gradients for a longer time period than the two-week CONT11 campaign, namely for all VLBI observations from 2006 through 2014<sup>5</sup>. However, this was not as easy as it may sound because generating ray-traced delays for such a long time span requires a significant amount of calculation time. Only after the programming of the ray-tracer *RADIATE* was converted from *MATLAB* to *Fortran*, the associated improvement in calculation speed allowed for generation of this vast amount of ray-traced delays. As even then the calculation time would have been too long for using the same ray-tracing specifications as in Table 4.3 on page 70, some more reductions were necessary. On the one hand, the NWM resolution had to be reduced; on the other hand, ray-traced delays were only generated 5 epochs before and after a measurement of a certain station, as this is the minimum number of observations which is required for the subsequent spline interpolation. Table 5.3 shows all properties of the ray-traced delays, which were also used for the determination of mapping

<sup>5</sup>as already mentioned in Chapter 4.5.1, intensive sessions are not considered here as they contain only few measurements between two or three stations at maximum. In common VLBI practice there is usually no gradient estimation done for intensive sessions for the same reason either

Table 5.3.: *Properties of the ray-traced delays that were generated using the ray-tracer RADIATE from 2006-2014, in addition to the ray-tracing standard approach (see Table A.4 on page 139).*

PARAMETER	SPECIFICATION
Ray-tracing software	<i>RADIATE</i> [Hofmeister, 2016]; 2D ray-tracer
NWM	ECMWF ERA Interim Pressure Level Data + ECMWF operational data
Horizontal resolution of the NWM	$1^\circ \times 1^\circ$
Horizontal coverage	all VLBI stations that made observations between 2006 and 2014
Temporal resolution	6-hourly at 00:00, 06:00, 12:00 and 18:00 UTC each day from 2006 through 2014 (= 13101 epochs)
Elevations per point	7 ( $3^\circ$ , $5^\circ$ , $7^\circ$ , $10^\circ$ , $15^\circ$ , $30^\circ$ and $70^\circ$ )
Azimuths per point	16 ( $0^\circ$ : $22.5^\circ$ : $337.5^\circ$ )

function coefficients but for a longer time period (cf. Table 4.11 on page 81).

Analogous to Sections 5.1.1.1 and 5.1.1.2, values for the gradient variables were determined in least-squares adjustments. The north and east gradients  $G_n$  and  $G_e$  as well as the extended gradient variables  $G_{n_2}$  and  $G_{e_2}$ <sup>6</sup> were determined following Eqs. (5.1) to (5.4) on page 93. Thus, gradient values were determined for every VLBI station at every relevant NWM epoch between 2006 and 2014. One can then determine the horizontal gradients (and, by implication, the azimuthal asymmetry caused by the current weather situation) of every single VLBI measurement of every VLBI station in this time period by means of spline interpolation.

The quality of the resulting gradients can be assessed by means of three comparisons: the upcoming Section 5.1.2.1 compares the resulting gradient values to others without giving any information about their quality yet. In the succeeding Section 5.1.2.2, VLBI analyses are performed and BLR are calculated for a variety of a priori gradients. Together with the results of the subsequent Section 5.1.3, where tropospheric delays are modeled using different gradient approaches and compared to ray-traced delays, it represents the final results in the research of azimuthal asymmetry of this thesis.

### 5.1.2.1. Comparison with other gradients

Before setting the focus on the total nine years of data a visual comparison is made between (1) the horizontal gradients derived in the previous Section 5.1.1 which are from now on

<sup>6</sup>strictly speaking, as a distinction is made each for the hydrostatic and the wet part, values for each  $G_{n_h}$ ,  $G_{e_h}$ ,  $G_{n_w}$ ,  $G_{e_w}$ ,  $G_{n_{2h}}$ ,  $G_{e_{2h}}$ ,  $G_{n_{2w}}$  and  $G_{e_{2w}}$  were calculated



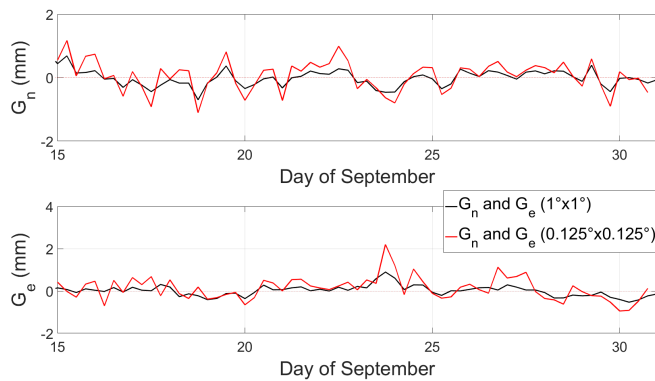


Figure 5.9.: Comparison of horizontal north (top) and east (bottom) gradients between the gradients calculated on the basis of  $0.125^\circ \times 0.125^\circ$  NWM (red line) and those calculated on the basis of  $1^\circ \times 1^\circ$  NWM (black line) for VLBI station YEBES40M (Yebe, Spain) during CONT11.

referred to as GRAD ( $0.125^\circ \times 0.125^\circ$ ) and (2) the gradients GRAD determined in this section from the  $1^\circ \times 1^\circ$  resolved NWM. When limiting the time frame to CONT11, the different spatial resolution is the only difference inherent in the gradients<sup>7</sup>.

Fig. 5.9 reveals that the gradients which were determined with the higher-resolved NWM show higher fluctuations, both in negative and positive range. Indeed, when averaging the calculated gradients for all 14 CONT11 stations, it turns out that mean absolute values of the gradients from the higher-resolved NWM are significantly higher:  $0.52 \text{ mm} > 0.33 \text{ mm}$  for  $G_n$  and  $0.39 > 0.22 \text{ mm}$  for  $G_e$ . However, the bias between the two of them is approximately zero, what means that only the amplitudes are higher. At this stage, no conclusions can be made as to which of those gradients are more accurate or higher in quality; the upcoming Section 5.1.2.2 is about to address this question.

The LHG by *Böhm and Schuh* [2007a] are available from 2006 on, hence, they can be compared to the ones calculated in this chapter for the whole nine years of 2006 through 2014, too. This comparison, done for the same 14 CONT11 stations, indicates very similar behaviours of the both gradient datasets, while again no systematics could be detected. Section 5.1.2.2 deals with the quality of those gradients as well.

### 5.1.2.2. Comparison of BLR

After calculating the new horizontal gradients GRAD for all relevant NWM epochs of 2006 to 2014, they can be used as a priori gradients in a VLBI analysis using *VieVS*. First, this is done for the period of CONT11 only so that the BLR can be compared to that of the gradients GRAD ( $0.125^\circ \times 0.125^\circ$ ) which were calculated only for this time period, yielding Tab. 5.4. This reveals that in terms of gradient determination there is virtually no difference whether the gradients are calculated on the basis of NWM with  $1^\circ \times 1^\circ$  or

<sup>7</sup>in fact, there is also the difference that the gradients of case (1) were calculated with the *MATLAB* version of *RADIATE*, while those of case (2) were calculated with the *Fortran* version. However, the received results of those two versions are identical, given equal settings [*Hofmeister*, 2016]

<sup>8</sup>these results are different to those of Table 5.2 on page 102; the reason for this is that a different calculation strategy of *VieVS* was applied

Table 5.4.: Mean BLR (cm) from VLBI analyses considering several kinds of a priori gradients for the time period of CONT11. In column (1), only a priori gradients are used, while in column (2) the gradients are additionally estimated in the VLBI analysis using the standard gradient formula<sup>8</sup>.

GRADIENT MODEL	(1) (cm)	(2) (cm)
(a) no a priori gradients	1.18	0.98
(b) LHG	1.12	0.99
(c) GRAD-1	1.08	0.97
(d) GRAD-2	1.08	0.98
(c2) GRAD-1 ( $0.125^\circ \times 0.125^\circ$ )	1.08	0.97
(d2) GRAD-2 ( $0.125^\circ \times 0.125^\circ$ )	1.07	0.98

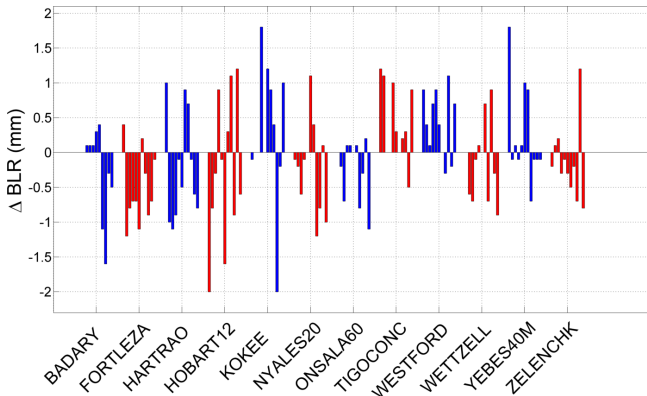


Figure 5.10.: Station-wise  $\Delta BLR$  from VLBI analyses when using GRAD ( $1^\circ \times 1^\circ$ ) instead of GRAD ( $0.125^\circ \times 0.125^\circ$ ) for the time period of CONT11. Referring to Table 5.2 this corresponds to the use of approach 1.c instead of 1.c2. All bars above zero imply improved repeatability of the respective baselines for the  $1^\circ \times 1^\circ$  version.

$0.125^\circ \times 0.125^\circ$  horizontal resolution. Figure 5.10 shows this in more detail for the individual baselines. From this, no conclusions can be drawn which version shall be preferred. Some stations perform better for the  $0.125^\circ \times 0.125^\circ$  version, such as FORTLEZA or HOBART12, however for other stations the situation is just the opposite (e.g. TIGOCONC, WESTFORD). In summary it can be said that no considerable loss of accuracy is to be expected when using the coarse-meshed NWM which helps saving a lot of calculation time (roughly 64-fold).

In order to get the most meaningful results, the nine years of data have to be analyzed. As for the comparison for the time period of CONT11, the new gradients GRAD can be used in a VLBI analysis as a priori gradients for the 1338 VLBI sessions from 2006 to 2014, what is thought to improve the BLR. The six-hourly available gradients are therefore interpolated to the very times of the VLBI observations through spline interpolations. The upcoming analysis is then performed with *VieVS* using the *VieVS* standard approach (see Table A.3 in the appendix on page 138). Important here is that if the gradients  $G_n$  and  $G_e$  are additionally estimated in the VLBI analysis, then this is done with the standard

Table 5.5.: Mean BLR (cm) from VLBI analyses for all 1338 sessions from 2006-2014. In column (1), only a priori gradients are used, while in column (2) the gradients are additionally estimated in the VLBI analysis.

GRADIENT MODEL	(1) (cm)	(2) (cm)
(a) no a priori gradients	1.68	1.65
(b) LHG	1.66	1.67
(c) GRAD-1	1.58	1.66
(d) GRAD-2	1.57	1.65
ray-traced delays	1.57	1.64

gradient formula by *Chen and Herring* [1997] (Eq. (2.11)) as piece-wise linear offsets every six hours using relative constraints of 0.05 cm. The upcoming findings refer to *Landskron et al.* [2016a], but with re-calculated numbers. For each of the several VLBI analyses, the standard approach is used. All baselines containing stations HARTRAO and TIGOCONC were excluded as they exhibit exceptionally high BLR. What is striking here is the substantial difference to the investigations for CONT11 (Table 5.4). Apparently the estimation of gradients in the VLBI analysis rather degrades than improves the results. The gradient estimation makes sense only when no a priori gradients are used; in all other cases, best results are attained when using sophisticated a priori gradient models without an additional estimation of the gradients in VLBI analysis. Then, GRAD-2 improves 43% of the BLR by more than 1 millimeter while it degrades only 5% by more than 1 millimeter<sup>9</sup> compared to the approach with no a priori gradients. In theory, for case (1) the most accurate results can be reached when using the ray-traced delays<sup>10</sup>, what is confirmed by the resulting BLR. It is very pleasant that with GRAD-2, which is actually only a model to approximate the ray-traced delays, equal performance can be achieved. This in turn means that with GRAD-2 already the maximum potential of improvement is reached, because the ray-traced delays are the absolute reference values which cannot be surpassed. What is also interesting is the fact that in case of ray-traced delays it is better not to estimate gradients, while in *Hofmeister* [2016] there was a very similar test done which did not come to this conclusion. However, Fig. 5.11 underlines the degradation in BLR when additionally estimating the gradients. There must be a unique reason why the gradient estimation in VLBI analysis yields worse BLR than without it; the obvious assumption is that the least-squares gradient estimation might not work so well for sessions with a lower number of observations. For CONT sessions this is no problem, as each of them contain a very high number of observations ( $\sim 5000$  for CONT08,  $\sim 4000$  for CONT11,  $\sim 7000$  for CONT14) from more than a dozen stations simultaneously, whereas the vast majority of

<sup>9</sup>the complementary 52% of the  $\Delta$ BLR are between -1 mm and +1 mm

<sup>10</sup>for case (2) this is not necessarily the case, as the parameter estimation in a least-squares adjustment is thought to be even more accurate

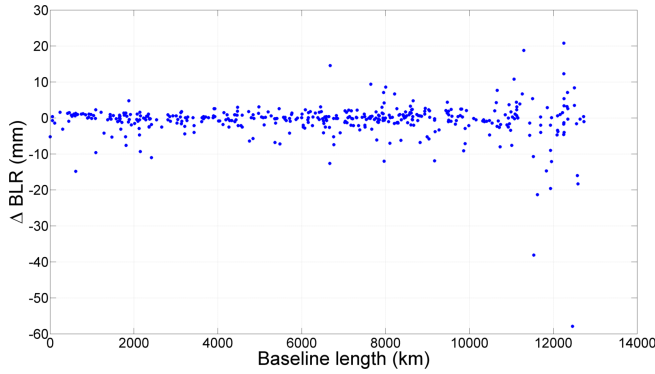


Figure 5.11.: *Station-wise  $\Delta$ BLR from VLBI analyses for ray-traced delays for all 1338 sessions from 2006-2014. Dots below zero indicate that BLR degrade when estimating gradients in the analysis.*

Table 5.6.: *Mean BLR (cm) from VLBI analyses for all those sessions from 2006-2014 that contain fewer than 3000 observations (1129 out of 1338 sessions, columns 1 and 2) and more than 3000 observations (209 out of 1338 sessions, columns 3 and 4). In (1), only a priori gradients are used, while in (2) the gradients are additionally estimated in the VLBI analysis. When having fewer than 3000 observations per session, using (1.d) instead of (1.a) improves 44% of the BLR by more than 1 mm while it degrades only 4% by more than 1 mm. On the other hand, when having more than 3000 observations per session, using (1.d) instead of (1.a) improves 41% of the BLR by more than 1 mm while it degrades only 9% by more than 1 mm.*

GRADIENT MODEL	<3000 observations		>3000 observations	
	(1) (cm)	(2) (cm)	(1) (cm)	(2) (cm)
(a) no a priori gradients	2.32	2.38	1.08	0.97
(b) LHG	2.32	2.36	1.06	1.04
(c) GRAD-1	2.21	2.39	1.00	0.99
(d) GRAD-2	2.19	2.37	1.01	0.98
ray-traced delays	2.18	2.33	1.01	0.99

”ordinary” VLBI sessions has only few stations participating and thus significantly fewer observations. To prove this assumption a maximum number of total observations per session has to be defined. This is done by means of various tests for observation intervals and comparing the resultant BLR, what eventually yields an appropriate boundary value of 3000 total observations per session, below which no additional gradient estimation shall be done. VLBI analyses are then carried out separately for all VLBI sessions that contain fewer than 3000 observations and for those that contain more than 3000 observations.

Table 5.6 unambiguously proves the assumption that the gradient estimation using a least-squares adjustment shall only be done for sessions that have more than 3000 stations in total. This is new as the commonly accepted opinion in VLBI analysis is to always estimate the gradients for any session. Following these new findings, the least-squares adjustment works properly and outputs well-fitting gradients only if there is a certain number of observations, and, in case of the boundary of the 3000 observations per session,

this applies to only 16% (209 out of 1338) of the VLBI sessions from 2006 to 2014. The boundary is quite easy to apply in VLBI analysis and ensure improved accuracy of the products. Apart from that, this comparison again proves that GRAD-2 facilitates best results which are as good as the ray-traced delays, while GRAD-1 is only marginally worse. In case of the third column in Table 5.6, the BLR of the modeled delays is even marginally better than that of the ray-traced delays what might seem peculiar at first glance, since the modeled delays are nothing but approximations of the ray-traced delays. However, this simply points out that the ray-traced delays are no perfect values either and the fact that the (even less perfect) modeled delays fit better in this case is pure coincidence.

Yet, there is still a shortcoming in the previous comparisons concerning a minimum number of observations per session, because it assumes the key factor to be only the total number of observations, regardless of the number of participating stations in the session. But, in fact, what is most important for the potential of the least-squares estimation of gradients in VLBI analysis is the number of observations *per station* per session<sup>11</sup>. As an example, the quality of the estimated gradients would be worse for a session *A* in which 16 participating stations made 3200 observations than for a session *B* that has 2000 observations from merely five participating stations, since the latter comprises more observations per station. The investigations concerning the minimum number of total observations per session of 3000 is therefore insufficient, as it would eliminate session *B* but allow session *A*. An appropriate solution would be to simply set a minimum number of observations *per station* per session that must be exceeded in order to qualify for additional gradient estimation, but this would be associated with a total restructuring of the estimation part of *VieVS*. Likewise, this criterion would not be easy to handle for users from other VLBI analysis software either. For this reason, its performance is not analyzed here. A compromise is to define a boundary value for observations per station and session averaged over all stations of the session. Thus the decision of estimating gradients or not can still be done for whole sessions. A minimum of 375 observations on average proved to be appropriate for this purpose. However, for the user it might still be easier to just use the boundary for total observations per session, then the previous investigation is of major interest. It is up to the user if easy handling or utmost accuracy is more important. Table 5.7 lists the BLR for the empirically obtained gradient estimation criterion of 375 observations per station on average.

Even though the differentiation between sessions that have 375 observations per station on average or less is more accurate, it remains easier to just set a boundary for the total observations in a session. Another possibility as presented in a publication by *Landskron et al.* [2016b] is to make the decision on the basis of the data size of the respective NGS-file in ASCII format. The results are fairly equal to those in Table 5.7 and the application is very easy to handle, but on a scientific basis it is not optimal because the data size of an

---

<sup>11</sup>strictly speaking, the geometry of the observed sources is also important for the estimation of gradients. The same is true for estimating zenith wet delays. For the estimation of EOP, however, also the geometry of the observing stations would be an additional critical factor

Table 5.7.: Mean BLR (cm) from VLBI analyses for all those sessions from 2006-2014 that contain fewer than 375 observations per station on average (1133 out of 1338 sessions, columns 1 and 2) and more than 375 observations per station on average (205 out of 1338 sessions, columns 3 and 4). In (1), only a priori gradients are used, while in (2) the gradients are additionally estimated in the VLBI analysis. When having fewer than 375 observations per station and session, using (1.d) instead of (1.a) improves 44% of the BLR by more than 1 mm while it degrades only 3% by more than 1 mm. On the other hand, when having more than 375 observations per station and session, using (1.d) instead of (1.a) improves 40% of the BLR by more than 1 mm while it degrades only 9% by more than 1 mm.

GRADIENT MODEL	<375 obs. per station		>375 obs. per station	
	(1) (cm)	(2) (cm)	(1) (cm)	(2) (cm)
(a) no a priori gradients	1.77	1.76	1.06	0.98
(b) LHG	1.74	1.66	1.04	0.99
(c) GRAD-1	1.66	1.76	0.98	0.98
(d) GRAD-2	1.65	1.76	0.99	0.98
ray-traced delays	1.65	1.74	1.00	0.98

NGS-file is not only determined by its number of observations. In other words, NGS-files with e.g. 3000 observations each may have very different data sizes. Another obstacle is that not all VLBI analysts work with NGS files. A further possibility for a boundary value is be the number of scans. A scan represents all observations to one source at a time; however, BLR comparisons proved that the other criteria for estimating gradients or not are more appropriate.

The following itemization sums up all facts concerning the BLR analysis.

- The ray-traced delays, which represent the absolute reference values in this comparison, can be approximated perfectly well by the mapping function VMF1 plus the gradients GRAD, what in other words mean that, concerning BLR, higher accuracies may not be reached unless the ray-traced delays themselves become more accurate.
- Contrary to the commonly accepted opinion, gradients shall not always be estimated within VLBI analysis. In order to produce reliable results, the design matrix in the least-squares adjustment must be sufficiently over-determined. To ensure this, a certain criterion has to be fulfilled. Three distinctions are possible to decide whether gradients shall be estimated or not:
  - *Critical data size of the NGS-file*: according to Landskron et al. [2016b], gradients shall only be estimated when the respective NGS-file of the session exceeds 3 MB. This is the most user-friendly criterion as the NGS-files do not even need to be opened, but at the same time it is the least optimal criterion on a sci-

entific basis. And useless for all users which do not work with NGS-files but other data formats, such as e.g. netCDF<sup>12</sup>.

- *Number of total observations per session*: only estimate gradients of a session when it contains at least 3000 observations in total. This criterion is more meaningful than that above, but it is less easy-to-handle because the number of observations of each session must be determined beforehand.
- *Mean number of observations per station and session*: only estimate gradients when the stations participating in the session each have at least 375 observation on average. This criterion is the most exact one of the three criteria listed here, but also associated with the most work for the user. Even more exact would be to estimate gradients only for individual stations that show more than 375 observations per session, but NGS-files would need to be split up to handle this, what would require a total rearrangement of the least-squares adjustment in the VLBI software.

Now, if the respective boundary is exceeded, that is, the criterion is fulfilled, it is recommended to estimate gradients while the use of a priori gradients is redundant. On the other hand, if the criterion is not reached, then a priori gradients shall be used but the gradients shall not be estimated.

- When deciding to estimate gradients, it is circumstantial if a priori gradients are additionally applied or not.
- Best results are achieved with the a priori gradients GRAD-2. However, GRAD-1 is only marginally worse but does not require a new gradient formula.
- The gradients GRAD provide appreciably better BLR than the LHG from *Böhm and Schuh* [2007a].

### 5.1.3. Comparison of modeled delays with ray-traced delays

The following comparison was done for a regular global grid with 2592 grid points, unlike the preceding ones where gradients were determined for VLBI stations located at discrete spots on Earth. For each of these grid points, ray-traced delays were generated for the specifications listed in Table 5.8 as was already done for the derivation of VMF3 coefficients in Chapter 4.3. These new ray-traced delays were not only used for the calculation of horizontal gradients as described in this section; they were also utilized in order to calculate a new, global grid of empirical gradients (cf. Section 5.2) and, even more importantly, new mapping functions coefficients were calculated on their basis as shown in Chapter 4.

The procedure of the gradients calculation was done analogously to that of the previous section, that is, using least-squares adjustments. The design matrix from Eq. (5.3) and

---

<sup>12</sup>Network Common Data Format

Table 5.8.: *Properties of the ray-traced delays that were generated using the ray-tracer RADIATE for the global grid, in addition to the ray-tracing standard approach (see Table A.4 on page 139). Note that these are the same specifications as for the derivation of the VMF3 coefficients in Table 4.2.*

PARAMETER	SPECIFICATION
Ray-tracing software	<i>RADIATE</i> [Hofmeister, 2016]; 2D ray-tracer
NWM	ECMWF ERA Interim Pressure Level Data
Horizontal resolution of the NWM	$1^\circ \times 1^\circ$
Horizontal coverage	global grid with a resolution of $5^\circ \times 5^\circ$ (lat: $[87.5^\circ, -87.5^\circ]$ , lon: $[2.5^\circ, 357.5^\circ]$ ), resulting in 2592 grid points
Temporal resolution	mean values for every month from 2001 through 2010 (= 120 epochs)
Elevations per point	4 ( $3.3^\circ$ , $5^\circ$ , $15^\circ$ and $30^\circ$ )
Azimuths per point	8 ( $0^\circ:45^\circ:315^\circ$ )

the observation vector are reduced to  $32 \times 2$  and  $32 \times 1$  entries, respectively, owing to the lower number of azimuths and elevations. The gradients  $G_n$  and  $G_e$  and extended gradient variables  $G_{n_2}$ ,  $G_{e_2}$ ,  $G_{n_3}$  and  $G_{e_3}$  are then again calculated analogously to Eq. (5.11) on page 97 for every grid point at every epoch. This enables comparing the ray-traced delays, which are regarded as the "true" values, to those modeled with the three gradient formulae. Please note that the LHG gradients [Böhm and Schuh, 2007a] cannot be considered here, as they are only available for VLBI station locations and not for arbitrary points such as a global grid.

In Fig. 5.12 one sees the hydrostatic and wet parts of the calculated  $G_n$  and  $G_e$  from GRAD on a world map averaged over all 120 epochs in order to get an idea of the global distribution of the gradients.

In the following, a comparison is made concerning the residuals between the azimuth-wise ray-traced delays and ray-traced delays averaged over all azimuths for each of the 2592 grid points, 120 epochs, 8 azimuths and 4 elevations. Progressively, gradient formulae are applied in order to reveal their performance in bringing the modeled delays closer to the ray-traced delays, that is, reducing the residuals between them. Figures 5.13 and 5.14 feature the improvement of the residuals in bias and standard deviation, respectively, resulting from the application of gradient formulae. Here and in the upcoming Table 5.9 only the elevation  $5^\circ$  is considered; the relative improvement is proportionate for all elevations, while only the absolute amounts differ.

Besides bias and standard deviation, making comparisons regarding mean absolute residuals is also very meaningful since it describes the total difference to the reference values



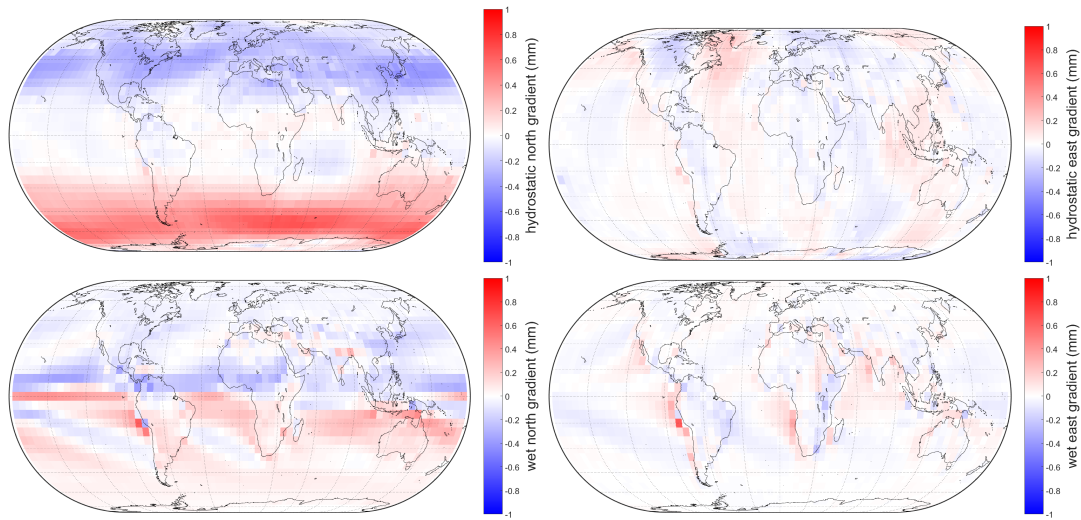


Figure 5.12.: Gradients  $GRAD$  on a global grid averaged over all 120 epochs. Top left:  $G_{nh}$  is most pronounced in higher latitudes, while its effect in the tropics is very low. On the other hand,  $G_{nw}$  (bottom left) is most dominant in the near-equator regions. The hydrostatic and wet east gradients  $G_{eh}$  and  $G_{ew}$  (top right and bottom right) are generally lower and exhibit a rather unsystematic behaviour than their counterparts.

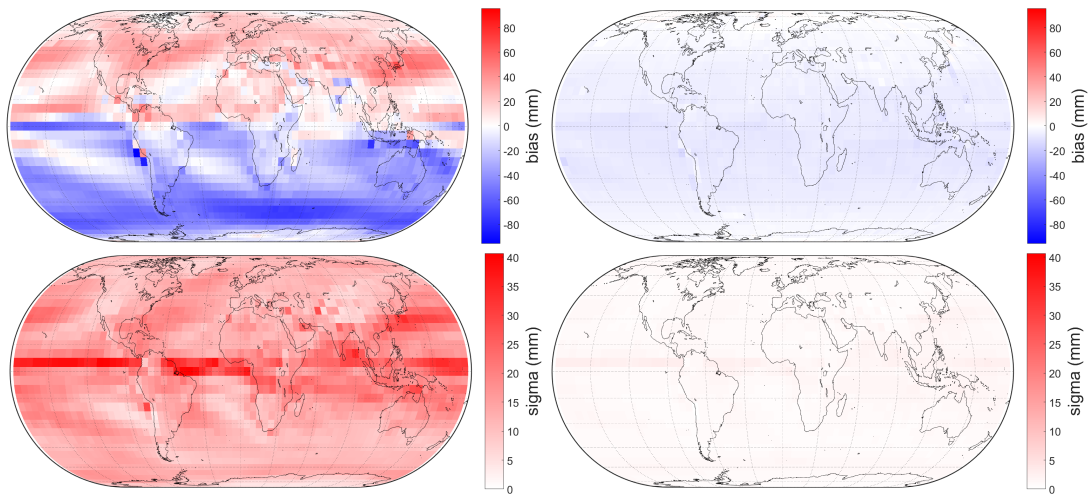


Figure 5.13.: Bias (top) and standard deviation (bottom) of the residuals in slant total delay at  $5^\circ$  elevation and  $180^\circ$  azimuth. Top left: bias of residuals between ray-tracing and azimuthal symmetry: in the Northern Hemisphere, the residuals are generally positive while in the Southern Hemisphere they are negative; this is due to the atmospheric bulge. Top right: bias of residuals between ray-tracing and GRAD-1; the residuals are now considerably lowered, albeit being slightly negative. Bottom left and bottom right: the same comparison as above, but regarding standard deviation. Here, as well, the application of GRAD-1 tremendously reduces the residuals at all levels.

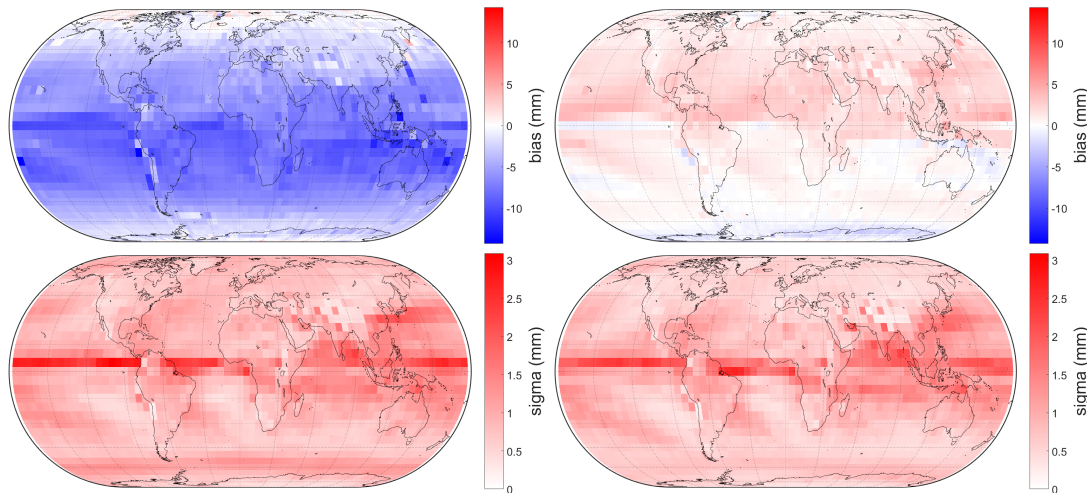


Figure 5.14.: *Bias (top) and standard deviation (bottom) of the residuals in slant total delay at  $5^\circ$  elevation and  $180^\circ$  azimuth. Top left: bias of residuals between ray-tracing and applying GRAD-1. This figure is equal to the top right plot of the figure before, but differently scaled. Top right: bias of residuals between ray-tracing and GRAD-2. Thus, the negative residuals are mainly removed. Bottom left and bottom right: the same comparison as above, but regarding standard deviation. Here, no noticeable difference is to be seen.*

averaged over all observations, while the bias is always dependent on the algebraic sign. Table 5.9 lists the mean absolute residuals for the different gradient formulae averaged over all grid points and epochs, sorted by azimuth. It reconfirms all previous results of gradient comparisons and resulting BLR comparisons, such as:

- Especially for small elevation angles like  $5^\circ$ , the consideration of azimuthal asymmetry is of particular importance.
- Azimuthal asymmetry is most pronounced in north and south direction, and is least pronounced in east and west direction. This is due to the presence of an atmospheric bulge.
- With the standard gradient formula of *Chen and Herring* [1997] (= GRAD-1), a mean improvement in the slant total delays of up to 20 mm can be reached at  $5^\circ$  elevation. On average, it improves the residuals by 86%.
- Using the second gradient formula (= GRAD-2) yields another improvement in the slant total delays, although smaller. On average, the residuals are lower by notable 95% compared to not considering azimuthal asymmetry.
- The third gradient formula (= GRAD-3) is not meaningful as it is not capable of further reducing the residuals. This is most likely owing to insufficient overdetermination, as six gradient variables shall be estimated from eight azimuths.

Table 5.9.: Mean absolute residuals (mm) in slant total delay between ray-tracing and applying no gradient formula vs. the three gradient formulae, each for different azimuths  $\alpha$  and  $5^\circ$  elevation, averaged over all 2592 grid points and 120 epochs from January 2001 to December 2010.  $VMF3_{LSM}$  is used as mapping function.

GRADIENT MODEL	MEAN ABS. DIFF. in $\Delta L$ (cm)					
	$\alpha = 0^\circ$	$\alpha = 45^\circ$	$\alpha = 90^\circ$	$\alpha = 135^\circ$	$\alpha = 180^\circ$	$\varnothing\alpha$
no a priori gradients	25.6	19.6	9.7	19.0	26.0	<b>20.0</b>
GRAD-1	4.1	1.1	4.1	1.1	4.2	<b>2.9</b>
GRAD-2	1.4	0.8	1.1	0.8	1.3	<b>1.1</b>
GRAD-3	1.4	0.8	1.1	0.8	1.3	<b>1.1</b>

#### 5.1.4. Results

Taking into account all of the above sections, we get the proof that the BLR improvement from Section 5.1.2.2 is no coincidence but scientifically sound, as especially the preceding Section 5.1.3 clearly evinces. The re-calculated values for the gradients  $G_n$  and  $G_e$  GRAD-1 as input to the standard gradient formula of *Chen and Herring* [1997] are the main results of this chapter. Their application does not require any new model and yields best performance compared to all other existing gradients. Values of GRAD-1 for all VLBI stations at each NWM epoch from 1999 through 2014 can be downloaded from the GGOS Atmosphere homepage [[ggosatm.hg.tuwien.ac.at/DELAY/ETC/GRAD/](http://ggosatm.hg.tuwien.ac.at/DELAY/ETC/GRAD/), date of access: 2016/08]. The second gradient formula using the respective new gradients GRAD-2 can be applied if highest accuracy is in demand, particularly for low elevations. However, due to the only very small increase of accuracy they are currently not provided for download. The third gradient formula can unhesitatingly be neglected, because its application does not yield any further improvement.

In terms of horizontal gradients in VLBI analysis, it is recommended to consider one of the criteria listed in the itemization on page 111 to decide whether a priori gradients shall be applied and/or gradients shall be estimated in VLBI analysis or not. It was found that contrarily to the common accepted opinion gradients shall not always be estimated in VLBI analysis; if a respective criterion is reached, then the recommendation is to solely apply a priori gradients (in the best case GRAD) and to not estimate the gradients in the analysis.

## 5.2. Determination of an empirical gradient grid

Up to this point only discrete values of horizontal gradients were regarded, calculated indirectly from NWM representing the actual state of the atmosphere. On the one hand,

these gradients were tuned for ray-traced delays through NWM to the respective NWM epochs, on the other hand they were computed within VLBI analysis in a least-squares adjustment for the very points of the measurements. However, it might be the case that the user has no chance to access such real, discrete data. As in the modeling of azimuth-independent delays where empirical mapping functions can be used as an approximation to the discrete ones, the same is possible for horizontal gradients. Empirical gradient models are needed especially for observations in the early years of VLBI up to about 1990 [Spicakova *et al.*, 2011], because at that time only few stations were observing only a small number of sources, what resulted in a non-uniform sky coverage that limits the ability of estimating the gradients in a least-squares adjustment [Heinkelmann and Tesmer, 2013]. For recent VLBI observations with a distinctively enhanced sky coverage the usage of empirical gradient models does not change the results significantly because the gradients can anyway be estimated reliably. Yet, for high latitude sites where the effect of the atmospheric bulge is most distinct and in general for deriving terrestrial reference frames (TRF) from VLBI, empirical gradient models make sense [Böhm *et al.*, 2011].

In Section 5.1.1.3 the two empirical gradient models APG [Böhm *et al.*, 2013b] and DAO [MacMillan and Ma, 1997] were introduced. Both of them are static in time; while APG is globally available based on a spherical harmonic expansion up to degree and order nine [Böhm *et al.*, 2013b], DAO is only available for a selected list of 174 VLBI stations (as of 2016/05). Apart from that, both models provide only total gradients and no separated hydrostatic and wet parts. Even though the DAO gradients are already 20 years old, Böhm *et al.* [2011] recommend their use in VLBI analysis for sessions prior than 1990 rather than APG. Nevertheless, this reveals the need of a new realization of empirical gradients based on a more sophisticated model.

On the basis of the discrete horizontal gradients  $G_n$  and  $G_e$  (GRAD-1) calculated on a global  $5^\circ \times 5^\circ$  grid in the course of the preceding Section 5.1.3, empirical approximations for the gradients and thus a new empirical gradient model can be determined<sup>13</sup>. That is, mean values of both hydrostatic and wet  $G_n$  and  $G_e$  per grid point plus their seasonal and half-seasonal behaviour need to be found. Thus, both a spatial variation as well as a temporal variation can be ensured. The user can then determine the actual gradients for the exact time and location of the measurement through bilinear interpolation. These empirical horizontal gradients are part of the new empirical troposphere model GPT3 (see Section 4.4).

The seasonally dependent signal is determined by the following formula which is taken from GPT2 [Lagler *et al.*, 2013] and GPT2w [Böhm *et al.*, 2015], where it is used for the

---

<sup>13</sup>the extended gradient variables  $G_{n2}$ ,  $G_{e2}$ ,  $G_{n3}$  and  $G_{e3}$  are not considered since their influence is believed to be much too low for empirical modeling

empirical modeling of other troposphere parameters:

$$r(t) = A_0 + A_1 \cdot \cos\left(\frac{doy}{365.25} \cdot 2\pi\right) + B_1 \cdot \sin\left(\frac{doy}{365.25} \cdot 2\pi\right) + A_2 \cdot \cos\left(\frac{doy}{365.25} \cdot 4\pi\right) + B_2 \cdot \sin\left(\frac{doy}{365.25} \cdot 4\pi\right) \quad (5.12)$$

where  $r(t)$  is the desired time-dependent parameter,  $A_0$  is the mean value of the parameter,  $A_1$  and  $B_1$  are the seasonal amplitudes of the parameter and  $A_2$  and  $B_2$  are the half-seasonal amplitudes of the parameter. Through least-squares adjustments over the discrete gradients (which after all were determined in least-squares adjustments themselves), error-minimized values for the parameters  $A_0$ ,  $A_1$ ,  $B_1$ ,  $A_2$  and  $B_2$  can be found. The design matrix set up for each of the 2592 grid points reads:

$$A = \begin{bmatrix} \frac{\partial r(\text{epoch}_1)}{\partial A_0} & \frac{\partial r(\text{epoch}_1)}{\partial A_1} & \frac{\partial r(\text{epoch}_1)}{\partial B_1} & \frac{\partial r(\text{epoch}_1)}{\partial A_2} & \frac{\partial r(\text{epoch}_1)}{\partial B_2} \\ \frac{\partial r(\text{epoch}_2)}{\partial A_0} & \frac{\partial r(\text{epoch}_2)}{\partial A_1} & \frac{\partial r(\text{epoch}_2)}{\partial B_1} & \frac{\partial r(\text{epoch}_2)}{\partial A_2} & \frac{\partial r(\text{epoch}_2)}{\partial B_2} \\ \vdots & \vdots & \vdots & \vdots & \vdots \\ \frac{\partial r(\text{epoch}_{120})}{\partial A_0} & \frac{\partial r(\text{epoch}_{120})}{\partial A_1} & \frac{\partial r(\text{epoch}_{120})}{\partial B_1} & \frac{\partial r(\text{epoch}_{120})}{\partial A_2} & \frac{\partial r(\text{epoch}_{120})}{\partial B_2} \end{bmatrix} \quad (5.13)$$

while the four observation vectors  $l$  consist of the discrete gradients  $G_{nh}$ ,  $G_{eh}$ ,  $G_{nw}$  and  $G_{ew}$ . The amplitudes are then determined through:

$$\begin{bmatrix} A_0 \\ A_1 \\ B_1 \\ A_2 \\ B_2 \end{bmatrix} = \hat{x} = (A^T A)^{-1} A^T l \quad (5.14)$$

The two Figs. 5.15 and 5.16 show mean values and cosine amplitudes of the empirical gradients. In general, the east gradients are much lower in magnitude than the north gradients, because they are not affected by such a large systematic component like the atmospheric bulge. The hydrostatic part of the delay shapes the regions outside the tropics, while the wet part is most distinct roughly between 25° N and 25° S (not in the figure). On closer inspection it becomes obvious that there is another systematic component near high mountain ranges such as the Himalayas or the Andes, which comes from the hydrostatic part of the delay. Because of the east-west-alignment of the Himalayas, especially north gradients are affected, namely in such a way as a signal coming from over the mountain range experiences a higher delay than from another direction. As a result, the (hydrostatic) north gradient is positive right south of the Himalayas and negative north of it. Likewise in case of the north-south-extended Andes, (hydrostatic) east gradients are positive west of the mountain range and negative east of it.

It was also tried to apply a 2D median filter to the empirical gradients in order to smooth the values. The median filter replaces each grid point by the median value of a

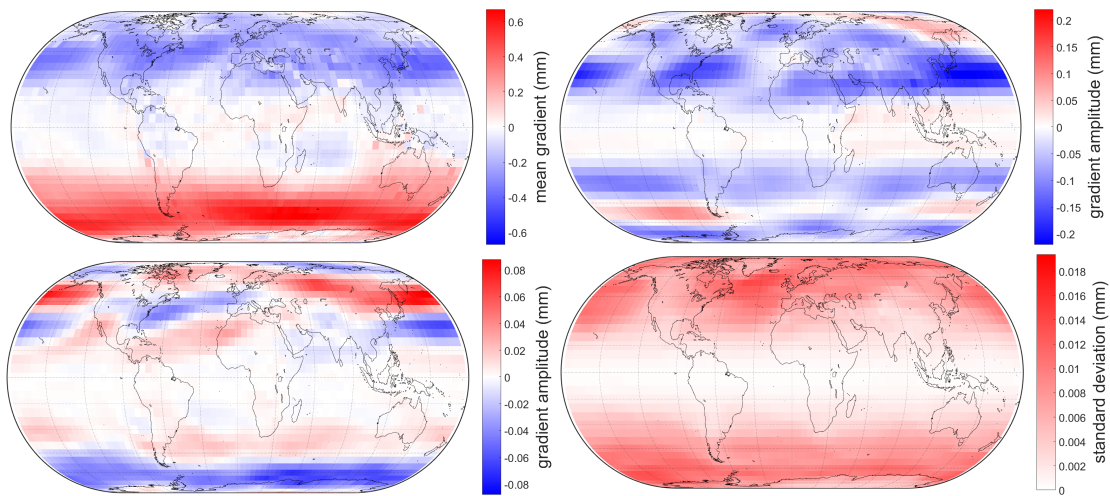


Figure 5.15.: Mean values  $A_0$  (top left), seasonal amplitudes  $A_1$  (top right), half-seasonal amplitudes  $A_2$  (bottom left) and standard deviation of the residuals (bottom right) of the hydrostatic north gradient  $G_{nh}$  from GPT3.

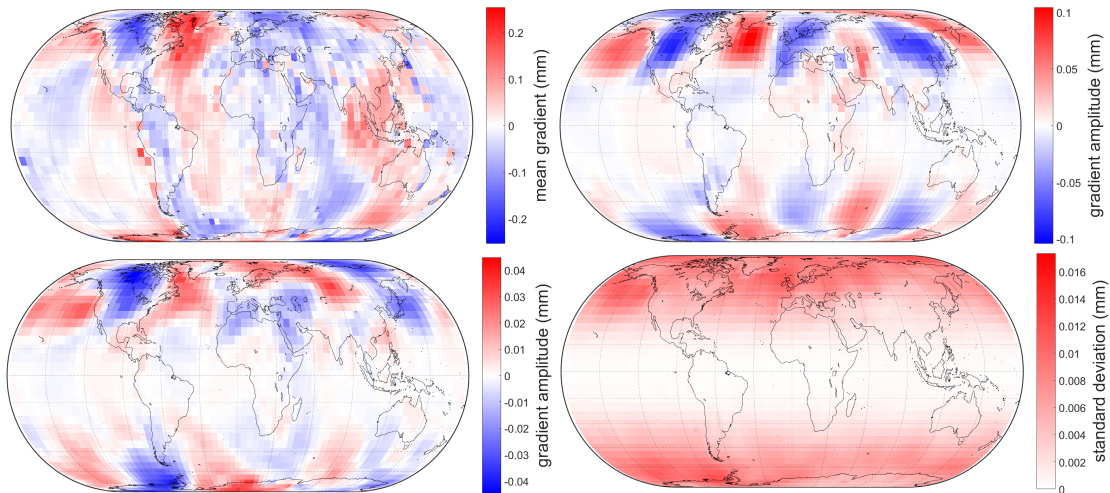


Figure 5.16.: Mean values  $A_0$  (top left), seasonal amplitudes  $A_1$  (top right), half-seasonal amplitudes  $A_2$  (bottom left) and standard deviation of the residuals (bottom right) of the hydrostatic east gradient  $G_{eh}$  from GPT3.

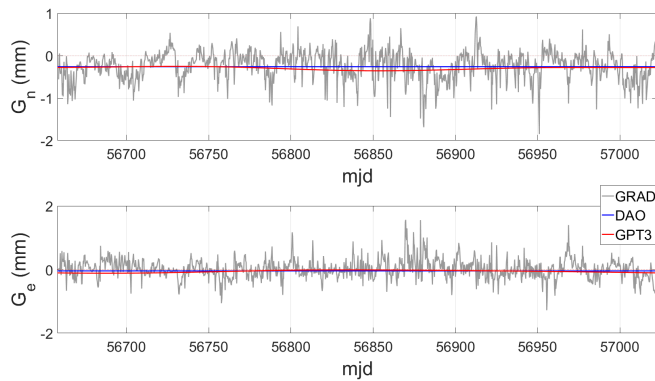


Figure 5.17.: Comparison between discrete and empirical north (top) and east (bottom) gradients for station WETTZELL during the second quarter of 2014. In case of GPT3, the gradients for a specific site are determined through bilinear interpolation from the four surrounding grid points.

Table 5.10.: Mean BLR (cm) from VLBI analyses considering several kinds of empirical a priori gradients for all sessions from 2006-2014. In column (1), only a priori gradients are used, while in column (2) the gradients are additionally estimated in the VLBI analysis. Using (1.h) instead of (1.a) improves 14% of the BLR by more than 1 mm while it degrades only 6% by more than 1 mm.

GRADIENT MODEL	(1) (cm)	(2) (cm)
(a) no a priori gradients	1.68	1.65
(f) APG	1.65	1.66
(g) DAO	1.64	1.66
(h) GPT3	1.63	1.66
(i) GPT3 (no temporal var.)	1.65	1.66

3x3 neighborhood around it [[mathworks.com/help/images/ref/medfilt2.html](http://mathworks.com/help/images/ref/medfilt2.html), date of access: 2016/10]. The final results did not improve though, why the original, unfiltered values were maintained.

As can be seen in Fig. 5.17, the empirical gradients are only capable of describing a small, apparently insignificant part of the actual, discrete gradients. In contrast to DAO, the GPT3 gradients possess a time-dependent component, although very small. But still there is no chance to sufficiently describe the significant random, short-term variations in the wake of weather events that dominate the behaviour of the gradients only by means of empirical values. Again, the BLR are also computed for sessions with a minimum/maximum number of 3000 observation in total (Table 5.11).

Apart from comparing BLR there is also a test made to which degree ray-traced delays can be reproduced through empirical gradients, or rather, how much closer the modeled delays get to the ray-traced delays compared to not considering azimuthal asymmetry. In fact this is exactly the same comparison as in Table 5.9 on page 115, but for empirical gradients instead of GRAD. In this table it can unambiguously be seen that despite being not able to capture short-term variations (cf. Fig. 5.17 on page 119) application of empir-

Table 5.11.: Mean BLR (cm) from VLBI analyses for all those sessions from 2006-2014 that contain fewer than 3000 observations (1129 out of 1338 sessions, columns 1 and 2) and more than 3000 observations (209 out of 1338 sessions, columns 3 and 4). In (1), only a priori gradients are used, while in (2) the gradients are additionally estimated in the VLBI analysis. When having fewer than 3000 observations per session, using (1.h) instead of (1.a) improves 16% of the BLR by more than 1 mm while it degrades only 4% by more than 1 mm. On the other hand, when having more than 3000 observations per session, using (1.h) instead of (1.a) improves 11% of the BLR by more than 1 mm while it degrades 7% by more than 1 mm.

GRADIENT MODEL	<3000 observations		>3000 observations	
	(1) (cm)	(2) (cm)	(1) (cm)	(2) (cm)
(a) no a priori gradients	2.32	2.38	1.08	0.97
(f) APG	2.25	2.39	1.09	0.97
(g) DAO	2.23	2.39	1.09	0.97
(h) GPT3	2.23	2.39	1.08	0.97
(i) GPT3 (no temporal var.)	2.25	2.39	1.09	0.97

ical gradients improves the modeled delays considerably with GPT3 obviously surpassing APG. DAO cannot be included in this test as it is only available for certain sites on Earth.

After close consideration of Tables 5.10 and 5.11 one can draw the following conclusions:

- For VLBI sessions with only few observations clearly better results are reached when applying empirical a priori gradients instead of estimating the gradients in the analysis.
- As soon as gradients are estimated in VLBI analysis, the use of empirical gradients is dispensable. For this reason, the upcoming items treat only the case that the

Table 5.12.: Mean absolute residuals (cm) in slant total delay between ray-tracing and applying no gradient formula vs. empirical gradients, each for different azimuths  $\alpha$  and  $5^\circ$  elevation, averaged over all 2592 grid points and 120 epochs from 2001-2010.  $VMF3_{LSM}$  is used as mapping function.

GRADIENT MODEL	MEAN ABS. DIFF. in $\Delta L$ (cm)					
	$\alpha = 0^\circ$	$\alpha = 45^\circ$	$\alpha = 90^\circ$	$\alpha = 135^\circ$	$\alpha = 180^\circ$	$\varnothing\alpha$
no gradient formula	25.6	19.6	9.7	19.0	26.0	<b>20.0</b>
APG	16.4	14.4	10.8	13.0	16.8	<b>14.3</b>
GPT3	9.4	7.5	7.4	7.5	9.5	<b>8.3</b>



gradients are not additionally estimated.

- Application of empirical gradients generally has a considerably smaller effect on the resulting BLR than the application of discrete a priori gradients. This is because random weather variations make up the bulk of gradient values which are not able to be captured through empirical models.
- Empirical a priori gradients are most useful for sessions with a comparatively low number of observations.
- GPT3, which possesses a more sophisticated empirical model than APG and DAO, performs best in all comparisons, although the differences between them are only small. The inclusion of annual and semi-annual terms in GPT3 has a perceptible influence, even though the variation is only very small (cf. Fig. 5.17).
- The topography has a significant impact on the resulting gradients, e.g. the presence of mountain ranges cause variant gradient values. For this reason, the provision on a grid with a coarse mesh size of  $5^\circ$  seems to be insufficient, as the grid points are up to 550 km away from each other what makes it impossible to consider any topography in between. Probably, the provision of new empirical gradients for individual sites (like DAO) would yield better results for VLBI purposes. But the fact that the grid-wise GPT3 is still better than the station-wise DAO gradients emphasizes their high quality. And through the provision on a global grid, GPT3 can be used for many more purposes than VLBI.
- DAO is slightly better than APG, not least because it was calculated for the exact locations of the VLBI stations, whereas APG is associated with a loss of accuracy due to its representation in spherical harmonics.

### 5.2.1. Deflections of the vertical (DOV) represented as horizontal gradients

Since geoid and reference ellipsoid do not coincide, the line perpendicular to the geoid (plumb line) and the line ellipsoid normal span an angle, the so-called deflection of the vertical. Such angles appear in north-south, meridional direction (DOV component  $\xi$ ) as well as in east-west, prime vertical direction (DOV component  $\eta$ ). Values for DOV range between 1" and 10" in flat terrain and 30" to 1' in mountainous areas [Torge, 1991]. For troposphere purposes, DOV can also be regarded as a tilting of the atmosphere by these angles. As a tilted atmosphere is the result of applying horizontal gradients<sup>14</sup>, the DOV can eventually be represented as horizontal gradients as well. The north component  $\xi$  is thus proportional to the north gradient  $G_n$ , while the east component  $\eta$  is equally proportional to the east gradient  $G_e$ . In Fig. 2.2 on page 15, this context is illustrated graphically. The effect of DOV is already taken into account in the ray-tracing, therefore the following investigation is done merely to get an idea of how large this effect in fact is.

<sup>14</sup>this is valid only for assuming a horizontally stratified atmosphere [Nilsson et al., 2013]

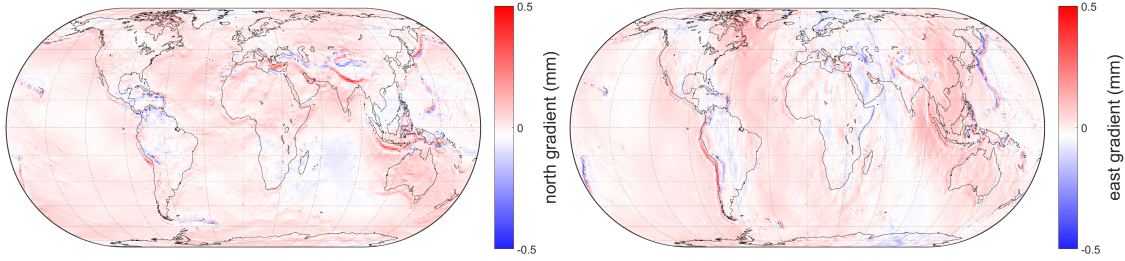


Figure 5.18.: *Left: world map for north gradients  $G_n$  as converted from the north component of DOV  $\xi$ . Right: world map for east gradients  $G_e$  as converted from the east component of DOV  $\eta$ .*

As a coarse grid containing DOV values was not available, they were instead derived indirectly from a  $1^\circ \times 1^\circ$  undulation grid of the whole earth. This grid providing undulations with respect to WGS84<sup>15</sup> comes from the EGM2008 website [[earth-info.nga.mil/GandG/wgs84/gravitymod/egm2008/egm08/wgs84.html](http://earth-info.nga.mil/GandG/wgs84/gravitymod/egm2008/egm08/wgs84.html), date of access: 2014/10] and first had to be interpolated to resolution  $1^\circ \times 1^\circ$ . The geoid undulations can be converted to the corresponding deflections of the vertical through a formula system as described in *Hofmann-Wellenhof and Moritz* [2005]. For the purpose of this thesis, however, it was sufficient to use a simplified calculation strategy which neglects the curvature between the grid points, because highest-possible accuracy is not necessary. Thus DOV are determined as follows:

- the north component  $\xi$  is the angle of the undulation difference of two consecutive undulations, more precisely between one grid point and the next grid point north of it
- the east component  $\eta$ , analogous to  $\xi$ , is the angle of the undulation difference between one grid point and the next grid point east of it

This yields a world map for the two deflections of the vertical  $\xi$  and  $\eta$ . The DOV can be converted to gradients through the simple equations:

$$\begin{aligned} G_n &= \Delta L^z \cdot \tan(\xi) \\ G_e &= \Delta L^z \cdot \tan(\eta) \end{aligned} \tag{5.15}$$

what gives reason to expect horizontal gradients in the range between 0.01 mm and 0.1 mm in flat terrain and 0.3 mm to 0.6 mm in mountainous areas, according to the figures by *Torge* [1991].

We thus get the final results as illustrated in Fig. 5.18, where it is discernible that almost for the entire earth the resulting gradients are negligibly small. Considerable gradients appear mostly at the boundaries of two tectonic plates, best visible at the boundaries between:

<sup>15</sup>World Geodetic System 1984; geodetic reference system

- the Nazca Plate and the South American Plate, where the Andes rise
- the Indian Plate and the Eurasian Plate, where the Himalayas rise
- the Philippine Plate and the Pacific Plate south of Japan
- the Indo-Australian and the Eurasian Plate alongside Indonesia

Moreover, there are large-scale deflections of the vertical in the region in and around Greenland which is due to past and present-day ice mass changes in the Greenland ice sheet [*Fleming et al.*, 2004]. Furthermore, there is no significant difference between  $G_n$  and  $G_e$  in terms of the general shape of the map, albeit the world map of  $\xi$  shows more east-west variations while the world map for  $\eta$  includes more north-south trends. In summary it can be said that the horizontal gradients resulting from deflections of the vertical (DOV) are too small to be considered in azimuthal asymmetry.



## 6. Conclusions and Outlook

In the course of this thesis there were generally two major topics considered:

1. the determination of new, enhanced troposphere mapping functions...
  - a) ...on the discrete level, with the Vienna Mapping Functions 3 (VMF3) [Landskron *et al.*, 2016c] providing new mapping function coefficients  $a$ ,  $b$  and  $c$  valid for discrete locations (so far only VLBI stations) and epochs (cf. Chapter 4.6). VMF3 significantly improves the performance of VMF1 as it gets up to one third closer to the reference ray-traced delays, which is of particular importance at low elevations. On the side of the user, VMF3 can be applied just like VMF1, with the only additional input argument being geographical longitude.
  - b) ...on the empirical level, with the blind troposphere model Global Pressure and Temperature 3 (GPT3) providing empirical mapping function coefficients  $a$  on the basis of  $b$  and  $c$  from VMF3 for any location and epoch (cf. Chapter 4.6). The performance of GPT3's mapping factors is equivalent to that of the GPT2w ones, however there is ongoing research to further improve GPT3. The big advantage of GPT3, however, is its full consistency with VMF3.
  - c) ...on the empirical site-augmented level, with the model Site-Augmented GPT2w (SA-GPT2w) [Landskron *et al.*, 2016a] utilizing in situ meteorological measurements of temperature and humidity to augment GPT2w (cf. Chapter 3.2.6). This improves the empirical zenith wet delays by up to one quarter to one third, where the input can come from in situ sensors as well as from NWM. Here, best performance can be achieved in all non-tropical regions.
2. the determination of new, enhanced tropospheric horizontal gradients...
  - a) ...on the discrete level, with the model GRAD [Landskron *et al.*, 2016b] providing new north gradients  $G_n$  and east gradients  $G_e$  valid for discrete locations (so far only VLBI stations) and epochs (cf. Chapter 5.1.4). GRAD outperforms the gradient model LHG on the basis of BLR as well as delay comparisons and can be applied just like it. The refined model GRAD-2, consisting of higher-order gradient variables  $G_{n_2}$  and  $G_{e_2}$ , makes for a further small improvement. Apart from that it was found that application of a priori gradients in VLBI is of fundamental importance for all sessions which have less than 3000 observations, what corresponds to 90% of all VLBI sessions. Contrary to the commonly accepted opinion, gradients shall not be estimated in the VLBI analysis for such

sessions.

- b) ...on the empirical level, comprising of a new empirical gradient model for any location and epoch incorporated into GPT3 (cf. Chapter 5.2). Realized on a  $5^\circ \times 5^\circ$  grid, it slightly surpasses the performances of APG and DAO and can be applied for GNSS as well as VLBI applications.

The basis for all these models are ray-traced delays from the highly sophisticated ray-tracer *RADIATE* developed by *Hofmeister* [2016], assuring highest possible precision. As the conclusion of Chapters 3, 4 and 5 point out, each of the above listed models is indeed able to surpass the performance of their respective counterparts, sometimes more, sometimes less. However, in all cases only a comparably small improvement is reached why one is forced to the conclusion that the state of the art of troposphere modeling following the currently common strategies is, for the most part, close to its top level. Determining geodetic troposphere parameters from ray-tracing through NWM is by far the most accurate approach in the history of troposphere modeling in space geodesy, remembering the vast leaps in accuracy caused by IMF and later VMF compared to their predecessors, for instance. There appears to be no other way to determine the distribution of geodetic quantities throughout the atmosphere with such high precision than with this technique. Nevertheless, as long as no fundamental findings are obtained in reconsidering the framework NWM + ray-tracing, which the determination of the products of this thesis is based on, a new generation of troposphere parameter acquisition (in terms of accuracy) is, in my opinion, not to be expected.

Regarding further research topics in this field by the author and the Department of Geodesy and Geoinformation at TU Wien in general, it is planned to compute and publish a new height correction for mapping functions to replace that of *Niell* [1996], once more on the basis of *RADIATE* ray-traced delays. It is supposed to be included in GPT3 and will hopefully be able to increase its performance. Furthermore, GPT3 will also be realized on a  $1^\circ \times 1^\circ$  grid. Upcoming publications of the author will deal with eventual releases of VMF3, GPT3 and GRAD for all IGS, IVS and IDS<sup>1</sup> stations, containing automatically processed values in real-time as well. In general, more tests and comparisons of the new models for GNSS applications will be made, since this thesis is mainly focussed on VLBI. For this purpose there is also high interest in experiences of external users with the new models.

Exact knowledge of geodetic parameters will undergo increasing importance in the future, in particular for understanding and modeling phenomena dealing with climate change. Great stress is laid upon sea level rise for whose determination space geodetic techniques play a major role. By the end of this century, the global mean sea level will rise between 0.3 and 2.5 meters [*Sweet et al.*, 2017] what is going to affect coastal areas all over

---

<sup>1</sup>International DORIS Service

the world severely. The higher the error budget of troposphere modeling, the lower the accuracy of the measured sea level and in further consequence the lower the understanding for making preparations and arrangements. Space geodetic techniques are increasingly suitable also for climatological studies, with the capability of GNSS to derive information about the air's water vapor content from distance measurements leading the way. However, it was demonstrated in *Heinkelmann* [2008] and *Greimeister* [2016] that long-term trends of atmospheric water may be derived from VLBI measurements as well. Future will also bring advanced interaction between GNSS, VLBI, SLR and DORIS in order to exploit the full potential of each technique for supporting the others and for determining local ties between the reference stations more precisely [*Hobiger*, 2014]. In all of these, accurate modeling of tropospheric delays is of particular importance. Nevertheless, this is only a selection of loads of applications where troposphere modeling is indispensable. In summary, there is need for much more research in further advancing the understanding of tropospheric effects on space geodetic signals following this thesis, in order to achieve these objectives.





# Appendices

# A. List of variables, acronyms and explanations of important terms

## Variables

In the following there is a list of variables which are mentioned throughout this thesis. Units, if specified, are in SI, although some formulae may require different units.

$a$	(total) mapping function coefficient of the first order
$a_h$	hydrostatic mapping function coefficient of the first order
$a_{nm}$	coefficients of the spherical harmonics expansion
$a_w$	wet mapping function coefficient of the first order
$A$	design matrix in least-squares adjustments
$A_0$	mean value in seasonal fit formula (Eq. (4.10) on page 59)
$A_1$	annual amplitude in seasonal fit formula (Eq. (4.10) on page 59)
$A_2$	semi-annual amplitude in seasonal fit formula (Eq. (4.10) on page 59)
$b$	(total) mapping function coefficient of the second order
$b_h$	hydrostatic mapping function coefficient of the second order
$b_{nm}$	coefficients of the spherical harmonics expansion
$b_w$	wet mapping function coefficient of the second order
$B_1$	annual amplitude in seasonal fit formula (Eq. (4.10) on page 59)
$B_2$	semi-annual amplitude in seasonal fit formula (Eq. (4.10) on page 59)
$c$	(total) mapping function coefficient of the third order
$c_h$	hydrostatic mapping function coefficient of the third order
$c_w$	wet mapping function coefficient of the third order
$C$	(total) gradient mapping function coefficient
$C_h$	hydrostatic gradient mapping function coefficient
$C_w$	wet gradient mapping function coefficient

---

$C_{nm}$	function of the spherical harmonics expansion
$dT$	temperature lapse rate ( $\frac{K}{km}$ )
$e$	water vapor pressure (Pa)
$f$	relative humidity (%)
$g_m$	mean gravity which equals 9.80665 ( $\frac{m}{s^2}$ )
$G_n$	(total) north gradient (m)
$G_{n_2}$	(total) gradient variable of the second order (m)
$G_{n_3}$	(total) gradient variable of the third order (m)
$G_{n_h}$	hydrostatic north gradient (m)
$G_{n_w}$	wet north gradient (m)
$G_e$	(total) east gradient (m)
$G_{e_2}$	(total) gradient variable of the second order (m)
$G_{e_3}$	(total) gradient variable of the third order (m)
$G_{e_h}$	hydrostatic east gradient (m)
$G_{e_w}$	wet east gradient (m)
$h_{ell}$	ellipsoidal height (m)
$H$	(total) scale height of the neutral atmosphere
$H_h$	hydrostatic scale height of the neutral atmosphere
$H_w$	wet scale height of the neutral atmosphere
$l$	observation vector in least-squares adjustments
$L$	observed observation vector in least-squares adjustments
$L_0$	computed observation vector in least-squares adjustments
$m$	order of spherical harmonics expansion
$mf(\varepsilon)$	(total) mapping function dependent on elevation $\varepsilon$
$mf_g(\varepsilon)$	gradient mapping function dependent on elevation $\varepsilon$
$mf_h(\varepsilon)$	hydrostatic mapping function dependent on elevation $\varepsilon$
$mf_w(\varepsilon)$	wet mapping function dependent on elevation $\varepsilon$
$M$	weighting factor in SA-GPT2w (cf. Section 3.2)
$M_{a_h}$	weighting factor in SA-GPT2w which weights the hydrostatic mapping function coefficient $a_h$ with temperature $T$ in Eq. (3.7) on page 28 ( $\frac{1}{K}$ )

---

$M_{zwd}$	weighting factor in SA-GPT2w which weights the zenith wet delay $\Delta L_w^z$ with temperature $T$ in Eq. (3.8) on page 28 ( $\frac{m}{K}$ )
$M_{zwd_1}$	weighting factor in SA-GPT2w which weights the zenith wet delay $\Delta L_w^z$ with temperature $T$ in Eq. (3.10) on page 28 ( $\frac{m}{Pa}$ )
$M_{zwd_2}$	weighting factor in SA-GPT2w which weights the zenith wet delay $\Delta L_w^z$ with water vapor pressure $e$ in Eq. (3.10) on page 28 ( $\frac{m}{Pa}$ )
$n$	degree of spherical harmonics expansion
$n_f$	degree of freedom in least-squares adjustments, determined by number of observations $n$ minus number of unknowns $u$
$N$	geoid undulation (m); or normal equation matrix in least-squares adjustments
$p$	pressure (Pa)
$P$	weight matrix in least-squares adjustments, always set to one in this thesis
$P_{nm}$	associated Legendre functions of degree $n$ and order $m$
$Q_{xx}$	cofactor matrix in least-squares adjustments
$r$	correlation coefficient
$R_d$	specific gas constant for dry constituents which equals 287.0464 ( $\frac{J}{K \cdot kg}$ )
$R_e$	Earth radius
$S_{nm}$	function of the spherical harmonics expansion
$T$	temperature (K)
$T_m$	mean temperature weighted with water vapor pressure (K)
$v$	system residuals in least-squares adjustments
$x$	unknowns in least-squares adjustments
$x_{pol}$	polar motion in $x$ direction (m)
$y_{pol}$	polar motion in $y$ direction (m)
$\alpha$	azimuth angle (rad); or right ascension (rad)
$\beta$	tilting angle as which a gradient $G$ can be described (rad)
$\delta$	declination (rad)
$\Delta a_h$	variation in hydrostatic mapping function coefficient $a_h$
$\Delta L_0(\varepsilon)$	isotropic part of the slant total delay (m), in Chapter 4 equated with $\Delta L(\varepsilon)$
$\Delta L(\varepsilon)$	slant total delay (m) dependent on elevation $\varepsilon$
$\Delta L(\alpha, \varepsilon)$	slant total delay (m) dependent on azimuth $\alpha$ and elevation $\varepsilon$

---

$\Delta L_h(\varepsilon)$	slant hydrostatic delay (m) dependent on elevation $\varepsilon$
$\Delta L_{res}(\alpha, \varepsilon)$	anisotropic, residual part of the slant total delay (m)
$\Delta L_w(\varepsilon)$	slant wet delay (m) dependent on elevation $\varepsilon$
$\Delta L^z$	zenith total delay (m)
$\Delta L_h^z$	zenith hydrostatic delay (m)
$\Delta L_w^z$	zenith wet delay (m)
$\Delta T$	variation in temperature $T$ ( $\frac{K}{m}$ )
$\varepsilon$	elevation angle (rad)
$\eta$	east component of deflection of the vertical (DOV) (rad)
$\vartheta$	polar distance (rad)
$\lambda$	geographic longitude (rad); or water vapor decrease factor ( $\frac{Pa}{km}$ )
$\xi$	north component of deflection of the vertical (DOV) (rad)
$\sigma$	standard deviation of a quantity
$\varphi$	geographic latitude (rad)

## Acronyms

<b>BLR</b>	baseline length repeatability
<b>DORIS</b>	Doppler Orbitography and Radiopositioning Integrated by Satellite
<b>DOV</b>	deflection of the vertical
<b>doy</b>	day of year
<b>dUT1</b>	irregularities of the Earth's rotation, determined by $UT1 - UTC$
<b>ECMWF</b>	European Centre for Medium-Range Weather Forecasts
<b>EOP</b>	earth orientation parameter(s)
<b>GNSS</b>	Global Navigation Satellite Systems
<b>GPS</b>	Global Positioning System
<b>GPT</b>	Global Pressure and Temperature
<b>IDS</b>	International DORIS Service
<b>IGS</b>	International GNSS Service
<b>IVS</b>	International VLBI Service for Geodesy and Astrometry

**LSM** least-squares method

**MJD** modified Julian Date

**NCEP** United States National Centers for Environmental Prediction

**NWM** numerical weather model(s)

**VieVS** Vienna VLBI Software

**VLBI** Very Long Baseline Interferometry

**VMF** Vienna Mapping Functions

**WGS84** World Geodetic System 1984

**zwd** zenith Wet Delay

## Explanation of important terms

### CONT11 campaign

The primary goal of the CONT11 campaign (*CONT* for "Continuous VLBI session") was to acquire state-of-the-art VLBI data in highest accuracy to study high-resolution Earth rotation and to investigate the stability of the reference frame and daily to sub-daily site motions [[ivscc.gsfc.nasa.gov/program/cont11/](http://ivscc.gsfc.nasa.gov/program/cont11/), date of access: 2016/10]. It contains continuous measurements from September 15, 2011, 00:00 UT (MJD: 55819) through September 29, 2011, 24:00 UT (MJD: 55833) of the stations listed in Table A.1 and Fig. A.1.

### CONT14 campaign

As with CONT11, the primary goal of the CONT14 campaign was to acquire state-of-the-art VLBI data in highest accuracy to study high-resolution Earth rotation and to investigate the stability of the reference frame and daily to sub-daily site motions [[ivscc.gsfc.nasa.gov/program/cont14/](http://ivscc.gsfc.nasa.gov/program/cont14/), date of access: 2016/10]. It contains continuous measurements from May 06, 2014, 00:00 UT (MJD: 56783) through May 20, 2014, 24:00 UT (MJD: 56797) of the stations listed in Table A.2 and Fig. A.2.

### The European Centre for Medium-Range Weather Forecasts (ECMWF)

The European Centre for Medium-Range Weather Forecasts (ECMWF) is an independent intergovernmental organization supported by 34 countries. It determines numerical weather models (NWM) and provides them to the national meteorological services of

Table A.1.: *Stations participating in CONT11.*

STATION ABBR.	FULL STATION NAME	COUNTRY
BADARY	Badary Radio Astronomical Observatory	Russia
FORTLEZA	Space Radio Observatory of the Northeast (ROEN), Fortaleza	Brazil
HARTRAO	Hartebeesthoek Radio Astronomy Observatory	South Africa
HOBART12	Mt. Pleasant Radio Astronomy Observatory, Hobart, TAS	Australia
KOKEE	Kokee Park Geophysical Observatory, Kauai, HI	USA
NYALES20	Ny Álesund Geodetic Observatory, Spitsbergen	Norway
ONSALA60	Onsala Space Observatory	Sweden
TIGOCONC	Transportable Integrated Geodetic Observatory (TIGO), Concepción	Chile
TSUKUB32	Tsukuba VLBI Station	Japan
WARK12M	Warkworth VLBI Station	New Zealand <sup>1</sup>
WESTFORD	Westford Antenna, Haystack Observatory, MA	USA
WETTZELL	Fundamentalstation Wettzell	Germany
YEBES40M	Astronomical Center at Yebes	Spain
ZELENCHK	Radioastronomical Observatory Zelenchukskaya	Russia



Figure A.1.: Map showing the locations of the CONT11 stations [*ivscc.gsfc.nasa.gov/program/cont11/*, date of access: 2016/10].

Table A.2.: *Stations participating in CONT14.*

STATION ABBR.	FULL STATION NAME	COUNTRY
BADARY	Badary Radio Astronomical Observatory	Russia
FORTLEZA	Space Radio Observatory of the Northeast (ROEN), Fortaleza	Brazil
HART15M	Hartebeesthoek Radio Astronomy Observatory	South Africa
HOBART12	Mt. Pleasant Radio Astronomy Observatory, Hobart, TAS	Australia
HOBART26	Mt. Pleasant Radio Astronomy Observatory, Hobart, TAS	Australia
KATH12M	Katherine Observatory, Katherine, NT	Australia
KOKEE	Kokee Park Geophysical Observatory, Kauai, HI	USA
MATERA	Centro di Geodesia Spaziale G. Colombo, Matera	Italy
NYALES20	Ny Ålesund Geodetic Observatory, Spitsbergen	Norway
ONSALA60	Onsala Space Observatory	Sweden
TSUKUB32	Tsukuba VLBI Station	Japan
WARK12M	Warkworth VLBI Station	New Zealand
WESTFORD	Westford Antenna, Haystack Observatory, MA	USA
WETTZELL	Fundamentalstation Wettzell	Germany
YARRA12M	Yarragadee Observatory, Yarragadee, WA	Australia
YEBES40M	Astronomical Center at Yebes	Spain
ZELENCHK	Radioastronomical Observatory Zelenchukskaya	Russia



Figure A.2.: Map showing the locations of the CONT14 stations [*ivscc.gsfc.nasa.gov/program/cont14/*, date of access: 2016/10].



---

its member states. These NWM consist of various forecast data on the one hand and re-analysis data on the other hand [[ecmwf.com/en/about/who-we-are](http://ecmwf.com/en/about/who-we-are), date of access: 2016/11]. They serve as the basis for ray-tracing techniques which are able to determine the time delay of electromagnetic waves during its passage through the troposphere.

### **International GNSS Service (IGS)**

The International GNSS Service<sup>2</sup> (IGS) is a voluntary federation of more than 200 agencies and universities with the aim of providing best possible GNSS products such as satellite orbits, clock solutions and Earth Orientation Parameters (EOP). The special thing about it is that all products are publicly available over the IGS data centers. The IGS consists of 18 analysis centers which analyze the measurements of all tracked GNSS satellites and produce data which is then archived and published by the four data centers [[igs.org/about](http://igs.org/about), date of access: 2016/11].

### **International VLBI Service for Geodesy and Astrometry (IVS)**

The International VLBI Service for Geodesy and Astrometry (IVS) is, like its pendant IGS, an international federation of organizations which aim at providing VLBI data and products to be publicly available for research. Some of those products are the VLBI contribution to the International Terrestrial Reference Frame (ITRF), the so-called VTRF, or also realizations of the International Celestial Reference Frame (ICRF) and EOP. Similar to the IGS, data processing is operated in analysis centers while data centers eventually archive and publish the various products, whereby the German Bundesamt für Kartographie und Geodäsie (BKG) plays a major role. The IVS also performs measurement campaigns such as CONT11 and CONT14 which shall demonstrate the potential of state-of-the-art global measurements for a variety of applications [[ivscc.gsfc.nasa.gov/about](http://ivscc.gsfc.nasa.gov/about), date of access: 2016/11].

### **NGS data format**

NGS (from National Geodetic Survey) is a data format for VLBI data transfer which contains all VLBI observation data; in addition to all data concerning observations of the quasars, NGS files contain also in situ measured meteorological quantities such as temperature, pressure and relative humidity. There is one NGS file for each VLBI session, starting in 1979.

---

<sup>2</sup>formerly referred to as International GPS Service

Table A.3.: *Settings of the VieVS standard approach.*

OPTION	DECISION
use OPT files	yes
mapping function	VMF1
zhd	from observational data (NGS)
use a priori gradients	no
terrestrial reference frame	VieVS TRF
celestial reference frame	ICRF2
tidal ocean loading	FES2000
tidal and non-tidal atmosphere loading	VIENNA
estimate zwd within the analysis	yes; as piece-wise linear offsets hourly using relative constraints of 1.5 cm
estimate gradients the VLBI analysis	yes; as piece-wise linear offsets every 6 hours using relative constraints of 0.05 cm

## Explanation of standard approaches

### VieVS standard approach

In this thesis it is quite often referenced to the so-called ”*VieVS* standard approach”. This term refers to a VLBI analysis with *VieVS* using the settings specified in Table A.3. Occasionally, slight deviations of the standard approach are meant, what is always clearly stated in the respective part of the thesis.

### Ray-tracing standard approach

Huge parts of the research outlined in this thesis are based on ray-traced delays created by the ray-tracer *RADIATE*, employing different specifications in obtaining the delays for the various tasks. However, many of these specifications are always equivalent, which are listed in Table A.4 [Hofmeister, 2016] under the name ”ray-tracing standard approach” and are referenced in the text as such.

Table A.4.: *Settings of the ray-tracing standard approach.*

PARAMETER	SPECIFICATION
ray-tracing method	2D piecewise-linear
NWM	ECMWF operational (for all observations since 2008/01/01 (MJD: 54466)), ECMWF ERA Interim Reanalysis (for all earlier observations)
vertical coverage	25 pressure levels in hPa: 1000, 950, 925, 900, 850, 800, 700, 600, 500, 400, 300, 250, 200, 150, 100, 70, 50, 30, 20, 10, 7, 5, 3, 2, 1

## B. Quality of the meteorological data

In the course of this thesis, input from many different meteorological data sources is used. In terms of SA-GPT2w (cf. Chapter 3.2) quantities from empirical models, from NWM and from GNSS data were used. In VLBI analyses, which are performed in several sections throughout this thesis, there is also meteorological data input from NGS files. Unfortunately the different sources do not always agree with each other which endangers the quality of the final results. In some cases differences can be neglected while in other cases outlier tests must be applied. This section is dedicated to the quality of the various data inputs which are utilized throughout this thesis.

### B.1. Problems of the meteorological measurements in the NGS-files

There are some strange errors in the meteorological data of the NGS-files at some points. In the following, some of them are explained in more detail<sup>1</sup>.

- At station WETTZELL, the measured temperature  $T$  suddenly drops to  $-30^{\circ}\text{C}$  for a number of 30 measurements in mid-August 2011. However, pressure  $p$  at that time seems to be correct, but water vapor pressure  $e$  is wrong too, because it is correlated with  $T$  which is one of the three input parameters for its calculation (see Eq. (2.4) on page 6).
- All meteorological data of KOKEE at one epoch of September 11, 2011 (MJD: 55819) are completely wrong. So as not to negatively influence all further investigations, these values of both WETTZELL and KOKEE were manually changed to more realistic ones.
- At some irregular dates, many stations (e.g. HOBART26, SVETLOE, TIGOCONC) do not have meteorological measurements.
- Usually there is one meteorological measurement for each observation, that is, each epoch. Some stations (e.g. ZELENCHK), however, show only one value for  $T$ ,  $p$  and  $e$  for a whole day or for an interval of some hours, even though there were many observations done during that time.

---

<sup>1</sup>this list is not complete; it only covers errors which were detected more or less coincidentally during the analysis for this thesis

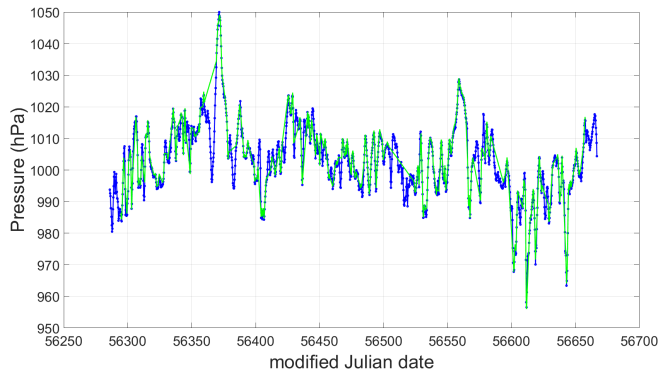


Figure B.1.: *Comparison of pressure from NWM (blue line) and from in situ measurements (green line) for station NYALES20 in 2013. At first sight, the high pressure values of around 1050 hPa look suspicious, however, the in situ measurements show the same result.*

- There are some further gross errors in the NGS data of several stations, but which are not as large as the aforementioned ones.

A practical way to detect flaws in the NGS data is to manually compare it to the (much more trustworthy) NWM data. Figure B.1 shows such a situation. However, although being much more trustworthy than the meteorological data from NGS files there were also flaws in NWM data detected. On February 28, 2008 (MJD: 54524) and March 5, 2008 (MJD: 54530) the temperature and pressure values for arbitrary stations on the whole globe were unrealistically high or low, for example indicating  $-40^{\circ}\text{C}$  and pressures of around 800 hPa at station WETTZELL, which is by far too low for the station's geographical location in south-east Bavaria. Another proof for the failure of the NWM data on these two dates was that all NGS measurements show entirely different, much more realistic values. We subsequently re-downloaded the NWM for these dates, what fixed the problem.

## B.2. Comparing several meteorological data

Comparing meteorological data from several sources to each other illustrates that the different values are anything but consistent. This is most noticeable when comparing NGS data with NWM data, as shown in Fig. B.2 for temperature differences during CONT11. In Fig. B.3 for station WETTZELL during CONT11 also the pressure measurements do not match, here it seems that  $p$  from the NGS-files is generally higher than  $p$  from NWM. Linear interpolation of the NGS data to the NWM epochs<sup>2</sup> allows to make a comparison of the differences in each meteorological quantities between NWM and NGS. Averaging these differences for the time of 2009 through 2014 for the sampling of the stations of CONT11 without FORTLEZA and WARK12M (= 12 stations) constitutes a meaningful picture of the whole situation. The results are shown in Table B.1.

<sup>2</sup>it would also be possible to do the linear interpolation the other way round, that is, interpolating the NWM data to the NGS epochs; this yields very similar results

<sup>3</sup>the  $3 \cdot \sigma$  criterion means, exemplified with temperature  $T$  here, that all values outside  $\bar{T} \pm 3 \cdot \sigma T$  are regarded as outliers

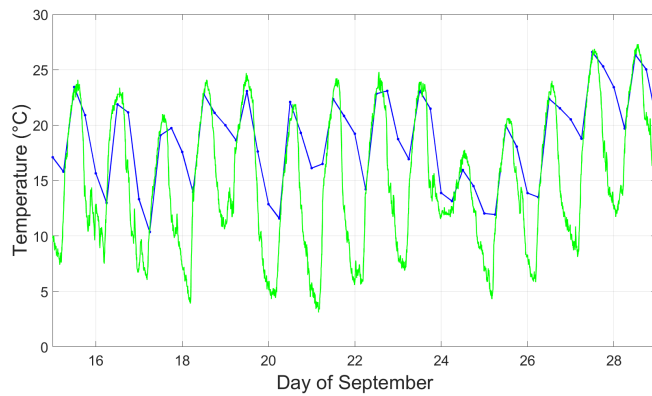


Figure B.2.: Comparison between  $T$  from NWM (blue line) and from NGS files (green line) for VLBI station HARTRAO for the time period of CONT11. As is evident, the temperatures are not consistent. In particular, the extreme values cannot be captured well by the comparatively low temporal resolution of the NWM data.

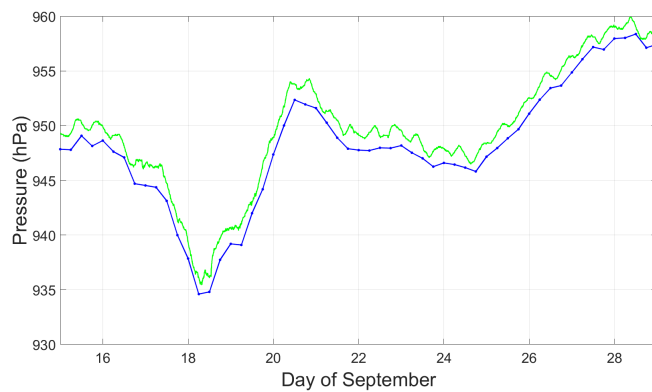


Figure B.3.: Comparison between  $p$  from NWM (blue line) and from NGS files (green line) for VLBI station WETTZELL for the time period of CONT11. Additionally, the pressure values from GPT2w are delineated (red line). It can clearly be seen that the NGS pressures are systematically higher than those from NWM.

Table B.1.: Mean absolute differences between the NWM and NGS data for the three meteorological quantities  $T$ ,  $p$  and  $e$  and the respective biases and standard deviations  $\sigma$ . Outliers were excluded beforehand using the  $3 \cdot \sigma$  criterion<sup>3</sup>.

QUANTITY	MEAN ABS. DIFF.	BIAS	$\sigma$
$T$ (°C)	2.3	-0.6	2.9
$p$ (hPa)	1.4	1.1	1.2
$e$ (hPa)	1.4	0.6	1.6

Interpreting this table allows to draw some conclusions:

- In general,  $p_{NWM}$  and  $p_{NGS}$  coincide best, given the larger value range of pressure than of temperature or water vapor pressure. The reason for this may be that pressure measurements are not so prone to direct sunlight or to rapid temporal changes as  $T$  and  $e$  are.
- As already pointed out before,  $p_{NGS}$  is systematically higher by 1.1 hPa than  $p_{NWM}$ . It appears as if at many VLBI stations the pressure is recorded at the Earth's surface whereas the actual observation is valid for the height of the reference point of the antenna, which is located up to 40 meters aboveground. Tests for several stations showed that this systematic behaviour is reflected in the magnitudes of the pressure differences very well, although no proof is found so far.
- The higher scattering of  $T_{NGS}$  is probably because temperature sensors at the Earth's surface capture more near-ground effects than the NWM, where most data comes from satellites [[ecmwf.com/en/research/data-assimilation/observations](http://ecmwf.com/en/research/data-assimilation/observations), date of access: 2016/12]. Many of these near-ground effects are most likely not relevant for overlying air layers.
- For  $T$  and  $e$  there are also systematic differences between NWM and NGS, however not as distinct as with  $p$ .
- The mean absolute differences and standard deviations between  $T_{NWM}$  and  $T_{NGS}$  are much higher than those of  $e$ , what means that the temperature measurements coincide even less.
- In general, the values from NGS scatter more than the values from NWM at most stations.

## **C. Additional figures**



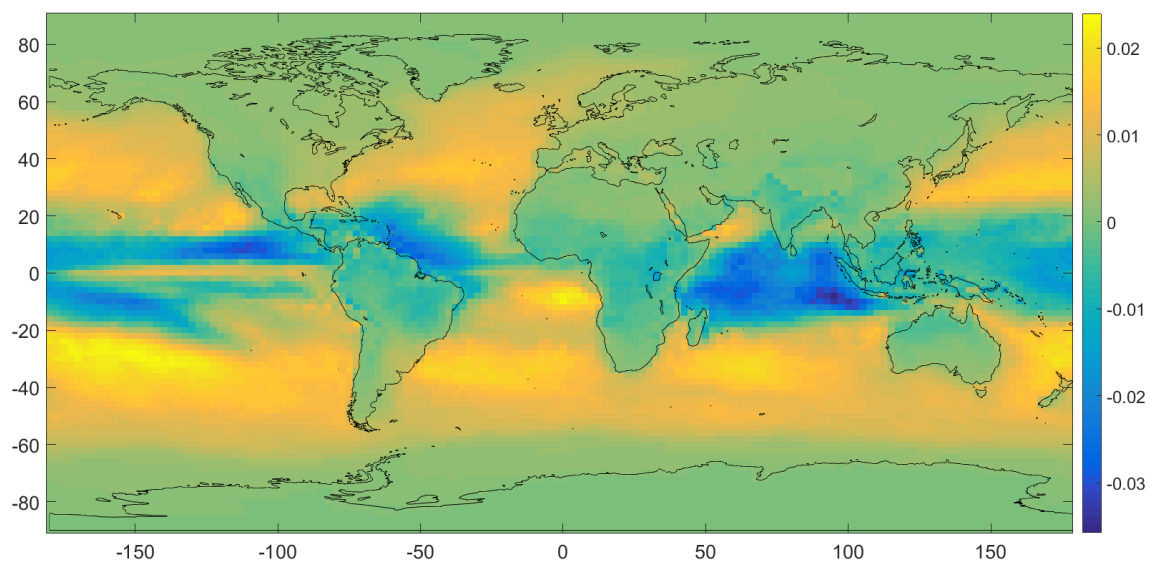


Figure C.1.: Map showing temporally averaged values for the  $M_{zwd}$  coefficient of Eq. (3.4) on page 24. The values are fairly constant on land but vary significantly over the seas, where they are apparently connected to ocean currents.

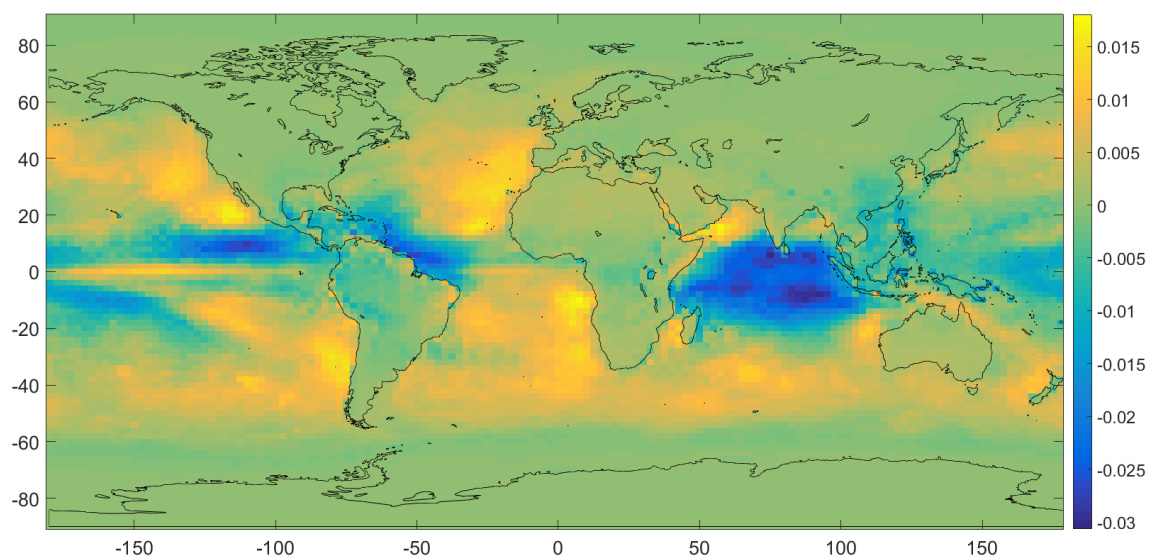


Figure C.2.: Map showing averaged values for the  $M_{zwd1}$  coefficient of Eq. (3.5) on page 24, option A. Also here, the presence of ocean currents may play a dominant role for the  $M$  coefficient. On land, the coefficients vary most in areas close to the coast.

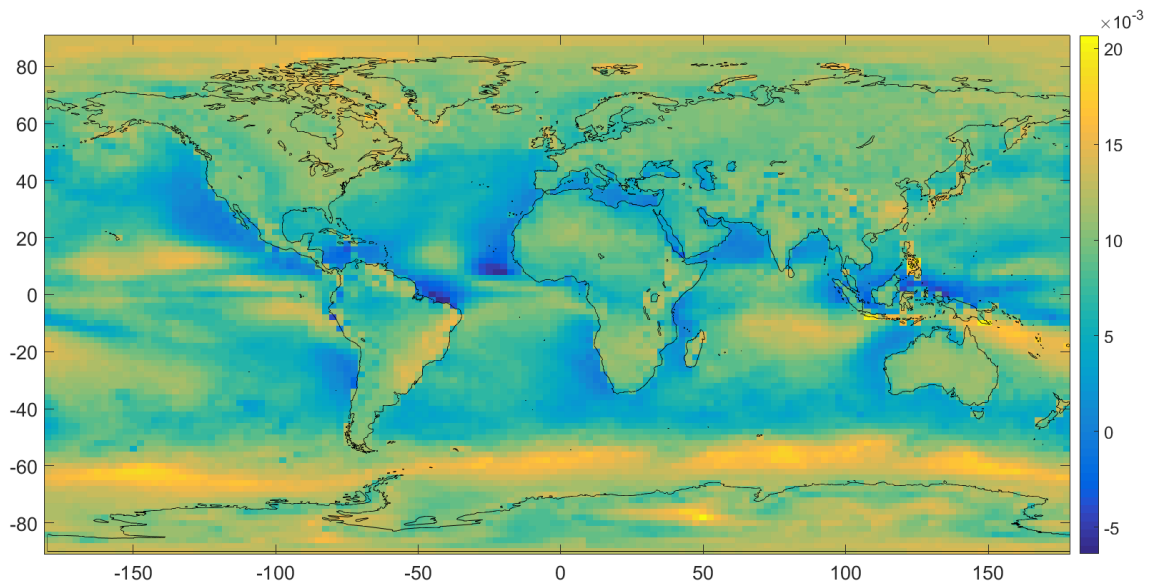


Figure C.3.: Map showing averaged values for the  $M_{zwd_2}$  coefficient of Eq. (3.5) on page 24, option B. The general pattern of this is fairly similar to the plot on top.

# Epilogue

While struggling with the demand of ever-increasing accuracies and knowledges and finding oneself right in the middle of this race, the somehow philosophic question arises whether it is really necessary to eternally seek for further improvements or if there exists a certain point at which one can say with clear conscience that it is enough, that status quo of VLBI or GNSS is sufficient considering the costs it occasions? And even if, where is this point? And who defines it? After all it appears to be a part of human nature to wanting to understand the entirety of the complex processes the universe is equipped with, sometimes approving there is no proper sense behind it. To me as a kind of space researcher, for instance, it is not fully justifiable why spending billions of euros in scanning the sky for redshifts occurring light years away whose existence could possibly hint at the existence of an exoplanet (without wanting to bring discredit on the profession of researchers working in this field), instead of using them for combating the current problems on Earth that we have brought ourselves into; which are not necessarily getting fewer, as everyone who more or less carefully follows the news will notice. Others, perhaps the exoplanet researchers themselves, may in return call into question to which extent it is reasonable to spend three years in deep research in order to ultimately publish troposphere models that are able to describe the propagation path of electromagnetic signals from GNSS more accurate by a factor of  $0.00000000007 (7 \cdot 10^{-11})$ <sup>1</sup>. On the other hand, it is an interaction of precisely these tiny steps that, as a whole, can add up to a major step forward in science, or - on a larger scale - in the evolution of mankind. It would have never been possible to invent the combustion engine without the preparatory work of thousands of cave dwellers spending ages to find out that rubbing two stones against each other can produce a fire; without the uncountable empirical stages which must have been necessary to find out that a flintstone works best for this purpose. It would have never been possible to build up a globally operating aviation system if it had not been for the experiences of countless experimenters taking themselves in the air sitting in their idea of a plane and sailing meter by meter further before inevitably breaking their neck. It would in the same way not have been possible to ever launch the Global Positioning System (GPS) without thousands of researchers worldwide having done the groundwork by gaining knowledge about processes whose importance they perhaps did not even understand yet in the beginning. The accuracy increase owing to VMF3 may likewise constitute an important contribution to further research, albeit it will most likely not herald a new era in geodesy.

---

<sup>1</sup>assuming an elevation angle of  $5^\circ$ , what results in an approximate flight altitude of a GNSS satellite of 27.000 km and a resulting increase in accuracy of 2 mm when using VMF3 instead of VMF1

Whatsoever, for this reason I visualize science as a puzzle consisting of countless pieces; some researchers design the pieces, however small, others fit them together in order to form a whole. Nonetheless, no matter how much intelligence, wisdom, passion and honesty each researcher inputs in his actions, it's crucial to always keep in mind the sense of doing and, most importantly: to never miss the forest for the trees.

# Bibliography

## Books, Papers, Articles

**Askne, J. and H. Nordius (1987)**, *Estimation of tropospheric delay for microwaves from surface weather data*. Radio Sci., Vol. 22, Issue 3, 379–386

**Bevis, M., S. Businger, S. Chiswell, T.A. Herring, R.A. Anthes, C. Rocken, R.H. Ware (1994)**, *GPS meteorology: Mapping zenith wet delays onto precipitable water*. J. Appl. Meteorol. Clim., 33, 379-386

**Böhm, J. (2004)**, *Troposphärische Laufzeitverzögerungen in der VLBI*. Dissertation, Institut für Geodäsie und Geophysik, TU Wien, Supervisor: H. Schuh

**Böhm, J. and H. Schuh (2001)**, *Spherical Harmonics as a Supplement to Global Tropospheric Mapping Functions and Horizontal Gradients*. Proceedings of the 15th Working Meeting on European VLBI for Geodesy and Astrometry, pp. 143-148

**Böhm, J. and H. Schuh (2004)**, *Vienna Mapping Functions in VLBI analyses*. Geophys. Res. Lett., Vol. 31, DOI: 10.1029/2003GL018984

**Böhm, J. and H. Schuh (2007a)**, *Troposphere gradients from the ECMWF in VLBI analysis*. J. Geodesy, Vol. 81:403-408 DOI: 10.1007/s00190-007-0144-2

**Böhm, J. and H. Schuh (2007b)**, *Forecasting data of the troposphere used for IVS Intensive sessions*. In: Böhm J., Pany A., Schuh H. (eds): Proceedings of the 18th European VLBI for geodesy and astrometry working meeting, 12–13 April 2007, Geowissenschaftliche Mitteilungen, Heft Nr. 79, Schriftenreihe der Studienrichtung Vermessung und Geoinformation, Technische Universität Wien, pp 153–157. ISSN 1811–8380

**Böhm, J., M. Ess, H. Schuh (2005)**, *Asymmetric Mapping Functions for CONT02 from ECMWF*. In: Proceedings of the 17th Working Meeting on European VLBI for Geodesy and Astrometry, edited by M. Vennebusch and A. Nothnagel, April 22-23 2005, 64-68

**Böhm, J., B. Werl, H. Schuh (2006a)**, *Troposphere mapping functions for GPS and VLBI from European Centre for Medium-Range Weather Forecasts operational analysis data*. J. Geophys. Res. 111:B02406. DOI: 10.1029/2005JB003629

**Böhm, J., A. Niell, P. Tregoning, H. Schuh (2006b)**, *Global Mapping Function (GMF): A new empirical mapping function based on numerical weather model data*. Geo-

phys. Res. Lett., Vol. 33, DOI: 10.1029/2005GL025546

**Böhm, J., R. Heinkelmann, R. Weber (2007)**, *A Global Model of Pressure and Temperature for Geodetic Applications*. J. Geodesy, Vol. 81, Issue 10, pp. 679–683, DOI: 10.1007/s00190-007-0135-3

**Böhm, J., J. Kouba, H. Schuh (2009)**, *Forecast Vienna Mapping Functions 1 for real-time analysis of space geodetic observations*. J. Geodesy, Vol. 83:397–401, DOI: 10.1007/s00190-008-0216-y

**Böhm, J., H. Spicakova, L. Urquhart, P. Steigenberger, H. Schuh (2011)**, *Impact of A Priori Gradients on VLBI-Derived Terrestrial Reference Frames*. in: Proceedings of the 20th Meeting of the European VLBI Group for Geodesy and Astrometry, W. Alef, S. Bernhart, A. Nothnagel (eds.), Schriftenreihe des Instituts für Geodäsie und Geoinformation der Universität Bonn, Nr. 22, pp. 128-132, ISSN 1864-1113

**Böhm J. et al. (2012)**, *The new Vienna VLBI Software VieVS*. In: Geodesy for Planet Earth, Proceedings of the 2009 IAG Symposium, issued by: International Association of Geodesy Symposia; Springer, ISBN: 978-3-642-20337-4, 1007 - 1012

**Böhm J., Salstein D., M.M. Alizadeh, D.D. Wijaya (2013a)**, *Geodetic and Atmospheric Background*. In: Böhm J., Schuh H. (eds): Atmospheric Effects in Space Geodesy. Springer Verlag, ISBN: 978-3-642-36931-5

**Böhm, J., L. Urquhart, P. Steigenberger, R. Heinkelmann, V. Nafisi, H. Schuh (2013b)**, *A priori gradients in the analysis of space geodetic observations*. Submitted to Proceedings of the IAG Commission 1 Symposium 2010 (REFAG2010), Paris, France, 4-8 October 2010, International Association of Geodesy Symposia Series, X. Collileux, Z. Altamimi (eds.)

**Böhm, J., G. Möller, M. Schindelegger, G. Pain, R. Weber (2015)**, *Development of an improved blind model for slant delays in the troposphere (GPT2w)*. GPS Solut. 19:433. DOI: 10.1007/s10291-014-0403-7

**Chen, G. and T.A. Herring (1997)**, *Effects of atmospheric azimuthal asymmetry on the analysis of space geodetic data*. J. Geophys. Res., Vol. 102, No. B9, Pages 20,489-20,502, September 10, 1997

**Davis, J.L., T.A. Herring, I.I. Shapiro, A.E.E. Rogers, G. Elgered (1985)**, *Geodesy by radio interferometry: Effects of atmospheric modeling errors on estimates of baseline length*. Radio Sci., 20(6): 1593-1607

**Davis, J.L., G. Elgered, A.E. Niell, C.E. Kuehn (1993)**, *Ground based measurement of gradients in the "wet" radio refractivity of air*. Radio Sci., Vol. 28, No. 6, Pages 1003-101

**Dousa, J. and M. Elias (2014)**, *An improved model for calculating tropospheric wet delay*. Geophys. Res. Lett., 41, 4389–4397, doi:10.1002/2014GL060271

- Eriksson, D., D.S. MacMillan, J.M. Gipson (2014)**, *Tropospheric delay ray tracing applied in VLBI analysis*. J. Geophys. Res. Solid Earth, 119, 9156–9170, doi:10.1002/2014JB011552
- Fleming, K., Z. Martinec, J. Hagedoorn (2004)**, *Geoid displacement about Greenland resulting from past and present-day mass changes in the Greenland Ice Sheet*. Geophys. Res. Lett., Vol. 31, L06617, DOI:10.1029/2004GL019469
- Geerts, B. and E. Linacre (1997)**, *The Height of the Tropopause*, University of Wyoming, Atmospheric Science
- Gegout, P., R. Biancale, L. Soudarin (2011)**, *Adaptive mapping functions to the azimuthal anisotropy of the neutral atmosphere*. J. Geodesy, Vol. 85, pp. 661–677, DOI: 10.1007/s00190-011-0474-y
- Greimeister, P. (2016)**, *Trends of Atmospheric Water Vapor from VLBI and GPS*. Diploma Thesis, Department of Geodesy and Geoinformation, TU Wien, Supervisor: J. Böhm
- Hackman, C., G. Guerova, S.M. Byram, J. Dousa, U. Hugentobler (2015)**, *International GNSS Service (IGS) Troposphere Products and Working Group Activities*. FIG Working Week 2015, "From the Wisdom of the Ages to the Challenges of the Modern World", Sofia, Bulgaria, 17-21 May 2015
- Hackman, C. and S.M. Byram (2014)**, *Troposphere Working Group Technical Report 2014*. In: Jean J., Dach R. (eds): IGS Technical Report 2014.
- Heinkelmann, R. (2008)**, *Bestimmung des atmosphärischen Wasserdampfes mittels VLBI als Beitrag zur Klimaforschung*. Dissertation, Institut für Geodäsie und Geophysik, TU Wien, Supervisor: H. Schuh
- Heinkelmann, R. and V. Tesmer (2013)**, *Systematic inconsistencies between VLBI CRF and TRF solutions caused by different analysis options*. In: Reference Frames for Applications in Geosciences, pp. 181-189, Springer Berlin Heidelberg
- Heiskanen, W.A. and H. Moritz (1967)**, *Physical Geodesy*. W.H. Freeman and Company San Francisco
- Herring, T.A. (1992)**, *Modeling atmospheric delays in the analysis of space geodetic data*. In: *Publications on Geodesy*, Vol. 36, *Proceedings of Refraction of Transatmospheric Signals in Geodesy*, edited by J. C. DeMunck and T.A. Th. Spoelstra, pp. 157-164, Netherlands Geodetic Commission Publications in Geodesy, The Hague, Netherlands
- Hobiger, T. and T. Otsubo (2014)**, *Combination of GPS and VLBI on the observation level during CONT11 — common parameters, ties and inter-technique biases*. J. Geodesy, Vol. 88: 1017. DOI:10.1007/s00190-014-0740-x
- Hobiger, T., R. Ichikawa, T. Takasu, Y. Koyama, T. Kondo (2008a)**, *Ray-traced troposphere slant delays for precise point positioning*. Earth Planets Space, Vol. 60, e1–e4

- Hobiger, T., R. Ichikawa, Y. Koyama, T. Kondo (2008b)**, *Fast and accurate ray-tracing algorithms for real-time space geodetic applications using numerical weather models*. J. Geophys. Res., 113, D20302, DOI:10.1029/2008JD010503
- Hofmann-Wellenhof, B. and Moritz H. (2005)**, *Physical Geodesy*. Springer-Verlag Wien - New York, ISBN: 3-211-23584-1
- Hofmann-Wellenhof, B., H. Lichtenegger, J. Collins (1992)**, *GPS. Theory and Practice*. Springer-Verlag Wien
- Hofmeister, A. (2016)**, *Determination of path delays in the atmosphere for geodetic VLBI by means of ray-tracing*. PhD thesis. Department für Geodäsie und Geoinformation, Fakultät für Mathematik und Geoinformation, Technische Universität Wien.
- Jean, Y. and R. Dach (eds.) (2016)**, *International GNSS Service Technical Report 2015 (IGS Annual Report)*. IGS Central Bureau and University of Bern; Bern Open Publishing DOI: 10.7892/boris.80307
- Jones, F.E. (1981)**, *The refractivity of Air*. J. Res. Nat. Bur. Stand., Vol. 86, No.1
- Kouba, J. (2008)**, *Implementation and testing of the gridded Vienna Mapping Function 1 (VMF1)*. J. Geodesy, Vol. 82:193–205, DOI: 10.1007/s00190-007-0170-0
- Kraus, H. (2004)**, *Die Atmosphäre der Erde: eine Einführung in die Meteorologie*. Springer Verlag
- Lagler, K., M. Schindelegger, J. Böhm, H. Krasna, T. Nilsson (2013)**, *GPT2: empirical slant delay model for radio space geodetic techniques*. Geophys. Res. Lett. 40(6):1069–1073. DOI: 10.1002/grl.50288
- Landskron, D., G. Möller, A. Hofmeister, J. Böhm, R. Weber (2015a)**, *Refined and Site-Augmented Tropospheric Delay Models for GNSS*. Proceedings of the 5th International Galileo Science Colloquium, Braunschweig, Deutschland; 2015-10-27 - 2015-10-29;
- Landskron, D., G. Möller, A. Hofmeister, J. Böhm, R. Weber (2015b)**, *Refined and site-augmented tropospheric delay models in the analysis of VLBI observations*. 26th IUGG General Assembly , Prague, Czech Republic; 2015-06-22 - 2007-07-02
- Landskron, D., A. Hofmeister, J. Böhm (2015c)**, *Refined Tropospheric Delay Models for CONT11*. International Association of Geodesy Symposia pp 1-5, Springer Berlin Heidelberg, DOI: 10.1007/1345\_2015\_56
- Landskron D., G. Möller, A. Hofmeister, J. Böhm, R. Weber (2016a)**, *Refined and site-augmented tropospheric delay models for GNSS applications*. Poster: IGS Workshop 2016, Sydney, Australia; 2016-02-08 - 2016-02-12
- Landskron, D., A. Hofmeister, D. Mayer, J. Böhm (2016b)**, *Six hourly time series of horizontal troposphere gradients in VLBI analysis*. European Geosciences Union General Assembly 2016, Vienna, 2016-04-17 - 2016-04-22



- Landskron, D., A. Hofmeister, J. Böhm (2016c)**, *Can VMF1 be improved by the use of new ray-tracing data?*. IAG Commission 4 Symposium, Wroclaw, Poland, 2016-09-04 - 2016-09-07
- Landskron, D., G. Möller, A. Hofmeister, J. Böhm, R. Weber (2016d)**, *Site-Augmentation of Empirical Tropospheric Delay Models in GNSS*. Österreichische Zeitschrift für Vermessung und Geoinformation (VGI), No. 3/2016, pp. 128-135
- MacMillan, D.S. (1995)**, *Atmospheric gradients from very long baseline interferometry observations*. Geophys. Res. Lett. 22(9):1041–1044
- MacMillan, D.S. and C. Ma (1997)**, *Atmospheric gradients and the VLBI terrestrial and celestial reference frames*. Geophys. Res. Lett., Vol. 24, No. 4, pp. 453-456, DOI: 10.1029/97GL00143
- Marini, J.W. (1972)**, *Correction of satellite tracking data for an arbitrary tropospheric profile*. Radio Sci., Vol. 7, No. 2, pp. 223-231
- Marini, J.W. and C.W. Murray (1973)**, *Correction of laser range tracking data for atmospheric refraction at elevation angles above 10°*. Technical Report X-591-73-351, NASA
- Niell, A.E. (1996)**, *Global mapping functions for the atmosphere delay at 310 radio wavelengths*. J. Geophys. Res., 101, 3227–3246
- Niell, A.E. (2000)**, *Improved atmospheric mapping functions for VLBI and GPS*. Earth Planets Space, Vol. 52, Issue 10, pp 699–702
- Nilsson, T., J. Böhm, D.D. Wijaya, A. Tresch, V. Nafisi, H. Schuh (2013)**, *Path Delays in the Neutral Atmosphere*. In: Böhm J., Schuh H. (eds): Atmospheric Effects in Space Geodesy. Springer Verlag, ISBN: 978-3-642-36931-5
- Rocken, C., S. Sokolovskiy, J.M. Johnson, D. Hunt (2001)**, *Improved mapping of tropospheric delays*. J. Atmos. Ocean Tech., Vol. 18, 1205–1213, DOI: 10.1175/1520-0426(2001)018<1205:IMOTD>2.0.CO;2
- Saastamoinen, J. (1972)**, *Atmospheric correction for the troposphere and stratosphere in radio ranging of satellites*. In S.W. Henriksen et al., editors, *The use of Artificial Satellites for Geodesy*, Vol. 15, pp. 247-251, AGU, Washington, D.C.
- Sachs, L. (1974)**, *Angewandte Statistik*. Springer Verlag Berlin Heidelberg New York
- Santer, B.D., M.F. Wehner, T.M.L. Wigley, R. Sausen, G.A. Meehl, K.E. Taylor, C. Ammann, J. Arblaster, W.M. Washington, J.S. Boyle, W. Brüggemann (2003)**, *Contributions of Anthropogenic and Natural Forcing to Recent Tropopause Height Changes*. Science, Vol. 301, Issue 5632, pp. 479-483, DOI: 10.1126/science.1084123
- Santos, M.C., M. McAdam, J. Böhm (2012)**, *Implementation Status of the UNB-VMF1*. European Geosciences Union General Assembly 2012, Vienna, 2012-04-22 - 2016-

04-27

**Schunk, R.W. and A.F. Nagy (2009)**, *Ionospheres. Physics, Plasma Physics, and Chemistry. Second Edition*. Cambridge Atmospheric and Space Science Series, Cambridge University Press, ISBN: 978-0-521-87706-0

**Selsis, F. (2011)**, *Neutral Atmosphere*. In: Gargaud, M. (Editor-in-Chief) et al.: Encyclopedia of Astrobiology. Second Edition, Springer Berlin Heidelberg, pp. 1112-1112, DOI: 10.1007/978-3-642-11274-4.1050

**Spicakova, H., L. Plank, T. Nilsson, J. Böhm, H. Schuh (2011)**, *Terrestrial reference frame solution with the Vienna VLBI Software VieVS and implication of tropospheric gradient estimation*. Proceedings of the 20th Meeting of the European VLBI Group for Geodesy and Astrometry (EVGA)

**Sweet, W.V., R.E. Kopp, C.P. Weaver, J. Obeysekara, R.M. Horton, E.R. Thieler, C. Zervas (2017)**, *Global and regional sea level rise scenarios for the United States*. NOAA Technical Report National Ocean Service CO-OPS 083, Silver Spring, Maryland

**Teke, K., R. Heinkelmann, J. Böhm, H. Schuh (2008)**, *VLBI Baseline Length Repeatability Tests of IVS-R1 and -R4 Session Types*. In: 'Measuring the Future', Proceedings of the 5th IVS General Meeting, A. Finkelstein and D. Behrend (Eds.), ISBN 978-5-02-025332-2, pp. 173-177

**Teke, K., J. Böhm, T. Nilsson, H. Schuh, P. Steigenberger, R. Dach, R. Heinkelmann, P. Willis, R. Haas, S. García-Espada, T. Hobiger, R. Ichikawa, S. Shimizu (2011)**, *Multi-technique comparison of troposphere zenith delays and gradients during CONT08*, Journal of Geodesy, Vol. 85(7):395-413, doi:10.1007/s00190-010-0434-y

**Torge, W. (1991)**, *Geodesy. 2nd Edition*. Walter de Gruyter & Co, Berlin, ISBN: 3-11-012408-4

**Urquhart, L., F.G. Nievinski, M.C. Santos (2014a)**, *Assessment of troposphere mapping functions using three-dimensional ray-tracing*. GPS Solut., Vol. 18:345-354, DOI: 10.1007/s10291-013-0334-8

**Urquhart, L., M.C. Santos, F.G. Nievinski, J. Böhm (2014b)**, *Generation and Assessment of VMF1-Type Grids Using North-American Numerical Weather Models*. IAG Symp., Vol. 139, Pages 3-12, DOI: 10.1007/978-3-642-37222-3\_1

**Zus, F., G. Dick, J. Dousa, S. Heise, J. Wickert (2014)**, *The rapid and precise computation of GPS slant total delays and mapping factors utilizing a numerical weather model*. Radio Sci., 49, 207-216, doi:10.1002/2013RS005280

**Zus, F., G. Dick, J. Dousa, J. Wickert (2015)**, *Systematic errors of mapping functions which are based on the VMF1 concept*. GPS Solut. 19: 277. DOI: 10.1007/s10291-014-0386-4

## Websites

[earth-info.nga.mil/GandG/wgs84/gravitymod/egm2008](http://earth-info.nga.mil/GandG/wgs84/gravitymod/egm2008), Official website of the Earth Gravitational Model 2008 (EGM2008). Last access: 2014/10

<ftp://cddis.gsfc.nasa.gov/gnss/products>, GNSS data and products archive of the Crustal Dynamics Data Information Center (CDDIS) at Goddard Space Flight Center (GSFC). Last access: 2016/08

[ecmwf.com](http://ecmwf.com), Official website of the European Center for Medium-Range Weather Forecasts (ECMWF). Last access: 2017/01.

[ggosatm.hg.tuwien.ac.at/DELAY/](http://ggosatm.hg.tuwien.ac.at/DELAY/), Data archive of the GGOSATM project of TU Wien. Last access: 2016/09

[igs.org](http://igs.org), Official website of the International GNSS Service (IGS). Last access: 2016/11

[ivscc.gsfc.nasa.gov](http://ivscc.gsfc.nasa.gov), Homepage of the "International VLBI service for Geodesy & Astrometry" (IVS). Last access: 2016/11

[mathworks.com](http://mathworks.com), Homepage of the Makers of MATLAB and Simulink. Last access: 2016/12

<https://de.wikipedia.org/>, German Homepage of Wikipedia, The Free Encyclopedia. Last access: 2016/11



# List of Figures

2.1	<i>Comparison of the simple mapping function approach <math>mf(\varepsilon) = \frac{1}{\sin(\varepsilon)}</math> with the hydrostatic VMF1, in this case exemplarily for VLBI station WETTZELL on September 15, 2011, 00:00. It can be seen that the mapping functions diverge particularly at low elevations. . . . .</i>	7
2.2	<i>From Nilsson et al. [2013]: the context between a horizontal gradient <math>G</math> and the resulting angle <math>\beta</math> from zenith direction. In this way the signal experiences an additional delay that equals <math>mf_g(\varepsilon) = mf_h(\varepsilon) \cdot \cot(\varepsilon)</math>, what corresponds to the assumption of MacMillan [1995] (Eq. (2.10)). . . . .</i>	15
3.1	<i>Flow chart of the general principle of the site-augmentations of GPT2w and VMF1. . . . .</i>	17
3.2	<i>Map of 19 VLBI stations which are used for calculating new coefficients for the MTT mapping function by means of a least-squares adjustment. . . . .</i>	18
3.3	<i>An extract of a VLBI VMF1-file of the year 2011. There is one such file per year since 1979, each containing VMF1 data for more than 100 VLBI stations in a temporal resolution of four epochs per day. . . . .</i>	21
3.4	<i>Correlation between surface temperature <math>T</math> and the mapping function coefficient <math>a_h</math>. Here, the blue points mark all 1460 NWM epochs of the year 2011 for VLBI station WETTZELL, each with their respective temperatures on the <math>x</math>-axis and <math>a_h</math> coefficients on the <math>y</math>-axis. Their close-to-line alignment reveals a clear correlation between the two datasets. In fact, the correlation coefficient for these points is 0.91. . . . .</i>	22
3.5	<i>Correlation between surface water vapor pressure <math>e</math> and zenith wet delay <math>\Delta L_w^z</math>. Here, again, the blue points mark all 1460 NWM epochs of the year 2011 for VLBI station WETTZELL, each with their respective water vapor pressures on the <math>x</math>-axis and zenith wet delays on the <math>y</math>-axis. Their close-to-line alignment reveals a clear correlation between the two datasets. In fact, the correlation coefficient for these points is also 0.91 [Landskron et al., 2016d]. . . . .</i>	23
3.6	<i>Correlation between surface temperature <math>T</math> and the zenith wet delays <math>\Delta L_w^z</math>. This correlation is not as distinct as with water vapor pressure, the correlation coefficient for these points of same data as in Figs. 3.4 and 3.5 is only 0.74 [Landskron et al., 2016d]. . . . .</i>	23

- 3.7 *Map of 19 VLBI stations which are used for the determination of the  $M$  coefficients for SA-GPT2w in least-squares adjustments. VLBI station PENTICTN has not carried out any observation, and stations FD-VLBA and URUMQI have only contributed with a few observations in the specified time window, but as the VMF1-files are available for these stations in the same way as for all the others, they are included. . . . . 25*
- 3.8 *Plot for the seasonal behaviour of the  $M_{a_h}$  coefficient. The different colours each represent one year. . . . . 27*
- 3.9 *Map showing temporally averaged values for the  $M_{a_h}$  coefficient of Eq. (3.3). The values vary especially over the seas, where it is apparently connected to ocean currents. On land, the values only slightly deviate around the equator. 27*
- 3.10 *Map of 14 VLBI stations that were selected for assessing the performance of SA-GPT2w. . . . . 30*
- 3.11 *Comparison of zenith wet delays  $\Delta L_w^z$  for station WETTZELL during the first quarter of 2011. It can be seen that when using the in situ meteorological measurements, the curve of SA-GPT2w approximates that of the VMF1-files much better than the empirical GPT2w does, which appears as a kind of averaged curve. . . . . 32*
- 3.12 *Comparison of several zenith wet delays  $\Delta L_w^z$  for station HOBART12 during the VLBI campaign CONT11. Here as well, in situ meteorological measurements get the curve of SA-GPT2w to approximate the VMF1-files much better than GPT2w alone does. . . . . 33*
- 3.13 *Map of 29 IGS stations that each have a close-by weather station in order to estimate the performance of SA-GPT2w for GNSS applications. . . . . 36*
- 3.14 *Comparison of  $\Delta L_w^z$  from various sources for IGS station BZRG in Bolzano, Italy during the first quarter of 2013: the true  $\Delta L_w^z$  (dark blue), the empirical  $\Delta L_w^z$  from GPT2w (red), the  $\Delta L_w^z$  augmented by using in situ measured  $T$  (green) and the  $\Delta L_w^z$  augmented by using in situ measured  $T$  and  $e$  (light blue) [Landskron et al., 2016d]. . . . . 36*
- 3.15 *Top: Station-wise improvement in  $\Delta L_w^z$  (%) of SA-GPT2w 1 compared to GPT2w only, using the universal  $M$  coefficient. Bottom: Station-wise improvement in  $\Delta L_w^z$  (%) of SA-GPT2w 2 compared to GPT2w only, also using the universal  $M$  coefficients. . . . . 37*
- 3.16 *Map of 26 selected IGS stations that are equipped with temperature, pressure and humidity sensors in order to estimate the performance of SA-GPT2w for GNSS applications. . . . . 39*

- 3.17 *Comparison of  $\Delta L_w^z$  from various sources for IGS station DAV1 at Davis Station in Antarctica during the first quarter of 2013: the true  $\Delta L_w^z$  (dark blue), the empirical  $\Delta L_w^z$  from GPT2w (red), the  $\Delta L_w^z$  augmented by using in situ measured  $T$  (green) and the  $\Delta L_w^z$  augmented by using in situ measured  $T$  and  $e$  (light blue). As this station is located at a very high latitude ( $-68^\circ 34' 48''$ ) what involves a generally lower water vapor content of the air, measuring  $T$  alone yet augments the empirical delay very well, although in some places the correlation is very low. . . . . 39*
- 3.18 *Map of 45 IGS stations that were selected for analyzing the potential of meteorological quantities from NWM as input for SA-GPT2w in order to augment empirical  $\Delta L_w^z$ . These stations are simply those of the two previous GNSS comparisons combined. . . . . 41*
- 3.19 *Map of 13 IGS stations that were selected for analyzing the potential of site-augmented GPT2w for GNSS stations located close to the equator. The meteorological quantities as input for SA-GPT2w in order to augment empirical  $\Delta L_w^z$  come from NWM. . . . . 42*
- 3.20 *The red line shows  $\Delta L_w^z$  as determined by the Lagrange interpolation (red dots represent NWM epochs), while the blue line shows a possible progression of the real  $\Delta L_w^z$ . The difference between the black dot and the blue dot then marks the error in the modeled  $\Delta L_w^z$ . . . . . 47*
- 3.21 *Context between  $T$  and  $a_h$  (top) and between  $e$  and  $\Delta L_w^z$  (bottom) for VLBI station WETTZELL during first half of 2013. . . . . 47*
- 3.22 *Exemplary  $T$  from in situ measurement (green) and from NWM (red) at station WETTZELL in early 2011. The  $T_{int}$  are linearly interpolated from the observational data to the NWM epochs, and it can be seen that they are considerably different from the respective NWM values. The green dot  $T_X$  marks an exemplary point for which the augmented VMF1 shall be applied. 48*
- 4.1 *From Nilsson et al. [2013]: The geometric principle of the piecewise linear ray-tracing approach which is used as the basis for the determination of mapping functions. Note that the refractivity changes only with every height level (pressure level). For reasons of simplicity, here only the 1D case is shown. . . . . 54*
- 4.2 *Parameters of the seasonal fit for the mapping function coefficient  $b_h$ . Top left: mean values  $A_0$ , top right: annual amplitude  $A_1$ , center left: annual amplitude  $B_1$ , center right: semi-annual amplitude  $A_2$ , bottom left: semi-annual amplitude  $B_2$ . . . . . 61*
- 4.3 *Data fitting of  $b_h$  exemplarily for the grid point  $\varphi = 7.5^\circ$  and  $\lambda = 237.5^\circ$  from 2001 to 2004. . . . . 61*

- 4.4 *Standard deviations of the parameters of the seasonal fit for the mapping function coefficient  $b_h$ . Left: standard deviation of mean values  $A_0$ , right: standard deviation of the amplitudes  $A_1$ ,  $B_1$ ,  $A_2$  and  $B_2$ , all of which are equivalent. It is obvious that the amplitudes generally have a higher standard deviation than the mean values. At a rough estimate, given the uncertainty of  $2 \cdot 10^{-6}$  in  $A_0$  and of  $5 \cdot 10^{-6}$  in all amplitudes of  $b_h$  (as is the case at the poles), the resulting slant hydrostatic delay at  $5^\circ$  elevation would change at worst by 3 mm. . . . . 62*
- 4.5 *The effect of filtering using the example of the parameter  $A_0$  of  $b_h$ ; left: the original grid (corresponds to the top left plot in Fig. 4.2), right: the grid after applying a 2D median filter. . . . . 62*
- 4.6 *Spherical harmonics of the coefficient  $b_h$  for increasing degrees  $n$  of expansion at the arbitrary epoch January 15, 2001 (MJD: 51924). Top left: degree  $n = 1$ , top right: degree  $n = 4$ , center left: degree  $n = 8$ , center right: final degree  $n_{max} = 12$ . Bottom: the original grid which is to be represented by the spherical harmonics. . . . . 65*
- 4.7 *Mean values  $A_0$  (top left), seasonal amplitudes  $A_1$  (top right), half-seasonal amplitudes  $A_2$  (bottom left) and standard deviation of the residuals of  $A_0$  (bottom right) of the hydrostatic mapping function coefficient  $a_h$  from GPT3. At a rough estimate, given the uncertainty of  $6 \cdot 10^{-7}$  in  $A_0$  and of  $8 \cdot 10^{-7}$  in all amplitudes of  $a_h$  (as is the case at the poles), the resulting slant hydrostatic delay at  $5^\circ$  elevation would change at worst by 4 mm. . . . . 68*
- 4.8 *Mean values  $A_0$  (top left), seasonal amplitudes  $A_1$  (top right), half-seasonal amplitudes  $A_2$  (bottom left) and standard deviation of the residuals of  $A_0$  (bottom right) of the wet mapping function coefficient  $a_w$  from GPT3. At a rough estimate, given the uncertainty of  $3 \cdot 10^{-6}$  in  $A_0$  and of  $4 \cdot 10^{-6}$  in all amplitudes of  $a_h$  (as is the case over North Africa), the resulting slant wet delay at  $5^\circ$  elevation would change at worst by 0.3 mm. . . . . 68*
- 4.9 *Map of all VLBI stations which performed observations in the 1338 sessions between 2006 and 2014; intensive sessions and a set of stations which do not meet the defined requirements are not considered here. . . . . 73*
- 4.10 *Differences in slant delays at  $5^\circ$  elevation between VMF1<sub>repro</sub> (left) and VMF3 (right) to the ray-traced delays, averaged over all 120 epochs (= bias). Top: differences in slant total delay  $\Delta L$ , center: differences in slant hydrostatic delay  $\Delta L_h$ , and bottom: differences in slant wet delay  $\Delta L_w$  [Landskron et al., 2016c]. . . . . 76*
- 4.11 *Standard deviation  $\sigma$  of the differences in slant delays at  $5^\circ$  elevation between VMF1<sub>repro</sub> (left) and VMF3 (right) to the ray-traced delays, averaged over all 120 epochs. Top:  $\sigma$  for slant total delay  $\Delta L$ , center:  $\sigma$  for slant hydrostatic delay  $\Delta L_h$ , and bottom:  $\sigma$  for slant wet delay  $\Delta L_w$  [Landskron et al., 2016c]. . . . . 77*



- 4.12 *Differences in slant delays at 5° elevation between VMF3 (left) and VMF3<sub>LSM</sub> (right) to the ray-traced delays, averaged over all 120 epochs. Top: bias in slant total delay  $\Delta L$ , center top: bias in slant hydrostatic delay  $\Delta L_h$ , center bottom: bias in slant wet delay  $\Delta L_w$  and bottom: standard deviation in slant total delay  $\Delta L$ . The general shape is the same, but the amplitudes of VMF3<sub>LSM</sub> are slightly lower in bias as well as in standard deviation. . . . .* 78
- 4.13 *Differences in slant delays at 5° elevation between GPT2w (left) and GPT3 (right) to the ray-traced delays, averaged over all 120 epochs (= bias). Top: bias in slant total delay  $\Delta L$ , center top: bias in slant hydrostatic delay  $\Delta L_h$ , center bottom: bias in slant wet delay  $\Delta L_w$  and bottom: standard deviation in slant total delay  $\Delta L$ . The bias is significantly reduced with GPT3 but the standard deviation is only slightly lower. . . . .* 79
- 4.14 *Map of all 33 VLBI stations that were selected for the comparison of slant delays w.r.t. ray-traced delays from 1999-2014. . . . .* 81
- 4.15 *Left: the 32 ray vectors that were generated for each considered grid point of the global 5° × 5° grid. Right: the 112 ray vectors that were generated for each active VLBI station from 1999-2014. As usual for this purpose, lower elevations are covered more densely than higher elevations since they are greatly influenced by azimuthal asymmetry. . . . .* 82
- 4.16 *Mean differences in slant hydrostatic delays (top) and slant wet delays (bottom) at 5° elevation between VMF1<sub>repro</sub> (left) and VMF3 (right) to the ray-traced delays. VMF3 outperforms VMF1<sub>repro</sub> at 25 of the 33 stations in hydrostatic as well as wet delay. . . . .* 85
- 4.17 *Mean differences in slant hydrostatic delays (top) and slant wet delays (bottom) at 5° elevation between VMF3 (left) and VMF3<sub>LSM</sub> (right) to the ray-traced delays. Interestingly, this leads to a general improvement at every single station. . . . .* 85
- 4.18 *Mean differences in slant hydrostatic delays (top) and slant wet delays (bottom) at 5° elevation between VMF1<sub>repro</sub> (left) and VMF3<sub>LSM</sub> (right) to the ray-traced delays. VMF3<sub>LSM</sub> outperforms VMF1<sub>repro</sub> at 27 of the 33 stations in hydrostatic delay and at all stations in wet delay. . . . .* 86
- 4.19 *Mean differences in slant hydrostatic delays (top) and slant wet delays (bottom) at 5° elevation between GPT2w (left) and GPT3 (right) to the ray-traced delays. GPT3 improves slant hydrostatic delays at 17 of the 33 stations and slant wet delays at 15 of the 33 stations compared to GPT2w. . . . .* 86
- 5.1 *Comparison of horizontal north (top) and east (bottom) gradients for VLBI station WETTZELL derived by using total slant delays (red line) and separated slant delays (blue line) during CONT11. The dashed lines represent the hydrostatic and wet parts of the gradients from the separated approach. Additionally, there are errorbars for the standard deviations (for better visibility only plotted for the separated approach). . . . .* 95

- 5.2 Comparison of horizontal north (top) and east (bottom) gradients derived by using slant total delays for the standard elevation angles [ $3^\circ$ ,  $5^\circ$ ,  $7^\circ$ ,  $10^\circ$ ,  $15^\circ$ ,  $30^\circ$ ,  $70^\circ$ ] (red line) and for additionally adding the elevation angles [ $1^\circ$ ,  $2^\circ$ ] (green line) for VLBI station WETTZELL (Wetzell, Bavaria, Germany) during CONT11. . . . . 95
- 5.3 Comparison of horizontal total north (top) and east (bottom) gradients from ray-tracing (red line) to the LHG by Böhm and Schuh [2007a] (cyan line) for VLBI station NYALES20 (Ny Alesund, Svalbard, Norway) during CONT11. 96
- 5.4 Comparison of the various gradients for station WESTFORD (Westford, Massachusetts, USA) for the time period of CONT11. . . . . 98
- 5.5 Comparison of the residuals in slant total delays for station WESTFORD (Westford, Massachusetts, USA) for the epoch September 26, 2011, 18:00 GMT [Landskron et al., 2015b]. Top left: residuals after subtraction of a mean over the 16 constantly distributed azimuths without applying any gradient formula; simply put, the yellow and blue amplitudes show the presence of azimuthal asymmetry, and it is obvious that its influence is highest for low-elevation observations. The high residuals in north ( $0^\circ$  azimuth) and south ( $180^\circ$  azimuth) direction are mainly a result of the high latitude location of the site and the consequent effect of the atmospheric bulge. Top right: residuals after applying gradients by using the standard gradient formula (GRAD-1); this lowers the residuals significantly, what means that thus the bulk of azimuthal asymmetry is explained. However, small amplitudes between the cardinal points remain. Bottom left: residuals after applying gradients by using the second gradient formula (GRAD-2); again, the residuals are lowered considerably, also the amplitudes between the cardinal directions almost vanish. Bottom right: residuals after applying gradients by using the third gradient formula (GRAD-3); the residuals hardly change compared to the second gradient formula. . . . . 99
- 5.6 Comparison of mean absolute residuals that arise from azimuthal asymmetry averaged over all stations and epochs of CONT11. Left: comparison of the residuals for the different gradient models. Right: the percental improvement of the gradient models w.r.t. no consideration of azimuthal asymmetry. 100
- 5.7 Comparison of the horizontal north (top) and east (bottom) gradients from ray-traced delays (red line) and from estimation in VLBI analysis using VieVS for all three a priori gradient approaches (dotted green, cyan and blue line) for VLBI station ONSALA60 (Onsala, Sweden) during CONT11. 101
- 5.8 Station-wise improvement in BLR from VLBI analyses when using GRAD-2 instead of using no a priori gradients for the time period of CONT11. Referring to Table 5.2 this corresponds to the use of approach 1.d instead of 1.a. All bars above zero imply improved repeatability of the respective baselines for GRAD-2. . . . . 102

- 5.9 Comparison of horizontal north (top) and east (bottom) gradients between the gradients calculated on the basis of  $0.125^\circ \times 0.125^\circ$  NWM (red line) and those calculated on the basis of  $1^\circ \times 1^\circ$  NWM (black line) for VLBI station YEBES40M (Yebes, Spain) during CONT11. . . . . 105
- 5.10 Station-wise  $\Delta$ BLR from VLBI analyses when using GRAD ( $1^\circ \times 1^\circ$ ) instead of GRAD ( $0.125^\circ \times 0.125^\circ$ ) for the time period of CONT11. Referring to Table 5.2 this corresponds to the use of approach 1.c instead of 1.c2. All bars above zero imply improved repeatability of the respective baselines for the  $1^\circ \times 1^\circ$  version. . . . . 106
- 5.11 Station-wise  $\Delta$ BLR from VLBI analyses for ray-traced delays for all 1338 sessions from 2006-2014. Dots below zero indicate that BLR degrade when estimating gradients in the analysis. . . . . 108
- 5.12 Gradients GRAD on a global grid averaged over all 120 epochs. Top left:  $G_{n_h}$  is most pronounced in higher latitudes, while its effect in the tropics is very low. On the other hand,  $G_{n_w}$  (bottom left) is most dominant in the near-equator regions. The hydrostatic and wet east gradients  $G_{e_h}$  and  $G_{e_w}$  (top right and bottom right) are generally lower and exhibit a rather unsystematic behaviour than their counterparts. . . . . 113
- 5.13 Bias (top) and standard deviation (bottom) of the residuals in slant total delay at  $5^\circ$  elevation and  $180^\circ$  azimuth. Top left: bias of residuals between ray-tracing and azimuthal symmetry: in the Northern Hemisphere, the residuals are generally positive while in the Southern Hemisphere they are negative; this is due to the atmospheric bulge. Top right: bias of residuals between ray-tracing and GRAD-1; the residuals are now considerably lowered, albeit being slightly negative. Bottom left and bottom right: the same comparison as above, but regarding standard deviation. Here, as well, the application of GRAD-1 tremendously reduces the residuals at all levels. . 113
- 5.14 Bias (top) and standard deviation (bottom) of the residuals in slant total delay at  $5^\circ$  elevation and  $180^\circ$  azimuth. Top left: bias of residuals between ray-tracing and applying GRAD-1. This figure is equal to the top right plot of the figure before, but differently scaled. Top right: bias of residuals between ray-tracing and GRAD-2. Thus, the negative residuals are mainly removed. Bottom left and bottom right: the same comparison as above, but regarding standard deviation. Here, no noticeable difference is to be seen. . 114
- 5.15 Mean values  $A_0$  (top left), seasonal amplitudes  $A_1$  (top right), half-seasonal amplitudes  $A_2$  (bottom left) and standard deviation of the residuals (bottom right) of the hydrostatic north gradient  $G_{n_h}$  from GPT3. . . . . 118
- 5.16 Mean values  $A_0$  (top left), seasonal amplitudes  $A_1$  (top right), half-seasonal amplitudes  $A_2$  (bottom left) and standard deviation of the residuals (bottom right) of the hydrostatic east gradient  $G_{e_h}$  from GPT3. . . . . 118

- 5.17 *Comparison between discrete and empirical north (top) and east (bottom) gradients for station WETTZELL during the second quarter of 2014. In case of GPT3, the gradients for a specific site are determined through bilinear interpolation from the four surrounding grid points. . . . . 119*
- 5.18 *Left: world map for north gradients  $G_n$  as converted from the north component of DOV  $\xi$ . Right: world map for east gradients  $G_e$  as converted from the east component of DOV  $\eta$ . . . . . 122*
- A.1 *Map showing the locations of the CONT11 stations [ivscc.gsfc.nasa.gov/program/cont11/, date of access: 2016/10]. . . . . 135*
- A.2 *Map showing the locations of the CONT14 stations [ivscc.gsfc.nasa.gov/program/cont14/, date of access: 2016/10]. . . . . 136*
- B.1 *Comparison of pressure from NWM (blue line) and from in situ measurements (green line) for station NYALES20 in 2013. At first sight, the high pressure values of around 1050 hPa look suspicious, however, the in situ measurements show the same result. . . . . 141*
- B.2 *Comparison between  $T$  from NWM (blue line) and from NGS files (green line) for VLBI station HARTRAO for the time period of CONT11. As is evident, the temperatures are not consistent. In particular, the extreme values cannot be captured well by the comparatively low temporal resolution of the NWM data. . . . . 142*
- B.3 *Comparison between  $p$  from NWM (blue line) and from NGS files (green line) for VLBI station WETTZELL for the time period of CONT11. Additionally, the pressure values from GPT2w are delineated (red line). It can clearly be seen that the NGS pressures are systematically higher than those from NWM. . . . . 142*
- C.1 *Map showing temporally averaged values for the  $M_{zwd}$  coefficient of Eq. (3.4) on page 24. The values are fairly constant on land but vary significantly over the seas, where they are apparently connected to ocean currents. 145*
- C.2 *Map showing averaged values for the  $M_{zwd_1}$  coefficient of Eq. (3.5) on page 24, option A. Also here, the presence of ocean currents may play a dominant role for the  $M$  coefficient. On land, the coefficients vary most in areas close to the coast. . . . . 145*
- C.3 *Map showing averaged values for the  $M_{zwd_2}$  coefficient of Eq. (3.5) on page 24, option B. The general pattern of this is fairly similar to the plot on top. 146*

# List of Tables

2.1	<i>Properties of the ray-traced delays which are used to determine VMF1 [Böhm, 2004; Böhm et al., 2006a]. . . . .</i>	10
3.1	<i>Mean BLR (cm) from VLBI analysis when applying the MTT mapping function for CONT11, using temperature from the NGS-files (1), from numerical weather models (2) and from the empirical models GPT (3) and GPT2w (4). . . . .</i>	19
3.2	<i>Correlation coefficients between the quantities averaged over all 14 CONT11 stations from 2011 through 2014 [Landskron et al., 2016d]. . . . .</i>	22
3.3	<i>Values for the <math>M</math> coefficients as determined from NWM data of 19 VLBI stations from 2009-2014 [Landskron et al., 2016d]. . . . .</i>	26
3.4	<i>Values for the <math>M</math> coefficients as determined from NWM data of all 13104 grid points from 2012-2014. . . . .</i>	28
3.5	<i>Mean absolute differences in slant hydrostatic delay <math>\Delta L_h</math> at <math>5^\circ</math> elevation (first column) and zenith wet delay <math>\Delta L_w^z</math> (second column) between high quality values from VMF1 and several SA-GPT2w approaches averaged over 14 VLBI stations and all epochs from 2011-2014. The input parameters for SA-GPT2w, <math>T</math> and <math>e</math>, come from the NGS-files. . . . .</i>	31
3.6	<i>Mean absolute differences in zenith wet delay <math>\Delta L_w^z</math> between high quality zenith wet delays estimated in VieVS and several SA-GPT2w approaches averaged over 13 VLBI stations during CONT11. The input parameters for SA-GPT2w, <math>T</math> and <math>e</math>, come from the NGS-files. . . . .</i>	33
3.7	<i>Mean absolute differences in zenith wet delay <math>\Delta L_w^z</math> between high quality zenith wet delays from the IGS and several SA-GPT2w approaches averaged over 29 IGS stations and all epochs in 2013. The input parameters for SA-GPT2w, <math>T</math> and <math>e</math>, come from close-by weather stations. . . . .</i>	37
3.8	<i>Mean absolute differences in zenith wet delay <math>\Delta L_w^z</math> between high quality zenith wet delays from the IGS and several SA-GPT2w approaches averaged over 26 IGS stations and all epochs in 2013. The input parameters for SA-GPT2w, <math>T</math> and <math>e</math> come from meteorological sensors mounted directly at the GNSS site. . . . .</i>	40

3.9	<i>Mean absolute differences in zenith wet delay <math>\Delta L_w^z</math>, between ray-tracing and several SA-GPT2w approaches averaged over 45 IGS stations and all epochs from 2011-2014. The input parameters for SA-GPT2w, <math>T</math> and <math>e</math> come from NWM interpolated to the very location of the IGS site. . . . .</i>	41
3.10	<i>Mean absolute differences in zenith wet delay <math>\Delta L_w^z</math>, between ray-tracing and several SA-GPT2w approaches averaged over 13 IGS stations close to the equator and all epochs from 2011-2014. The input parameters for SA-GPT2w, <math>T</math> and <math>e</math> come from NWM interpolated to the very location of the respective IGS site. . . . .</i>	42
3.11	<i>Mean BLR (cm) from VLBI analyses for different time periods considering several kinds of models. The input parameters for SA-GPT2w, <math>T</math> and <math>e</math>, come from the NGS-files. The last column shows the averaged values from CONT11 and CONT14, which are regarded as the final results. . . . .</i>	43
3.12	<i>Mean BLR (cm) from VLBI analyses for 1339 VLBI sessions from 2006-2014 considering several kinds of models. Stations TIGOCONC and DSS13 were excluded from the solution, as repeatabilities of baselines containing these stations are extraordinarily high. . . . .</i>	44
4.1	<i>A list of all mapping function approaches mentioned in this chapter. . . . .</i>	52
4.2	<i>Properties of the ray-traced delays that were generated for the derivation of VMF3, in addition to the ray-tracing standard approach (see Tab. A.4 in the appendix on page 139). . . . .</i>	59
4.3	<i>Properties of the ray-traced delays that were generated using the ray-tracer RADIATE for the time period of CONT11, in addition to the ray-tracing standard approach (see Tab. A.4 on page 139). . . . .</i>	70
4.4	<i>Mean BLR (cm) from VLBI analyses for different NWM resolutions for CONT11. . . . .</i>	71
4.5	<i>Mean BLR (cm) from VLBI analyses considering several kinds of mapping functions for the time period of CONT11. In column (1), zenith wet delays <math>\Delta L_w^z</math> are NOT estimated in VLBI analysis, while in column (2) <math>\Delta L_w^z</math> are estimated in VLBI analysis. . . . .</i>	71
4.6	<i>Mean BLR (cm) from VLBI analyses considering several kinds of mapping functions for the time period of 2006-2014. In column (1), zenith wet delays <math>\Delta L_w^z</math> are NOT estimated in VLBI analysis, while in column (2) <math>\Delta L_w^z</math> are estimated in VLBI analysis. Baselines containing VLBI stations AIRA and TIGOCONC are excluded from this comparison as they cause the BLR to increase disproportionately. . . . .</i>	73
4.7	<i>Mean absolute differences in slant total delay <math>\Delta L</math> at <math>5^\circ</math> elevation between ray-tracing and VMF3, once for <math>b</math> and <math>c</math> from the <math>5^\circ \times 5^\circ</math> grid (= VMF3<sub>LSM</sub> (gridded)) and once for <math>b</math> and <math>c</math> from spherical harmonics (= VMF3<sub>LSM</sub> (spherical harmonics)), averaged over all 2592 grid points and 120 epochs. VMF<sub>LSM</sub> is also presented here as a comparative value. . . . .</i>	75

4.8	<i>Mean absolute differences (first column), bias (second column) and standard deviation (third column) in slant total delay <math>\Delta L</math> at <math>5^\circ</math> elevation between ray-tracing and several mapping function approaches, averaged over all 2592 grid points and 120 epochs. . . . .</i>	76
4.9	<i>Mean absolute differences (first column), bias (second column) and standard deviation (third column) in slant total delay <math>\Delta L</math> at <math>3.3^\circ</math> elevation between ray-tracing and several mapping function approaches, averaged over all 2592 grid points and 120 epochs. . . . .</i>	77
4.10	<i>Mean absolute differences in slant total delay <math>\Delta L</math>, slant hydrostatic delay <math>\Delta L_h</math> and slant wet delay <math>\Delta L_w</math> at <math>5^\circ</math> elevation between ray-tracing and VMF1<sub>repro</sub>/VMF3, averaged over all 2592 grid points and 120 epochs. The values for <math>\Delta L</math> in the left column are just overtaken from Table 4.8. . . . .</i>	79
4.11	<i>Properties of the ray-traced delays that were generated using the ray-tracer RADIATE from 1999-2014, in addition to the ray-tracing standard approach (see Table A.4 on page 139). . . . .</i>	81
4.12	<i>Mean absolute differences (first column), bias (second column) and standard deviation (third column) in slant total delay <math>\Delta L</math> at <math>5^\circ</math> elevation between ray-tracing and several mapping function approaches, averaged over all 33 stations and epochs from 1999-2014. . . . .</i>	83
4.13	<i>Mean absolute differences (first column), bias (second column) and standard deviation (third column) in slant total delay <math>\Delta L</math> at <math>3^\circ</math> elevation between ray-tracing and several mapping function approaches, averaged over all 33 stations and epochs from 1999-2014. . . . .</i>	84
4.14	<i>Mean absolute differences at the observed elevation angles in slant total delay <math>\Delta L</math> (first column), slant hydrostatic delay <math>\Delta L_h</math> (second column) and slant wet delay <math>\Delta L_w</math> (third column) between ray-tracing and several mapping function approaches, averaged over all 33 stations and epochs from 1999-2014. . . . .</i>	87
5.1	<i>Properties of the ray-traced delays that were generated using the ray-tracer RADIATE for the time period of CONT11, in addition to the ray-tracing standard approach (see Table A.4 on page 139). . . . .</i>	92
5.2	<i>From Landskron et al. [2015b]: Mean BLR (cm) from VLBI analyses considering several kinds of a priori gradients for the time period of CONT11. In column (1), only a priori gradients are used, while in column (2) the gradients are additionally estimated in the VLBI analysis using the standard gradient formula. . . . .</i>	102
5.3	<i>Properties of the ray-traced delays that were generated using the ray-tracer RADIATE from 2006-2014, in addition to the ray-tracing standard approach (see Table A.4 on page 139). . . . .</i>	104

5.4	<i>Mean BLR (cm) from VLBI analyses considering several kinds of a priori gradients for the time period of CONT11. In column (1), only a priori gradients are used, while in column (2) the gradients are additionally estimated in the VLBI analysis using the standard gradient formula<sup>2</sup>. . . . .</i>	106
5.5	<i>Mean BLR (cm) from VLBI analyses for all 1338 sessions from 2006-2014. In column (1), only a priori gradients are used, while in column (2) the gradients are additionally estimated in the VLBI analysis. . . . .</i>	107
5.6	<i>Mean BLR (cm) from VLBI analyses for all those sessions from 2006-2014 that contain fewer than 3000 observations (1129 out of 1338 sessions, columns 1 and 2) and more than 3000 observations (209 out of 1338 sessions, columns 3 and 4). In (1), only a priori gradients are used, while in (2) the gradients are additionally estimated in the VLBI analysis. When having fewer than 3000 observations per session, using (1.d) instead of (1.a) improves 44% of the BLR by more than 1 mm while it degrades only 4% by more than 1 mm. On the other hand, when having more than 3000 observations per session, using (1.d) instead of (1.a) improves 41% of the BLR by more than 1 mm while it degrades only 9% by more than 1 mm. . . . .</i>	108
5.7	<i>Mean BLR (cm) from VLBI analyses for all those sessions from 2006-2014 that contain fewer than 375 observations per station on average (1133 out of 1338 sessions, columns 1 and 2) and more than 375 observations per station on average (205 out of 1338 sessions, columns 3 and 4). In (1), only a priori gradients are used, while in (2) the gradients are additionally estimated in the VLBI analysis. When having fewer than 375 observations per station and session, using (1.d) instead of (1.a) improves 44% of the BLR by more than 1 mm while it degrades only 3% by more than 1 mm. On the other hand, when having more than 375 observations per station and session, using (1.d) instead of (1.a) improves 40% of the BLR by more than 1 mm while it degrades only 9% by more than 1 mm. . . . .</i>	110
5.8	<i>Properties of the ray-traced delays that were generated using the ray-tracer RADIATE for the global grid, in addition to the ray-tracing standard approach (see Table A.4 on page 139). Note that these are the same specifications as for the derivation of the VMF3 coefficients in Table 4.2. . . . .</i>	112
5.9	<i>Mean absolute residuals (mm) in slant total delay between ray-tracing and applying no gradient formula vs. the three gradient formulae, each for different azimuths <math>\alpha</math> and <math>5^\circ</math> elevation, averaged over all 2592 grid points and 120 epochs from January 2001 to December 2010. VMF3<sub>LSM</sub> is used as mapping function. . . . .</i>	115

---

<sup>2</sup>these results are different to those of Table 5.2 on page 102; the reason for this is that a different calculation strategy of *VieVS* was applied



5.10	<i>Mean BLR (cm) from VLBI analyses considering several kinds of empirical a priori gradients for all sessions from 2006-2014. In column (1), only a priori gradients are used, while in column (2) the gradients are additionally estimated in the VLBI analysis. Using (1.h) instead of (1.a) improves 14% of the BLR by more than 1 mm while it degrades only 6% by more than 1 mm. . . . .</i>	119
5.11	<i>Mean BLR (cm) from VLBI analyses for all those sessions from 2006-2014 that contain fewer than 3000 observations (1129 out of 1338 sessions, columns 1 and 2) and more than 3000 observations (209 out of 1338 sessions, columns 3 and 4). In (1), only a priori gradients are used, while in (2) the gradients are additionally estimated in the VLBI analysis. When having fewer than 3000 observations per session, using (1.h) instead of (1.a) improves 16% of the BLR by more than 1 mm while it degrades only 4% by more than 1 mm. On the other hand, when having more than 3000 observations per session, using (1.h) instead of (1.a) improves 11% of the BLR by more than 1 mm while it degrades 7% by more than 1 mm. . . . .</i>	120
5.12	<i>Mean absolute residuals (cm) in slant total delay between ray-tracing and applying no gradient formula vs. empirical gradients, each for different azimuths <math>\alpha</math> and <math>5^\circ</math> elevation, averaged over all 2592 grid points and 120 epochs from 2001-2010. VMF3<sub>LSM</sub> is used as mapping function. . . . .</i>	120
A.1	<i>Stations participating in CONT11. . . . .</i>	135
A.2	<i>Stations participating in CONT14. . . . .</i>	136
A.3	<i>Settings of the VieVS standard approach. . . . .</i>	138
A.4	<i>Settings of the ray-tracing standard approach. . . . .</i>	139
B.1	<i>Mean absolute differences between the NWM and NGS data for the three meteorological quantities <math>T</math>, <math>p</math> and <math>e</math> and the respective biases and standard deviations <math>\sigma</math>. Outliers were excluded beforehand using the <math>3 \cdot \sigma</math> criterion<sup>3</sup>. . . . .</i>	142

---

<sup>3</sup>the  $3 \cdot \sigma$  criterion means, exemplified with temperature  $T$  here, that all values outside  $\bar{T} \pm 3 \cdot \sigma T$  are regarded as outliers



# Curriculum Vitae

Name	<b>Dipl.-Ing. Daniel Landskron</b>
Date of Birth	1988/07/02
Place of Birth	Linz, Austria
Citizenship	Austria
Address	Treustraße 72/24 1200 Vienna Austria
Email	Daniel.Landskron@gmx.at



## Education

2014/06 – 2017/05	PhD program at Technische Universität Wien
2013/02 – 2013/06	Semester abroad at University of Alaska Fairbanks, USA
2012/02 – 2014/05	Master program "Geodesy and Geophysics" at Technische Universität Wien, graduated with honors
2008/10 – 2012/02	Bachelor program "Geodesy and Geomatics Engineering" at Technische Universität Wien
2007/07 – 2008/01	Basic military service, Weitra
1998/09 – 2007/06	Sports high school "Georg von Peuerbach Gymnasium", Linz
1994/09 – 1998/07	Elementary school, Puchenau

## Work Experience

since 2014/06	Project assistant at Technische Universität Wien
2012/09	Surveying activity for Austrian Federal Forests, throughout Austria
2011/08	Surveying activity for Austrian Federal Forests, throughout Austria
2010/07 – 2010/08	Lifesaver, Linz
2009/07 – 2009/08	Lifesaver, Linz
2008/05 – 2008/09	Lifesaver, Linz
2008/04	Concrete company "Asamer", Linz
2008/01 – 2008/03	Agriculture and forestry, Ottensheim
2006/07	Public works department, Puchenau
2005/07	Public works department, Ottensheim
2004/07	Agriculture and forestry, Ottensheim
2003/08	Public works department, Puchenau

## Hobbies

Sports	Mountaineering, hiking, cycling, soccer
Music	Guitar, piano
Traveling	Bicycle journeys, rail journeys, discovering the unknown

## Languages

German	Mother tongue
English	Fluent